AFOSR-TR- 92 0366

(2)

THE UNIVERSITY OF
ARIZONA
TUCSON ARIZONA

Final Report

AFOSR Grant No. 89-0460

Instabilities of Damage and Surface Degradation Mechanisms in Brittle Material Structural Systems

Submitted to:

Dr. Spencer Wu, Program Manager
Air Force Office of Scientific Research
Bolling Air Force Base
Washington, DC 20332

Submitted by:

F. F. Tang, G. N. Frantziskonis and C. S. Desai
Center for Material Modelling and Computational Mechanics
Department of Civil Engineering and Engineering Mechanics
College of Engineering and Mines
The University of Arizona
Tucson, AZ 85721

REPORT DOCUMENTATION PAGE

Form Approved
OMB No. 0704-0188

1. AGENCY USE ONLY (Leave blank)	2. REPORT DATE	3. REPORT TYPE AND DATES COVERED
	March 15, 1992	Final - 15Jul89 - 31Dec91

4. TITLE AND SUBTITLE
Instabilities of Damage and Surface Degradation Mechanisms in Brittle Material Structural Systems

5. FUNDING NUMBERS
Contract No.
AFOSR 890460

6. AUTHOR(S)
F. F. Tang, G. N. Frantziskonis and C. S. Desai

7. PERFORMING ORGANIZATION NAME(S) AND ADDRESS(ES)
Engineering Experiment Station, and Center for Material Modelling and Computational Mechanics
Department of Civil Engineering and Engineering Mechanics
University of Arizona
Tucson, AZ 85721

8. PERFORMING ORGANIZATION REPORT NUMBER
None

9. SPONSORING/MONITORING AGENCY NAME(S) AND ADDRESS(ES)
Air Force Office of Scientific Research
Bolling AFB, Washington DC 20332
Dr. Spencer Wu - Program Manager

10. SPONSORING/MONITORING AGENCY REPORT NUMBER
AFOSR-89-0460

11. SUPPLEMENTARY NOTES
Appendix contains other publications related to the research.

12a. DISTRIBUTION/AVAILABILITY STATEMENT
Available to public.

12b. DISTRIBUTION CODE

13. ABSTRACT (Maximum 200 words)

A review of the theoretical and experimental information on surface degradation and related instabilities is presented, and the physical significance of surface or skin effects is identified. The research involves study of relation between surface degradation and scale or size as well as shape effects, and surface damage growth instabilities and related bursting in brittle materials. A theory is developed to trace growth of surface degradation and to identify onset of relevant instabilities. Here the internal length is also estimated based on available experimental results. A comprehensive series of laboratory compression tests are performed on rectangular specimens with different dimensions of an artificial rock like material. Simultaneous nondestructive ultrasonic measurements are obtained at various locations on the specimens. The damage and instability distributions obtained by using a finite element procedure and symbolic computation are related to the dissipated energy derived from ultrasonic measurements. Comparisons of theoretical predictions and nondestructive measurements correlate very well.

14. SUBJECT TERMS	15. NUMBER OF PAGES
Surface effects, Degradation, Energy dissipation, Brittle materials, Experiments, Numerical predictions, Verification	217 + 94 (Appendix)
	16. PRICE CODE

17. SECURITY CLASSIFICATION OF REPORT	18. SECURITY CLASSIFICATION OF THIS PAGE	19. SECURITY CLASSIFICATION OF ABSTRACT	20. LIMITATION OF ABSTRACT
Unclassified	Unclassified	Unclassified	UL

PREFACE

INSTABILITIES OF DAMAGE AND SURFACE DEGRADATION MECHANISMS IN BRITTLE MATERIAL STRUCTURAL SYSTEMS

Cotract No. AFOSR-890460

RESEARCH OBJECTIVES

(i) Review the experimental and theoretical information on surface degradation and related instabilities.

(ii) Study the physical significance of surface (skin) effects.

(iii) Study the relation between surface degradation and scale (size) as well as shape effects.

(iv) Study surface damage growth instabilities and their relation to bursting observed in brittle material structures.

(v) Study analytically and/or numerically typical problems and compare with available experimental information.

(vi) Study the micromechanics of surface effects so that the introduced (surface related) internal length can be estimated from experiments.

(vii) Use symbolic computations by computer to obtain solutions for near-surface instability phenomena. Interpret the analytical solution with respect to internal length estimation.

(viii) Perform non-destructive (ultrasonic) and mechanical experiments to obtain quantitative measurements of the surface damage dissipated energy and its relation to instabilities. Compare theoretical predictions and non destructive measurements of dissipated energy.

(ix) Study the problem of transferring information from laboratory experiments to large scale engineering problems.

RESEARCH RESULTS

The research results are shown in the following. Part of the results formed the basis of F.F. Tang's Dissertation. Additional work appears in the appendix. The list of refereed Journal papers, published under the support of the contract , is given next.

PUBLICATIONS (Refereed Journal Papers)

1. G. Frantziskonis and C.S. Desai, 'Degradation Instabilities in Brittle Material Structures,' Mechs. Resear. Commun., 17, 135-141, 1990.
2. G. Frantziskonis and C.S. Desai, 'Surface Degradation Mechanisms in Brittle Material Structural Systems,' Int. J. Fracture, 48, 231-244, 1991.
3. G. Frantziskonis, F.F. Tang and C.S. Desai, 'Borehole Scale Effects and Related Instabilities,' Engr. Fracture Mechs., 39, 377-389, 1991.
4. G. Frantziskonis and I. Vardoulakis, 'On the Micro-Structure of Surface Effects and Related Instabilities,' Europ. J. Mechs., 11, 21-34, 1992.
5. I. Vardoulakis and G. Frantziskonis (1991), 'Micro-Structure in Kinematic-Hardening Plasticity,' Europ. J. Mechs., to appear.
6. G. Frantziskonis, 'Surface Effects In Brittle Materials and Internal Length Estimation,' Appl. Mech. Rev., to appear.
7. G. Frantziskonis, 'Heterogeneity, Microstructural Surface Effects and Internal Length Estimation, Proc. ASCE Specialty Conference, 1992, to appear (also to be submitted to refereed Journal).
8. G. Frantziskonis, C.S. Desai, F.F. Tang, and D. Daniewicz, 'Degradation Mechanisms in Brittle Materials Investigated by Ultrasonic Scanning,' Engr. Fracture Mechs., to appear.
9. F.F. Tang, C.S. Desai and G. Frantziskonis, "Heterogeneity and degradation In Brittle Materials, Engr. Fracture Mechs. submitted.

PARTICIPANTS

G. N. Frantziskonis, Assistant Professor
C. S. Desai, Regents Professor
F. F. Tang, Doctoral Student
D. J. Daniewicz, Research Assistant

ACKNOWLEDGEMENTS

I wish to thank my dissertation director, Dr. G. Frantziskonis, and my co-dissertation director, Dr. C.S. Desai, for their help, encouragement, suggestions, consultations and friendship which helped toward successful completion of my research program.

I would like to thank members of my committee, Dr. P. Kiousis, Dr. D. DaDeppo and Dr. J. Kemeny.

The involvement of Mr. David Daniewicz with the experiments is gratefully acknowledged. He contributed significantly in sample preparation, computer programming, execution, and data acquisition.

I would like to thank Prof. Z.Y. Tao and Dr. D.N. Contractor. Prof. Z.Y. Tao had been my graduate advisor for 4 years before I joined the University of Arizona. Drs. C.S. Desai and D.N. Contractor helped me complete successfully the research program on flow through porous media with cracks.

The ultrasonic test device that was modified for this research was conceived by Dr. C.S. Desai, and developed under grant No. CES-8711764 from the National Science Foundation in which S.V. Jagannath contributed through his doctoral dissertation and in which Dr. T. Kundu participated. The finite element procedure with the damage model used herein and modified was provided from the research grant No. CCE-8415417, Dr. C.S. Desai and Dr. J. Kujawski co-investigators, which formed a part of the doctoral dissertation of L. Woo. These contributions from other ongoing research projects were valuable toward timely and successful completion of the research herein.

I would be glad if I could extend my gratitude to Dr. D. Evans and Dr. T.C. Yeh who recognized my capability to do research on unsaturated flow and solute transport.

The research presented herein was supported from the Air Force Office of Scientific Research contract No. AFOSR-890460 to Dr. G. Frantziskonis and Dr. C.S. Desai. Financial support to the author from National Science Foundation grant No. MSS-9157237 to Dr. G. Frantziskonis is gracefully acknowledged.

Finally, I would like to take this opportunity to thank my wife GuangRong for being patient and understanding and my parents for moral support.

TABLE OF CONTENTS

Page

PREFACE i

ACKNOWLEDGEMENTS iii

LIST OF ILLUSTRATIONS 9

LIST OF TABLES 14

ABSTRACT 15

CHAPTER

1. INTRODUCTION AND SCOPE 17

1.1 General 17

1.2 Objective of Investigation 20

1.3 Summaries of Chapters 21

2. REVIEW AND DISCUSSION 24

2.1 Basic Laws and Concepts 24

2.1.1 Law of Kinetic Energy 24

2.1.2 First Law of Thermodynamics 24

2.1.3 Second Law of Thermodynamics 25

2.1.4 Holonomic (Nonholonomic) System 25

2.1.5 Conservative (Unconservative) System 25

2.2 Mathematical Theory for Stability and Bifurcation 26

2.2.1 General Concepts 26

2.2.2 Bifurcation and Stability of Steady Solutions of Evolution Equations in One Dimension 27

2.2.3 Stability of Steady Solutions of Evolution Equations in Two Dimensions and n Dimensions 29

2.3 Stability for Holonomic Conservative System 30

2.4 Instability of Unconservative System 31
2.4.1 Drucker's Stability Postulate 31
2.4.2 Hill's Stability Condition 32
2.4.3 Mandel's Stability Threshold 35
2.4.4 Instability in Domain 36
2.4.5 On Plastic Flow Localization 36
2.5 Griffth's Criterion 40
2.6 Surface Instabilities and Interface Instabilities 43
2.6.1 General 43
2.6.2 Biot's Surface Instability Theory 44
2.7 Other Subjects 47
2.8 Calculation of Bifurcation Points 49
2.9 Theory for Post-Bifurcation Analysis 51
2.9.1 Gradient Theory 52
2.9.2 Cosserat Continuum Model 53
2.9.3 Non-local Theory 54
3. ENERGY BASED INSTABILITY THEORY 56
3.1 General 56
3.2 Damage Model 57
3.3 Stability of Damage Growth 61
3.4 Surface Degradation 63
3.4.1 General Concepts 63
3.4.2 Surface Degradation with Size and Shape Effects 67
3.4.3 Material Constants Concerned with Surface Effects 68
3.5 Degradation Instabilities and Surface Degradation Instabilities . . . 71
3.6 Conclusion 72

4. IMPLEMENTATION OF THE INSTABILITY CRITERIA 82
4.1 Constitutive Relations for the Elastic-Plastic Undamaged Fraction . 82
4.2 Numerical (Finite Element) Procedures 83
4.3 On Global Degradation Instabilities 85
4.3.1 Analytical Solution of A Simple Problem 85
4.3.2 Numerical Solutions 87
4.3.3 Discussion 88
4.4 On Surface Degradation Instabilities 89
4.4.1 Simple Analysis of A Borehole Problem 89
4.4.2 Numerical Solutions 91
4.4.3 Comments 93
4.5 Conclusion 93
5. PHYSICAL EXPERIMENTS 111
5.1 General 111
5.2 Ultrasonic Experiments 112
5.2.1 Fundamental Terms 112
5.2.2 Absorption and Scattering 114
5.2.3 Intensity Methods for the Ultrasonic Testing of Materials . . . 115
5.2.4 Review of the Existing Literature 116
5.3 Objectives of the Experiments 118
5.4 Equipment and Testing Material 119
5.4.1 Ultrasonic Apparatus 119
5.4.2 Mechanical Load and Material Tested 121
5.4.3 Strain Gages 122
5.5 Ultrasonic Measurements 122
5.6 Test Results 126

5.6.1 Strain Gage Test Results 126
5.6.2 Ultrasonic Test Results 128
5.7 Analytical Considerations 133
5.8 Conclusion 136
6. INITIAL HETEROGENEITY AND DEGRADATION 173
6.1 General 173
6.2 Implementation of Initial Damage 175
6.3 Numerical Solutions 176
6.3.1 Damage Growth Consideration 177
6.3.2 Damage Growth and Surface Degradation Consideration 178
6.3.3 Discussion 179
6.4 Conclusions 180
7. EXTENSION TO POST-INSTABILITY STUDY 193
7.1 General 193
7.2 Gradient Consideration 193
7.2.1 Gradient Regularization for A Plastic Model 193
7.2.2 Gradient Regularization for A Specific Model 198
7.3 Non-Local Damage Consideration for A Specific Model 200
7.4 Physical Modification through Diffusion Assumption 202
8. SUMMARY AND CONCLUSIONS 203
APPENDIX A: ELASTOPLASTIC CONSTITUTIVE RELATIONS . . . 206
LIST OF REFERENCES 208
APPENDIX

LIST OF ILLUSTRATIONS

Figure page

2.1 Schematic of Stress-Strain Curve 32

2.2 An Elastic-Plastic Material (Time-Independent): Rising Curve $\dot{\sigma}\dot{\epsilon} > 0$ (after Drucker 1959) 33

2.3 Wedge-Shaped Region of Stress Path with Decreasing Stresses in which Granular Materials with Nonassociative Flow may be Unstable during Hardening inside the Failure Surface (after Lade 1989) 34

2.4 Half-Space and Co-ordinate System (after Biot 1963) 45

2.5 (a) Particle Velocity and Spin in A Cosserat Continuum; (b) Stresses and Couple Stresses Acting on the Faces of A Material Element in A Cosserat Continuum 55

3.1 Schematic of Damage Influence Zones (after Frantziskonis and Desai 1987) 59

3.2 Schematic of Surface Degradation Zones 65

3.3 Measured Stress-Strain Curves (after Desai, Kundu and Wang 1990) . . 75

3.4 Distribution of Damage Parameter r_t 76

3.5 Distribution of Weighted Damage Parameter $\hat{r}_t$ 77

3.6 Damage Parameter v.s. Deviatoric Strain Trajectory, (a) D=constant, (b) L=constant (after Desai, Kundu and Wang 1990) . 78

3.7 (a) $\ln(\kappa)$ v.s. $C = L^2/D$, (b) R v.s. $C = \mathrm{L}^2/D$ (after Desai, Kundu and Wang 1990) 79

3.8 Distribution of Weighted Damage Parameter $\hat{r}_t$ 80

3.9 Distribution of Weighted Damage Parameter $\hat{r}_t$ 81

4.1 Variation of Apparent Poisson Ration ν 96

4.2 Values of r for Stability at Peak Strength for Uniaxial Load Condition . 97

4.3 Example Problems and Finite Element Meshes 98

4.4 Force-Displacement Curve Using 1 Element;
Circles Indicate Onset of Instability 99

4.5 Force-Displacement Curve Using 4 Element;
Circles Indicate Onset of Instability 100

4.6 Force-Displacement Curve Using 16 Elements;
Circles Indicate Onset of Instability 101

4.7 Stress-Strain Curves and Photograph of Test Specimens at Different
Stress Levels (after Hallbauer, Wagner and Cook 1973) 102

4.8 Experimental Data for Scale Effects for Borehole Problems
(after Haimson and Herrick 1989) 103

4.9 Geometry of A Borehole Problem Structure
under Uniaxial Compressive External Load 104

4.10 Scale Effect Predicted through the Simplified Analysis 105

4.11 Finite Element Mesh for the Numerical Analysis of the Borehole
Problem Depicted in Figure 4.9 106

4.12 Predicted Scale Effect through Examination of the Normal Stress σ_{yy}
at Element 2. 107

4.13 Predicted Scale Effect through Examination of the Maximum
External Applied Stress 108

4.14 Damaged Volume V_{ds} v.s. Energy e for the Borehole Problem of
$R = 10$ cm, $D = 100$ cm. 109

4.15 Predicted Scale Effect through Examination of
Surface Degradation Instability 110

5.1 Schematic of Intensity Method with Sound Transmission 141

5.2 Schematic of the Test System for Ultrasonic Measurements
while Sample Are Subjected to Mechanical Load;
A: External Load Applied through MTS Frame,
B: Device for Movement of Transducers, Shown
in Figure 5.3, C: Strain Gages, D: Transmitting
Transducers, E: Receiving Transducer (after Jagannath, Desai
and Kundu 1991 and Frantziskonis, Desai, Tang and Daniewicz 1991) . 142

5.3 System Designed for the Movement of the Transmitting
and Receiving Transducer; A: Transducer Housing,

B: Stepper Motors for X-Movement (Horizontal),
C: Stepper Motors for Y-Movement (Vertical),
D: Vertical Motion Screws, E: Horizontal Motion Screws,
F: Air Pressure Connections, G: MTS Frame 143

5.4 Photograph of the Setting-up of Test 144

5.5 (a) Prismatic Sample $W \times H \times D$ Showing Direction of
External Load and of Ultrasonic Wave,
(b) Location of Center of Transducers where Measurements
Were Taken for the Three Series of Specimens 145

5.6 Prismatic Sample and Strain Gage Locations
for Strain Gage Tests 146

5.7 Position of Four Strain Gages for Combined
Strain Gage and Ultasonic Scanning Tests 147

5.8 Average Measured Stress-Strain Curves 148

5.9 Data from Test-M4s, (a) Average Stress-Strain Response;
(b) Strain Gage Readings 149

5.10 Strain Gage Readings for Sample PL1 150

5.11 Strain Gage Readings for Sample PL2 151

5.12 Strain Gage Readings for Sample PS1 152

5.13 Strain Gage Readings for Sample PS2 153

5.14 Strain Gage Readings for Sample PM1 154

5.15 Schematic of Surface Slabbing (Spalling) 155

5.16I (a) Picture of Three Samples after Failure at Peak; (a) Sample S3,
(b) Sample M2, (c) Sample L1 156

5.16II Showing of Surface Spalling From Sample PM2 157

5.17 The Change of G with Load Stress for Test-M2, (a) for location 1,2,3,4;
(b) for location 5,6,7,8; (c) for location 9,10,11,12 158

5.18 Spatial Distribution of Initially Received Energy and G for Test-M2 . 159

5.19 Spatial Distribution of Initially Received Energy and G for Test-S3 . . 160

5.20 Spatial Distribution of Initially Received Energy and G for Test-L1 . . 161

5.21 Spatial Distribution of initially Received Energy and G for Loading and Unloading State (P/Ppeak=0.09) for Test-M4s 162

5.22 Spatial Distribution of Initially Received Energy and G for Loading, Unloading, and Reloading for Test-S4s 163

5.23 For Test-S4s, (a) Changes of G of Different Columns with Loading; (b) Strain Gage Readings 164

5.24 For Test-L4s, (a) Spatial Distribution of Initially Received Energy; (b) Strain Gage Readings 165

5.25 Spatial Distribution of initially Received Energy and G for Test-M3 . 166

5.26 For Test-M2, M3, M4s, (a) Change of Mechanically Dissipated Energy with Loading; (b) Change of G with Loading 167

5.27 a v.s. load level $c = P/P_{peak}$ and power fit curve for Test-M2, M3, M4s 168

5.28 a v.s. load level $c = P/P_{peak}$ for Test-S1 169

5.29 a v.s. load level $c = P/P_{peak}$ for Test-S2 170

5.30 Energy $(\Pi + D_m)$ v.s. load level $c = P/P_{peak}$ for Test-M2 171

5.31 Energy $(\Pi + D_u)$ v.s. load level $c = P/P_{peak}$ for Test-M2 172

6.1 Contour of Initially Received Energy for Sample S4 181

6.2 Contour of Initially Received Energy for Sample M2 182

6.3 Function Plot for $\kappa = 50$, $R = 0.5$ 183

6.4 Initial Damage Distribution for Sample S4 184

6.5 Initial Damage Distribution for Sample M2 185

6.6 Finite Element Mesh for Sample S4 186

6.7 Finite Element Mesh for Sample M2 187

6.8 Comparison of Theoretical and Experimental Results for Sample S4 . 188

6.9 Comparison of Theoretical and Experimental Results for Sample S4 . 189

6.10 Comparison of Theoretical and Experimental Results for Sample M2, (a) Theoretical Results without Surface Degradation Consideration, (b) Experimental Results, (c) Theoretical Results with Surface Degradation Consideration 190

6.11 Comparison of Theoretical and Experimental Results for Sample M2 . 191

6.12 Modified Finite Element Mesh to Consider Surface Degradation for Sample M2 192

LIST OF TABLES

Table page

3.1 Measured Peak Stress for Artificial Rock with Various Dimensions (after Desai, Kundu and Wang 1990) 74

3.2 Material Constants κ and R (after Desai, Kundu and Wang 1990) . . . 74

4.1 Summary of Numerical Results 95

5.1 Strain Gage Readings at $P/P_{peak} = 0.5$ 138

5.2 Strain Gage Readings at $P/P_{peak} = 0.85$ 138

5.3 Strain Gage Readings at $P/P_{peak} = 1.0$ 138

5.4 Relative Numbers for Strain Gage Readings at $P/P_{peak} = 0.5$ 139

5.5 Relative Numbers for Strain Gage Readings at $P/P_{peak} = 0.85$ 139

5.6 Relative Numbers for Strain Gage Readings at $P/P_{peak} = 1.0$ 139

5.7 Statistical Distribution of Strain Gage Readings 140

ABSTRACT

In this dissertation, first, the theoretical and experimental viewpoints of instability and bifurcation in mechanics are reviewed and discussed. The onset of instability of bifurcation depends on the constitutive assumptions, and is marked by the loss of ellipticity, singularity of the stiffness matrix, and negative or complex eigenvalues. Non-traditional regularization is necessary to obtain useful post-instability solutions.

Based on dissipated energy and elastic potential, energy based instability criterion is considered and developed. The global instability criterion is concerned with global non-uniform deformation while the surface degradation instability criterion deals with near surface non-uniformities. In addition, the connection between surface degradation and size, shape effects for brittle materials is examined.

The energy based stability theory is applied for some typical problems through analytical and numerical implementations. It is shown that the onset of both surface instability and global degradation instability occurs in the strain hardening stage, that is, before and close to the peak strength. The theoretical results are compared with experimental observations.

Both strain gage tests and ultrasonic scanning tests are processed to study the degradation mechanisms of a brittle material. The surface effects are highlighted by the experiments. Ultrasonically dissipated energy shows a random distribution and it follows, in general, the initial non-homogeneity pattern. The relationship between the ultrasonically dissipated energy and mechanically dissipated energy is dependent on deformation and can be approximated by a power function of the factor of load level.

The theory for surface degradation consideration involves a few material constants, and these constants are identified against experimental observations.

The degradation mechanism and damage growth patterning of simulated rock under uniaxial load are modeled numerically by implementing the theory for damage and surface degradation with initial state consideration. The theoretical

results are compared with experimental observations obtained through ultrasonic scanning tests.

To extend the study to post-instability modelling by using various constitutive models, three alternative considerations are proposed to achieve so-called regularization of the problem.

CHAPTER 1

INTRODUCTION AND SCOPE

1.1 General

Brittle materials such as rock and concrete contain a multitude of defects in the form of micro-voids and/or micro-cracks even before any external load is applied. The term "structure" is associated with such defects. During a loading-unloading process, these voids/cracks may undergo irreversible growth and new ones may nucleate. The ultimate coalescence of such defects may result in macro-crack initiation. The existence of structure and its evolution occurring under the action of an external load affects the local mechanical properties of the material as well as the global behaviour of the material system. It is widely accepted that brittle materials fail by the transformation (nucleation and growth) of the structure. Stress cycling tests have also shown that the structure-transformation manifests as a decrease in the stress/strength and in the unloading stiffness. The structural transformation in particular is the main reason for softening, that is, reduction in strength at increasing straining. The degradation process of the material by structural transformation is termed as damage evolution. The damage is treated as a kinematic variable or tensor (usually second order), the evolution of which results in the gradual degradation of the material. The transformation of structure absorbs energy, named as damage energy, and is an irreversible process. That is, the damage energy is irrecoverable. So it is reasonable to call the damage energy as dissipated energy.

It is recognized that total deformation (strain) in such brittle materials as rock and concrete is attributed to elastic deformation, plastic deformation and to formation of damage. The plastic flow (deformation) corresponds to the propagation of plastic slip, which is also irreversible. So the energy corresponding to plastic deformation, called as plastic energy, is not recoverable either. However, the elastic energy is recoverable. The laws of plastic flow do not differ formally from the kinetic equation for damage evolution in the sense that in both cases they

reflect effects of strain history on the current response of the material. However, they describe different physical processes each of which corresponds to different scales of structure.

The dissipated energy from both damage and plastic flow is a mark of the structural transformation which provides a description of the physical state of the material system. With the increase in the dissipated energy, the apparent stress-strain (force-displacement) curve shows the phenomenon of strain hardening and strain softening, while local stress in the material system changes from homogeneous to inhomogeneous (e.g. uniaxial compression test) and the material system undergoes stable and unstable responses. Some relationship exists between the dissipated energy and the material state (e.g. stable or unstable). In this study, the relationship between instability onset and energy dissipation (rate) is investigated. The stability problem is a wide area and can be divided into mathematical or numerical instability and physical instability. Sometimes they are related, while in other cases they are not. This is concerned with the constitutive law assumed.

Loss of stability and bifurcation are common phenomena in non-linear continuum mechanics. In non-linear structural mechanics, for example, a large body of literature exists mainly concerned with buckling of rods, plates and shells. In non-linear elasticity, bifurcation appears even in seemingly simple problems involving fairly standard constitutive models, such as the classical problem of multiple bifurcation in a cube of Neo-Hookean Mooney- Rivlin materials subjected to hydrostatic pressure [Marsden and Hughes 1983]. Loss of stability also plays a central role in non-linear inelastic constitutive theory. Classical examples include the diffusion necking bifurcation from a homogeneous state which arises in the simple tension test of an elastic-plastic material, and situations where loss of ellipticity of the governing equations takes place leading to localization and the formation of shear bands.

The localization implies a non-uniqueness in the incremental elasto-plastic response of a homogeneous, homogeneously strained body [Rice 1977], and also implies a vanishing speed of acceleration waves [Thomas 1961; Hill 1962; Mandel 1966]. This non-uniqueness consists of the possibility of the occurrence of more than

one strain pattern related to the equilibrated fundamental stress state. It is believed that a constitutive equation can only be used when localization of deformation is excluded, otherwise, the solution (if available) is not unique. So it is important to find out the instability point when dealing with nonlinear continuum mechanics.

Mathematically, the instability usually arises at a critical point in the constitutive behavior, particularly a bifurcation or limit point. The occurrence of such a critical point in a numerical stress analysis is marked by singularity of the stiffness matrix and negative or complex eigenvalues - conditions that traditionally produce severe numerical instability sufficient to disrupt a conventional finite element program. It appears that the subject of direct calculation of stability point has not received adequate attention in the engineering literature. Most of the methods currently employed rely on the inspection of the determinant of the tangent stiffness matrix, and employ simple bisection procedures [Wagner and Wriggers 1988] to calculate the critical points.

In this study, the degradation instabilities include surface degradation and global degradation ones. Surface degradation instability may be related to the onset of surface spalling and/or bursting on stress free surfaces. Global degradation instability refers to the incipient growth of inhomogeneities e.g. shear bands. It is pointed out that the spalling or rock bursting occurs, in general, prior to the global failure or structure collapse. The point where global degradation instability takes place is a critical point from which, when further deformed, the material system is no longer homogeneous and numerical problems may be met for boundary value or initial value problems.

As pointed out previously, the onset of instability of brittle materials is due to the damage accumulation or progressive structural transformation. The term degradation is often associated with damage evolution. The investigation of degradation mechanisms would be helpful to understand the physical process of the onset of instability. The degradation process of brittle materials under external mechanical load can be monitored experimentally, e.g. by using ultrasonic scanning method, and therefore, the degradation patterning can be identified.

1.2 Objective of Investigation

In general terms, the objective of this investigation is to study the relation between instabilities and degradation mechanisms of brittle materials. The energy dissipation due to damage and plastic flow is addressed. Both experimental and theoretical viewpoints are considered, with emphasis on the theoretical studies and interpretation of experimental results.

The objectives of the present work can be summarized as follows:

i) To review the existing theoretical and experimental literature. Mathematical or physical instability criteria for nonlinear inelastic material are addressed. Although post instability analysis is not addressed as part of the theme of this dissertation, the relevant literature on this subject is reviewed. and possible extensions of the present approach are discussed.

ii) To examine an instability criterion which is physically based on dissipated energy and potential.

iii) To extend the instability criterion to consider the surface degradation instability.

iv) To determine the material constants associated with surface degradation for a brittle material.

v) To implement the instability theory into a finite element model.

vi) To examine the instability theory for some typical problems, e.g. borehole problem, analytically and numerically.

vii) To study the degradation mechanism and patterning of a brittle material under external load as observed through experimental measurements.

viii) To identify the surface effects in a brittle material and to estimate the internal material length associated with surface degradation.

ix) To study the degradation patterning numerically with the consideration of initial state and to compare the numerical results with the experimental measurements.

x) To propose possible approaches to overcome the mesh-dependent problem in the post-instability equilibrium path for various models including plasticity and damage effects.

The main contributions of this dissertation can be summarized as:

1) Investigation of the relation between instability onset and energy dissipation.
2) Numerical implementation and analytical examination of energy based instability criteria (global and surface degradation) and solution of typical problems.
3) Experimental investigation of surface effects and degradation inhomogeneity.
4) Determination of material constants and estimation of internal material length associated with surface degradation.
5) Study of evolution of heterogeneity through numerical analysis and comparison with experimental data.
6) Proposition of possible approaches to regularize the solutions for models including plasticity and damage consideration.

1.3 Summaries of Chapters

Following the introduction and scope chapter, chapter 2 reviews the existing literature, in which, important theoretical and experimental viewpoints are considered. First, the basic laws and definitions concerned with this study is reviewed. Then a large part of chapter 2 is devoted to the review of recent literature, particularly stability-related issues.

Chapter 3 describes, in detail, the instability theory which includes global instability criterion and surface degradation instability criterion. The definition for surface degradation zone is discussed and the material constants concerned with surface degradation are identified.

Chapter 4 presents the implementation of the instability theory for some typical problems. For simple problems with linear elastic material behavior, analytical solution is feasible. But for problems with non-linear, inelastic material behavior, search for analytical solution becomes very difficult and numerical procedure is necessary. It is shown that the onset of both surface degradation instability

and global degradation instability occur in the strain hardening stage, that is, before and close to the peak strength. It is also identified that the onset of surface degradation instability occurs before the onset of global degradation instability.

In chapter 5 relevant experimental results are presented. The physical experiments include strain gage tests and ultrasonic scanning tests. The design and setup for ultrasonic scanning tests is described in detail. Some typical experimental observations and analysis are presented. It is found that the degradation patterning follows, in general, the initially received ultrasonic energy distribution. The surface degradation phenomena in brittle materials under external mechanical load is identified and the material constant related to surface degradation zone is obtained. The relationship between ultrasonically dissipated energy and mechanically dissipated energy is approximated by a power function of the factor of load level.

Brittle materials, e.g. rock and concrete, are initially (prior to load application) inhomogeneous (in the macro sense). The initial heterogeneity influences significantly the spatial variation of degradation in a brittle material structure subjected to mechanical load. In chapter 6, the initial heterogeneity is considered by virtue of the concept of initial state and the degradation progress is simulated numerically by using the theory for damage and surface degradation growth. The numerical results are compared with experimental observations.

Chapter 7 proposes methods to overcome problems involved in post-instability analysis. Based on microstructural theories, an internal length parameter can be incorporated into the nonlinear post-instability analysis. It is expected that the introduction of internal length parameter can eliminate the mesh-dependent problem which is met after the onset of instability when FEM is used. The possibility of using the nonlocal damage concept to eliminate the mesh-dependency problem is discussed. There is another possibility to overcome the mesh-dependency problem for a specific damage model, e.g. by considering the deformation inconsistency between the damaged part and intact part. This is also discussed in this chapter.

Finally, a summary of the current work, conclusions, recommendations for extensions of the study are presented in Chapter 8.

CHAPTER 2

REVIEW AND DISCUSSION

As mentioned before, instability in mechanics is a broad and extensively studied area. Mathematically, instability means that a small input may induce large response. In mechanical field, there are many definitions for instability each of which may depict a different physical phenomenon. The whole review for instability is not attempted here. However, only the literature related to this study will be reviewed [Tang, Frantziskonis and Desai 1992b].

2.1 Basic Laws and Concepts

It would be helpful to present some basic laws and fundamental definitions before we go through the general review. It is worth noting that the basic laws and fundamental definitions can be found from the referenced books [Langhaar 1962; Howerton 1962]

2.1.1 Law of Kinetic Energy

The work of all the forces (internal and external) that act on a mechanical system equals the increase of kinetic energy of the system.

In symbols, the law of kinetic energy is expressed by the equation

$$W = \Delta T \tag{2.1}$$

where ΔT is the increment of kinetic energy that results from work W.

2.1.2 First Law of Thermodynamics

The work that is performed on a mechanical system by external forces plus the heat that flows into the system from the outside equals the increase of kinetic energy plus the increase of internal energy.

In symbols, the first law of thermodynamics is expressed by the equation

$$W_e + Q = \Delta T + \Delta U \tag{2.2}$$

Here, W_e is the work performed on the system by external forces, Q is heat that flows into the system, ΔT is the increase of kinetic energy, and ΔU is the increase of internal energy. For adiabatic process, $Q = 0$, then eq. (2.2) becomes

$$W_e - \Delta U = \Delta T \tag{2.3}$$

2.1.3 Second Law of Thermodynamics

The total entropy S contained in the volume V of the medium consists of two parts: the entropy S_e which is exchanged with the environment by means of heat through the surface A, and the entropy S_i contained in the volume under consideration. According to thermodynamics, this second part of the entropy must satisfy the Clausius-Duhem inequality [Derski 1989]:

$$\dot{S}_i = \dot{S} - \dot{S}_e \geq 0 \tag{2.4}$$

where overdot means increment. The second law of thermodynamics is necessarily statistical, and its validity is limited by the laws of statistics [Howerton 1962].

2.1.4 Holonomic (Nonholonomic) System

A material system, between whose possible positions all conceivable continuous motions are also possible motions, is called a holonomic system [H. Hertz 1899]. A system constituted by an elastic material is a holonomic system. A system constituted by the material with plasticity or/and damage behavior is a nonholonomic system.

2.1.5 Conservative (Unconservative) System

A mechanical system is said to be conservative if the virtual work in a virtual displacement that carries the system around any closed path is zero. The internal force of a material with the behavior of elasticity is conservative. The internal force of a material with plasticity and/or damage behavior is unconservative.

2.2 Mathematical Theory for Stability and Bifurcation

2.2.1 General Concepts

In its most general form bifurcation theory is a theory of equilibrium solutions of nonlinear equations [Iooss and Joseph 1980]. By equilibrium solutions, it is meant, for example, steady solutions, time-periodic solutions, and quasi-periodic solutions. It is not possible, yet necessary, to review here all the mathematical theories for stability and bifurcation. However, some basic concepts are presented to give insight in the investigation.

Consider evolution equations of the form

$$\frac{d\mathbf{U}}{dt} = \mathbf{F}(t, \mu, \mathbf{U}) \tag{2.5}$$

Where $t \geq 0$ is the time and μ is a parameter which lies on the real line $-\infty < \mu < \infty$. The unknown in (2.5) is $\mathbf{U}(t)$. $\mathbf{F}(t, \mu, \mathbf{U})$ is a given nonlinear function or operator. When $\mathbf{F}$ is independent of t, t is omitted and write $\mathbf{F}(\mu, \mathbf{U})$. Equation (2.5) governs the evolution of $\mathbf{U}(t)$ from its initial value $\mathbf{U}(0) = \mathbf{U}_0$. An equilibrium solution is a solution to which $\mathbf{U}(t)$ evolves after the transient effects associated with the initial values, have died away.

When $\mathbf{F}(\mu, \mathbf{U})$ is independent of t, the problem

$$\frac{d\mathbf{U}}{dt} = \mathbf{F}(\mu, \mathbf{U}) \tag{2.6}$$

is said to be autonomous. When $F(t, \mu, \mathbf{U})$ is periodic in t with period T, the problem

$$\frac{d\mathbf{U}}{dt} = \mathbf{F}(t, \mu, \mathbf{U}) = \mathbf{F}(t + T, \mu, \mathbf{U}) \tag{2.7}$$

is said to be nonautonomous, T-periodic.

Bifurcation solutions are equilibrium solutions which form intersection branches in a suitable space of functions. For example, when U lies in R^1 the bifurcating steady solutions form intersection branches of the curve $F(\mu, U) = 0$ in the μ, U plane. When $\mathbf{U}$ lies in R^2 the bifurcation solutions form connected intersection surfaces or curves in the three dimensional (μ, U_1, U_2) space. One equilibrium solution bifurcates from another at $\mu = \mu_0$ if there are two distinct

equilibrium solutions $\mathbf{U}^{(1)}$ and $\mathbf{U}^{(2)}$ of the evolution problem, continuous in μ, and such that $\mathbf{U}^{(1)}(\mu_0, t) = \mathbf{U}^{(2)}(\mu_0, t)$.

Not all equilibrium solutions arise from bifurcation. Isolated solutions and disjoint branches of solutions are common in nonlinear problems (G.Iooss and D.Joseph 1980).

Let us subject an equilibrium solution to a small initial perturbation to obtain the linearized theory. If the perturbation grows the equilibrium solution is unstable, and if it eventually decays the equilibrium solution is stable to small disturbances. It may be unstable to larger disturbances, but if it is stable to small disturbances then there is no other equilibrium solutions of the evolution problem close to the given one. Since solutions which bifurcate from a given branch are off that one in a continuous fashion, it is often true (but not always) that a necessary condition for bifurcation is the instability of the equilibrium solution to indefinitely small disturbances. The stability theory for indefinitely small disturbances is linear because quadratic terms in the disturbance equations are negligible compared to linear one.

2.2.2 Bifurcation and Stability of Steady Solutions of Evolution Equations in One Dimension

Consider an evolution equation in R^1 of the form

$$\frac{du}{dt} = F(\mu, u) \tag{2.8}$$

Where $F(.,.)$ has two continuous derivatives with respect to μ and u. Let equilibrium solutions of (2.8) satisfy $u = \epsilon$, independent of t and

$$F(\mu, \epsilon) = 0 \tag{2.9}$$

The study of bifurcation of equilibrium solutions of the autonomous problem (2.8) is equivalent to the study of singular points of curves (2.9) in the (μ, ϵ) plane.

In the study of equilibrium solutions, the following classification of points is introduced [Iooss and Joseph 1980].

i) A regular point of $F(\mu, \epsilon) = 0$ is one for which the implicit function theorem works:

$$\frac{\partial F}{\partial \mu} \neq 0 \quad or \quad \frac{\partial F}{\partial \epsilon} \neq 0 \tag{2.10}$$

if (2.10) holds, then a unique curve $\mu = \mu(\epsilon)$ or $\epsilon = \epsilon(\mu)$ through the point can be found.

ii) A regular turning point is a point at which $d\mu(\epsilon)/d\epsilon$ changes sign and $\partial F(\mu, \epsilon)/\partial \mu \neq 0$.

iii) A singular point of the curve $F(\mu, \epsilon) = 0$ is a point at which

$$\frac{\partial F}{\partial \mu} = \frac{\partial F}{\partial \epsilon} = 0 \tag{2.11}$$

iv) A double point of the curve $F(\mu, \epsilon) = 0$ is a singular point through which pass two and only two branches of $F(\mu, \epsilon) = 0$ possessing distinct tangents. It is assumed that all second derivatives of F do not simultaneously vanish at a double point.

v) A singular turning (double) point of the curve $F(\mu, \epsilon) = 0$ is a double point at which $\frac{\partial \mu}{\partial \epsilon}$ changes sign on one branch.

vi) A cusp point of the curve $F(\mu, \epsilon) = 0$ is a point of second order contact between two branches of the curve. The two branches of the curve have the same tangent at a cusp point.

vii) A conjugate point is an isolated singular point solution of $F(\mu, \epsilon) = 0$.

viii) A higher-order singular point of the curve $f(\mu, \epsilon) = 0$ is a singular point at which all three second derivatives of $f(\mu, \epsilon)$ are null.

Some of the solutions which bifurcate are stable and some are unstable. To study the stability of solution $\mu = \epsilon$ people often study the linearized equation

$$\frac{dz}{dt} = \frac{\partial F(\mu, \epsilon)}{\partial \epsilon} z \tag{2.12}$$

the general solution of which is

$$z = e^{\sigma t} z_0 \tag{2.13}$$

where

$$\sigma = \frac{\partial F(\mu, \epsilon)}{\partial \epsilon} \tag{2.14}$$

Since all solutions of (2.11) are in the form (2.13). It is found that disturbances z or ϵ grow when $\sigma > 0$ and decay when $\sigma < 0$. The linearized theory then implies that $(\mu(\epsilon), \epsilon)$ satisfying $F(\mu, \epsilon) = 0$ is stable when $\sigma < 0$ and is unstable when $\sigma > 0$. This is the so called Conditional Stability Theorem.

2.2.3 Stability of Steady Solutions of Evolution Equations in Two Dimensions and n Dimensions

The most complete results known in bifurcation theory are for problems which can be reduced to one or two dimensions. Consider two-dimensional autonomous problems

$$\frac{d\mathbf{u}}{dt} = \mathbf{f}(\mu, \mathbf{u}) \tag{2.15}$$

where

$$f_i(\mu, \mathbf{u}) = A_{ij}(\mu)u_j + B_{ijk}(\mu)u_j u_k + C_{ijkl}(\mu)u_j u_k u_l + 0(\| u \|^4) \tag{2.16}$$

The same equations (2.15) and (2.16) hold in R^n. In general, the subscripts range over (1,2,...,n); in R^2, n=2.

To test the stability of the steady solution $\mathbf{U}(\mu)$ corresponding to the zero solution $\mathbf{u} = 0$ of (2.15), people examine the evolution of a disturbance $\mathbf{v}$ of $\mathbf{u} = 0$ which, in the linearized approximation, satisfies

$$\frac{d\mathbf{v}}{dt} = \mathbf{f}_\mathbf{u}(\mu, 0|_\mathbf{v}) = \mathbf{A}(\mu).\mathbf{v} \tag{2.17}$$

or, in index notation,

$$\frac{dv_i}{dt} = A_{ij}(\mu)v_j \tag{2.18}$$

The stability to small disturbances of the solution $\mathbf{u} = 0$ is controlled by the eigenvalues of $\mathbf{A}(\mu)$. Set $\mathbf{v} = e^{\sigma t}\mathbf{x}$ in (2.17), it is found that

$$\mathbf{A}(\mu)\mathbf{x} = \sigma\mathbf{x} \tag{2.19}$$

where

$$\sigma(\mu) = \xi(\mu) + i\eta(\mu) \tag{2.20}$$

is an eigenvalue of $\mathbf{A}(\mu)$ if $\mathbf{x} \neq 0$. $\mathbf{u} = 0$ is stable by the criterion of the spectral problem of $\xi(\mu) < 0$ for all eigenvalues $\sigma(\mu)$, and is unstable if there is a value σ solving (2.19) with $\mathbf{x} \neq 0$ for which $\xi(\mu) > 0$.

2.3 Stability for Holonomic Conservative System

The stability for a conservative system can be described by the principle of minimum potential energy. The principle of minimum potential energy dictates that a conservative holonomic system is in a configuration of stable equilibrium if, and only if, the value of potential energy is a relative minimum. From this definition it is understood that:

1) For any mechanical system, it is a sufficient condition. The equilibrium is unstable if there is a path away from the equilibrium position for which virtual work is not negative.
2) A mechanical system is sometimes understood to be in a state of stable equilibrium if positive work must be done on the system in any small displacement away from the equilibrium configuration.

For systems with finite degrees of freedom, the mathematical implications of the principle of minimum potential energy are comparatively simple. The potential energy is a single-valued function of the generalized coordinates $x_1, x_2, ...x_n$. Also, the potential energy V depends on the external loads on the system. The coordinates x_i are considered as regular in a region R of configuration space that includes the configuration of interest. (Coordinates x_i are said to be regular if two conditions are satisfied: (1) the x_i's are independent; (2) on incremental change Δx_i ($\Delta x_j = 0, j \neq i$) in the i^{th} generalized coordinate, will produce a displacement in configuration space (of magnitude) Δs^i that is of the same order of magnitude of Δx_i.) For values of the x's in R, the function V and its partial derivatives to the third order with respect to x's are postulated to be continuous functions of the x's. Then the equilibrium configuration is said to be stable if the second order deviation of the potential energy is positive [Langhaar 1962]. The condition turns out that the stiffness matrix of the system is positive definite.

For systems with infinite degrees of freedom, the mathematical implication of the principle of minimum potential energy is relatively complicated, because the analytical solution can not be obtained for general boundary value problems. The solution is approached by numerical analysis. As computer science develops, the finite element method is popularly used to solve boundary value problems. When the finite element method is used, the infinite degrees of freedom of the system are replaced by finite degrees of freedom [Desai 1972; R.D. Cook 1981]. Then the stability of the system can be evaluated by the general stiffness matrix if proper elements are used.

2.4 Instability of Unconservative System

Brittle materials, such as rock and concrete, when subjected to external mechanical load exhibit the feature of plastic flow and damage accumulation and constitutes an unconservative system, and when compressed at e.g. constant axial strain rate under conditions of either uniaxial stress or triaxial compression exhibits a phenomenon called 'strain softening'. Materials which exhibit such softening are characterized by a constitutive response in which the stress rises monotonically with strain (strain hardening) to a peak, and then decreases with further increases in strain (Figure 2.1). Under general states of small deformation, a material element is said to undergo strain softening when its fourth order tangent stiffness tensor C_{ijkl} is negative definite [Read and Hegemier 1984; Valanis 1984]. Experiments show that even under very low stress, these brittle materials behave nonholonomically. There are many definitions for stability for these brittle material system. In this section, the related theories and concepts are reviewed.

2.4.1 Drucker's Stability Postulate

The stability postulate formulated by Drucker [1951,1956,1959] is basically for solid metals which exhibit associated flow. According to this postulate, stability requires that the second order increment of plastic work is positive or zero.

$$\dot{\sigma}_{ij}\dot{\epsilon}^{p}_{ij} \geq 0 \tag{2.21}$$

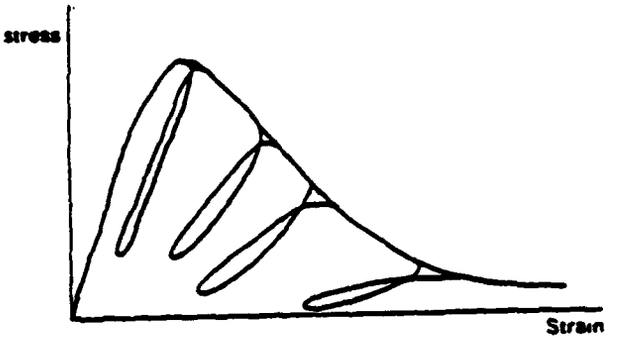

Figure 2.1 Schematic of Stress-Strain Curve

in which $\dot{\sigma}_{ij}$ is the increment of stress and $\dot{\epsilon}^p_{ij}$ is the resulting increment in plastic strain. For metals, positive values of the second increment of plastic work are always associated with the stable, ascending part of the stress-strain relationship, whereas negative values are associated with the unstable, descending part of the stress-strain curve obtained after peak failure, Figure 2.2.

2.4.2 Hill's Stability Condition

Figure 2.3 shows a schematic illustration of the region in which (2.21) is not fulfilled for a material with nonassociated flow. The region is shaped as a wedge

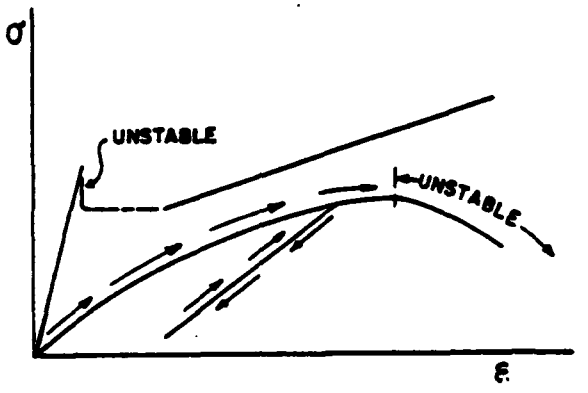

Figure 2.2 An Elastic-Plastic Material (Time-Independent): Rising Curve $\dot{\sigma}\dot{\epsilon} > 0$ (after Drucker 1959)

between the current yield surface f and the plastic potential surface g corresponding to the current stress point. All stresses, including the stress difference $\sigma_1 - \sigma_3$ are decreasing within the wedge between f and g, whereas the effective stress ratio $\sigma_1 / / \sigma_3 /$ is increasing in this region.

According to Hill's condition (Hill,1958), stability should be maintained as long as

$$\int_V \dot{\sigma}_{ij}\dot{\epsilon}^t_{ij}dV = \int_V (\dot{\sigma}_{ij}\dot{\epsilon}^e_{ij} + \dot{\sigma}_{ij}\dot{\epsilon}^p_{ij})dV \geq 0 \qquad (2.22)$$

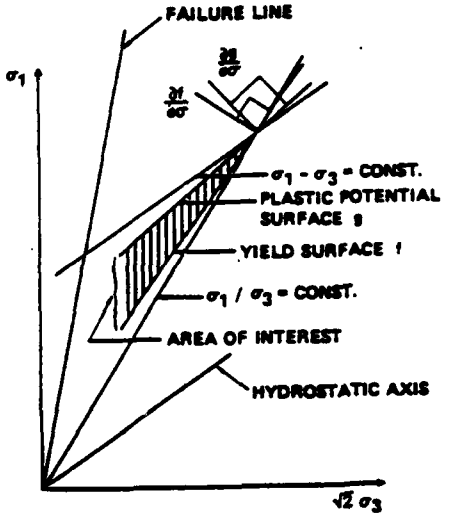

Figure 2.3 Wedge-Shaped Region of Stress Paths with Decreasing Stresses in which Granular Materials with Nonassociated Flow May Be Unstable during Hardening inside the Failure Surface (after Lade 1989)

in which $\dot{\epsilon}_{ij}^{t}$ and $\dot{\epsilon}_{ij}^{e}$ are the total and elastic strain increments, respectively. Along stress paths with decreasing stresses of the type shown in Figure 2.3, the elastic second energy increment has opposite sign of the plastic second energy increment. Hill's stability condition therefore guarantee stability a little beyond the condition given by Drucker [Lade 1989].

2.4.3 Mandel's Stability Threshold

For elastic-plastic solids we can assume that stress and strain rates are related through a fourth order tensor **D** in general non-symmetric:

$$\dot{\sigma} = \mathbf{D} : \dot{\epsilon} \tag{2.23}$$

Tensor **D** is different in loading and in unloading. Assuming that the elastic behavior (unloading) at every point is characterized by a positive definite tensor, Hill's condition is always fulfilled [Ranecki and Bruhns 1981]. If a much more restrictive condition holds, requiring that at every point of the body that the second order work ψ is positive for every strain rate and corresponding stress rate (2.23):

$$\psi = \frac{1}{2}\dot{\sigma} : \dot{\epsilon} > 0 \tag{2.24}$$

Equation (2.24) is referred to as the local criterion for uniqueness [Bigoni and Hueckel 1991]. The central property of the local criterion is the restriction that imposes on the constitutive law (2.23). In fact, substituting (2.23) into (2.24), an equivalent condition of positive definiteness of the constitutive rate tensor **D** is obtained:

$$\mathbf{x} : \mathbf{D} : \mathbf{x} > 0, \quad \forall \mathbf{x} \in Sym - \{0\} \tag{2.25}$$

The above requirement restricts only the tensor **D** during elastoplastic loading.

A condition weaker with respect to the criterion (2.24), but sufficient to exclude strain localization, may be obtained by specializing tensor **x** in (2.25) to a particular rate deformation mode defined by a tensor product $\mathbf{g} \otimes \mathbf{n}$ of a vector **n** and a vector **g**. This yields the requirement of the positive definiteness of every tensor **n.D.n**, i.e.:

$$\mathbf{g} \odot \mathbf{n} : \mathbf{D} : \mathbf{n} \odot \mathbf{g} > 0, \quad \forall \mathbf{g} \neq 0, \forall \mathbf{n} \ni |\mathbf{n}| = 1 \tag{2.26}$$

The requirement (2.26) is the condition of strong ellipticity of the system of differential equations governing the local incremental equilibrium. If the constitutive tensor **D** is symmetric, the condition (2.26) is equivalent to the requirement that all eigenvalues of the tensor are real and strictly positive. The latter condition was stated by Mandel [1966] as a threshold to material stability.

2.4.4 Instability in Domain

The instability of a finite rather than an infinite body has been studied by Kondaurov, Nikitin and Ryzhak [1989]. The instability criterion used can be described as: the equilibrium state of the body is considered unstable if there exists a small virtual displacement field $\delta\mathbf{u}$ for which the work done by the boundary tractions is not compensated by the work done by the internal stresses. Consider elasto-plastic material for which the constitutive law is a piecewise-linear relation between the stress increments and virtual strains, i.e.

$$\delta^J\mathbf{T} = \begin{cases} \mathbf{L^e} : \delta\epsilon, & \text{for } \delta\epsilon : \mathbf{S} < 0; \\ \mathbf{L^p} : \delta\epsilon, & \text{for } \delta\epsilon : \mathbf{S} \geq 0 \end{cases} \tag{2.27}$$

where $\delta^J\mathbf{T}$ is the Jaumann increment of the Cauchy stress tensor, $\mathbf{L}^e$ and $\mathbf{L}^p$ are the fourth rank tensors of elastic and elasto-plastic moduli, $\delta\epsilon$ is strain corresponding to $\delta\mathbf{u}$, and $\mathbf{S}$ is tensor prescribing the normal to the yield surface.

The integral criterion of instability reduces to the requirement of loss of the positive definiteness of the piecewise-quadratic functional [Kondaurov, Nikitin and Ryzhak 1989]

$$\phi\{\delta\mathbf{u}\} = \int_V (\delta\epsilon : \mathbf{L} : \delta\epsilon - \delta^J\mathbf{T}^b : \delta\epsilon)dV \leq 0 \tag{2.28}$$

where $\mathbf{T}^b$ is an auxiliary stress tensor such that $\mathbf{T}^b.\mathbf{n} = \mathbf{t}^b$, $\boldsymbol{\Delta}.\mathbf{T}^b = 0$, and $\mathbf{t}^b$ are the boundary tractions.

The preferable mode of instability is assumed to be that one which corresponds to the earliest moment of loading, i.e. to the greatest value of plastic modulus. Under these assumptions, the effect of constraint on the form of rheological instability manifestation was investigated. Two types of the constraint were considered, namely kinematic and stiffness ones. It was shown that the appearance of a localized mode of instability is influenced by the stiffness constraint [Kondaurov, Nikitin and Ryzhak 1989].

2.4.5 On Plastic Flow Localization

Plastic flow localization refers to circumstances where a macroscopically homogeneous or smoothly varying pattern of plastic deformation develops at low

strains and then at larger strains gives way, more or less abruptly, to a highly localized deformation pattern [Needleman 1990]. There are several plastic instability phenomena that can be regarded as localization in this sense. Shear band localizations are observed in a variety of solids; for example, in geological materials, Waversik and Brace [1971], Vardoulakis [1979], and Lade [1989]. Depending on circumstances, localization can arise either as a consequence of the plastic flow process itself or as the result of progressive damage. Since shear bands have significance as a precursor to fracture and as a mechanism of large strain plastic response, much attention has been given to the mechanics of shear band localization phenomena, Rice [1977], and Needleman and Rice [1978].

For quasi-static deformation histories and rate independent material response, there is a framework that regards localization as a material instability. Deformations in a localized band are permitted provided the velocity field remains continuous and continuing equilibrium at the band interface is satisfied. Bifurcation and imperfection analyses within this framework have proved useful in revealing the influence of constitutive features and stress state on localization, Rudnicki and Rice [1975], Rice [1977] and Needleman and Rice [1978]. In more general circumstances, regions of localization propagate from strain concentrations and a full solution to the relevant initial/boundary value problem is required.

The classical elastic-plastic solid with a smooth yield surface is quite resistant to localization, Rudnicki and Rice [1975] and Rice [1977]. Deviations from the classical constitutive description, in particular yield surface vertex effects and plastic non-normality, significantly lower the strain required for the initiation of localization. Localization can also emerge as a consequence of an explicit softening process, e.g. damage [Frantziskonis and Desai 1987b]. For structural metals yield vertex effects are of general significance since, within the rate independent idealization, the discreteness of slip systems implies a yield surface vertex at the current loading point [Needleman 1990]. Although on quite general grounds the flow potential surfaces for rate dependent solids are expected to be smooth [Rice 1970], the high curvature of flow potential surfaces at the current loading point that comes from the discreteness of slip systems promotes localization when initial

imperfection are accounted for. However, increasing material rate sensitivity can act to delay the onset of localization [Needleman 1988].

The existence of stationary body wave disturbance signals the onset of bulk localization [Hill 1962; Biot 1963; Mandel 1966; Rice 1977]. The effects of boundaries and interfaces on localization were investigated by considering conditions for stationary waves where boundary condition do play a role [Needleman and Ortiz 1991]. In particular, stationary Rayleigh waves along stress free boundaries and stationary stoneley waves along interfaces were considered. The significance of stationary waves stems from their role in signifying the transition from stability to instability; when all possible wave speeds c are such that $c^2 < 0$ for some waves, there is divergence type growth [Rice 1977].

Analysis of Shear Band Localizations:

An element of a solid is considered subject to displacement boundary conditions that in a homogeneous (and homogeneously deformed) solid would give rise to a uniform gradient field. Conditions are sought under which bifurcation into a localized band mode can occur. Current values of field quantities and material properties inside and outside the band are presumed identical so that one possible solution for the incremental quantities corresponds to the homogeneous one. At the considered stage of the deformation history, suppose that within a thin planar band of orientation $\mathbf{n}$ in the reference configuration incremental field quantities are permitted to take on values differing from the uniform values outside the band. The band is presumed sufficiently narrow to be regarded as homogeneously deformed.

Two requirements must be satisfied across the band interface. First, compatibility requires [Thomas 1961; Hill 1962; Mandel 1966; Rice 1977]

$$\dot{\mathbf{F}}_b = \dot{\mathbf{F}}_o + \dot{\mathbf{q}} \otimes \mathbf{n} \tag{2.29}$$

where $()_b$ and $()_o$ denote field quantities inside the band and outside the band, respectively, and $\otimes$ denotes the tensor product so that the component form of $\dot{\mathbf{q}} \otimes \mathbf{n}$ is $\dot{q}^i n_j$, $\dot{\mathbf{F}}$ is strain rate.

For an incompressible solid, the strain rate jump across the band is a shear strain rate jump and, hence, the band is a shear band.

Next, incremental equilibrium requires

$$\mathbf{n}.(\dot{\mathbf{S}}_\mathbf{b} - \dot{\mathbf{S}}_\mathbf{o}) = 0 \tag{2.30}$$

where $\dot{\mathbf{S}}$ is stress rate.

For classical, rate independent plasticity, and for a material element subject to continued plastic loading, a localization bifurcation is possible when

$$[\mathbf{n}.\mathbf{K}_{tan}..\mathbf{n}].\dot{\mathbf{q}} = 0 \tag{2.31}$$

where the operator .. is defined so that the component form of (2.31) is $n_i K^{ijkl}_{tan} n_k \dot{q}_l = 0$ and $\mathbf{K}_{tan}$ corresponds to the plastic loading branch. A localization bifurcation first becomes possible at the earliest stage in the deformation history at which (2.31) has a nontrivial solution, i.e. when the determinant of coefficients in (2.31) vanishes. The outcome of the bifurcation analysis is a critical orientation, $\mathbf{n}$, as well as a critical strain.

Localization is associated with a change in the character of the governing equations. Under quasi-static loading conditions the equations governing incremental equilibrium lose ellipticity, while under dynamic loading conditions wave speeds become imaginary. As a consequence the width of the band of localized deformation is arbitrarily narrow and numerical solutions to localization problems for rate independent solids exhibit an inherent mesh dependence, as discussed in Needleman [1988].

Localization analyses based on (2.31) have revealed the implications of various constitutive features, e.g. yield surface vertices and plastic non-normality, and stress state for the onset of shear localization, Rice [1977], Needleman and Rice [1978]. The Mises solid is quite resistant to localization, Rudnicki and Rice [1975], Rice [1977]. Deviations from the Mises idealization permit a shear band localization to occur with positive hardening. However, the greater susceptibility to localization under plane strain loading conditions remains [Needleman 1990].

For the rate dependent elastic-viscoplastic solids, the counterpart to (2.31) is

$$[\mathbf{n}.\mathbf{K}_{elastic}..\mathbf{n}].\dot{\mathbf{q}} = 0 \tag{2.32}$$

As long as stress levels remain small compared to elastic stiffnesses, the only solution to (2.32) is the trivial one and a localization bifurcation does not occur. Hence, when material rate dependence is accounted for, there is no loss of ellipticity in quasi-static problems and wave speeds remain real. Material rate dependence, in effect, introduces a length scale into the boundary value problem, although the constitutive description does not explicitly contain a material parameter with the dimensions of length, Needleman [1988]. In quasi-static problems, the length scale is one characterizing the imperfection or inhomogeneity. In dynamic problems, it is a characteristic length of propagation of elastic waves. Accordingly, for the viscoplastic constitutive relation, pathological mesh dependence does not occur in numerical solutions for rate-dependent solids.

2.5 Griffth's Criterion

The renowned method of studying fracture in the continuum picture employs energy rate considerations. Consider first the situation of an arbitrarily shaped body, arbitrarily loaded, containing a single traction free propagating crack with instantaneous surface area $A(t)$. Balance of the global energy requires that at each instant of propagation [Eftis and Liebowitz 1975]

$$\dot{W} + Q = \dot{E} + \dot{K} + \dot{\Gamma} \tag{2.33}$$

In (2.33), $\dot{W}$ is external work rate, Q is the energy related to the temperature change in the system, $\dot{E}$ is the strain energy rate, $\dot{K}$ is the kinetical energy rate, and $\dot{\Gamma}$ is the fracture energy rate. By Griffth,

$$\dot{\Gamma} = \gamma \dot{A}(t) \tag{2.34}$$

where $\gamma > 0$ is a fracture surface energy density which represents the energy required to form a unit of new surface and which is assumed to be a constant for

a given material. The usual practice assumes that the loading process is quasi-static, which makes the kinetic energy negligible, and that an initially uniform temperature distribution through the specimen will remain . Then (2.33) becomes as

$$\dot{W} = \dot{E} + \dot{\Gamma} \tag{2.35}$$

By using the chain rule $\frac{\partial}{\partial t} = \dot{A}\frac{\partial}{\partial A}$ we get

$$\frac{\partial W}{\partial A} - \frac{\partial E}{\partial A} = \frac{\partial \Gamma}{\partial A} \tag{2.36}$$

That part of the work rate of the applied forces which is not taken up as change in the elastic and plastic strain work is the energy available to promote crack growth.

Consider the situation where the separation is essentially brittle in nature and the plastic enclave regions are small enough to be ignored. Then E is just the elastic strain energy. Suppose that at some particular level of applied load the existing crack experiences a small increment of growth ΔA. An incremental balance of energy requires that

$$-\Delta P = \Delta W - \Delta E = \Delta \Gamma = \gamma \Delta A \tag{2.37}$$

where $P = E - W$ is the elastic potential energy. Two limiting cases are frequently discussed in the literature. The first assumes that for an arbitrarily small increment of crack growth the outer boundary surface of the solid on which the load is applied can be considered to remain stationary, "fixed grips". If, in addition, the body force distribution is ignored then the work rate contribution of the applied force vanishes and equation (2.36) becomes in the limit as Δa approaches zero

$$-\frac{\partial P}{\partial A} = -\frac{\partial E}{\partial A} = G = \frac{\partial \Gamma}{\partial A} \tag{2.38}$$

In this case the symbol G is appropriately referred to as the "elastic strain energy release rate", since the energy rate required to promote crack growth is supplied at the expense of the existing global elastic strain energy field. In the second case during an arbitrarily small increment of crack growth the applied load is

assumed to remain fixed, the "dead-load" situation. The applied surface traction on the boundary surface does work as the crack extends. However by application of Clapeyron's theorem of linear elasto-statics the work done by the unchanging boundary loads (neglecting body force) is twice the increase of elastic strain energy [Eftis and Liebowitz 1975]. Thus $\frac{\partial W}{\partial A} = 2\frac{\partial E}{\partial A}$ and it follows from equation (2.36) that at the onset of "dead-load" crack extension

$$-\frac{\partial P}{\partial A} = \frac{\partial E}{\partial A} = G = \frac{\partial \Gamma}{\partial A} \tag{2.39}$$

Here there is an increase of global elastic strain energy with "dead-load" crack extension. When the increment of crack extension is sufficiently small, implying correspondingly small load and small displacement changes, then the absolute values of the left sides of equations (2.38) and (2.39) are approximately the same. Hence the magnitude of the elastic strain energy rate associated with such crack extension is about the same in both cases, even though the global elastic strain energy decreases under "fixed-grips" and increases under "dead-load".

Equation (2.38) and (2.39) are both equivalent to part of Griffth's criterion for brittle crack extension, which states that the energy $P + \Gamma = E - W + \Gamma$ of a cracked body has a stationary-maximum value at the inception of crack expansion. i.e.,

$$\frac{\partial(P + \Gamma)}{\partial A} = 0 \tag{2.40}$$

In other words, for an existing crack to expand the quantity $P + \Gamma$ cannot increase with increase in the size of the crack. A sufficient condition for $P + \Gamma$ to be maximum is the added requirement

$$\frac{\partial^2(P + \Gamma)}{\partial A^2} < 0 \tag{2.41}$$

The two conditions (2.40) and (2.41), taken together, represent an analytical statement of Griffth's criteria.

2.6 Surface Instabilities and Interface Instabilities

2.6.1 general

About three decades ago Germer et al [1961] observed surface irregularities in homogeneously strained metal solids. Based on electron diffraction measurements it was concluded that displacements of a superficial layer toward the interior of the metal solid is five times as large as that of the next layer.

The possibility that a plane, tractionless surface of a homogeneously strained solid losses flatness and develops surface undulations, or waves was noted by Biot [1963] in his study of the plane strain deformation of non-linearly elastic solids. His bifurcation analysis of the static deformation of a semi-infinite half-space reveals that the onset of surface modes occurs at a critical stress, or strain, which depends on the properties of the solid. Following Biot's philosophy, an exploratory study was carried out of various aspects of the development of instabilities of traction-free surfaces of statically strained, rate-independent elastic-plastic solids, Hutchinson and Tvergaard [1980]. It is addressed that the surface instability phenomena are closely related to yield vertex effects. In other words, existence of surface instabilities is strongly dependent on the type of constitutive law assumed. Then, localized shear band formation developing from a stress-free surface in a highly strained elastic-plastic material under plane strain was studied by Kitagawa and Matsushita [1987], in which, both geometrical and material factors were considered. Rock bursting as a surface instability phenomenon was investigated by Vardoulakis [1984]. The instability criterion is formulated both in terms of the ratio of the strengths of the material in uniaxial extension and compression, and in terms of an appropriate hardening parameter. Based on Mindlin's theory [Mindlin 1964] for material micro-structure, a single perturbation parameter was introduced to the study of surface effects and related instabilities by Frantziskonis and Vardoulakis [1992].

Thompson [1969] and Benallal et al [1989] have noted that the failure of the complementing condition at the boundary is equivalent to the existence of stationary Rayleigh surface waves. An analogous condition for an ill-posed problem

that arises in cases where interfaces are present is the existence of stationary stoneley waves. Similar to the localization condition, the stationary Rayleigh and stoneley wave conditions determine the condition of shear bands intersecting free surfaces and interfaces, respectively. The stationary wave analyses [Needleman and Ortiz 1991] are related to the surface instabilities investigated by Biot [1965] and Hutchinson and Tvergaard [1980] to the short wavelength limit of the bifurcation solution obtained by Hill and Hutchinson [1975] for plane strain, by Triantafylidis [1980] in pure bending for solids obeying normality and by Needleman [1979] for plane strain and for solids where the symmetry $K_{ijkl} = K_{klij}$ is lacking, and to the interface instabilities analyzed by Biot [1963c]. While these stationary–wave solutions generally correspond to the onset of instability, their shear-band interpretation is restricted to the immediate vicinity of the surface or interface when they precede bulk localization.

In order to understand these studies, it is helpful to review Biot's theory.

2.6.2 Biot's Surface Instability Theory

A solid half-space is subject to a uniform compressive stress P parallel with the surface. Consider an incompressible elastic medium of orthotropic incremental properties. The x axis coincides with the surface, and the y axis is directed positively outward (Figure 2.4). They are also axes of symmetry for the mechanical properties of the medium. The incremental deformation analyzed is a state of plane strain where all variables are functions of x and y. The two-dimensional equations of equilibrium for the stress field are (Biot 1965)

$$\frac{\partial s_{11}}{\partial x} + \frac{\partial s_{12}}{\partial y} - P\frac{\partial \omega}{\partial y} = 0 \qquad (2.42a)$$

$$\frac{\partial s_{12}}{\partial x} + \frac{\partial s_{22}}{\partial y} - P\frac{\partial \omega}{\partial x} = 0 \qquad (2.42b)$$

The rotation ω is defined by

$$\omega = \frac{1}{2}\left(\frac{\partial v}{\partial x} - \frac{\partial u}{\partial y}\right) \qquad (2.43)$$

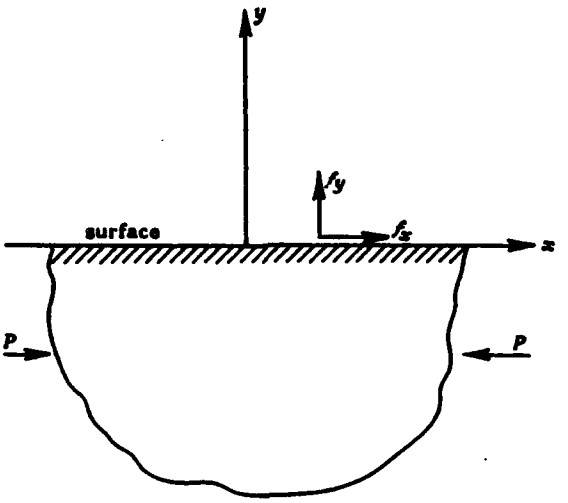

Figure 2.4 Half Space and Coordinate System (after Biot 1963)

where u and v are the displacement components. The stress components s_{11} , s_{22}, s_{12} are the incremental stresses referred to rectangular axes rotated locally through the angle ω. The strains are related to the incremental stress by the relations [Biot 1963]

$$s_{11} - s = 2Ne_{xx} \tag{2.44a}$$

$$s_{22} - s = 2Ne_{yy} \tag{2.44b}$$

$$s_{12} = 2Qe_{xy} \tag{2.44c}$$

These relations introduce two elastic coefficients N and Q and represent a material of orthotropic symmetry. It reduces to the familiar isotropic stress-strain relation for an incompressible material if

$$N = Q \tag{2.45}$$

To consider the medium being incompressible, add the condition:

$$e_{xx} + e_{yy} = 0 \tag{2.46}$$

The condition (2.46) of incompressibility is satisfied by putting

$$u = -\frac{\partial \phi}{\partial y}, \quad v = \frac{\partial \phi}{\partial x} \tag{2.47}$$

The field equations (2.42) then reduce to two equations with two unknowns:

$$\frac{\partial s}{\partial x} - \frac{\partial}{\partial y}[(2N - Q + \frac{1}{2}P)\frac{\partial^2 \phi}{\partial x^2} + (Q + \frac{1}{2}P)\frac{\partial^2 \phi}{\partial y^2}] = 0 \tag{2.48a}$$

$$\frac{\partial s}{\partial y} + \frac{\partial}{\partial x}[(2N - Q - \frac{1}{2}P)\frac{\partial^2 \phi}{\partial y^2} + (Q - \frac{1}{2}P)\frac{\partial^2 \phi}{\partial x^2}] = 0 \tag{2.48b}$$

Solutions of these equations are of the form

$$\phi l^2 = f(ly)\sin(lx) \tag{2.49}$$

$$s = F(ly)\cos(lx) \tag{2.50}$$

Then Biot [1963] derived:

$$(Q + \frac{1}{2}P)f'''' - 2(2N - Q)f'' + (Q - \frac{1}{2}P)f = 0 \tag{2.51}$$

$$F(ly) = (2N - Q + \frac{1}{2}P)f' - (Q + \frac{1}{2}P)f''' \tag{2.52}$$

The primes denote differentiation with respect to the argument ly. The function of f is the general solution of equation (2.51), i.e.

$$f = c_i e^{\beta_i ly} \tag{2.53}$$

where repeat incident means summation and β_i are any of the four roots of the equation

$$\beta^4 - 2m\beta^2 + k^2 = 0 \tag{2.54}$$

It was enforced that:

$$k^2 = \frac{1-\zeta}{1+\zeta}, \quad \zeta = \frac{P}{2Q}, \quad m = \frac{2(N/Q)-1}{1+\zeta} \tag{2.55}$$

Exclude all cases where one of the roots is pure imaginary and assume that

$$m > 0 \qquad with \quad k^2 > 0 \tag{2.56a}$$

$$m < 0 \qquad with \quad m^2 - k^2 < 0 \tag{2.56b}$$

Under these conditions the roots β of equation (2.54) are either real or complex conjugate. Their real part is different from zero, and it is always possible to choose two of them such that their real parts are positive, i.e.

$$\beta_1 = \sqrt{\{m + \sqrt{(m^2 - k^2)}\}} \tag{2.57a}$$

$$\beta_2 = \sqrt{\{m - \sqrt{(m^2 - k^2)}\}} \tag{2.57b}$$

The solution adopted is then

$$f = c_1 e^{\beta_1 l y} + c_2 e^{\beta_2 l y} \tag{2.58}$$

It vanishes at $y = -\infty$.

2.7 Other Subjects

The stability of the flow of saturated inelastic porous media has been investigated in idealized initial and boundary value problems in both quasi-static [Rice 1975; Rudnicki 1983, 1984] and dynamic contents [Vardoulakis 1986]. Emphasis is laid there on the fluid-solid coupling that occurs due to the inelastic volume change taking place in the solid phase. Typically, the point is to analyse the growth of small prescribed inhomogeneities. The qualitative and quantitative results depend

crucially on the assumed initial inhomogeneities. The analysis given by Loret and Harireche [1991] aims at defining the acceleration wave-speeds in inelastic rate-independent porous materials and is centered around the two modes in which the dynamic equilibrium equations lose their hyperbolic character. These modes are referred to as stationary discontinuity (one wave speed is zero) and flutter instability (the squares of two wave speeds are complex conjugate). It is shown that in some circumstances, some wave-speeds cease to be real in the very early stages of the inelastic deformation process due to the incipience of a flutter instability.

Petukhov and Linkov [1979] associate the instability with transformation of the difference between the external forces work increment and the intrinsic energy-to-kinetic energy transition increment accompanied by acquisition of a certain velocity by elements of the medium, and define the lose of stability as the external forces work increment excess (or, at least, non-decrease) over the intrinsic energy increment under constant external conditions. The difference is denoted by ΔK. The state of equilibrium is unstable if a possible field of increment of displacements exist which make $\Delta K \geq 0$. It is pointed out by this theory that the material system may not lose stability in the strain softening stage. The stability termed there is for engineering practice, such as for calculation of pressure acting on support.

The instability in atomic level is referred to the existence of an unstable-symmetric point of bifurcation which precipates the development of an unexpected shearing strain violating the basic symmetry of the system, Thompson and Shorrock [1975]. This kind of instability is highly relevant to crack nucleation and development, since an unstable bifurcation in the tensile zone at the tip of a crack could be a mechanism for destroying the symmetry of a plane propagating crack. Macmillan and Kelly [1972] have confirmed on the basis of a linear eigenvalue analysis that a mechanically stressed perfect crystal can exhibit a bifurcational instability at stresses ranging to 20 per cent below that of the limiting maximum of the primary stress-strain curve. This means that the bifurcational instability in atomic level is met before the peak point is reached.

2.8 Calculation of Bifurcation Points

In the finite element literature, mostly the so called arc-length or path-following procedures are applied to trace stability points, Riks [1972, 1979], Ramm [1981]. Within this approach several algorithms have been introduced to detect bifurcation or limit points [de Borst 1989]. Simple methods for this purpose are given by inspection of the determinant of the tangent stiffness matrix or the calculation of the current stiffness parameter. These methods may not provide a tool to calculate stability points accurately since the basis of path-following is an incremental procedure [Stein, Lammering and Wagner 1989]. A Newton-type method for the direct calculation of stability points has been presented in [Wriggers, Wagner and Miehe 1988] and [Wriggers and Simo 1990] which leads to an extension of the nonlinear set of equation by constraint conditions. By using the linearized eigenproblem at a single bifurcation point as the constraint condition, one obtains the bifurcation mode as part of the solution process [Wriggers and Simo 1990]. The standard iterative solution of extended systems employes a modification of the classical bordering algorithm. From a computational standpoint, two main issues arise in the implementation of this procedure. First, Newton's method often experiences a severe degradation of the asymptotic rate of quadratic convergence near a multiple bifurcation point. Second, the implementation of Newton's method involves the directional derivatives of the tangent stiffness which can only be computed in closed form for a very limited class of problems. In the study given by Wriggers and Simo [1990], the first issue is dealt with by a penalty regularization of the extended system which improves the condition number of the Hessian near a bifurcation point as well as the rate of convergence of Newton's method. In addition, these derivatives are formulated in an alternative form suitable for an approximation by a difference quotient. In the following the general method for bifurcation analysis in geomechanics is presented.

Bifurcation Analysis in Geomechanics

Incremental equilibrium of a structure requires that a stress rate distribution, say $\dot{\sigma}_A$, satisfies

$$\int_V \delta\epsilon^T \dot{\sigma}_A dV = \delta \mathbf{a}^{\mathbf{T}} \dot{\mathbf{F}} \tag{2.59}$$

for all kinematically admissible virtual strain vectors $\delta\epsilon$. Here $\dot{\mathbf{F}}$ is the rate at which the external forces vary and $\delta\mathbf{a}$ is the virtual displacement vector. At a bifurcation point there must exist yet another stress rate distribution, say $\dot{\sigma}_B$, that satisfies incremental equilibrium. Consequently, $\dot{\sigma}_B$ must also satisfy (2.59) and subtraction of both equilibrium equations results in

$$\int_V \delta\epsilon^T \Delta\dot{\sigma} dV = 0 \tag{2.60}$$

with $\Delta\dot{\sigma}$ as difference between both stress rate distributions.

Define $\mathbf{B}$ as the strain-nodal displacement matrix that relates the strain rate vector $\dot{\epsilon}$ to the nodal velocities $\dot{\mathbf{a}}$, i.e.

$$\dot{\epsilon} = \mathbf{B}\dot{\mathbf{a}} \tag{2.61}$$

and suppose that both stress rate distributions are related to strain rate $\dot{\epsilon}$ by the same tangential ralation $\mathbf{D}$:

$$\dot{\sigma} = \mathbf{D}\dot{\epsilon} \tag{2.62}$$

Using (2.61) and (2.62), (2.60) can be written as

$$\delta\mathbf{a}^{\mathbf{T}}\mathbf{K}\Delta\dot{\mathbf{a}} = 0 \tag{2.63}$$

with

$$\mathbf{K} = \int_V \mathbf{B}^{\mathbf{T}}\mathbf{D}\mathbf{B} dV \tag{2.64}$$

where $\Delta\dot{\mathbf{a}}$ is the difference between both velocity distributions, and $\mathbf{K}$ is the tangential stiffness matrix. Since (2.63) must hold for any virtual displacement, the following set of equations is to be valid at bifurcation point [de Borst 1989]:

$$\mathbf{K}\Delta\dot{\mathbf{a}} = 0 \tag{2.65}$$

Write $\Delta\dot{\mathbf{a}}$ as a linear combination of the n right eigenvectors $\mathbf{v}_i$ and the n left eigenvectors $\mathbf{w}_i$ of the matrix $\mathbf{K}$:

$$\Delta\dot{\mathbf{a}} = \Sigma(\mathbf{w}_i^T \Delta\dot{\mathbf{a}})\mathbf{v}_i \tag{2.66}$$

Then (2.65) can be recast in the form

$$\Sigma(\mathbf{w}_i^T \Delta\dot{\mathbf{a}})\lambda_i \mathbf{v}_i = 0 \tag{2.67}$$

Since $\mathbf{K}\mathbf{v}_i = \lambda_i \mathbf{v}_i$ (no summation implied). Assuming that $\mathbf{K}$ is not singular, the right eigenvectors $\mathbf{v}_i$ and the left eigenvectors $\mathbf{w}_i$ each constitute a set of n linearly independent eigenvectors. Consequently, $(\mathbf{w}_i^T \Delta\dot{\mathbf{a}})\lambda_i$ must vanish for each i. Since $\Delta\dot{\mathbf{a}}$ can not be orthogonal to each left eigenvector $\mathbf{w}_i$, this means that at least one eigenvalue, say λ_1, must vanish at a bifurcation point.

In practical numerical analysis, a point where the tangential stiffness has exactly one or more vanishing eigenvalues will never be encountered. Instead it is assumed that a bifurcation point has been passed when at least one (slight) negative eigenvalue is extracted on a monotonically rising part of the load-deflection curve or when two or more negative eigenvalues have been calculated on a descending branch of this curve [de Borst 1989].

2.9 Theory for Post-Bifurcation Analysis

Classical theories of plasticity are not suited for addressing problems of strain localization and deformation patterning. In particular, they break down in the post-bifurcation regime where ellipticity is lost. This is evidenced by the inability of the classical theories to provide any information on shear band thickness and spacings, or any estimate on preferred wavelength in surface instability and liquefaction phenomena [Vardoulakis and Aifantis 1991]. Moreover, the loss of ellipticity manifests itself dramatically in the numerical analysis of large scale problems where one often encounters a critical dependence of the solution on the mesh-size, accompanied by stability and convergence problems.

In classical plasticity analysis, frequent recomputation of the stiffness matrix improves convergence. Yet paradoxically it is a common experience for a

satisfactory program to encounter numerical difficulties when tangent stiffness matries replace a constant elastic matrix in the iterations. Typically, the increments converge with fewer iterations, but the program becomes temperamental about incremental size and eventually reaches a point where no reasonable choice of size will permit convergence [Willam, Pramono and Sture 1986, Crisfield and Wills 1988]. Stable iterations merely indicate convergence to the solution of the finite element model. They do not show whether the discretization in the model is good or whether the physics underlying it is adequate. Thus shear band programs utilizing the strategies mentioned above may converge to a solution, but the shear band width will shrink indefinitely as the mesh is refined instead of stopping at a realistic value. Furthermore, the energy dissipated will be wrongly predicted to be zero [Warburton 1991].

A few approaches have been proposed for removing the aforementioned mathematical difficulties of classical theory. These approaches are gradient theory. Cosserat continuum model, non-local theory, and rate dependent consideration. Brief reviews of these theories are presented in the following.

2.9.1 Gradient Theory

It was shown that inclusion of the second order gradients into the strain energy function of hyperelastic solids prevents loss of ellipticity to occur in the governing equilibrium equations and allows for the description of localized deformations beyond the bifurcation point when the material is well into the softening regime. Triantaphyllidis and Aifantis [1986], Aifantis [1987], Zbib and Aifantis [1988]. Similarly, inclusion of the gradient of equivalent plastic strain into the yield condition has led to the prediction of stationary shear-band widths in rigidly plastic metals and the spacing of travelling Portevin-Le Chatelier bands in viscoplastic metals [Zbib and Aifantis 1988]. The origin of higher order strain gradients in relation to the underlying inhomogeneously evolving microstructures has been discussed by Aifantis [1988]. Another approach for incorporating higher gradients through a "complete balance law" for the inelastic strain containing both a rate and a flux term was proposed by Muhlhaus and Aifantis [1991].

A modified theory of soil plasticity for frictional/dilatant materials was proposed by incorporating second order strain gradients into the dilatancy condition with the remaining structure of both deformation and flow theory being left unaltered [Vardoulakis and Aifantis 1989]. The assumption of a gradient-dependent dilatancy condition was dictated by the experimental observation that localization phenomena in granular media are characterized by strong spatial density variations. These gradients provide a physically sound internal length scale into the problem allowing for the determination of the shear band thickness and the spacing of liquefying strips. The problem of extra boundary conditions required as a result of the presence of higher order strain gradients has been recently addressed in connection with the proposed gradient modification of both flow rule and yield condition with the aid of a variational formulation of the problem [Vardoulakis and Aifantis 1991]. A variational principle and the associated problem of boundary conditions has also been addressed recently by Muhlhaus and Aifantis [1991] in connection with a gradient modification of metal plasticity incorporating gradients of the equivalent plastic strain up to the fourth order into the yield condition. It is noted that Mindlin [1964] was among the first to deal with mechanical theories incorporating higher order strain gradients in the context of linear elasticity, without reference to instability and patterning. However, the underlying continuum model given by Vardoulakis and Frantziskonis [1991] is formally related to Mindlin's elasticity theory with micro-structure. A gradient regularization of the classical kinematic-hardening plasticity was presented in Vardoulakis and Frantziskonis [1991], in which, the flow rule of classical plasticity was modified by incorporating the Laplacian of the plastic multiplier.

2.9.2 Cosserat Continuum Model

Unlike the gradient approach, in the Cosserat model [Cosserat, E. & F. 1909; Muhlhaus 1985, 1986] both the continuum and the constitutive description are altered as compared to the classical description. In the pre-bifurcation regime of the classical description, the assumption is made that mean particle rotations coincide with the average spin of the representative grain assembly [Vardoulakis

1989]. Beyond the bifurcation point this assumption must be relaxed. This can be done by employing the concept of a Cosserat continuum that allows for both particle displacements and particle rotations. In plane-strain problems, this means that at any material point of the continuum both a velocity $\mathbf{v} = v_i \mathbf{e}_i$ (i=1, 2) and a spin vector $\mathbf{w}^c = \omega^c \mathbf{e}_3$ are assigned, Figure 2.5(a). In this case the objective strain-rate measures

$$\dot{\epsilon}_{ij} = \dot{\eta}_{ij} + \dot{\omega}_{ij} - \dot{\omega}^c_{ij}, \qquad \dot{\chi}_i = \omega^c_{3,i} \tag{2.68}$$

are introduced [Muhlhaus and Vardoulakis 1987] where $\dot{\eta}_{ij} = (v_{i,j} + v_{j,i})/2$ and $\dot{\omega}_{ij} = (v_{i,j} - v_{j,i})/2$ are the classical strain rate and spin tensors, $\dot{\omega}^c_{ij} = -e_{ij3}\omega^c_3$ is the Cosserat spin tensor and $\dot{\chi}_i$ the curvature-rate vector. Furthermore, strain-rate and curvature-rate tensors are decomposed into an elastic and a plastic part:

$$\dot{\epsilon}_{ij} = \dot{\epsilon}^e_{ij} + \dot{\epsilon}^p_{ij}, \qquad \dot{\chi}_i = \dot{\chi}^e_i + \dot{\chi}^p_i \tag{2.69}$$

At any material point of the Cosserat continuum a non-symmetric stress tensor σ_{ij} and a couple stress tensor m_i are defined, Figure 2.5(b). Intergranular tractions t_i are defined through an equivalent stress tensor which in turn is related to the Cauchy stress and the couple stress

$$t_i = \tau_{ij} n_j, \qquad \tau_{ij} = \sigma_{ij} + e_{ij3} m_k n_k / R \tag{2.70}$$

For vanishing couple stresses, the equivalent stress coincides with Cauchy stress. Notice that the above defined intergranular tractions are dual in energy to the Cosserat kinematic field.

2.9.3 Non-local Theory

The concept of non-local continuum, introduced on the basis of statistical analysis of heterogeneous materials by Kroner [1967] and Krumhanzl [1968], and widely applied by Eringen and Edelen [1972] and others, was proposed for application to strain-softening models in Bazant [1984] and Bazant, Belytschko and Chang [1984]. Then, numerous particular forms of non-local formulations were developed. For example, in Pijaudier-Cabot and Bazant [1987], only the softening

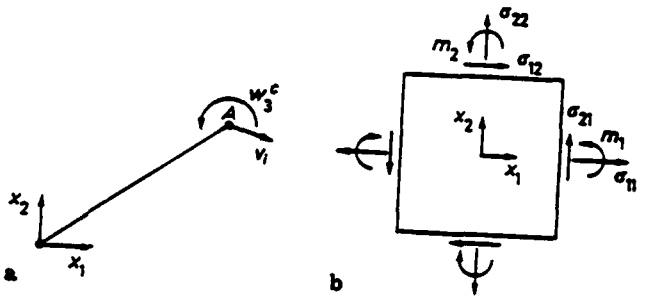

Figure 2.5 (a) Particle Velocity and Spin in a Cosserat Continuum; (b) Stresses and Couple Stresses Acting on the Faces of A Material Element in A Cosserat Continuum

damage was treated as non-local while the elastic behaviour was treated as local; in Bazant and Pijaudier-Cabot [1987], the model for strain-softening subjected to non-local description those variables which cause strain softening and retained a local definition of strain, that is, the material model is characterized as a non-local continuum with local strain; in Bazant and Lin [1988], some of the variables in the constitutive equations (e.g. plastic strain) were defined by spatial averaging.

CHAPTER 3

ENERGY BASED INSTABILITY THEORY

In this chapter, energy based instability theory is presented. A surface degradation zone is defined to consider the surface effects of brittle materials under external load. The material constants concerned with surface degradation are identified against experimental observations.

3.1 General

In the field of mechanics, instability can be classified, generally, as material instability and geometrical instability. Neglecting the geometrical non-linearity and considering the inelastic material behavior, then the relevant instabilities belong to the category of material instability. For brittle materials such as rock and concrete, for the displacement gradient, $|u_{i,j}| << 1$ stands. For example, the maximum strain corresponding to the peak strength for uniaxial compressive test on rock and concrete is less than 3%. So it is reasonable to assume small deformation and consider geometrical linearity. However, as pointed out previously, the mechanical system composed of these brittle materials is a nonholonomic one, and the total deformation is attributed to elastic deformation, plastic deformation and to formulation of damage. Then, the instability criteria established in this study is restricted to material instability. However, the basic idea might be extended to geometrical instability study.

As for material instability, quite a few criteria have been proposed, as reviewed in chapter two. Drucker's stability postulate, Hill's stability condition and Mandel's stability threshold are for elastic-plastic materials. Griffth's criteria describes the stability of macro-crack development. When the kinematic damage evolution is included in an elasto-plastic model, a new instability criterion is needed to predict the onset of unstable damage growth. In this chapter, the proposed instability criteria are described in detail. These instability criteria are, in some sense, similar to the well-known Griffth's criterion. However, essential difference exists

between the two instability criteria. The Griffth's criterion deals with the macro-crack, while the proposed instability criteria deal with the degradation process. The onset of unstable damage growth may manifest inhomogeneous deformation, e.g. shear bands.

The proposed instability criteria are implemented with the two-component damage model originated by Frantziskonis and Desai [1987]. So, for completeness, discussion and basic formulation of the two-component damage model will be presented first. It should be noted that these instability criteria are, in general, applicable to every model accounting (in some form) for material degradation and relevant dissipated energy. Here, however a specific model is employed, as described below. Another important part of this chapter is devoted to the description of surface degradation instability which depicts the common phenomenon for brittle materials under external load such as surface spalling and/or borehole collapse. The formulation of surface degradation instability criterion is the extension of the concept of general damage instability description. However, as can be seen later, the surface degradation instability criterion can capture some important aspects such as shape and scale effects.

3.2 Damage Model

A number of investigators have considered the effects of damage on the mechanical behavior of brittle materials directly or indirectly [Yamaguchi and Chen 1991]. Within the so-called phenomenological framework, the nonlinear inelastic response of brittle materials is attributed to the combination of micro-crack growth and frictional slip. The goal of the phenomenological theory is to evaluate the effective properties of the material, through consideration of a representative volume element. This element is a subregion of the heterogeneous material that represents itself over the entire body. A microcrack or microcrack network contributes to the properties of the region around it. Thus the region can be regarded as a composite material having two distinct phases: damaged material characterizing the nucleation and evolution of the microcracks; and undamaged or "normal" accommodating such microcracks that will develop. This region may appear homogeneous at a

large scale with certain effective properties that describe the medium in an average sense. With this in mind appropriate average static and kinematic variables can be introduced. In order to determine the effective material properties, the assumption of absence of diffusion has been employed in [Frantziskonis and Desai 1987] which leads to equal strains with the two phases. This can be considered equivalent to the so-called Voigt assumption for composites [Yamaguchi and Chen 1991].

In terms of the decomposition and description of softening, the damage model proposed by Frantziskonis and Desai [1987] is similar to that proposed by Kachanov [1958], Desai [1974]. It is noted that the formulation presented in the following is referred to Frantziskonis and Desai [1987], and Frantziskonis [1989].

Consider a small volume ΔV of the material. This volume is subdivided into an intact (undamaged) part, ΔV_u, and into a "fractured" (damaged) part, ΔV_d, (Figure 3.1). The first part or fraction represents topical (continuum) behavior, and the material in it is intact in the sense that no microcracks are induced. Due to inhomogeneity of the material behavior at the microlevel, weak planes are developed leading to crack formulation and subsequent propagation. The effect of an isolated or coupled fracture site is that an influenced zone exists around it as shown schematically in Figure 3.1. This influence zone has volume ΔV_d. Under continued loading, influence zones increase so that ΔV_d increases. At every instant of time, the ratio

$$r = \frac{\Delta V_d}{\Delta V} \tag{3.1}$$

is called damage volume ratio. The material point consists of the superposition of a material point of the undamaged fraction (called the u-part) and of a material point of the damaged fraction (called the d-part). This suggests the use of the theory of interacting continua, Bowen [1975]. As a consequence, the following relation is applicable

$$\sigma_{ij} = (1 - r)\sigma^u_{ij} + r\sigma^d_{ij} \tag{3.2}$$

where σ^u_{ij}, σ^d_{ij} denote the stress tensors in the u and d -part of the material element respectively and σ_{ij} is the average stress tensor. The general theory of mixture [Bowen 1969, 1975] is simplified considerably if diffusion is absent. In the proposed

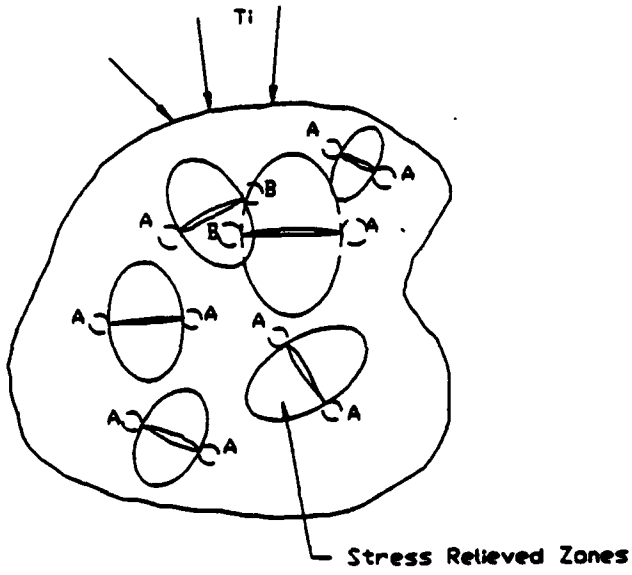

Figure 3.1 Schematic of Damage Influence Zone (after Frantziskonis and Desai 1987)

theory, the assumption of no diffusion is employed and as mentioned previously this is equivalent to the Voigt assumption serving as a bound to the Voigt-Reuss one [Yamaguchi and Chen 1991; Tang, Desai and Frantziskonis 1991]. Then the strains in the two material phases are considered equal [Bowen 1975].

Now, a material element is considered. Due to the enforced deformation in the element, damage influence zones have been created but failure has not occurred yet. Such influence zones depict the mechanical influence of a system of microcracks. The constitutive equations for the d-part can be established as

$$\dot{\sigma}^d_{ij} = C^d_{ijkl}\dot{\epsilon}_{kl} \tag{3.3}$$

and C^d_{ijkl} is a function of parameters related to the degraded properties of the material. Since there are no microcracks in the u-part, its constitutive relations can be identified as

$$\dot{\sigma}^u_{ij} = C^u_{ijkl}\dot{\epsilon}_{kl} \tag{3.4}$$

and if the undamaged fraction is linearly elastic (e.g. for composites), C^u_{ijkl} contains the usual linear elasticity constants. If plasticity effects are included then a generalized hierarchical elastic-plastic model is employed [Desai et al 1986].

The irreversible nature of damage implies that the material experiencing it obeys nonholonomic laws. Thus the problem is formulated in rate form of the governing equations and the constitutive relations are derived from (3.2)-(3.4) as

$$\dot{\sigma}_{ij} = L_{ijkl}\dot{\epsilon}_{kl} - \dot{r}(\sigma^u_{ij} - \sigma^d_{ij}) \tag{3.5}$$

where

$$L_{ijkl} = (1-r)C^u_{ijkl} + rC^d_{ijkl} \tag{3.6}$$

From (3.5) it can be seen that although r, $\dot{r}$ are scalers, a tensor namely, $\dot{r}(\sigma^u_{ij} - \sigma^d_{ij})$. is introduced in the formulation. This tensor is responsible for damage induced anisotropy, an obvious property of cracked materials. Further, an evolution law for r is defined and it is directly related to failure where r reaches a critical value r_{cr}. A general law can be written as

$$\dot{r} = f(\epsilon_{ij}, \dot{\epsilon}_{ij}) \tag{3.7}$$

Specifically, the following is used:

$$r = r_u - r_u exp(-\kappa \xi_d{}^R) \tag{3.8}$$

where

$$\dot{\xi}_D = (\dot{e}^p_{ij} \dot{e}^p_{ij})^{1/2} \tag{3.9}$$

and e_{ij} denotes the deviator tensor of ϵ_{ij}. r_u is the ultimate value of r and κ, R are damage related material constants.

3.3 Stability of Damage Growth

In the previous section a structural transformation theory was introduced for the description of the process of damage growth. When a structural system is subjected to increasing external load, depending on the state of the material an instability may occur resulting to sudden and often localized deformation. The purpose of this section is to establish an instability criterion to examine the stability of damage growth, Frantziskonis and Desai [1987], Frantziskonis, Tang and Desai [1991].

From the thermodynamic point of view, the state of the material can be characterized by its strain energy density ψ defined as

$$\rho\psi = \frac{1}{2}\sigma_{ij}\epsilon_{ij} \tag{3.10}$$

where ρ is mass density. The dissipated energy density (due to plastic slip and damage growth) is expressed as

$$\phi = \int_0^t \sigma_{ij}\dot{\epsilon}_{ij}dt - \frac{1}{2}\sigma_{ij}\epsilon^e_{ij} \tag{3.11}$$

where ϕ is the total dissipated energy density over real time t and superscript e indicates elastic (recoverable). From (3.10) and (3.11) the internal elastic energy density rate is obtained as

$$\dot{W} = \frac{1}{2}(\sigma_{ij}\dot{\epsilon}^e_{ij} + \dot{\sigma}^e_{ij}\epsilon^e_{ij}) = \sigma_{ij}\dot{\epsilon}_{ij} - \dot{\phi} \tag{3.12}$$

The total dissipated energy density rate is decomposed into plastic energy density rate and damage energy density rate, as

$$\dot{\phi} = \dot{p} + \dot{d} \tag{3.13}$$

with

$$\dot{p} = \frac{1}{2}(\sigma_{ij}\dot{\epsilon}^p_{ij} + \dot{\sigma}_{ij}\epsilon^p_{ij}) \tag{3.14}$$

$$\dot{d} = \frac{1}{2}(\sigma_{ij}\dot{\epsilon}_{ij} - \dot{\sigma}_{ij}\epsilon_{ij}) \tag{3.15}$$

Let V be the volume of a structure and S its boundary. The rate of work of external forces T_i (neglecting body force) is

$$\dot{H} = \int_S T_i\dot{u}_i dS \tag{3.16}$$

with u_i being the displacements. Let

$$\dot{U} = \int_V \sigma_{ij}\dot{\epsilon}_{ij} dV \tag{3.17}$$

$$\dot{E} = \frac{1}{2}\int_V (\sigma_{ij}\dot{\epsilon}^e_{ij} + \dot{\sigma}_{ij}\epsilon^e_{ij}) dV \tag{3.18}$$

$$\dot{P} = \frac{1}{2}\int_V (\sigma_{ij}\dot{\epsilon}^p_{ij} + \dot{\sigma}_{ij}\epsilon^p_{ij}) dV \tag{3.19}$$

$$\dot{D} = \frac{1}{2}\int_V (\sigma_{ij}\dot{\epsilon}_{ij} - \dot{\sigma}_{ij}\epsilon_{ij}) dV \tag{3.20}$$

Considering adiabatic process, then from (3.12-3.20) and from the equation of balance of rate of energy

$$\dot{H} = \dot{U} = \dot{P} + \dot{D} + \dot{E} \tag{3.21}$$

The potential energy Π is expressed as

$$-\Pi = H - E \tag{3.22}$$

and since during the deformation process the total volume V_d changes

$$-\frac{\partial \Pi}{\partial V_d} = \frac{\partial D}{\partial V_d} + \frac{\partial P}{\partial V_d} = G \tag{3.23}$$

G being the strain energy transformation (from u to d-phase) rate. The stability of the transformation law is then governed by

$$-\frac{\partial^2 \Pi}{\partial (V_d)^2} - \frac{\partial^2 D}{\partial (V_d)^2} - \frac{\partial^2 P}{\partial (V_d)^2} > 0 \tag{3.24}$$

If the above inequality is satisfied at any time during the loading process, unstable deformation is possible. Such an unstable deformation could, depending on the problem, localize into a small portion of the structure or could lead to periodic localizations. It is noted that the above relation represents an analytical criterion similar to the one proposed according to Griffth's theory [Eftis and Liebowitz 1975]. The physical interpretation of (3.24) may be expressed as: a brittle material system may undergo unstable damage growth if the rate of the increment of external work per unit damaged volume is higher than that of internal energy per unit damaged volume.

3.4 Surface Degradation

3.4.1 General Concepts

Review on surface degradation is presented here. Further details can be found in Frantziskonis [1989], Frantziskonis and Desai [1991], Frantziskonis, Tang and Desai [1991].

It has been observed that in many engineering materials surface unevenness (roughness) grows with increase in strain [Kitagawa and Matsushita 1987]. Surface roughness is induced by microstructural inhomogeneity and its growth is initially stable. It is necessary to mention that there is certain evidence that this phenomenon acts as a trigger effect on shear bands appearing in the specimen.

The sudden growth of surface roughness results in the occurrence and development of shear band penetrating into the body [Kitagawa and Matsushita 1987; Yukutake 1989]. Microscopically a heterogeneous structure of the material produces an inhomogeneous deformation field from a very early straining stage. However, irregularity of deformation in the body is not uniform, but there is a part in which the irregularity is greater than that in other ones, that is, near the surface. These observations are also evident in existing extensive experiments on brittle materials [Hudson, Brown and Fairhurst 1971; Fairhurst and Cook 1966]. Because the constraints to crack development are smaller near the surface than far from the surface and the near surface microcracks have a greater tendency toward propagation (for the reason that the stress intensity factor for such a crack is higher than for a same size or even bigger crack in the interior), development of microcracks is more pronounced near the free surface. Then damage distribution at the edge of a specimen where surface degradation is of importance is expected to be significantly different from the damage distribution far from the edge.

Consider that damage at the edge due to surface effects is additive to the damage accumulation due to deformation without surface effects. So at the edges a small volume (the total elementary volume) ΔV_s is subdivided into an intact part ΔV_{su} and into a damaged part ΔV_{sd}, and further, ΔV_{sd} includes ΔV_{sd1} (damaged volume without surface effects consideration) and ΔV_{sd2} (damaged volume due to surface effects only). It is considered that the above subdivision holds for a distance ρ from the edge (Figure 3.2), where ρ is a positive real number dependent on the material properties, the geometry, and the load on the structure. At an instant of time the edge damage parameter is defined as

$$r_t = \frac{\Delta V_{sd}}{\Delta V_s} = \frac{\Delta V_{sd1}}{\Delta V_s} + \frac{\Delta V_{sd2}}{\Delta V_s} \tag{3.25a}$$

or

$$r_t = r + r_e \tag{3.25b}$$

with

$$r = \frac{\Delta V_{sd1}}{\Delta V_s} \tag{3.25c}$$

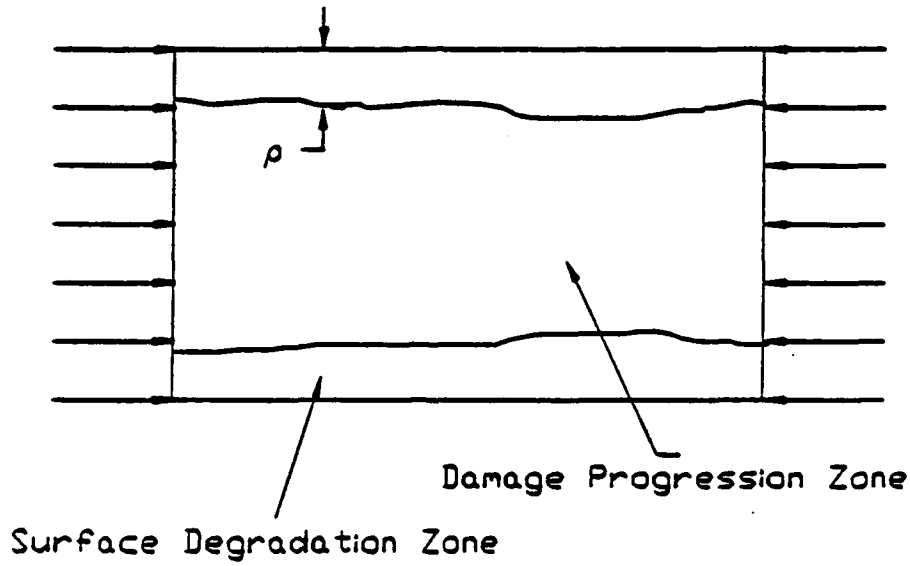

Figure 3.2 Schematic of Surface Degradation Zones

$$r_e = \frac{\Delta V_{sd2}}{\Delta V_s} \tag{3.25d}$$

Here r_e is expected to be maximum at the edge and its value decreases continuously till a minimum value expected to be at a distance ρ from the edge. Let us consider the following volume average, per unit area in the plane parallel to the stress-free surface:

$$\hat{r} = \frac{1}{\rho}\int_{\rho} r_e ds \tag{3.26}$$

Also the following average stress can be introduced

$$\hat{\sigma}_{ij} = \frac{1}{\rho}\int_{\rho} \sigma_{ij} ds \tag{3.27}$$

Based on physical reasoning, it is possible to establish a connection between the average values of damage and stress as defined above and the dimension related parameter ρ. At the effective surface degradation volume total damage ratio is considered as

$$\hat{r}_t = r + \hat{r} \tag{3.28}$$

Note that $\hat{r}_t$ can be greater than r_{cr} since $0 \leq r \leq r_{cr}$. Here r_{cr} is the ultimate value of damage variable r. But in general

$$0 \leq \hat{r}_t \leq 1 \tag{3.29}$$

The parameter r as a function of ξ_D is well defined [in section 2 at this chapter, Frantziskonis and Desai 1987]. It is possible to express parameter r_e as another function of ξ_D and space. But it may be more convenient to consider the damage parameter r_t along the surface degradation zone(s) be depicted by the damage parameter without surface degradation consideration multiplied by an amplification function. Consider the problem as shown in Figure 3.2, we can write

$$r_t = r\{exp[\lambda(x - D/2 + \rho)]\}, \quad D/2 - \rho \leq x \leq D/2 \tag{3.30}$$

where

$$\lambda = \lambda(\hat{r}) \tag{3.31}$$

and x is the distance from the center of the sample to free surface, and D is the diameter (or width) of the sample. Then, we have

$$r_e = r\{exp[\lambda(x - D/2 + \rho)] - 1\}, \quad D/2 - \rho \leq x \leq D/2 \tag{3.32}$$

It is noted that the exponential assumption considered here agrees with the surface bifurcation studies originated by Biot [1963, 1965]. Considering the weighting integration (3.26), we obtain

$$\hat{r} = r(\frac{e^{\rho\lambda}}{\lambda} - \frac{1}{\lambda} - 1), \quad D/2 - \rho \leq x \leq D/2 \tag{3.33}$$

For a sample with height=5", width (diameter) D=4", and ρ = 1" (to be discussed in the following chapters) under uniaxial compression, if we take $\lambda = constant = 2$ (a simplified case and to be discussed later), the distribution of damage parameter r_t and weighted damage parameter $\hat{r}_t$ can be obtained as shown in Figure 3.3 and Figure 3.4, respectively. Here, it is noted that, in an average sense, the damage parameter in the internal zone is amplified by 3.19 times in the surface degradation zone.

3.4.2 Surface Degradation With Size and Shape Effects

It is well known that the deformational characteristics of brittle materials depend on the size and shape of a structure. In a specimen subjected to uniaxial stress, when the ratio of height to width (diameter for cylindrical specimens) of the sample is increased the level of (macroscopic) stress at unstable failure decreases, as shown by experiments [Hudson, Brown and Fairhurst 1971; Desai, Kundu and Wang 1990].

Let us introduce the concept of effective surface degradation volume. For high ratios of height to width this volume occupies a large percentage of the sample volume. On the other hand, for low ratio of height to width the effective surface degradation volume is small as compared to the whole volume of the specimen. It is expected that as height to width ratio increases surface degradation becomes the predominant damage mode resulting to an instability at a low stress level. As the height to width ratio decreases, the effect of surface degradation decreases and pure damage growth becomes the predominant instability mode.

From the above discussion it seems that the degradation instability theory is capable of capturing the essential features of the scale effects. This will be shown further in the next chapter. The characteristic length, ρ, acts as the bridge and is

defined as that specimen size (critical radius for cylindrical sample) such that for that length the entire specimen would experience surface degradation. The length ρ is defined as [Frantziskonis and Desai 1991; Frantziskonis, Tang and Desai 1991]

$$\rho = \alpha \left[\int_c W ds - l \right], \qquad \rho \leq d/2 \tag{3.34}$$

where W is a weighting function, α is a material constant, l is the so-called surface degradation material length and c is the path of maximum (absolute) principal compressive stress. Putting $W = unity$, Frantziskonis and Desai [1991] used this formula to a simple case where a cylindrical specimen is subjected to an uniaxial compressive load and got satisfactory results. Next, we will find the material constants from experimental measurements.

3.4.3 Material Constants Concerned with Surface Degradation

A series of uniaxial tests on different size cylindrical specimens of a simulated rock were performed [Desai, Kundu and Wang 1990]. The simulated rock used consisted of sand, cement, plaster of paris and water at proportions 15:2:3:4. A wide range of different cylindrical specimens were tested under displacement controlled uniaxial compression. An MTS testing machine with appropriate data acquisition system was used. Both axial and lateral displacements were measured in addition to the axial force. Figure 3.5 shows typical results reported in [Desai, Kundu and Wang 1990]. Depending on the specimen size the peak strength and the post peak response vary. The samples tested had different combinations of length L and diameter D. Table 3.1 shows the dimensions of the samples used as well as the peak strength values.

In order to find out the material constant α, let us consider a cylindrical specimen of length L and diameter D subjected to compressive load P, Figure 3.2. The load acts parallel to length L and the cylindrical surface is load free. Let σ_{11} be the uniform stress in the core of the sample and $\hat{\sigma}_{11}$ the average stress in the surface degradation zone. Then

$$P = \frac{\pi}{4}(D - 2\rho)^2 \sigma_{11} + \frac{\pi}{4}[D^2 - (D - 2\rho)^2]\hat{\sigma}_{11} \tag{3.35}$$

We consider the simplest possible constitutive equations for the u and d-parts expressed in (3.3) and (3.4). Thus we consider C^u_{ijkl} and C^d_{ijkl} to be elastic constitutive tensors. Then, considering the strains in the core and in the surface degradation zone to be equal

$$\sigma_{11} = (1-r)E^u\epsilon_{11} + rE^d\epsilon_{11} \tag{3.36}$$

$$\hat{\sigma}_{11} = (1-\hat{r})E^u\epsilon_{11} + \hat{r}E^d\epsilon_{11} \tag{3.37}$$

where E^u, E^d are Young's moduli for the u-part and d-part, respectively and $\hat{r}$ is defined in (3.26). From (3.35-3.37) we have

$$P = a_1D^2 + a_2\rho^2 - a_2\rho D \tag{3.38}$$

where

$$a_1 = \frac{\pi}{4}[E^u - r(E^u - E^d)]\epsilon_{11} \tag{3.39}$$

$$a_2 = \pi[E^u - \hat{r}(E^u - E^d)]\epsilon_{11} \tag{3.40}$$

For the uniaxial case, with $W = 1$

$$\rho = \alpha(L-l) \leq D/2 \tag{3.41}$$

From (3.35) and (3.41) we obtain

$$\sigma = c_1 + c_2\frac{(L-l)^2}{D^2} - c_3\frac{(L-l)}{D} \tag{3.42}$$

where

$$c_1 = 4a_1/\pi, \quad c_2 = 4a_2\alpha^2/\pi, \quad \textit{and} \quad c_3 = 4a_2\alpha/\pi \tag{3.43}$$

and σ is the average or measured stress.

Assuming that a_1, a_2 are constant at the peak strength, from the series of tests shown in Table 3.1, the values of c_1, c_2 and c_3 at peak strength can be determined. By using the least square fit method, The Values of $c_1 = 2197$, $c_2 = 343$, $c_3 = 1622$ were obtained. From (3.43)

$$\alpha = \frac{c_2}{c_3} \tag{3.44}$$

Then we find the material constant α of the artificial rock is approximately 0.21.

Assuming the damage parameter r_t in the surface degradation zone follows the relation as given in (3.8). The material constants associated with damage in surface degradation zone are κ^s and R^s. They are different from the constants κ^d and R^d in the internal pure damage zone. It is expected that the damage amplification along the surface degradation zone can be considered through the introduction of κ^s and R^s. For cylindrical sample, the parameters were obtained for various D and L, as shown in Table 3.2. Now, let us find the constants κ^s and R^s.

For a cylindrical specimen as shown in Figure 3.2, the pure surface degradation occurs with the size of $D = 1$" and $L = 3.38$", and the pure damage occurs with the size of $D = 1$" and $L = 1$" (the assumption $l = 1$" is used). The results shown in Table 3.2 can be plotted as shown in Figure 3.6 and 3.7 [Desai, Kundu and Wang 1990], with L^2/D as the horizontal axis. From these two figures, the damage constants for the pure damage zone are obtained as $\kappa^d = 200.34$ and $R^d = 1.92$, and the damage constants for the surface degradation zone are obtained as $\kappa^s = 362217.45$ and $R^s = 2.95$.

These two parameters are used for back-predictions of the weighted damage parameter distribution as shown in Figure 3.8 and Figure 3.9. In Figure 3.8, the damage parameter (0.05) in the internal zone is amplified, in an average sense, by 5.38 times along the surface degradation zone. In Figure 3.9, the damage parameter (0.1) in the internal zone is amplified, in an average sense, by 3.4 times (very close to the number predicted through eq. (3.33)) along the surface degradation zone. Through comparison of the two amplification numbers, we understand that it is appropriate and necessary to consider the damage amplification parameter along the surface degradation zone is a function of damage evolution rate. Further, the function should be inversely proportional to the damage evolution rate. This consideration is connected to the development of surface effects observed through strain gage tests discussed in chapter 5.

3.5 Degradation Instabilities and Surface Degradation Instabilities

Let us define the region R of a body as $R = R_1 + R_2$ where R_2 is the surface degradation volume bounded from the stress-free surface and extended to a distance ρ from it. Then, R_1 is the rest of R such that $R_1 = R - R_2$. The dissipated energy from internal damage and surface degradation growth is

$$\dot{D} = \dot{Q} + \dot{S} \tag{3.45}$$

with

$$\dot{Q} = \frac{1}{2}\int_{R_1} (\sigma_{ij}\dot{\epsilon}_{ij} - \dot{\sigma}_{ij}\epsilon_{ij})dV \tag{3.46}$$

and

$$\dot{S} = \frac{1}{2}\int_{R_2} (\sigma_{ij}\dot{\epsilon}_{ij} - \dot{\sigma}_{ij}\epsilon_{ij})dV \tag{3.47}$$

where $\dot{Q}$ and $\dot{S}$ represent the energy density dissipated from internal damage growth and from surface degradation growth, respectively. Let $\dot{P}$ be the rate of dissipated energy from plastic deformation such that

$$\dot{\Phi} = \dot{P} + \dot{Q} + \dot{S} \tag{3.48}$$

where

$$\dot{\Phi} = \int_R \dot{\phi} dV \tag{3.49}$$

$$\dot{P} = \frac{1}{2}\int_R (\sigma_{ij}\dot{\epsilon}_{ij} + \dot{\sigma}_{ij}\epsilon_{ij})dV \tag{3.50}$$

ϕ is the dissipated energy per unit volume in the period of time t as defined in (3.11). Considering quasi-static loading, in the absence of body force, rate of energy balance requires

$$\int_{\partial R} T_i \dot{u}_i dS = \int_R \dot{W} dV + \dot{Q} + \dot{S} + \dot{P} \tag{3.51}$$

where T_i is the external load applied on boundary ∂R, u_i denote displacement, and $\dot{W}$ is the internal energy density rate which is given as (3.12).

Depending on the external load level, the geometry of the structure and the material properties, the following instabilities may develop:

- Surface degradation instability resulting in spalling of material from the surface.

- Damage progression instability resulting in overall failure by shear band or other failure mode.

Note that the surface degradation instability does not necessarily imply overall failure of the structure. In other words, "post-spalling" is possible until a global instability develops. The total potential energy is expressed as

$$\Pi = \int_R W dV - \int_{\partial R} T_i u_i dS \tag{3.52}$$

From (3.24), (3.45-52) the conditions for unstable global damage and surface degradation growth are established as

$$\frac{\partial^2 \Pi}{\partial (V_d)^2} + \frac{\partial^2 P}{\partial (V_d)^2} + \frac{\partial^2 Q}{\partial (V_d)^2} + \frac{\partial^2 S}{\partial (V_d)^2} < 0 \tag{3.53}$$

$$\frac{\partial^2 \Pi}{\partial (V_s)^2} + \frac{\partial^2 P}{\partial (V_s)^2} + \frac{\partial^2 Q}{\partial (V_s)^2} + \frac{\partial^2 S}{\partial (V_s)^2} < 0 \tag{3.54}$$

where V_d is the internal damaged volume, and V_s is the surface degradation volume.

In the following chapter, these two instability criteria will be implemented and applied for some typical problems. It will be shown that the instability theory is powerful and easy to implement. From this theory, it is understood that the onset of instability is influenced by the material behavior (constitutive law and/or flow rule), structural geometry, and the external load.

3.6 Conclusion

In this chapter, energy based degradation instability theory has been considered and developed. The degradation instability criteria are comparable with that of Griffith's and can capture information relevant to damage growth. In order to consider the surface effects of brittle materials, a surface degradation zone was defined. The material constants concerned with surface degradation were identified

against experimental observations. The surface degradation instability criterion is expected to predict the shape and scale effects of brittle materials under external load. The implementation and verification of the proposed theory will be presented in the following chapter.

Table 3.1 Measured Peak Stress for Artificial Rock with Various Dimensions (after Desai, Kundu and Wang 1990)

Diameter(D) (inches)	Length(L) (inches)	Stress at Peak (psi)
3	2	1333
3	3	1303
3	4	1228
3	5	976
3	6	952
1	3	324
1.5	3	650
2	3	918
2.5	3	1130
3	3	1303

Table 3.2 Material Constants κ and R (after Desai, Kundu and Wang 1990)

Length of Sample (inches)	Diameter of Sample (inches)	κ	R
2	3	131.736	1.847
3		1615.616	2.178
4		17321.240	2.537
5		49199.268	2.725
6		721019.129	2.988
3	1	99242.230	2.583
	1.5	13922.442	2.370
	2	4139.004	2.221
	2.5	2846.494	2.205

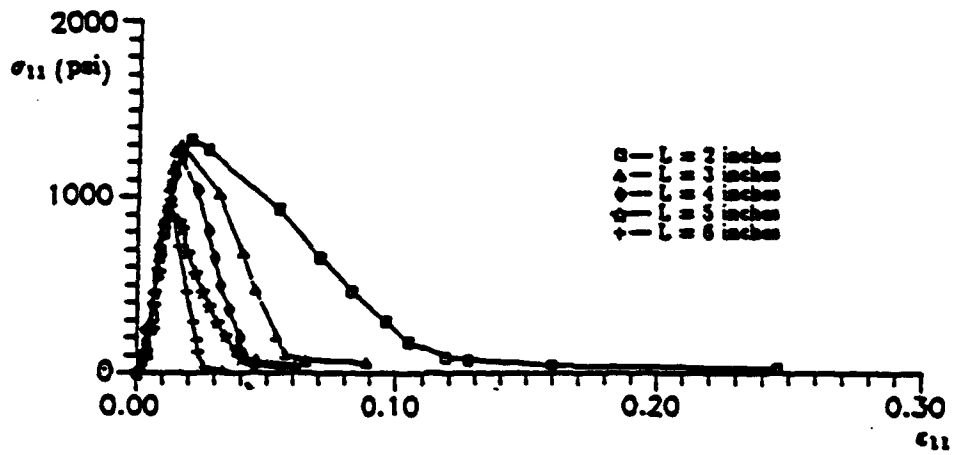

Figure 3.3 Measured Stress-Strain Curve (after Desai, Kundu and Wang 1990)

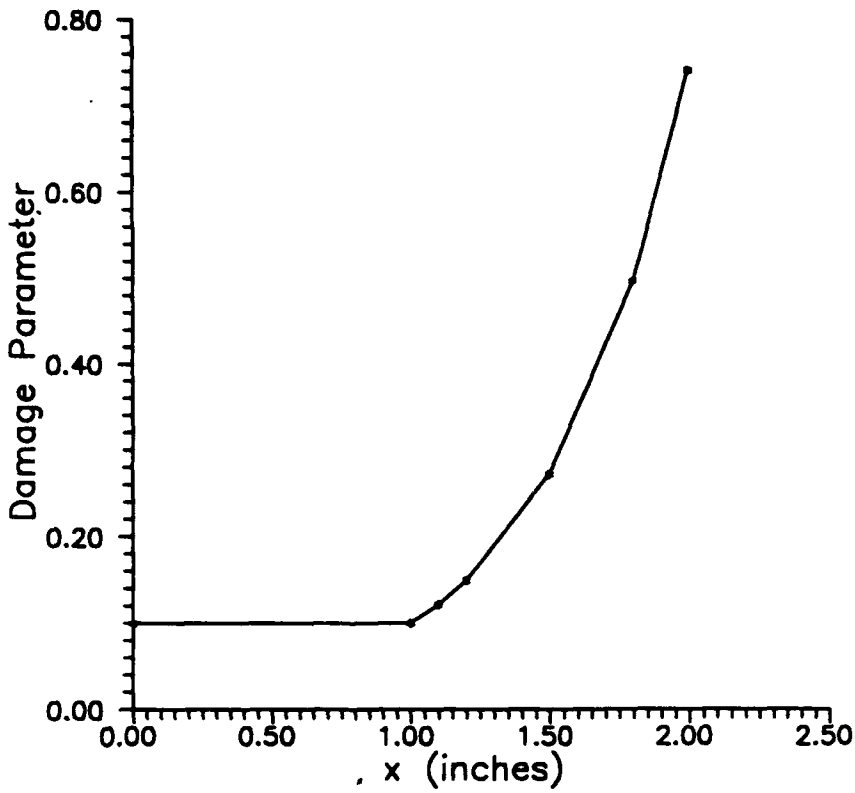

Figure 3.4 Distribution of Damage Parameter r_t

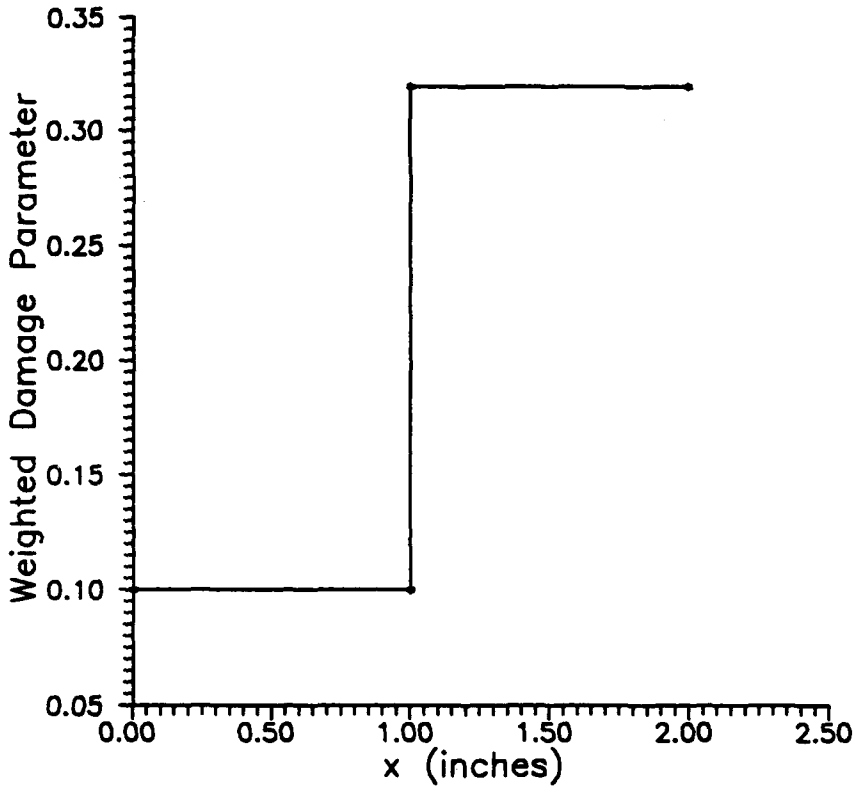

Figure 3.5 Distribution of Weighted Damage Parameter $\hat{r}_t$

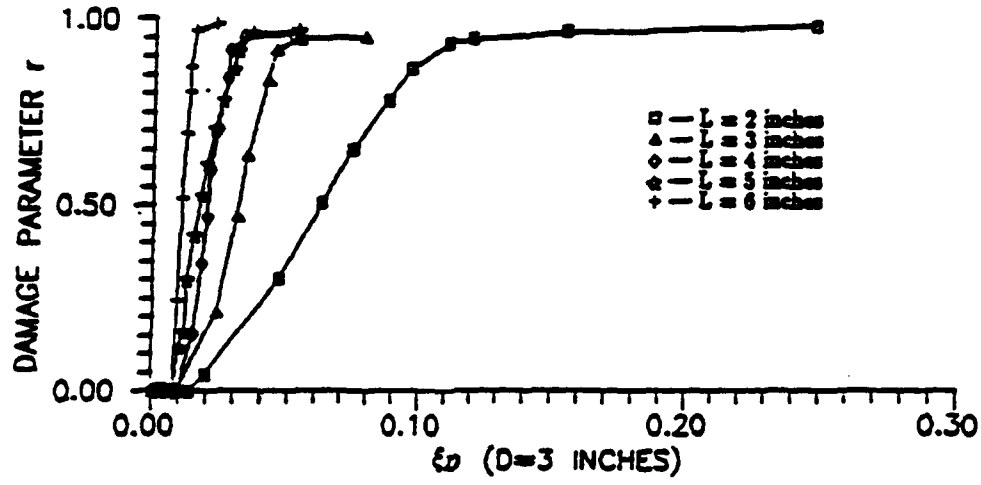

(a)

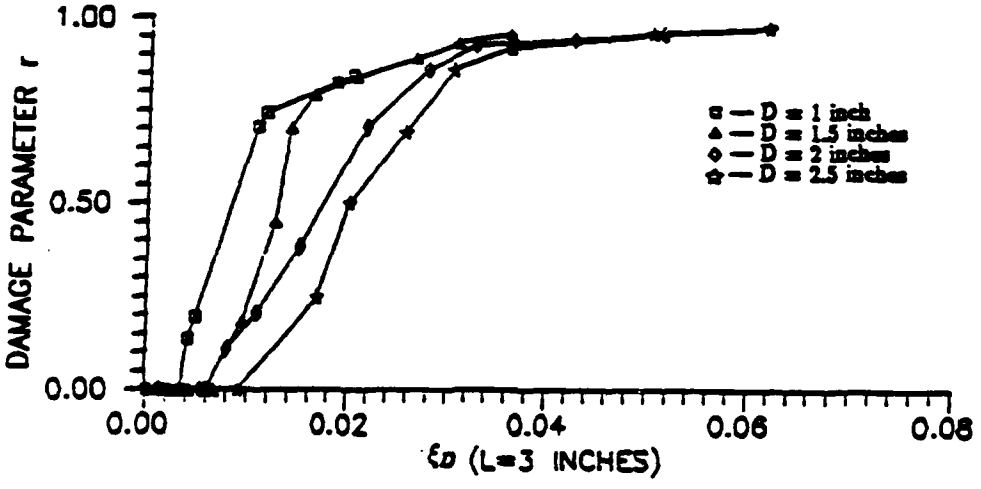

(b)

Figure 3.6 Damage Parameter v.s. Deviatoric Strain Trajectory, (a) D=constant, (b) L=constant (after Desai, Kundu and Wang 1990)

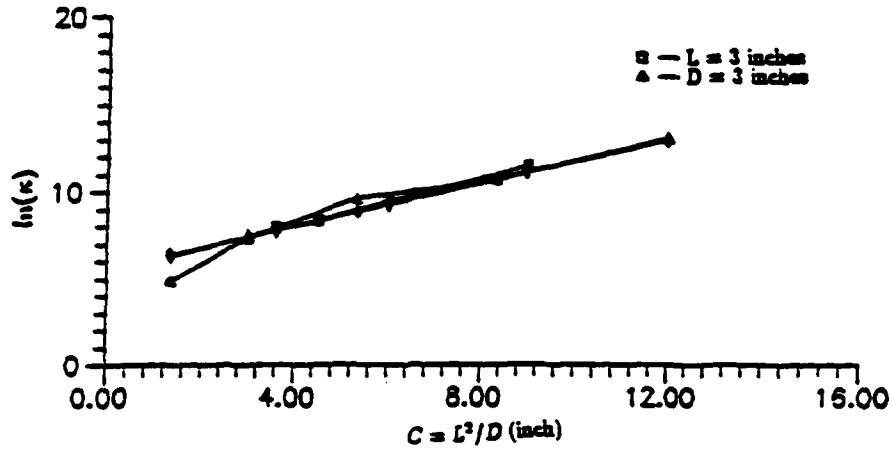

(a)

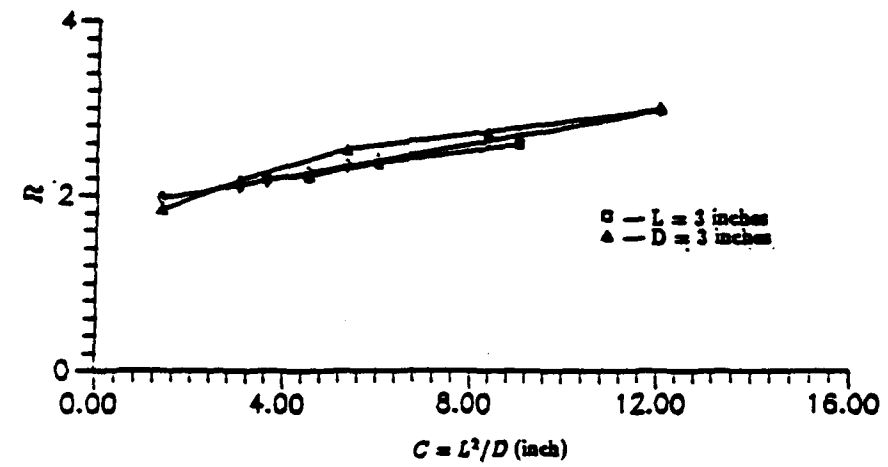

(b)

Figure 3.7 (a) $\ln(\kappa)$ v.s. $C = L^2/D$, (b) R v.s. $C = L^2/D$ (after Desai, Kundu and Wang 1990)

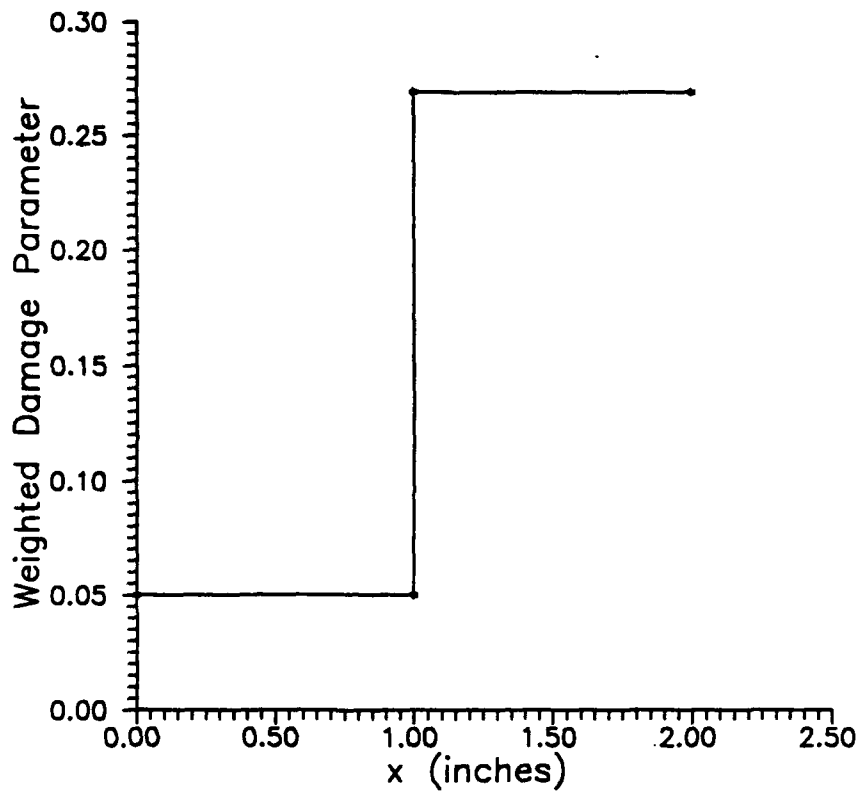

Figure 3.8 Distribution of Weighted Damage Parameter $\hat{r}_t$

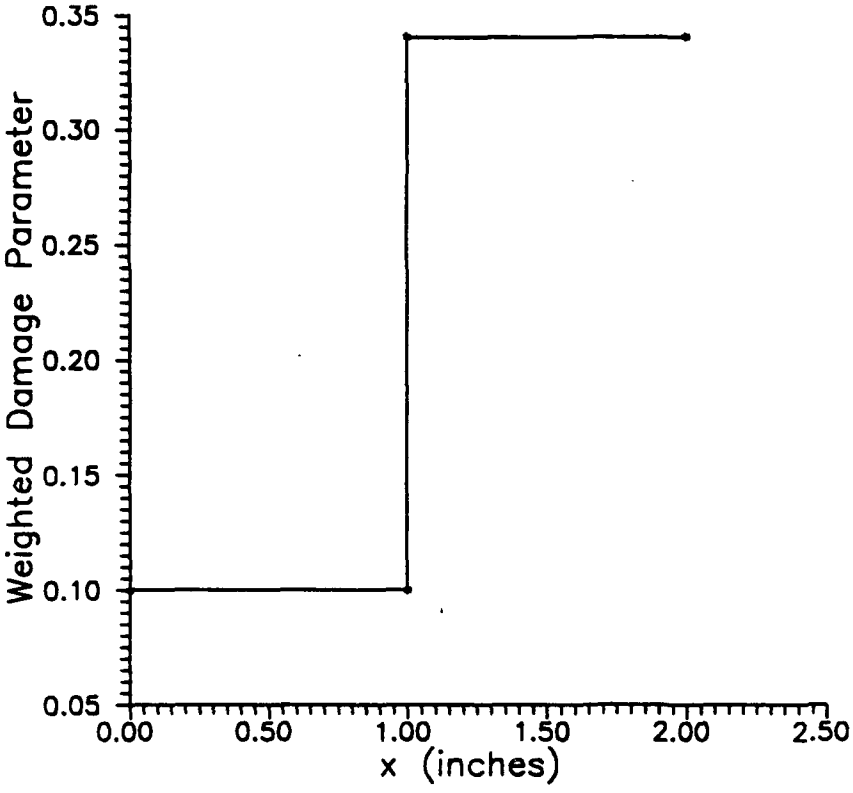

Figure 3.9 Distribution of Weighted Damage Parameter $\hat{r}_t$

CHAPTER 4

IMPLEMENTATION OF THE INSTABILITY CRITERIA

In this chapter, applications of the degradation instability theory will be presented through both analytical and numerical solutions. For analytical solutions, we consider (for simplicity) the undamaged fraction as linear elastic material. However, for numerical solutions, the elastic-plastic behavior of the undamaged fraction is considered. First, the elastic-plastic constitutive relations and the numerical procedure will be presented, and then, some solutions concerned with both global degradation instability and surface degradation instability will be given.

4.1 Constitutive Relations for the Elastic-Plastic Undamaged Fraction

The following brief description of the plasticity model used for the u-fraction is adopted from Desai, Somasundaram and Frantziskonis [1986]. As mentioned in 3.2, the material behavior is decomposed into two parts, namely the u-part and d-part. The undamaged part is assumed to obey an elastic-plastic constitutive law. Since the damaged part "follows" the deformation of the u-part and since it has no shear resistance, the damage constitutive relations may be termed as rigid perfectly plastic with zero yield strength [Frantziskonis and Desai 1987]. The elastic-plastic constitutive relations for the u-part are written as

$$\dot{\sigma}_{ij} = C^{ep}_{ijkl}\dot{\epsilon}_{kl} \tag{4.1}$$

for loading, and as

$$\dot{\sigma}_{ij} = C^{e}_{ijkl}\dot{\epsilon}_{kl} \tag{4.2}$$

for unloading. Here, σ_{ij} is stress tensor, ϵ_{kl} is strain tensor, C^{ep}_{ijkl} is the elastic-plastic tangential stiffness matrix, and C^{e}_{ijkl} is the unloading stiffness matrix. (.) denotes increment.

A general hierarchical procedure for developing elastic-plastic models for isotropic and anisotropic, nonassociative responses and applications for soils, rocks and concrete are described in Desai [1980], Desai and Siriwardane [1983], Desai and

Faruque [1984], Desai, Somasundaram and Frantziskonis [1986], and others. This approach is used here to describe the u-part with basic isotropic hardening and associative model δ_0, here δ_0 denotes zero deviation from normality. It is assumed that the associative behavior holds for the u-part, and the yield function is given [Desai, Samasundaram and Frantziskonis 1986]

$$F = J_{2d}^u - \left[-\frac{\alpha_1}{\xi^{\eta_1}} \bar{J}_1^n + \gamma \bar{J}_1^2 \right] (1 - \beta S_r)^{-1/2} \tag{4.3}$$

where $\bar{J}_1 = J_1 - b$, and b is a material constant representing the distance from the stress origin to the intersection of the surface with the tensile hydrostatic axis. $J_1 = \sigma_{kk}^u$ is the first invariant of σ_{ij}^u stress, $S_r = (J_{3d}^u)^{1/3}/(J_{2d}^u)^{1/2}$ is the stress ratio, J_{3d}^u (J_{2d}^u) is the third (the second) invariant of the deviatoric part of σ_{ij}^u, β, γ, n are assumed to be material constants related to the shape of the yield function, α_1, η_1 are material constants related to hardening and $d\xi = (d\epsilon_{ij}^p d\epsilon_{ij}^p)^{1/2}$, superscript p indicating plastic. In order to derive the C_{ijkl}^{ep} tensor, the usual relations of elastic-plastic theory are used [Chen and Han 1988]. Finally, the C_{ijkl}^{ep} tensor is written as (appendix A)

$$C_{ijkl}^{ep} = \left(C_{ijkl}^e - \frac{C_{ijmn}^e \frac{\partial F}{\partial \sigma_{mn}} \frac{\partial F}{\partial \sigma_{uv}} C_{uvkl}^e}{\frac{\partial F}{\partial \sigma_{pq}} C_{pqst}^e \frac{\partial F}{\partial \sigma_{st}} - \frac{\partial F}{\partial \xi} \left(\frac{\partial F}{\partial \sigma_{st}} \frac{\partial F}{\partial \sigma_{st}} \right)^{1/2}} \right) \tag{4.4}$$

4.2 Numerical (Finite Element) Procedures

As mentioned before, if the two fractions of the mixture are considered to be elastic-plastic, it is difficult to obtain an analytical solution even for the simplest uniaxial load case. Hence numerical procedure, here, the finite element method are used. Let

$$\mathbf{u} = \mathbf{N}\mathbf{q} \tag{4.5}$$

$$\epsilon = \mathbf{B}\mathbf{q} \tag{4.6}$$

where $\mathbf{u}$ is the displacement vector, ϵ is the strain vector, $\mathbf{N}$ is the shape function matrix, and $\mathbf{B}$ is strain-displacement matrix. The principle of virtual work leads to the following incremental equations [Desai and Abel 1972]:

$$\int_R \mathbf{B}^T d\sigma dV = d\mathbf{Q} \tag{4.7}$$

where $d(.)$ denotes increment, $d\mathbf{Q}$ is the increment of the external force, superscript T denotes transpose matrix, and V is the volume. The constitutive relations (3.5), (3.6) are written as

$$d\sigma = \mathbf{L}d\epsilon - dr\mathbf{S} \tag{4.8}$$

From (4.6), (4.7) and (4.8), it follows that

$$\mathbf{K}d\mathbf{q} = d\mathbf{Q} + d\mathbf{Q}^d \tag{4.9}$$

where

$$\mathbf{K} = \int_R \mathbf{B}^T \mathbf{L}\mathbf{B} dV \tag{4.10}$$

is the incremental stiffness matrix for the u-part, and

$$d\mathbf{Q}^d = \int_R \mathbf{B}^T dr\mathbf{S} dV \tag{4.11}$$

is termed as the "damage force".

In order to evaluate the second partial derivatives appearing in the instability inequalities (3.53) and (3.54) numerically, the central difference method is employed, thus for example

$$\frac{\partial^2 Q}{\partial (V_d)^2}|_{(\xi)} = \frac{\left(\frac{\partial Q}{\partial V_d}\right)_3 - \left(\frac{\partial Q}{\partial V_d}\right)_1}{(V_d)_3 - (V_d)_1} \tag{4.12a}$$

where

$$\left(\frac{\partial Q}{\partial V_d}\right)_3 = \frac{Q_3 - Q_2}{(V_d)_3 - (V_d)_2} \tag{4.12b}$$

$$\left(\frac{\partial Q}{\partial V_d}\right)_1 = \frac{Q_2 - Q_1}{(V_d)_2 - (V_d)_1} \tag{4.12c}$$

and subscripts 1, 2, 3 denote values at three consecutive increments of load. ξ is located somewhere between $(V_d)_1$ and $(V_d)_3$.

The programme including strain softening and dynamic analysis [Woo and Desai 1991; Desai and Woo 1992] was modified for our purposes. In Woo and Desai [1991], a few alternatives to implement the damage model [Frantziskonis and Desai 1987] into FEM code were discussed, and the mesh dependency of the damage model was investigated against a footing problem. It is shown that at local level, mesh dependency is significant at post-peak stage. However, it is also shown that the mesh dependency can be constrained to a certain level through the introduction of a simple weighting procedure. Although post-instability investigation is not the theme of this dissertation, some considerations will be presented in chapter 7.

4.3 On Global Degradation Instabilities

The analytical solution of a simple problem will be presented first, and then some numerical solutions will be followed.

4.3.1 Analytical Solution of A Simple Problem

If we consider the two fractions in a stressed brittle material to be linear and elastic, it is feasible to examine the stability inequalities analytically. Then, the two constitutive tensors C^u_{ijkl} and C^d_{ijkl} are functions of the two Lame's constants, namely μ_u, λ_u and μ_d, λ_d respectively. For uniaxial load, from (3.3) and (3.4)

$$\sigma^u_{ij} = C^u_{ijkl}\epsilon_{kl} \tag{4.13}$$

$$\sigma^d_{ij} = C^d_{ijkl}\epsilon_{kl} \tag{4.14}$$

and since $\sigma_{22} = \sigma_{33} = 0$ we obtain that the apparent Poisson ratio ν is expressed as

$$\nu = \frac{\lambda_u - r(\lambda_u - \lambda_d)}{2(\mu_u + \lambda_u) - 2r(\mu_u - \mu_d + \lambda_u - \lambda_d)} \tag{4.15}$$

Since ν is a function of r, and r continuously increases with the damage progression, the apparent Poisson ratio is not constant. An increase in ν is expected, and this reflects the change in volume due to crack expansion. Figure 4.1 shows the variation

of ν with respect to r (4.15), where an initial Poisson ratio of 0.2 has been assumed. In figure 4.1, F is the ratio of Young's modulus between the d-part and u-part. As shown in the following, the Poisson effect is important for the stability analysis. If we assume homogeneous deformation under uniaxial load (surface degradation effects are not considered for the time being), and neglect the volume change in the process, then the instability inequality (3.24) reduces to

$$\frac{1}{V^2}\left[-\frac{\partial^2\Pi}{\partial r^2}-\frac{\partial^2 D}{\partial r^2}\right]>0 \tag{4.16}$$

where (3.1) has been used. From (3.48), (4.13) and (4.14), for uniaxial load in direction 1, the potential energy Π is expressed as

$$\Pi = V\epsilon_{11}^2\left[-\frac{2\mu_u+\lambda_u}{2}+\frac{r(2\mu_u-2\mu_d+\lambda_u-\lambda_d)}{2}+\nu\lambda_u-r\nu(\lambda_u-\lambda_d)\right] \tag{4.17}$$

where V is the total volume of the structure (specimen). From (3.20), (4.13) and (4.14), for uniaxial load in direction 1 we obtain

$$\frac{\partial D}{\partial r}=\dot{r}\epsilon_{11}^2\left[-2\nu^2(\mu_u-\mu_d+\lambda_u-\lambda_d)-\frac{2\mu_u-2\mu_d+\lambda_u-\lambda_d}{2}+2\nu(\lambda_u-\lambda_d)\right] \tag{4.18}$$

From (4.17) and (4.18) the derivatives $\partial^2\Pi/\partial r^2$ and $\partial^2 D/\partial r^2$ can be calculated, noting that ϵ_{11} and ν are functions of r. Although the final expression for the left side of (4.16) is lengthy, at the peak $\partial\sigma_{11}/\partial r=0$ and this simplifies the calculations significantly. Relation (4.16) after algebraic manipulations finally reduces to

$$3\mu_u(1+2\nu^2)a-\frac{3}{2}\lambda_u\left[\frac{1}{\nu}-2\nu-1\right]a^2+\frac{8\mu_u^2}{\lambda_u}\nu^3<0 \tag{4.19}$$

where

$$a=\frac{E_u-E_d}{(1-\nu)E_u+rE_d} \tag{4.20}$$

and E_u, E_d is the the Young's modulus for the u-part and d-part, respectively. From the above relation (4.19) by setting the left hand side equal to zero (the implicit function of r with respect to ν is obtained), the curves of Figure 4.2 are obtained, where the initial Poisson ratio is assumed to be 0.2. In this figure $F=E_d/E_u$.

Inequality (4.19) is satisfied for all combinations of ν_d and r that are below the curves shown in Figure 4.2. For example, if $F = 0.05$ is assumed (a reasonable value if one considers the the physical interpretation of damage) and $\nu_d = 0.3$ then for stable behavior at peak r must be greater than 0.9 (approximately). Such a high value of r may only be possible for the post peak range. Even in the case where such high r values are physically acceptable, it is reached at high strain values far after peak where the material reaches a residual strength. In addition, for the material parameters determined for materials like concrete [Frantziskonis and Desai 1987], the value of r at peak is between 0.1 and 0.3.

In the above analysis, the two material fractions were considered linear and elastic. Thus no plastic deformation is present. However, for uniaxial load, the plastic energy versus strain or r curve is convex around the peak stress level. Convexity implies $\partial^2 D_p/\partial r^2 < 0$. Then from (4.16) plastic deformation promotes instability. Thus the present analytical solution suggests that a homogeneous post peak state is impossible since basic energy based stability conditions are violated.

In the above analytical solution, surface degradation effects were not considered. If surface degradation effects are included in the instability analysis, it is expected that a surface degradation instability will occur first. The onset of such an instability may indicate spalling type of failure. The remaining part of the body may still be stable until (3.53) is satisfied. This will be shown later.

4.3.2 Numerical Solutions

For illustration purposes of the occurrence of instability, the following problems are considered. Figure 4.3 shows the problems considered as well as the finite element meshes. Two cases were considered. Case A is uniaxial plane strain, simulating a plane strain test such that there is no friction between load platen and specimen. Case B imposes non-uniform deformation since horizontal displacements at the top and bottom were restrained; this represents a full friction condition between load platen and specimen. For both cases A and B increments of vertical displacements were applied along the top and bottom interfaces. For each increment the instability inequalities were checked. The purpose of the present analysis

is to examine the global degradation instability. Thus (3.24) is used for both cases A and B.

Figure 4.4 shows the force-displacement curve from the finite element analysis using one element. The onset of damage growth instability is indicated by a circle. In case A uniaxial plane strain is simulated. For this case instability implies the onset of non-uniform deformation that may result to a shear band formation or other types of non-uniformity. Similar observations hold for case B. Figure 4.5 shows the force-displacement response from the analysis with 4 elements. Figure 4.6 represents the results from the analysis with 16 elements. Table 4.1 shows the percentage of load with respect to peak load, at the onset of instability. As can be concluded from this table the finite element analysis converges to the solution of about 86% of peak load for instability onset for case A and about 85% for case B.

4.3.3 Discussion

Analytical and numerical results on degradation instabilities clearly indicate that the global damage growth instability is to occur before and close to the peak strength. This prediction is supported by the experimental results of a series of triaxial compression tests on quartzite [Hallbauer, Wagner and Cook 1973; Read and Hegemier 1984]. The tests were done on cylindrical specimens which were jacketed in thin copper tubes so that their lateral expansion would be resisted by the increasing confinement. The rate of axial straining was kept constant at 1.675×10^{-5}/sec during the tests. The purpose of these tests was to determine the microstructural changes that progressively take place in the rock as it is compressed to failure. Particular emphasis was given to the structural changes that occur in the vicinity of the peak of the stress-strain curve. To accomplish this, the tests were stopped at various predetermined points along the strain path; the specimens were unloaded and removed for sectioning and microscopic examination. Figure 4.7 shows the nominal stress-strain curve obtained from the tests, and photographs of specimen sections at the various points along this curve. It was reported that as the stress is increased from 80 to 90 percent of ultimate, a rapid proliferation of microcracks occurs, with the number of microcracks increasing about seven-fold.

4.4 On Surface Degradation Instabilities

Borehole instabilities and breakouts are often characterized by the slabbing mode that affects a portion of the material close to the borehole wall [Kemeny and Tang 1990]. In addition, it is clear that the borehole size has significant effect on the initiation of breakout. Haimson and Herrick [1989] studied the behavior of samples with different central hole sizes subjected to external stress. Square blocks of dry Alabama limestone having different diameters of central holes, ranging from 2 to 12 cm were subjected to uniaxial stress. All blocks had side length to borehole diameter ratio of 5:1. Is was found that small diameter holes required larger stresses to induce breakouts, Figure 4.8. Since laboratory size boreholes are usually smaller than the ones in the field, the importance of hole size and its relation to breakouts is of basic and quantitative nature. Thus in order to achieve a well-grounded statement about borehole stability that complies with laboratory and field observations, the dependency of borehole stability on its size (scale effect) must also be modeled.

Borehole scale effects is an example of the fact that the deformational characteristics of brittle materials depend on the size as well on the shape of the structure (specimen) [Frantziskonis, Tang and Desai 1991]. As pointed out before, the theory for surface degradation instability can capture the information of scale effects. In the theory, the surface effect region is described by a distance ρ which is given by (3.34). The material constants α, κ^s, R^s, κ^d and R^d associated with the theory have been found from experiments in section 5 at chapter 3. Now, we will present a simplified solution for a borehole problem, and show some numerical solutions of borehole problems [Frantziskonis, Tang and Desai 1991].

4.4.1 Simple Analysis of A Borehole Problem

Let us consider the problem depicted in Figure 4.9. The borehole structure of length and width D contains a central circular hole of radius R. The ratio D/R is considered constant such that $D/2R = 5$. Uniaxial compressive stress σ is applied

externally. If the material is considered linear, isotropic and elastic, the σ_{max} occurs at point A [Roark and Young, 1989]:

$$\sigma_{max} = \sigma_A = k\sigma_{nom} \tag{4.21}$$

where

$$\sigma_{nom} = \frac{\sigma D}{D - 2R} \tag{4.22}$$

$$k = 3.00 - 3.13(\frac{2R}{D}) + 3.66(\frac{2R}{D})^2 - 1.53(\frac{2R}{D})^3 \tag{4.23}$$

In order to demonstrate analytically the capability of the theory to capture the scale effects in this problem, we make the following simplified assumptions. We consider that the material is linear elastic and isotropic. This, of course, represents a "stiffer" material than actual rocks. In addition, we assume that for the external stress levels at breakout the material in the surface degradation zone has zero stiffness. Thus at breakout initiation this problem can be analyzed by using the solution presented in equations (4.21)-(4.23), but now the radius of the hole is $R + \rho$. For this problem equation (3.34) reduces to

$$\rho = \alpha(2\pi R - l) \tag{4.24}$$

and

$$\sigma_{max} = k\frac{\sigma D}{D - 2(R + \rho)} \tag{4.25}$$

and k is given from (4.23) where $R+\rho$ is substituted instead of R. For the simulated rock [Desai, Kundu and Wang 1990] it was found that $\alpha = 0.21$ and l was assumed to be one inch (for the time being, further discussion in presented in chapter 5). If we consider that at breakout, σ_{max} in (4.25) assumes a constant value we can obtain solutions for different R where always $D/2R = 5$. The curve in Figure (4.10) is obtained where the diameter (2R) is plotted on the horizontal axis and the external stress at breakout is plotted on the vertical one. Clearly, the shape and trend of this curve is similar to the experimental one given in Figure 4.8.

4.4.2 Numerical Solutions

The finite element method has been used, long ago, for the stress-deformation and stability analysis of borehole problems. Initial work in this area, Desai and Reese [1970], considered nonlinear elastic material response and the Mohr criterion was used as the criterion for development of plastic zones. It was found that plastic zones advance close to the borehole at a certain distance depended on the geostatic loading. The extent of plastic zone may be related to the surface degradation zone discussed in this study. However, since the surface degradation zones are dependent on the geometry of the structure, such a relation would be based on fixed radius of the borehole.

The problem shown in Figure 4.9 is investigated numerically for six different values of the central hole radius. For all problems, the ratio of D over R is constant such that $D/2R = 5$. The finite element mesh used is shown in Figure 4.11. Eight-noded quadrilateral elements are used. For the six problems studied the hole radii are 0.5, 1, 2.5, 5, 7.5, and 10 cm. For each problem the surface degradation distance is calculated. The elements next to the central hole extend to a distance ρ. The material properties assigned for these elements are the surface degradation ones. The purpose of this analysis is to study the surface degradation instabilities close to the hole. Thus no surface degradation is considered close to the lateral surfaces of length D, since the surface degradation growth at these points is much slower than the growth close to the hole.

The calculated load-deformation curve for these problems is monotonically increasing until a peak load is reached. Beyond the peak load, softening response is calculated. In Figure 4.12 radius R is plotted on the horizontal axis and the normal stress σ_{yy} at the peak load for the lower left Gauss point of element 2 is plotted on the vertical axis. Here σ_{yy} represents the so called tangential stress at the end of surface degradation zone. A simple criterion for spalling of the surface degradation zone calls for σ_{yy} reaching a critical value. In this case, Figure 4.12 shows the capability of the theory to represent the scale effect. The shape of this curve is similar to the one shown in Figure 4.8 [Haimson and Herrick 1989]. Since the material constants for Alabama limestone are not available, no quantitative

comparison can be made. Figure 4.13 is similar to Figure 4.12, but the maximum (peak) stress is plotted on the vertical axis.

At every increment of load, the instabilities (3.53) and (3.54) are examined. Surface degradation growth (Figure 4.14) showed the following interesting characteristics for these problems. Surface degradation showed an initial unstable region from the beginning of the external load application. Subsequently the response became stable until a second instability was initiated. This trend is similar to the crack propagation problem studied by Sammis and Ashby [1986]. In that reference the crack propagation problem of a notched specimen with a central hole has been studied theoretically and experimentally. The geometry of the problem is similar to the one shown in Figure 4.9 and the propagation of initial surface cracks parallel to the external compressive load is studied. Crack propagation was found (theoretically and experimentally) to be initially unstable (from the beginning of the load application) then stable and then unstable again. Here we note that the instability inequalities (3.53) and (3.54) are necessary but not sufficient conditions for instability initiation. Let

$$e = \Pi + D_p + Q + S \tag{4.26}$$

In Figure (4.14), e is plotted with respect to the surface degradation volume V_{ds} for the case $R = 10cm$ and $D = 100cm$. Similar curves were obtained for the other five cases considered. When the curve is convex, surface degradation instability is possible. The curve shown in Figure 4.14 is initially convex implying possible unstable growth, up to point A. After point A the surface degradation growth is stable up to point B. After point B the curve is convex again. Note that the convexity after B increases rapidly. Point C on this curve is at peak load.

This analysis is similar, in trend, to the problem studied by Desai and Reese [1970]. It implies that the material is susceptible to surface degradation instability from the beginning of the load application. After a certain amount of surface damage has been achieved, the damage growth response is stable for a rather small range of external load. Then surface damage instability is expected to occur, after

point B. The scale effect shown in Figure 4.15 corresponds to instability initiation at point B, where radius R is plotted on the horizontal axis and the externally applied stress at surface instability is plotted on the vertical axis [Frantziskonis, Tang and Desai 1991].

4.4.3 Comments

Surface degradation growth is shown to play an important role for phenomena observed in borehole problems such as scale effects and surface degradation instabilities. Analytical and numerical results show the capability of the theory to predict such phenomena.

For many problems in brittle material mechanics, analysis is based on simple elastic-perfectly plastic models that are calibrated on test data from conventional triaxial compression experiments. These models lead to irregular stability of the borehole as compared to experimental observations. Maury [1987] and Guenot [1987] demonstrated that classical design procedures lead to overestimation of the drilling fluid density by a factor of 2-8.

Papanastasiou and Vardoulakis [1991] used the bifurcation theory to examine the effect of borehole radius on borehole stability. Material behavior was described by the deformation theory of plasticity, and internal length was introduced in the formulation through employment of Cosserat theory. The numerical solutions showed an increase of the bifurcation stress with decreasing borehole radius. It would be interest to note that the present study is different from the one given by Papanastaiou and Vardoulakis [1991], in the sense that length is introduced through surface degradation consideration rather than in the constitutive equations. Furthermore, instabilities are based on global energy consideration.

4.5 Conclusion

Through application to some typical problems analytically and numerically, it is our understanding that the global degradation instability theory predicts the instabilities concerned with non-uniform deformation and the surface degradation

instabilities concerned with spalling and size, shape effects for brittle materials like rock and concrete.

Table 4.1 Summary of Numerical Results

n	P_{max} Nx10^6	P_{in} Nx10^6	Case	P_{in} /P_{max} (%)
1	103	76.9	A	74.7
1	123	95.2	B	77.4
4	102	88.4	A	86.3
4	117	94.5	B	80.6
16	102	88.0	A	86.3
16	111	94.3	B	84.9

n: number of elements
P_{max}: peak load
P_{in}: load at degradation instability

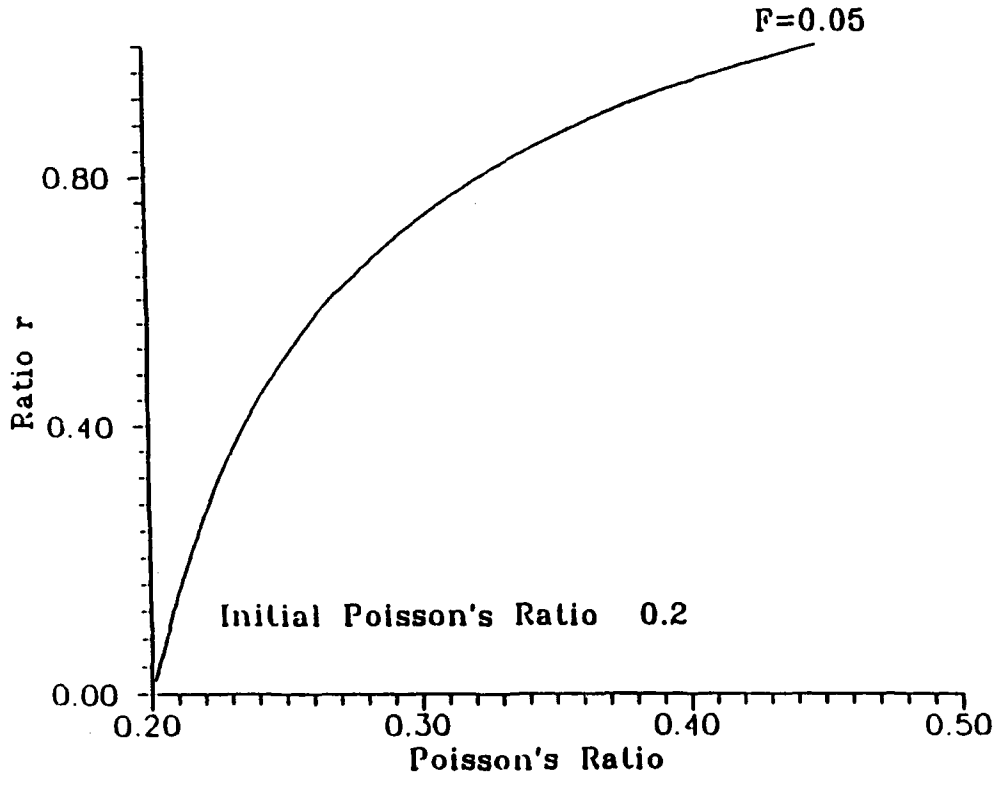

Figure 4.1 Variation of Apparent Poisson Ration ν

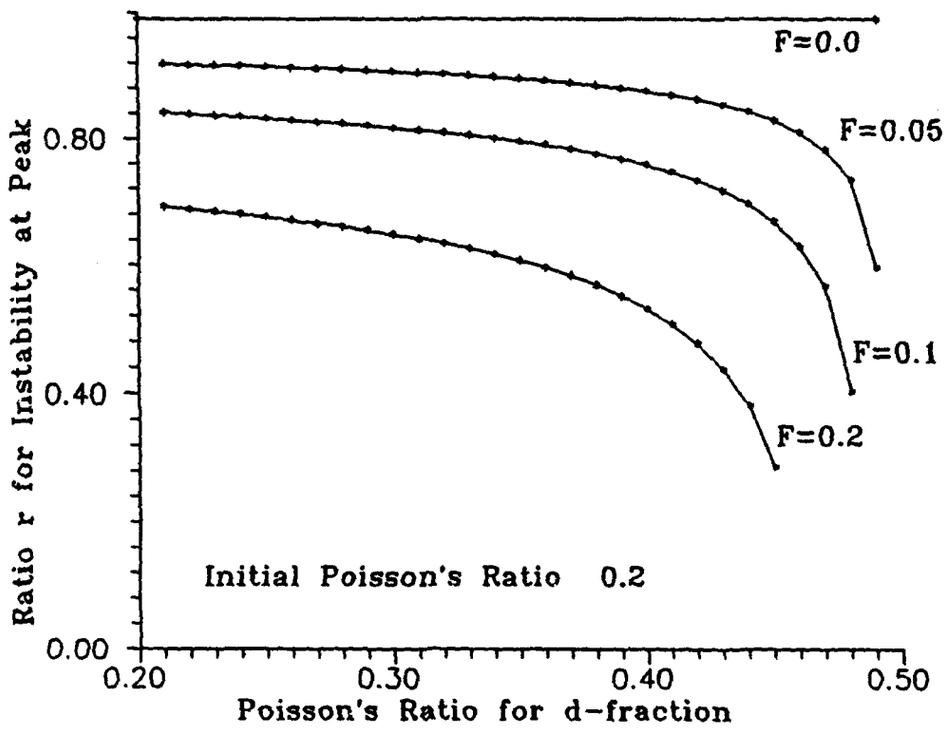

Figure 4.2 Values of r for Stability at Peak Strength for Uniaxial Load Condition

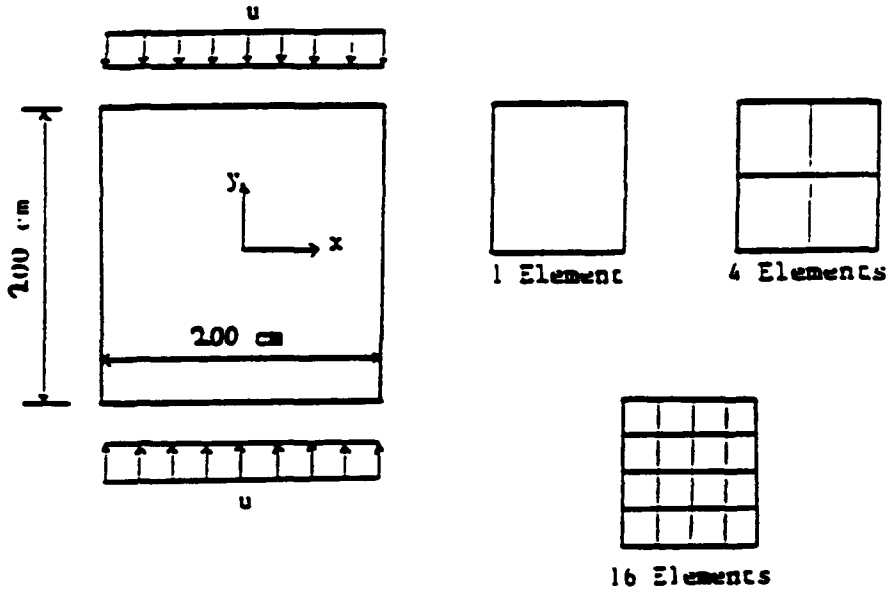

Figure 4.3 Example Problems and Finite Element Meshes

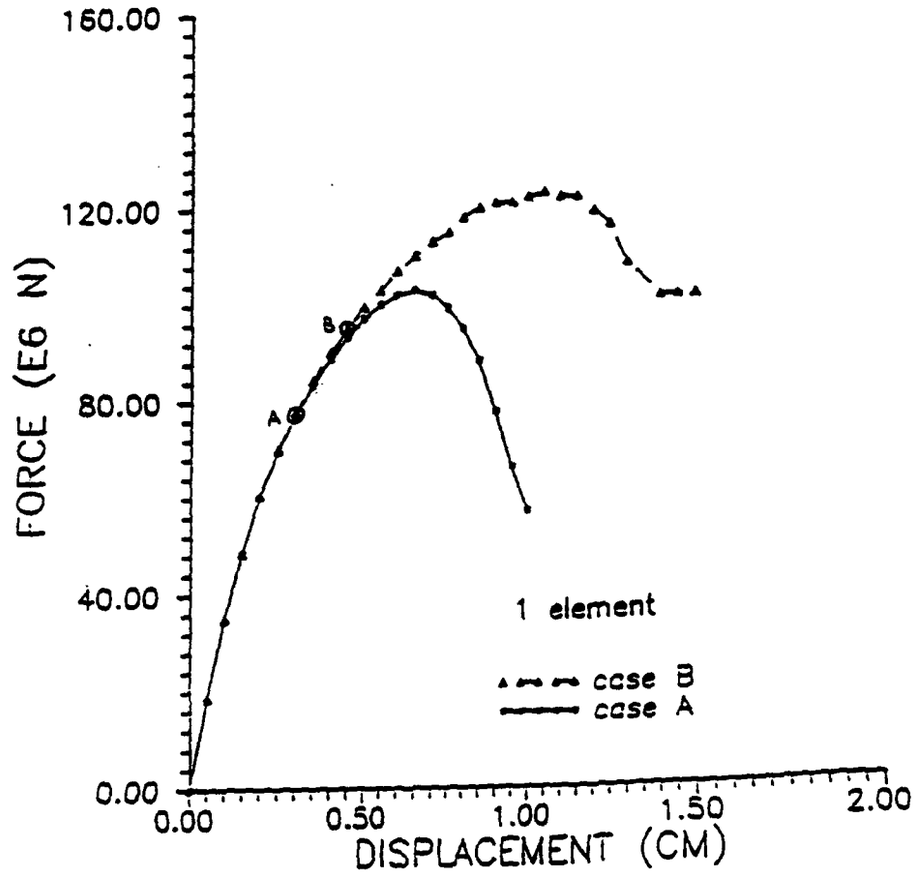

Figure 4.4 Force-Displacement Curve Using 1 Element; Circles Indicate Onset of Instability

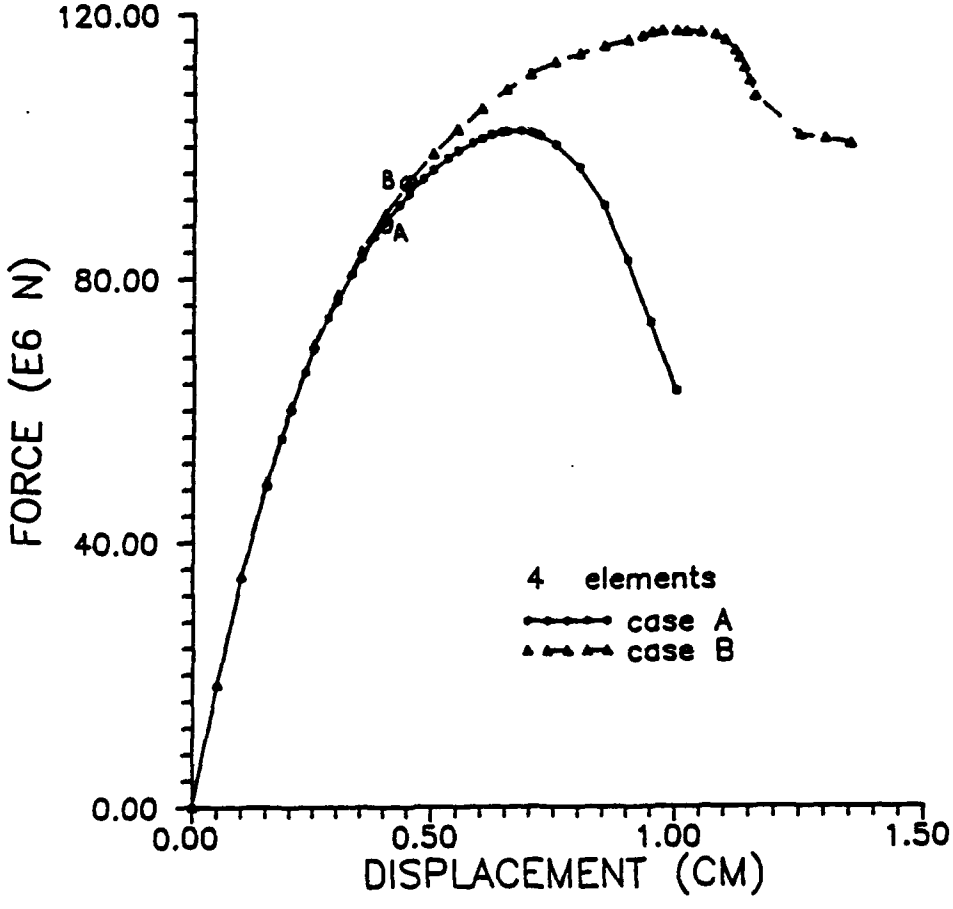

Figure 4.5 Force-Displacement Curve Using 4 Element; Circles Indicate Onset of Instability

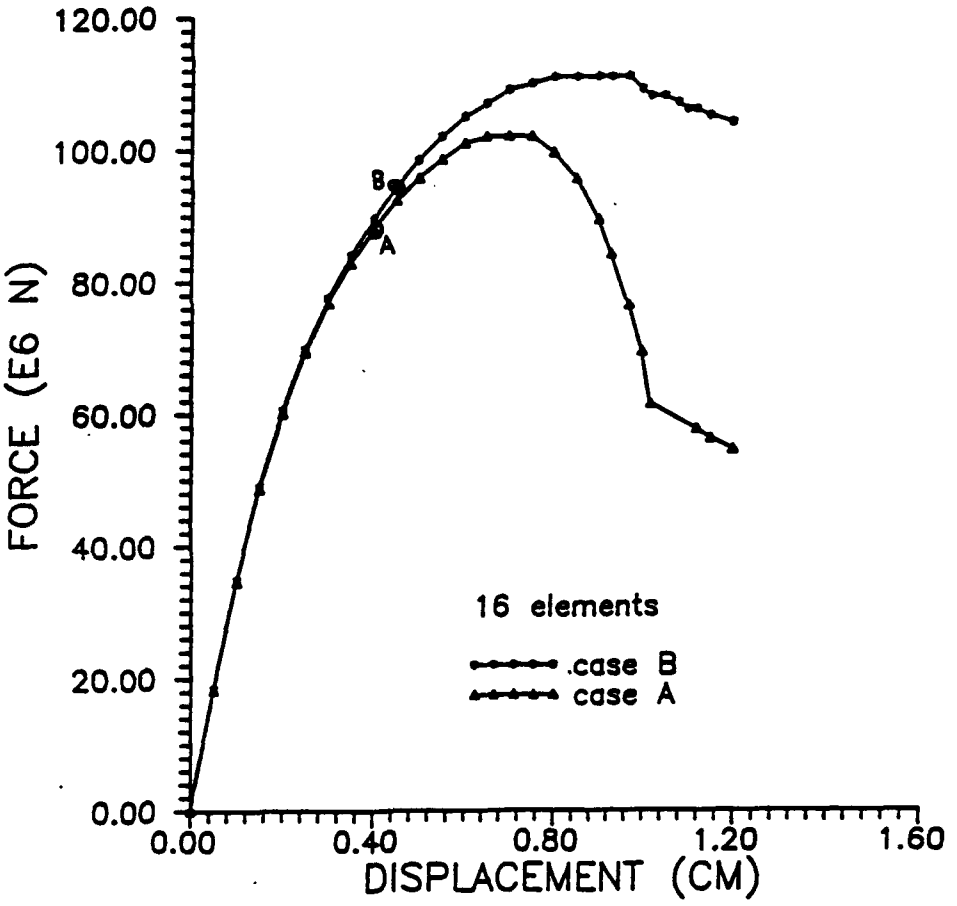

Figure 4.6 Force-Displacement Curve Using 16 Element; Circles Indicate Onset of Instability

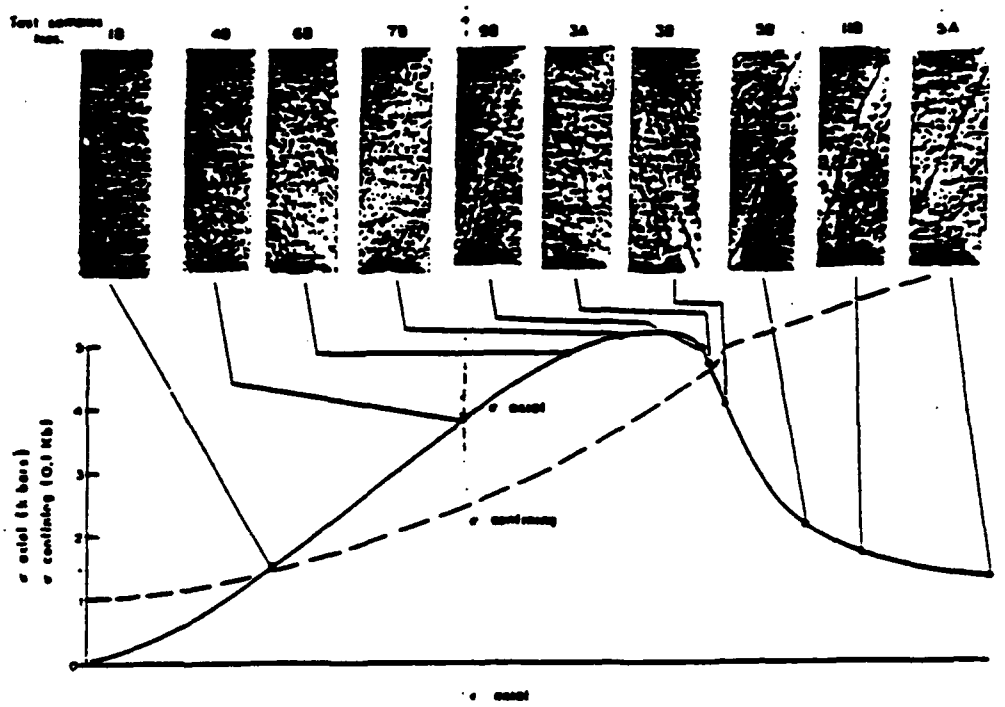

Figure 4.7 Stress-Strain Curves and Photograph of Test Specimens at Different Stress Levels (after Hallbauer, Wagner and Cook 1973)

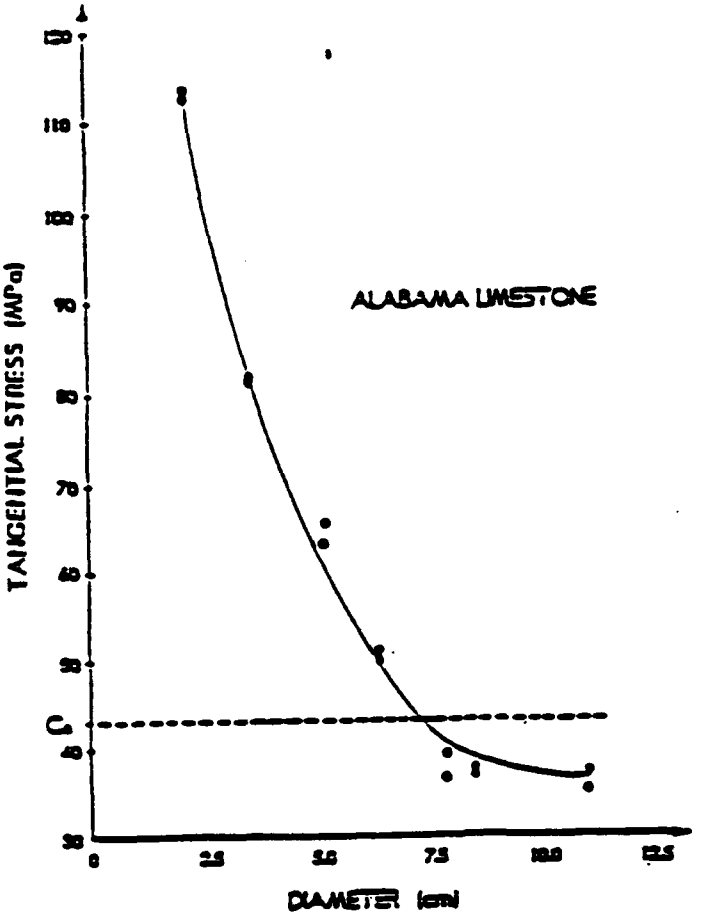

Figure 4.8 Experimental Data for Scale Effects for Borehole Problems (after Haimson and Herrick 1989)

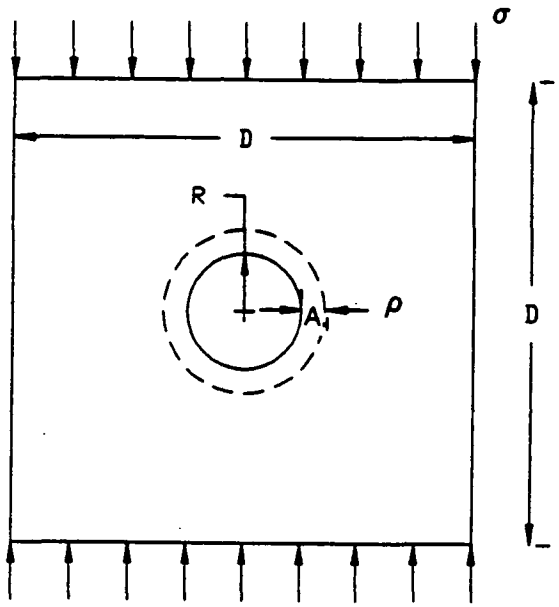

Figure 4.9 Geometry of A Borehole Problem Structure under Uniaxial Compressive External Load

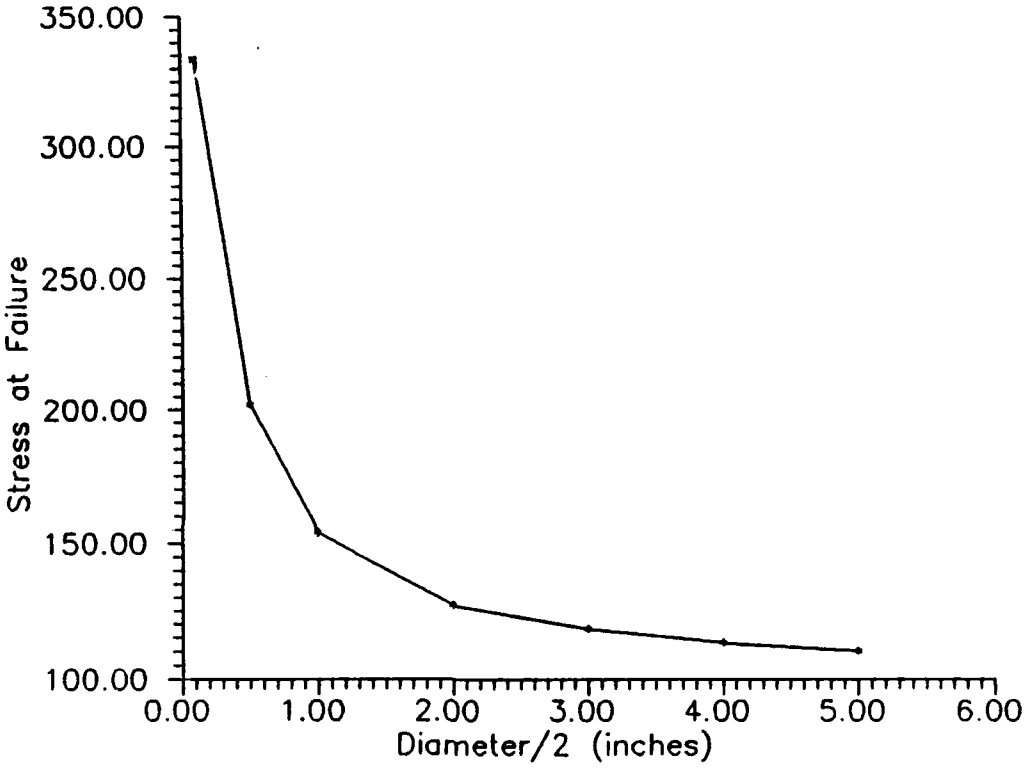

Figure 4.10 Scale Effect Predicted through the Simplified Analysis

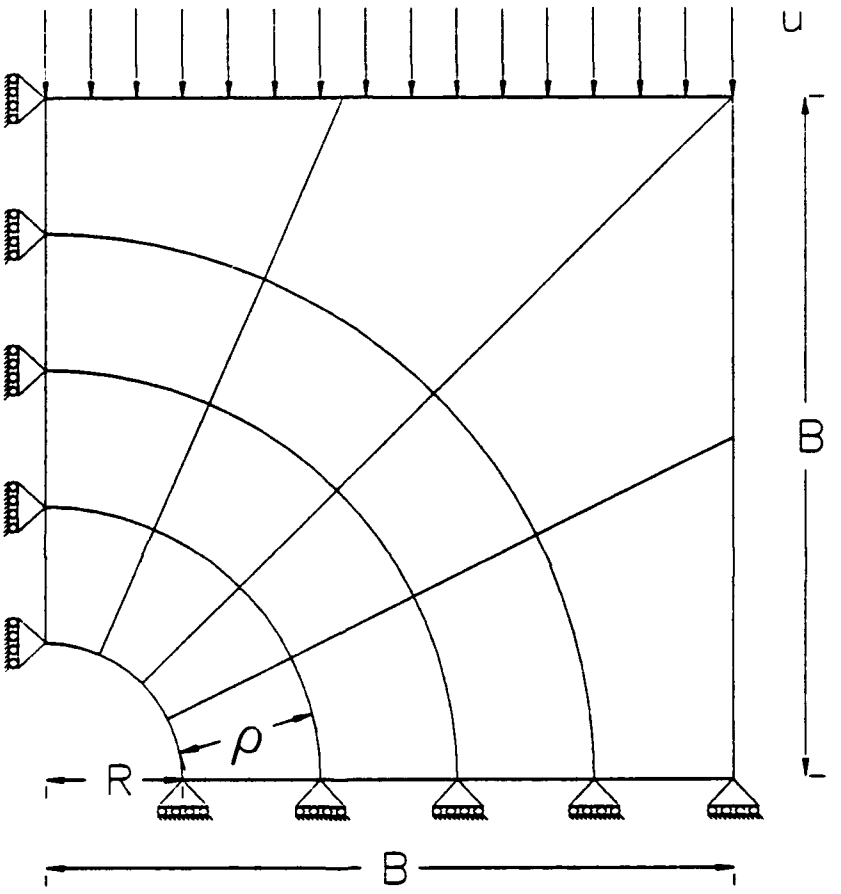

Figure 4.11 Finite Element Mesh for the Numerical Analysis of the Borehole Problem Depicted in Figure 4.9

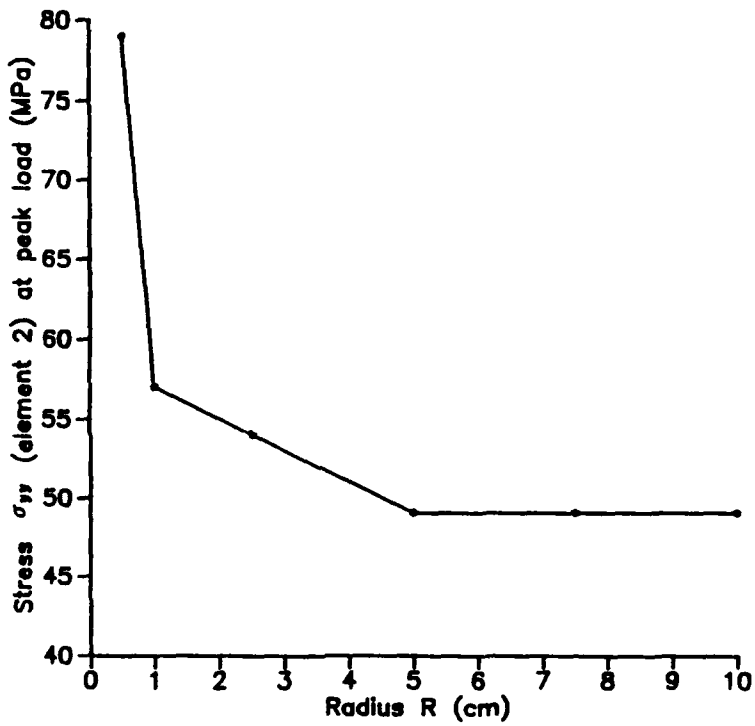

Figure 4.12 Predicted Scale Effect through Examination of the Normal Stress σ_{yy} at Element 2

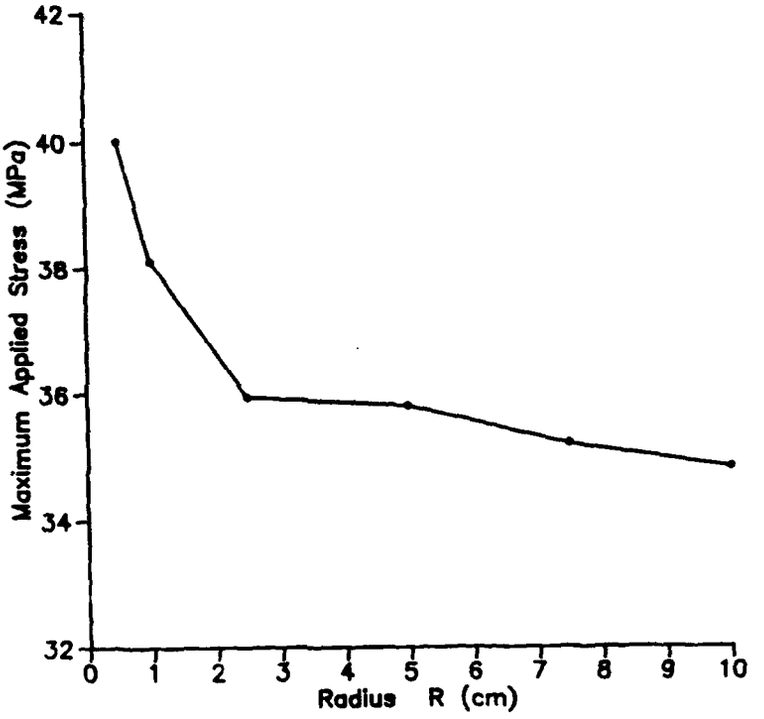

Figure 4.13 Predicted Scale Effect through Examination of the Maximum External Applied Stress

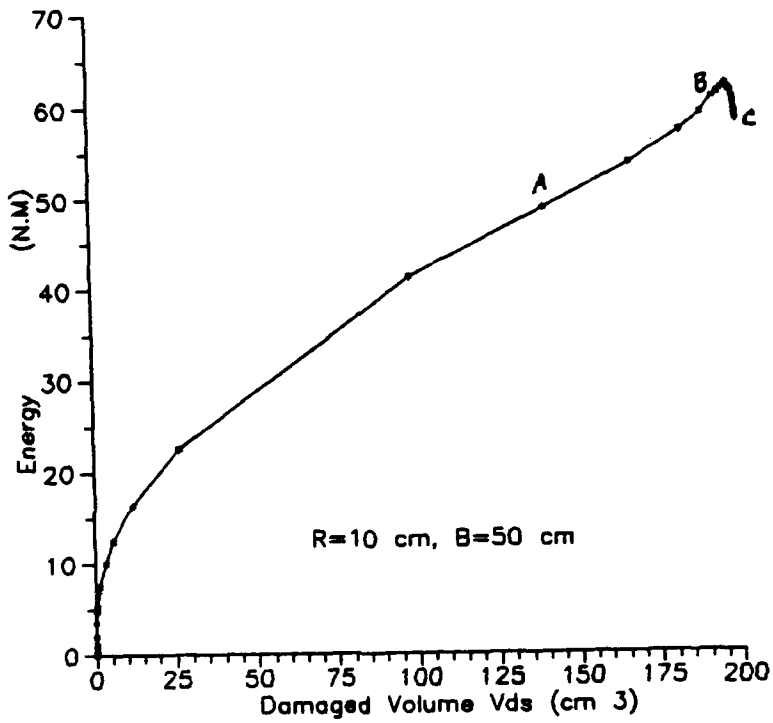

Figure 4.14 Damaged Volume V_{ds} v.s. Energy e for the Borehole Problem of $R = 10$ cm, $D = 100$ cm

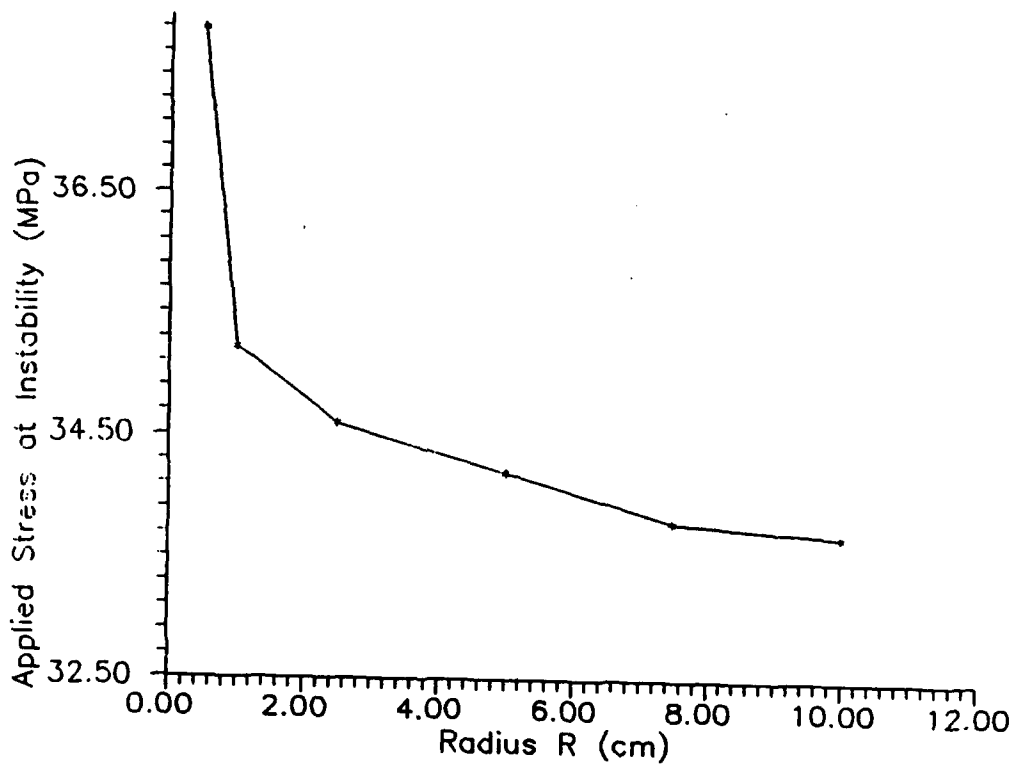

Figure 4.15 Predicted Scale Effect through Examination of Surface Degradation Instability

CHAPTER 5

PHYSICAL EXPERIMENTS

In this chapter, relevant non-destructive tests including strain gage tests and ultrasonic scanning tests are presented and discussed. For a brittle material under external load, degradation mechanism and patterning are studied, and the surface effects are identified. The material internal length associated with surface degradation (defined in chapter 3) is estimated against the ultrasonically dissipated energy distribution. The relationship between ultrasonically dissipated energy and mechanically dissipated energy is dependent on deformation and can be approximated by a power function of load level.

5.1 General

In the previous two chapters, the proposed instability criteria and applications to some typical problems have been presented. It is understood that the instability criteria are based on the energy consideration, that is, on the dissipated energy and elastic potential. Because energy dissipation corresponds to degradation, the instability criteria are called degradation instability criteria. It is also pointed out that the onset of the instability may manifest the onset of inhomogeneous deformation. In this chapter, relevant experiments are presented.

Surface effects have been reported theoretically and experimentally, especially for metal materials. For example, a few tests have been made in the laboratory to observe surface roughness that develops on aluminum bars by Hutchinson and Tvergaard [1980]. In these tests, it is clear that a large grain size gives more roughness and that the roughness increases with increasing strain. It is seen that the large strains at the very bottom of the wave troughs lead to shear fracture that propagates deep into the bar [Hutchinson and Tvergaard 1980]. Surface effects for brittle materials are not, as discussed previously, analogous to surface roughness in metals. Experimental evidence on such materials that identify the surface effects are available in Yukutake [1989] for example, or in other relevant references discussed previously.

The surface degradation instability involves the material constants associated with the surface degradation zone. To identify the internal material l associated with the surface degradation is another purpose of this chapter. Also, we are going to study the degradation patterning and see if some relationship exists between the degradation patterning and the final failure modes. Then through the investigation of degradation mechanism, we may better understand the physical inclusion of the degradation instability criteria.

Numerous methods ranging from the X-radiograph, to neutron radiography and diffraction have been developed as non-destructive techniques (NDT), to assess the integrity of structures, machines and other systems involving engineering materials. However, several non-radiation methods, such as ultrasonic/acoustic, light and electron microscopy, thermographic and optic, offer very attractive alternatives to radiation. Each NDT has its own advantages and limitations. A major problems of many techniques is that the information they provide is qualitative. However, people, especially engineers, are more interested in quantitative information. In the experiments described herein, the ultrasonic tests have been chosen.

In addition to the ultrasonic scanning tests, the strain gage tests are preceded, to study the local strain changes with average stress at some typical locations along the specimen. This may provide information about surface effects for brittle materials.

The performed experiments involved a lot of work and team effort. Mr. David Daniewicz contributed significantly in sample preparation, computer programming, execution, and data acquisition during the period the experiments were performed. His involvement is acknowledged.

5.2 Ultrasonic Experiments

5.2.1 Fundamental Terms

Ultrasonic testing of materials makes use of mechanical waves in contrast, for instance, to X-ray techniques which use electromagnetic waves. Any mechanical wave is composed of oscillations of discrete particles of material. The frequency of a wave is the number of oscillations of a given particle per second. Within a

given wave it is the same for all particles and it is identical with the frequency of the generator which can be chosen arbitrarily. The wave length is the distance between two planes in which the particles are in the same state of motion. It is inversely proportional to the frequency: high frequencies corresponding to short wave lengths, and vice versa. The speed of sound is the velocity of propagation of an acoustic wave. This velocity is a characteristic of the material concerned and in general is constant for a given material for any frequency and any wave length. The velocities of the various kinds of sound waves can be calculated from the elastic constants of the material concerned, namely, the modulus of elasticity E and Poisson's ratio ν.

For longitudinal waves:

$$C_l = \sqrt{\frac{E}{\rho}\frac{1-\nu}{(1+\nu)(1-2\nu)}} \tag{5.1}$$

for transverse waves:

$$C_t = \sqrt{\frac{E}{\rho}\frac{1}{2(1+\nu)}} = \sqrt{\frac{G}{\rho}} \tag{5.2}$$

where ρ is the density of material, and G is the shear modulus of material.

For us the most important quantity in a given sound field is the sound pressure. At points of higher particle density the pressure is likewise higher than the normal pressure, while in the dilated zones it is lower. A very small and inertialess pressure gauge placed in the path of the sound wave would indicate alternately high pressure and low pressure in sinusoidal sequence. This alternating pressure is the sound pressure. It occurs not only in gases, but also in liquid and solid bodies. The maximum deviation from the normal pressure (without sound wave) is called the amplitude of the sound pressure which is closely connected to the amplitude of movements, i.e. the maximum deflection of the particles from their position of rest.

In the case of plane and spherical waves sound pressure and particle amplitude are connected to each other by the relation [Krautkramer, J. and Krautkramer, H. 1983]

$$p = \rho c \omega \xi = Z \omega \xi \tag{5.3}$$

where p is the sound pressure, ρ is the density of the material, c is the velocity of sound, ω is the angular frequency, and ξ is the particle displacement. $Z = \rho c$ is called acoustic impedance (specific acoustic impedance). Materials with high acoustic impedance are called "sonically hard", in contrast to "sonically soft" materials.

In the case of plane and spherical waves, the intensity of a wave (J) is related to the sound pressure or the amplitude as follows [Krautkramer, J. and Krautkramer, H. 1983]:

$$J = \frac{1}{2}\frac{p^2}{Z} = \frac{1}{2}Z\omega^2\xi^2 \tag{5.4}$$

The intensity is thus proportional to the square of the amplitude of the sound pressure.

5.2.2 Absorption and Scattering

In ideal materials, the sound pressure is attenuated only by virtue of the spreading of the wave. A plane wave would thus show no attenuation whatever the value of the sound pressure along its path, and a spherical wave, or the sound beam of a probe in the far field, would merely decrease inversely with the distance from the source. Natural materials, however, all produce a more or less pronounced effect which further weakens the sound. This results from two causes, that is, scattering and (true) absorption which can both be combined by the concept of attenuation (sometimes also called extinction).

The scattering results from the fact that the material is not strictly homogeneous. It contains boundaries on which the acoustic impedance changes abruptly because two materials of different density or sound velocity meet at these interfaces. Such inhomogeneities may either be inclusions, e.g., granular materials or pores in concrete. They may be genuine flaws of the material concerned, or also natural or intentional flaws such as porosity in sintered materials. They may also be material which by their nature are inhomogeneous, e.g. cast iron, in which an agglomeration of elastically completely different ferrite and graphite grains occurs. There are, however, also materials which experience anisotropy under deformation.

In a material with very coarse grain compared with the wave length the scatter can be visualized geometrically: on an oblique boundary the wave is split into various reflected and transmitted wave types. This process repeats itself for each wave at the next grain boundary. Thus, the original sound beam is constantly divided into partial waves which along their long and complex paths are gradually converted into heat because of the always present true absorption.

In the frequency range used in testing materials the grain size is usually smaller than the wave length. Under these conditions scatter occurs instead of geometric division.

The second cause of the attenuation, absorption, is a direct conversion of sound energy into heat, for which several processes can be responsible [Mason 1958]. Absorption can roughly be visualized as a sort of braking effect of the oscillations of the particles, which also makes it clear why a rapid oscillation loses more energy than a slow oscillation; the absorption usually increases with increasing frequency [Krautkramer, J. and Krautkramer, H. 1983].

5.2.3 Intensity Methods for the Ultrasonic Testing of Materials

Methods for the ultrasonic testing of materials can be divided into three categories: intensity methods, pulse-echo method and transit-time method. The intensity methods have been chosen for our study. As discussed in the sequence the transit time method did not provide consistent and/or useful information. Then the following brief description is restricted to intensity methods.

The intensity method in which the intensity of the ultra-sound is measured after it has passed through the test piece, is the oldest application of the ultrasonic waves for non-destructive testing. It dates back to 1930 and was originated by Sokolov and Muhlhauser [Krautkramer, J. and Krautkramer, H. 1983]. The principle is shown in Figure 5.1 in which the intensity method is portrayed schematically by passing sound through a test plate, at a flawless and alternately at a defective point.

The voltage produced by a high-frequency generator excites the transmitting probe to ultrasonic oscillations which are propagated in the coupled test piece.

A second probe positioned coaxially on the opposite side receives a portion of the radiated wave and transmits to the input of an amplifier a high-frequency voltage which is proportional to the sound pressure at the contact point of the receiver. The amplified voltage is read on an indicating instrument. At the flawed point the propagation of the ultrasonic wave is impeded by the discontinuity in the material, resulting in reduced sound pressure at the receiver and thus a lower reading on the measuring instrument. Strictly speaking, this measures not the intensity but primarily the amplitude of the sound pressure if a piezoelectric receiver is used. Provided the characteristics of both the amplifier and the instruments are linear, the indication in this case is therefore proportional to the square root of the intensity.

5.2.4 Review of the Existing Literature

Various researchers have attempted to establish correlations between mechanical properties of brittle materials and ultrasonic measurements. As concrete is concerned, ultrasonic pulse measurement has been applied to assess the compressive strength [Jones 1952], compaction deficiencies, and maturity of young concrete. The relation between compressive strength and pulse velocity in concrete have been studied [Sturrup et al 1984; Ben-Zeitun 1986], but the scatter is found to be considerable. Mindess [1982] loaded specimens in compression monotonically to failure and measured the pulse velocity at the same time. He found that the velocity remains constant until significant internal cracking occurs, i.e. between 1/3 and 2/3 of the strength. Spooner and Dougill [1975], however, experienced in their experiments that pulse velocity decreased only near the peak stress. Al-Kubaisy and Young [1975] showed that transit time increases in a specimen when the tensile loading is increased and that strain discontinuities also cause transit time discontinuities. Reinhardt and Hordijk [1988] used ultrasonic pulse measurements for the assessment of damage in high strained zones such as that between two saw cuts. It was concluded that close correlation between ultrasonic pulse measurements and strength, and the size of the damage zone within a specimen can be established.

Shah and Chandra [1970] studied the velocity and attenuation changes of ultrasonic pulses transmitted across concrete and paste specimens subjected to monotonically increasing, cyclic, and sustained loading. The measurements were used in contrasting mechanisms of fracture. It was observed that:

1) There is no pulse velocity change for hardened paste specimens;
2) For mortar specimens, the velocity decreases prior to failure;
3) The same observation is true for concrete specimens as for mortar. However, the velocity decrease is more pronounced for concrete than for mortar specimens. It was also observed that for concrete specimens attenuation starts to continuously increase at 48.5 percent of the ultimate and for mortar specimens at 89.5 percent of ultimate, while there was very little change in amplitude until failure in paste specimens. It is noted that Robinson [1965] also found that, the greater the quantity of aggregates, the lower the relative values of stress at which the pulse velocity begins to decrease.

The effects of frequency of crystals were also investigated by Shah and Chandra [1970]. The following observations were made from those tests:

1) The initial no-load velocity of the ultrasonic pulse increases with an increasing frequency of the crystal. The average initial velocity for the 25-kHZ crystals was 13,300 ft/s, while that for the 2250-kHZ crystals was 83,200 ft/s.
2) Initial amplitudes or intensities of the pulse decreased with increasing frequencies.
3) The higher the frequency of the crystal for a given amount of cracking, the greater the changes in the ultrasonic measurements.

A geological material when subjected to a sequence of loading, unloading and reloading, exhibits anisotropic response. This is usually attributed to reorientation of particles and to the formation of micro-cracks and damage within the material. To characterize the induced anisotropy in geological materials and to compare, to quantify, and to correlate such response with the anisotropic response, Jagannath, Desai and Kundu [1991] developed an ultrasonic testing procedure. The ultrasonic response was presented in the form of wave signatures, velocities and attenuations.

In Jagannath, Desai and Kundu [1991], the mechanical anisotropy is computed based on the available constitutive laws [Desai et al 1986]. Let $\dot{\epsilon}_i$ be the strain increment in three main directions, and $\bar{\dot{\epsilon}}$ be the average incremental strain in the material. Then, the ratio $\dot{\epsilon}_i/\bar{\dot{\epsilon}}$ gives a measure of anisotropy in the ith direction. An over-all measure of mechanical anisotropy at any given state is defined as [Jagannath, Desai and Kundu 1991]:

$$M_{anis} = \sqrt{[\Sigma_{i=1}^{3}(1 - \dot{\epsilon}_i/\bar{\dot{\epsilon}})^2]} \tag{5.5}$$

The ultrasonic anisotropy is a physical measure of the anisotropy and can be quantified based on the experimentally available velocities and attenuations. Let $\bar{V}$ and $\bar{A}$ be the average velocity and attenuation in the material, respectively. Then, the ratio $V_i/\bar{V}$ and $A_i/\bar{A}$ gives a measure of ultrasonic anisotropy in the ith direction at any given state of the material. An over-all measure of ultrasonic anisotropy at any given state was defined as [Jagannath, Desai and Kundu 1991]:

$$V_{anis} = \sqrt{[\Sigma_{i=1}^{3}(1 - V_i/\bar{V})^2]} \tag{5.6}$$

$$A_{anis} = \sqrt{[\Sigma_{i=1}^{3}(1 - A_i/\bar{A})^2]} \tag{5.7}$$

Based on experimental results, correlation functions between mechanical anisotropy and ultrasonic anisotropies have been established [Jagannath, Desai and Kundu 1991]. It is found that the mechanical anisotropy can be expressed as a second order polynomial of ultrasonic anisotropies.

5.3 Objectives of the Experiments

For decades, laboratory tests on brittle materials sought to achieve a homogeneous state of stress and deformation on samples subjected to uniaxial load. However, even under ideal testing conditions, the heterogeneous micro-structure of the material yields an inhomogeneous deformation field from the early straining stage, Fairhurst and Cook [1966], Hudson et al [1971], Read and Hegemier [1984], Yukutake [1989]. In the uniaxial compression test the density of microcracks rapidly proliferates, leading to vertically aligned microcracks resulting in gross slabbing

of material from the tractionless surfaces. It is difficult to observe and/or simulate the spatial pattern of material heterogeneity on the microscale. Undoubtedly, important information can be extracted from models simulating the microstructure and spatial randomness of heterogeneity, Bazant et al [1990].

The proposed experiments include pure strain gage tests, ultrasonic scanning tests, and combined strain gage and ultrasonic scanning tests. The uniaxial external mechanical load is exerted through a servo-controlled MTS system as described in detail later. The purposes of the experiment studies may be generalized as:

1) to identify the initial (without external load exerted) material state.
2) to study the spatial variation of degradation mechanisms in a brittle material subjected to mechanical load.
3) to study the local deformation development and damage evolution and provide information to identify the surface effects for a brittle material.
4) to estimate the internal material length l associated with surface degradation for a brittle material.
5) to investigate the relationship between mechanically dissipated energy and ultrasonically dissipated energy and see if the relationship is scale or size dependent.
6) to generate data to verify the theory for damage and surface degradation.

A scanning device was developed for these purposes and existing ultrasonic equipment was used.

5.4 Equipment and Testing Material

5.4.1 Ultrasonic Apparatus

The ultrasonic test device described below was acquired, and its use for modeling and testing of geomaterials experiencing induced anisotropy due to plastic straining, damage and microcracking was conceived and developed by C.S. Desai under a grant No. CES-8711764 from the National Science Foundation, Washington, D.C. Mr. S.V. Jagannath participated in this research project for his doctoral work, and the results of the study are available in Jagannath et al [1990, 1991]. A

Model 5055PR Pulser-Receiver, Panametrics, in combination with a digital oscilloscope, Hewlett-Packard 54501A was used.

For the purpose of this research, modifications and additions described below were made to develop computer controlled device for the movement of the transducers on the surfaces of the test specimen [Frantziskonis, Desai, Tang and Daniewicz 1991].

Figure 5.2 shows the schematic of the test system for ultrasonic measurements on specimens subjected to external mechanical load. The ultrasonic transducers used (D, E in Figure 5.2) were the P/N Z-10016-3, Zevex Inc., Salt Lake City, Utah, resonant frequency of 50 Khz. The diameter of each transducer is 1.5 inches (1 inch=2.54 cm). With these characteristics, the waves produced are appropriate for transmission through brittle attenuating materials like the one tested. In order to take ultrasonic measurements at several locations in a sample subjected to mechanical load, it was necessary to develop a scanning system that would provide the following:

(i) continuous alignment of the ultrasonic pulser and receiver through a frame, for the transmission of the wave through the sample,

(ii) arrangement for the movement of the frame in horizontal and vertical directions so that different points of the sample can be located accurately,

(iii) easy and quick alignment of the pulser and receiver,

(iv) constant and consistent contact pressure between the transducers faces and the sample while measurements are taken,

(v) movement of the transducers away from the sample when they progress from one measurement location to another.

For this purpose an appropriate system schematic shown in Figure 5.3, was developed. Horizontal (x) motion of the transducers is accomplished through two identical stepper motors (B in Figure 5.3) and so is the vertical (y) motion (C in Figure 5.3). In order to take measurements at a certain location of the sample, air pressure of 7 psi (1 psi=6.89 KPs) is applied to the transducers in the Z-direction. After measurements are taken the air pressure is released, negative air pressure is applied so the the transducers move away from the sample, and the transducers

move to the next measurement location. All four stepper motors (K33505, Airpax, Cheshire, Connecticut) and the air pressure regulators are controlled through prototype controllers from a micro-computer, Motorola M68KVOVER/09. Appropriate computer programs were developed for the automated horizontal and/or vertical movement of the transducers, and application of air pressure. Data were extracted from the oscilloscope and the pulser-receiver.

The contributions of Mr. Pete Boyle towards the development of the scanning device, and of Mr. Todd Booth and Mr. Tom Cram towards the electronics are gracefully acknowledged.

5.4.2 Mechanical Load And Material Tested

The system for the movement of the transducers described above was mounted on an MTS testing machine, Figures 5.2 and 5.4. This allowed acquisition of ultrasonic measurements while the sample was subjected to external compressive mechanical load from the MTS frame. Three series of prismatic samples were tested for ultrasonic scanning tests. For all samples the hight (H) was 5 inches (12.7 cm) and the depth (D) was 1.3 inches (3.302 cm), Figure 5.5a. For the three series, width (W) of the samples was 3.0, 3.5 and 4.0 inches (7.62, 8.89 and 10.16 cm), respectively. The ultrasonic pulse was transmitted through the depth (D) at different locations of the sample, Figure 5.5a. Compressive load was applied parallel to the height (H). Because eccentricity of loading will cause a lot of problems (e.g. consistent results can not be achieved), the placement of load platen was carefully processed.

In order to reduce friction between the sample and loading end platens, the following procedure was followed. The end platens and the faces of the sample subjected to compressive load were lubricated by a thin layer of silicon grease. In addition, a thin layer of teflon lubricated on both sides was placed between end platen and sample. All sides of each specimen were machined in order to obtain smooth surfaces for uniform load application, uniform coupling between transducers and specimen, and for mounting strain gages.

The material specimens were made of simulated rock and were cast in aluminum molds with casting direction parallel to the height. This material was developed by Desai et al [1990] through a parametric variation of various components such as sand, cement and plaster of Paris, and air entraining agent. The three main criteria used for the development of such a material were: (i) consistent material response, (ii) low compressive strength so that accuracy of measurements with available measuring devices is enhanced, (iii) to achieve as initial homogeneity as possible. In Desai et al [1990] it was concluded that the following combination showed the most consistent results from the view point of the above criteria: sand:cement:plaster of Paris:water=15:2:3:4, by volume.

5.4.3 Strain Gages

The bonded electrical resistance strain gage is widely recognized as the most practical technology for measurement of strains in loading-bearing parts, members, and structures. Because both excellent accuracy and repeatability can be achieved, strain gages are also becoming increasingly important as primary sensing elements in load cells as well as in pressure, force, torque, displacement, and others. To make strain measurements of acceptable quality, several parameters should be considered: quality of strain gage itself; environmental protection, and other strain gage accessories; proper circuit design, proper installation of the strain gage; and quality of the strain gage instrumentation. Specifically, the strain gage labeled CEA-06-500UW-120 manufactured by Measurements Group, Inc. Raleigh, North Carolina, USA was chosen for our tests. CEA gage is a general-purpose family of constant strain gages widely used in experimental stress analysis. The gages are supplied with a fully encapsulated grid and exposed copper-coated integral solder tabs. The temperature range is -100 to +400°F for continuous use in static measurements. The fatigue life is about 10^5 cycles.

5.5 Ultrasonic Measurements

Consider a structure (specimen) subjected to external mechanical load, Figure 5.5a. As load increases, the sample experiences degradation or microcracking.

Within the volume V of the structure an elementary volume dV_i with cross-sectional area dA_i perpendicular to the direction of the ultrasonic wave transmission is identified. For piezoelectric ultrasonic transducers of diameter d, $dA_i = \pi d^2/4$. Let Q_i be the dissipated energy due to degradation progression in dV_i. we can assume, in general

$$Q_i = \gamma R_i \tag{5.8}$$

where R_i is a measure of degradation within dV_i, and γ is the dissipated energy per unit of R_i.

Let an ultrasonic pulse be transmitted through dV_i. Let zero (0) denote the state of the sample where no external load is applied. Let the energy of the received (after transmission through dV_i) ultrasonic wave at zero state be E_{0i}. Let the energy of the received wave at a deformed state be E_i. Due to the degradation progression in dV_i, the attenuation of the transmitted wave increases. It can be written, in general

$$\Delta E_i = E_{0i} - E_i = cR_i \tag{5.9}$$

where c is the transformation coefficient relating degradation R_i to ultrasonic wave attenuation ΔE_i. It measures the intensity of influence of the structure transformation to the ultrasonic wave attenuation. From (5.8) and (5.9) we have

$$\Delta E_i = \frac{c}{\gamma} Q_i = aQ_i \tag{5.10}$$

Equation (5.10) indicates that the local ultrasonic attenuation is proportional to the local degradation dissipated energy; here local pertains to the fact that the ultrasonic wave passes through the volume dV_i. The question is whether a is a constant or not; its possible dependence on deformation or load level is considered later. For the specimens tested, volume dV_i is of cylindrical shape of diameter d = 1.5 inches (3.81 cm) and depth D = 1.3 inches (3.302 cm). It should be noted that when a pulse is transmitted from the ultrasonic transducer through the sample, the wave energy is not uniform on the transducer's face. The energy is maximum at the center of the circular face and reduced smoothly to a minimum

at the periphery. In addition, as discussed later, the transmitted wave experiences the so-called near field effects, in which the wave characteristics are different from the ones far from the pulser transducer's face [Krautkramer, J. and Krautkramer, H. 1983]. In this study, we assume that the wave energy is uniform on the area of the transducer's face. As shown subsequently, the near field is rather short so the received wave was not close to it.

The velocity of an ultrasonic P-wave in an elastic material can be related to the Young's modulus E and Poisson's ratio ν as shown in (5.1). The material examined in this study shows inelastic response from the early straining stages. For strains up to the peak the Young's modulus (from the unloading/ reloading slope) was found from the present study and Desai et al [1988, 1990] to be approximately 180,000psi (1240 MPa) and $\nu = 0.3$. The initial density of all samples tested was 0.066 lbm/in^3 (1.825 g/cm^3). For these values, if for the time being we assume that (5.1) is valid, we obtain $c_1 = 37,664$ in/s (957 m/s), thus for a sample depth of 1.3 inches (3.302 cm) the transit time is 33.8 μs. The transit time measured in the experiments was 34 μs with 0.5 μs accuracy of the time measurement. The pulse velocity remained constant while the sample was loaded and changed only when the external load was close to the peak. This is consistent with the results obtained for hardened paste and mortar specimens [Shah and Chandra 1970], and for concrete specimens [Spooner and Dougill 1975]. However, as discussed subsequently, the attenuation of the pulse showed significant changes from the early straining stages. Achenbach et al [1991] found increase in pulse velocity of surface waves while the attenuation increased. However, such effects may be peculiar to surface and not to P-waves. Through the measurement of the transient time, the constant pulse velocity for load levels in the load range between zero and close to peak was found to be $c_1 = 38,230$ in/s (971 m/s). Reduction in pulse velocity close to peak was not insensitive or very consistent in the performed tests. Thus the only conclusion is that pulse velocity remained constant and was reduced rapidly and inconsistently close to the peak load.

For the resonance frequency of the transducers of $f = 50,000$ cycles/s, the wave length λ of the transmitted pulse can be calculated, $\lambda = c_1/f = 1.94$ cm. For

the ultrasonic transducers of circular cross section of diameter d, the length of the near field N can be evaluated as [Krautkramer, J. and Krautkramer, H. 1983]

$$N = \frac{d^2 - \lambda^2}{4\lambda} \tag{5.11}$$

For the transducers used $d = 1.5$ inches (3.81 cm), and (5.11) yields $N = 1.38$ cm which is much smaller than the thickness of the samples used, which is 1.3 inches (3.302 cm). Thus the received wave was always far from the near field.

The average energy, E_i, of a received ultrasonic wave is proportional to the square of its maximum amplitude. Mathematically, we can write [Krautkramer, J. and Krautkramer, H. 1983]

$$E_i = \beta A_i^2 \tag{5.12a}$$

$$E_{0i} = \beta A_{0i}^2 \tag{5.12b}$$

where A is the maximum absolute voltage of the received wave while the sample is under external load, A_{0i} is the maximum absolute voltage of the received wave before any external load is applied, and β is a constant relevant to the electromechanical characteristics of the receiving transducer. From (5.9) and (5.12), it follows that

$$\Delta E_i = \beta(A_{0i}^2 - A_i^2) = \beta G \tag{5.13}$$

So $G = A_{0i}^2 - A_i^2$ can be used to monitor the structural transformation or degradation progress. From (5.10) and (5.13) we conclude that the mechanically dissipated energy is proportional to G. This connects the ultrasonic measurements with mechanical measurements and makes the quantitative assessment for the degradation of brittle materials subjected to external load be possible. For this reason, in all measurements presented in the following, by the term dissipated energy we imply the difference $G = A_{0i}^2 - A_i^2$. However this term could be replaced by "ultrasonic pulse attenuation", or "intensity reduction".

5.6 Test Results

5.6.1 Strain Gage Test Results

Eight specimens were processed with strain gages attached. Strain gages were mounted at specific locations along the specimen, as shown in Figure 5.6. Further, 3 tests (S4s, M4s, L4s) included strain gages and ultrasonic testing, Figure 5.7. Loading for all specimens was displacement controlled with the rate of strain increment about 10^{-6}/second. All specimens for strain gage tests were loaded monotonically up to peak and experienced with post-peak to residual stage. Figure 5.8 shows a typical (average) stress-strain curve including post-peak response. For each load step, in addition that the four strain gage readings were checked, the displacement of the top surface of the specimen was measured through the MTS system, to make the calculations of the average strain. Among the eight specimens, four specimens are relatively smaller, with the dimensions of $5 \times 3 \times 1.3$ (in^3), and are labeled with PS; another two specimens are medium, with the dimensions of $5 \times 4 \times 1.25$ (in^3), and are labeled with PM; the other two specimens are relatively bigger, with the dimensions of $5 \times 5 \times 1.25$ (in^3), and are labeled with PL. It was observed that the strains from strain gages are considerable smaller than the average strain obtained. On three specimens (S4s, M4s, L4s), four strain gages were mounted on the free surfaces as shown in Figure 5.7. Figure 5.9a shows the overall readings from the MTS load cell and the attached LVDT's of the MTS frame and Figure 5.9b shows the strain gage readings. One possible explanation of the considerable difference between the local strain on surface and the average strain is that unloading takes place in the outer surface layers of the specimen, and the carrying capacity of the fractured specimen is mainly due to the "intact" specimen core. Experiments on concrete justify this [Vanmier 1984]. Further discussion will be presented later. However, here we are interested in the local strain distributions and the relative changes of local strains with external load along characteristic points. Figure 5.10-5.14 are typical results with strain gage readings versus applied stress. It is obvious that the local deformation is not uniform, and the non-uniformity for different samples is different. It is also seen that the increasing rate of strains

from different locations are different. In order to analyze these data and to identify the information of surface effects, let us process the following procedure [Tang, Frantziskonis and Desai 1992a].

Pick up the local strains at different external mechanical load levels, say at P/P_{peak} =0.5, 0.85, and 1.0, as shown in Table 5.1, 5.2, and 5.3, respectively. For each sample at each external load level, find the smallest local strain and regard it as reference. If we assign a weight of 100 to the smallest local strain, the weights of other local strains can be obtained by calculation $\epsilon_i/\epsilon_s \times 100$, where ϵ_s is the smallest local strain, and ϵ_i are the local strains of the other gages. The weight distribution for P/P_{peak} =0.5, 0.85, and 1.0 are shown in Table 5.4, 5.5, and 5.6, respectively. The results for Test-1 are not shown in these tables, because one of the strain gages was broken by accident. We add together the weights of the same gage number for all the samples listed, and compare the results as shown in Table 5.7. It is interesting to see that, at the early straining stage, the deformation is concentrated at gage 4 which is located at top (or bottom) of the right (left) surface (perpendicular to the width) as shown in Figure 5.6, then with increase of external load, the strain concentration transfers to gage 1 which is located at the middle of the front surface (perpendicular to the depth), at or close to the peak, the maximum local deformation occurs at gage 1. It is noted that this conclusion is based on the statistical sense. Because of the randomness of the initial (without external load exerted) material inhomogeneity, some measurements do not agree with this conclusion.

The observations discussed above can be explained by the so-called surface spalling (slabbing) mechanism. The surface slabbing is depicted as shown in Figure 5.15. For the specimens tested, because the width is about three times as large as the depth, the surface spalling effects are more pronounced along the surface with normal perpendicular to depth (left or right surface). At the early straining stages, the damage is concentrated in the volume close to these surfaces. Along these two surfaces, the top and bottom part are more severly influenced by other boundaries, and the microcracks start to proliferate in these parts, so the strain gage readings there are expected to be relatively large. After some load steps, say

at $0.5 < P/P_{peak} < 0.8$, the macrocrack for surface spalling is formed, and inner part (other than the slabbed material) becomes the main load-supporting material. This may be the reason why fast increase in the rate of strain at gage 1 was observed at subsequent straining stages. As the stress is increased exceeding 80 to 90 percent of the peak strength, the non-uniform local deformations are greatly pronounced (comparing the changes of strain gage readings). This may be responsible for the physical explanation of the degradation instability theory discussed in the last two chapters.

5.6.2 Ultrasonic Test Results

In the following we first summarize the outcomes from the ultrasonic test results. Subsequently, various test results from the twelve specimens tested are presented in detail as discussed in [Frantziskonis, Desai, Tang and Daniewicz 1991].

Summary of the Observations:

- Scanning the samples at zero external load showed that all samples were not initially homogeneous with respect to the energy of the received wave. Note that the initial density of each sample was consistent and equal to about 0.066 lbm/in^3 (1.825 g/cm^3). In addition, in order to avoid non-homogeneous material (through depth D) due to casting, the casting surface was transverse to the direction of the transmitted wave. We consider that even before any external load is applied on the samples, the material contains flaws in the form of voids and microcracks. Thus since the energy of the transmitted pulse is constant, the energy of the received wave decreases with increasing initial density of flaws.
- The initial non-homogeneity was rather random for all samples. The pattern of inhomogeneity was different for each sample.
- For all load steps up to the peak, dissipated energy shows a random distribution and it follows, in general, the initial non-homogeneity pattern. The dissipated energy pattern showed no symmetry.

- Dissipated energy was, in general, concentrated on one of the two load-free surfaces.
- In those cases where the initial non-uniformity showed higher concentration of received pulse energy in the center of the specimen (far from the free-edges), the dissipated energy pattern under load did not follow the initial non-uniformity pattern.
- Surface concentration of dissipated energy is shown to extend over an identifiable distance ρ from the free surface, Figures 5.18, 5.19, and 5.22. This is used in connection with the proposed theoretical considerations on surface degradation mechanisms, as a tool to identify the internal material length l.
- Under unloading the dissipated energy essentially remains constant or decreases slightly.
- Although the dissipated energy pattern is random, more energy is dissipated close to the load-free surfaces. All twelve specimens tested experienced formation of a macro-crack network, in a brittle fashion, at peak or slightly before peak. Since each sample showed formation of different macrocrack pattern it seems appropriate to conclude that such a pattern is random. This is consistent with recent theoretical studies [Bazant et al 1990].
- For monotonically increasing load, a large percentage of the total dissipated energy occurred at relatively low load levels. Some measurements showed decrease in dissipated energy under increasing external load. This may imply unloading of partially formed cracks and is consistent theoretical considerations [Bazant et al 1990].

Figure 5.5b shows the location of the centers of the transducers that provided ultrasonic measurements. Since the diameter of the transducers is 1.5 inches only 12 point measurements were considered for the small and medium samples while 16 points were considered for the large samples. (A denser array of measurement locations would result in significant overlapping between measurement locations).

Loading for all specimens was displacement controlled, and all samples were broken finally to obtain the peak stress. Some specimens were loaded monotonically

up to peak and measurements were taken at different load levels. In order to study the effect of unloading and reloading on the energy dissipation distribution, some specimens were unloaded, and ultrasonic measurements were taken in the unloaded state. Then the specimens were reloaded for further measurements. It is noted that all the samples were loaded to peak to identify the peak strength. At the peak or slightly before the peak, formation of a macrocrack network occurred. After this crack formation it is rather impossible to take reliable ultrasonic measurements since the presence of macrocracks do not allow a consistent output signal. Thus the purpose of the experiments was to examine the behavior for loads up to or close to the peak load. Typical failure modes discussed later are shown in Figures 5.16I and 5.16II.

In the displacement controlled testing, the actuator fluctuates the load in a saw tooth way so that the prescribed displacement can not be controlled in a smooth manner. For this reason, very close to the peak it is difficult to "freeze" the load, even for short period of time. Ultrasonic measurements were taken for loads close to the peak, up to 95% of the peak stress.

Test Results:

We first present typical results from each series of tests. Four samples from each series were tested. S1, S2, S3 and S4s designate the four small samples tested and the lower case s indicates that strain gage measurements were taken in addition to the ultrasonic ones. Similarly, the medium series samples are designated as M1, M2, M3, and M4s, and the large ones as L1, L2, L3, and L4s. Figures 5.17a,b,c show the dissipated energy distribution ($G = A_{0i}^2 - A_i^2$) versus the external load for different locations (Figure 5.5b) within the sample for M2. The external load was increased monotonically until about 92% of the peak load and then unloaded to about 8% of the peak. As can be seen from this figure, significant energy is dissipated in the early loading stages. Up to about 20% of the peak, the energy dissipates rapidly. Subsequently, the dissipated energy increases at a much slower rate. For some locations, the dissipated energy decreases with increasing load, and

as discussed before this may indicate unloading of partially formed microcracks. After the specimen is unloaded, the dissipated energy decreased for locations 1,2,3,4,10,11,12 by small amounts, while greater decrease was observed for locations 5,6,7,8,9.

Figure 5.18a shows the spatial variation of the initial energy of the received wave. Clearly the sample is initially not uniform and shows a lower concentration of initial flaws along the middle column of the sample. However, this initial pattern is not followed when the sample is subjected to external load. This is depicted in Figure 5.18b where the dissipated energy distribution at 20% of the peak shows concentration near the right free surface. If we observe the failure mode of this sample (M2), Figure 5.16I(a), we see spalling near the top right corner indicating higher damage in that area. The dissipated energy pattern, Figure 5.18b shows such characteristics. A similar pattern was followed for subsequent loading; Figure 5.18c shows the distribution of G at 68% of peak. At the unloaded state, Figure 5.18d, the pattern changes slightly and dissipated energy shows concentration on both free surfaces.

Figure 5.19a, from test S3, shows that the initial energy E_0 (at zero load) of the received wave shows concentration at the upper end of the free surfaces. A similar pattern was observed when the sample was subjected to monotonically increasing load, Figure 5.19b,c, which show the dissipated energy pattern at 36%, 92% of peak, respectively. Failure of this sample occurred by severe damage concentration on the right top side and on the left side in the middle. Those two damage zones finally resulted in the macrocrack along the width, Figure 5.16II. We consider that higher received energy at the initial zero load state indicates a smaller level of initial flaws. Then, as implied from the test results, we observe higher rate of damage increase at places of low initial flaw concentration.

Figure 5.20a shows results from test L1, where the initial energy, E_0, of the received wave was concentrated on one surface with greater concentration near the right top. Figure 5.20b shows the dissipated energy distribution at 93% of peak. Figure 5.20 shows that the dissipated energy pattern remained similar to the initial

one. This sample failed by damage concentration near the right top corner and macrocrack initiation from the region, Figure 5.16I(c).

In the above typical results from a small, medium and large sample were presented. In order to demonstrate the concentration of dissipated energy close to the load free surfaces and to provide the ground for the estimation of the internal length, we present typical patterns observed from other samples. Figures 5.21a,b show the energy dissipation pattern for test M4s recorded at zero, 92% of the peak load, respectively. Failure of this sample occurred by macrocrack formation initiating near the top at the middle, (point 5), Figure 5.5b. This sample was loaded to 92% of peak then unloaded to 9% and then reloaded to failure. Figure 5.21c shows the dissipated energy distribution in the unloaded state.

Figures 5.22 and 5.23 show results obtained from test S4s. This specimen was loaded monotonically to 81% of peak, then unloaded to 8%, and then reloaded to peak. Figures 5.22a,b,c,d show the dissipated energy pattern for test S4s, at zero, 81%, unloaded state, reloaded state to 93% of the peak load, respectively. It can be seen that the energy dissipation pattern remained remarkably similar in shape from the very beginning of the load application. Figure 5.23a shows the distribution of G along columns 1, 2 and 3, for the loading steps. Energy dissipation is concentrated at the left side of the sample and the core experiences the least dissipation. Figure 5.23b shows the local strains along the left and right free surfaces versus external stress for specimen S4s. Figures 5.24a,b show the initially received energy distribution and local strains for specimen L4s. Sample M3 was loaded to 91% of peak, then unloaded to 7%. Figures 5.25a,b,c show the distribution of initially received energy and G for test M3 at zero, 23%, 91%, respectively. Again, for this sample, the G pattern shows concentration on the left side. Failure occurred by macrocrack formation on the left side.

Now, let us compare the initial states and local strain readings for specimens M4s, S4s, and L4s, Figure 5.19a, Figure 5.21b, Figure 5.22a, Figure 5.23b, Figure 5.24a and Figure 5.24b. For specimen S4s, the material around the right top is relatively more disintegrated, and the local deformation is relatively smaller there at early straining stages; the local strain reading is relatively larger for gage-3,

the damage development is concentrated along the left side, and after the load reaches about 70 percent of the peak, unloading occurs for the left top part. It is noted that, after the first load step (23 percent of the peak), there is only very small dissipated energy increase (Figure 5.23a). For specimens M4s and L4s, the right top is relatively more disintegrated as compared with the left top, readings from gage-1 are smaller than those from gage-3, but the local deformation is less diverted as compared with specimen S4s. It is important to know that the initial inhomogeneity is more pronounced for specimen S4s than for specimens M4s and L4s. For example, the initially received maximum and minimum energy for specimen S4s are 77.7 Joule and 12.5 Joule, while for specimen M4s, they are 86.1 Joule and 34.1 Joule, here, $\beta = unit$ is assumed for (5.12b).

5.7 Analytical Considerations

In chapter 3 and chapter 4 [Frantziskonis, Tang and Desai 1991; Frantziskonis and Desai 1991] a mechanics based theory and verification for surface degradation in brittle material systems was introduced. The basic idea behind the theory is that close to free surfaces degradation progression is different from the one occurring far from the surface. It is shown that surface degradation consideration can capture important properties of brittle materials such as scale (size) and shape effects, surface damage growth and subsequent bursting instabilities. Although the theory does not consider any type of statistical material inhomogeneity distribution, it describes the surface degradation process in an average sense. Damage distribution at the edge of a body where surface degradation is important is considered to be different from the damage distribution far from the edges (in the body). A so-called surface degradation zone is defined in (3.34). Consider α is independent of l and its value was estimated from a series of uniaxial compression tests reported in [Desai, Kundu and Wang 1990] for the same material described herein on different size cylindrical specimens. The value of $\alpha = 0.21$ was estimated (in section 4 at chapter 3). For the specimens tested, (3.34) reduces to

$$\rho = \alpha(H - l) \tag{5.14}$$

where H is the specimen height. From the test results reported herein, distance ρ can be estimated from the dissipated energy distribution within the samples tested. From the test results it seems that the concentration of G close to the free surfaces is distinguishable and can be approximated to about one inch, Figures 5.18, 5.19, and 5.22. Then from (5.14) $l = 0.24$ inches. In Frantziskonis and Vardoulakis [1991], material micro-structure is examined with respect to surface effects. Surface instability analysis shows nonuniform deformation for a layer of specified distance from the surface. It was identified that a significant percentage of the uniform deformation is obtained at a depth of $5l$. Then if we consider that the nonuniform deformation, in an average nonstatistical sense, is about one inch, the internal length l is estimated to be 0.2 inches [Frantziskonis, Desai, Tang and Daniewicz 1991].

From the average stress-strain response of the tested specimens, the dissipated energy in the whole sample can be estimated by subtraction of the elastic strain energy from the total one. In Figure 5.26, this dissipated energy is plotted with respect to the ratio P/P_{peak}, for tests M2, M3, and M4s. Note that the dimensions of these samples are the same. The curves in Figure 5.26a are similar in shape to the ones observed for concrete in [Spooner and Dougill 1975]. The ultrasonic dissipated energy G for the whole sample can be calculated from the local measurements on it. This results in the curves of Figure 5.26b for samples M2, M3 and M4s. If we compare Figures 5.26a and 5.26b we conclude the following. A significant percentage of the average ultrasonic attenuation occurs at low stress levels. This implies that relatively low energy is required to produce damage occurring at the prepeak load levels. The randomness of this damage distribution occurring at low levels could serve as an explanation of the fact that brittle materials show a wide scattering with respect to the peak load for specimens of the same size and shape. Also Figures 5.26a,b show that parameter a in (5.10) is not constant. Its value as can be determined from the curves in these figures shows a high value for low load levels and its value decreases continuously to a minimum close to peak load. The exact variation of a and its possible dependence can be examined through the following considerations.

Because β (5.13) is a constant for a specific ultrasonic system, we can assume $\beta = 100$ (arbitrarily). It is noted another value of β does not change the analysis procedure. Then, G/100 is regard as the ultrasonically dissipated energy. Considering Test-M2, Test-M3, and Test-M4s, we obtain the distribution of the values of a for different load levels as shown in Figure 5.27. Assume a is power function of load level $c = P/P_{peak}$, That is,

$$a = B_1 c^{B_2} \tag{5.15}$$

where B_1 and B_2 are constants. The two constants B_1 and B_2 are identified to be 1.7162 and -1.6 through best-fit analysis against Test-M2, Test-M3, and Test-M4s. The best-fit curve is shown in Figure 5.27.

The power function of (5.15) is used to process back-prediction of a for Test-S1 and Test-S2. The predictions are compared with the values obtained directly from experiments as shown in Figure 5.28 and Figure 5.29. It is seen that the power function (5.15) works well. But the experimental vulues are over-predicted. This may be due to the shape effects and different overlapping areas for ultrasonic measurements.

It is interesting to evaluate the change rate of a with respect to the load level $c = P/P_{peak}$. a changes very fast at low load levels and claim very small change at high load levels (say over 80% of the peak load). High change rate of a corresponds to faster microcrack development and slower plastic flow, relatively. However, low change rate of a corresponds to slower microcrack development and faster plastic flow, relatively. It is widely accepted that for brittle materials (such as rock and concrete) under uniaxial compression microcrack development is predominant at low load levels while shear band processes at load levels higher than about 85% of the peak stress [Hallbauer, Wagner and Cook 1973]. The discussions presented here support the theoretical considerations proposed in chapter 3.

In chapter 3, the onset of degradation instability corresponds mathematically to the change of the second derivative of energy with respect to the damaged volume. This has been implemented and examined against experimental observations [chapter 4, Frantziskonis, Tang and Desai 1991]. Here, we process the energy

analysis based on experimental measurements. From the average stress-strain response of the tested specimens, the elastic strain energy stored in the sample at each load level can be calculated. The external work can be calculated from the load and displacement readings. Then, the potential energy can be obtained at each load level. Figure 5.30 and Figure 5.31 show the chages of energy with load level. In Figure 5.30, the energy is given as the potential (Π) added by mechanically dissipated energy (D_m). In Figure 5.31, the energy is given as the potential (Π) added by ultrasonically dissipated energy (D_u). From these two curves, it is clear that the second derivative of the curve changes with respect to load level. Because the damaged volume or its connection with load level is not available by the time being, the instability point can not be identified, and the comparison between the experimental results and the numerical and analytical predictions presented in chapter 4 [Frantziskonis, Tang and Desai 1991] can not be achieved. Further, an appropriate evaluation of the changes of the second derivative requires smaller load steps. To identify the instability point experimentally and to compare it with numerical and analytical predictions and other experimental observations, and to identify the possible dependence of a on scale and shape effects, further experimental and theoretical investigation seems to be necessary.

5.8 Conclusion

The experimental program presented in this chapter was designed mainly to provide an insight into the problem of initial (under no external load) and subsequent (under load) inhomogeneity and damage distribution of brittle materials. Both the ultrasonic attenuation pattern and the failure mode were different for the specimens tested. The results from both strain gage tests and ultrasonic scanning tests highlight the surface degradation (skin) effects, the randomness of damage evolution, and their consequence on the phenomenological behavior of brittle materials. Relatively low external energy is required to produce degradation occurring before the peak load. This implies that from low load levels the specimen may be susceptible to instability, and this may explain the large range of peak load values

observed for specimens of the same shape and size. The relationship between mechanically dissipated energy and ultrasonically dissipated energy is dependent on deformation and can be approximated by a power function of load level. Further verification of the energy based instability theory requires further theoretical and experimental investigation.

Table 5.1 Strain Gage Readings at $P/P_{peak} = 0.5$

	Gage-1	Gage-2	Gage-3	Gage-4
Test-2	0.041	0.045	0.055	0.017
Test-3	0.043	0.046	0.045	0.074
Test-4	0.041	0.033	0.041	0.071
Test-5	0.0575	0.041	0.033	0.164
Test-6	0.02	0.028	0.025	0.082
Test-7	0.05	0.0445	0.03	0.048
Test-8	0.028	0.034	0.0305	0.066

Table 5.2 Strain Gage Readings at $P/P_{peak} = 0.85$

	Gage-1	Gage-2	Gage-3	Gage-4
Test-2	0.09	0.093	0.111	0.043
Test-3	0.05	0.052	0.052	0.081
Test-4	0.075	0.0675	0.071	0.0955
Test-5	0.1085	0.07	0.064	0.195
Test-6	0.098	0.08	0.0625	0.18
Test-7	0.099	0.0865	0.0615	0.075
Test-8	0.0875	0.083	0.067	0.0775

Table 5.3 Strain Gage Readings at $P/P_{peak} = 1.0$

	Gage-1	Gage-2	Gage-3	Gage-4
Test-2	0.1245	0.117	0.145	0.061
Test-3	0.116	0.091	0.099	0.115
Test-4	0.0985	0.093	0.09	0.103
Test-5	0.141	0.087	0.085	0.216
Test-6	0.13	0.1	0.075	0.2
Test-7	0.127	0.109	0.078	0.079
Test-8	0.108	0.098	0.077	0.0735

Table 5.4 Relative Numbers for Strain Gage Readings at $P/P_{peak} = 0.5$

	Gage-1	Gage-2	Gage-3	Gage-4
Test-2	241	265	324	100
Test-3	100	107	105	172
Test-4	124	100	121	215
Test-5	174	124	100	497
Test-6	100	140	125	410
Test-7	167	148	100	160
Test-8	100	121	109	236
Sum.	1006	1005	984	1790

Table 5.5 Relative Numbers for Strain Gage Readings at $P/P_{peak} = 0.85$

	Gage-1	Gage-2	Gage-3	Gage-4
Test-2	209	216	258	100
Test-3	100	104	104	162
Test-4	111	100	105	141
Test-5	174	109	100	305
Test-6	157	128	100	288
Test-7	161	141	100	122
Test-8	131	124	100	116
Sum.	1039	922	867	1234

Table 5.6 Relative Numbers for Strain Gage Readings at $P/P_{peak} = 1.0$

	Gage-1	Gage-2	Gage-3	Gage-4
Test-2	204	192	238	100
Test-3	127	100	109	126
Test-4	109	103	100	114
Test-5	166	102	100	254
Test-6	173	133	100	267
Test-7	163	140	100	101
Test-8	147	133	105	100
Sum.	1089	903	852	1062

Table 5.7 Statistical Distribution of Strain Gage Readings

	Gage-1	Gage-2	Gage-3	Gage-4
P/Ppeak=0.5	1006	1005	984	1790
P/Ppeak=0.85	1039	922	867	1234
P/Ppeqk=1.0	1089	903	852	1062

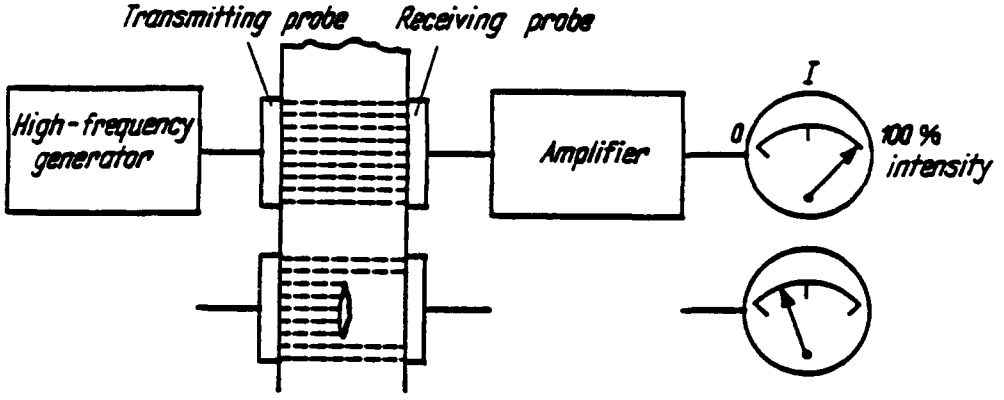

Figure 5.1 Schematic of Intensity Method with Sound Transmission

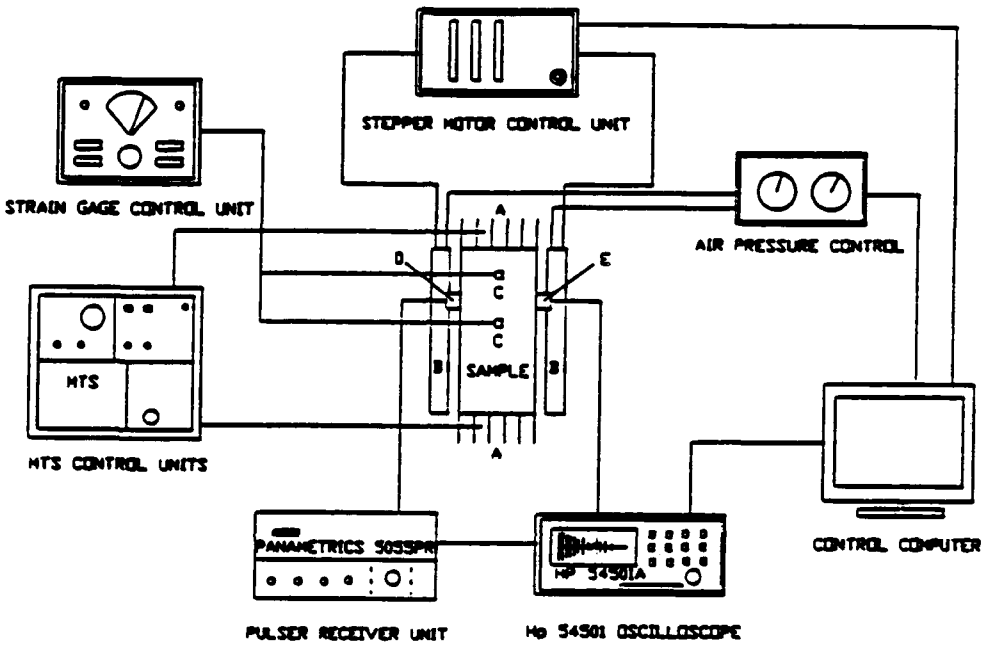

Figure 5.2 Schematic of the Test System for Ultrasonic Measurements while Sample Are Subjected to Mechanical Load; A: External Load Applied through MTS Frame, B: Device for Movement of Transducers, Shown in Figure 5.3, C: Strain Gages, D: Transmitting Transducers, E: Receiving Transducer (after Jagannath, Desai and Kundu 1991 and Frantziskonis, Desai, Tang and Daniewicz 1991)

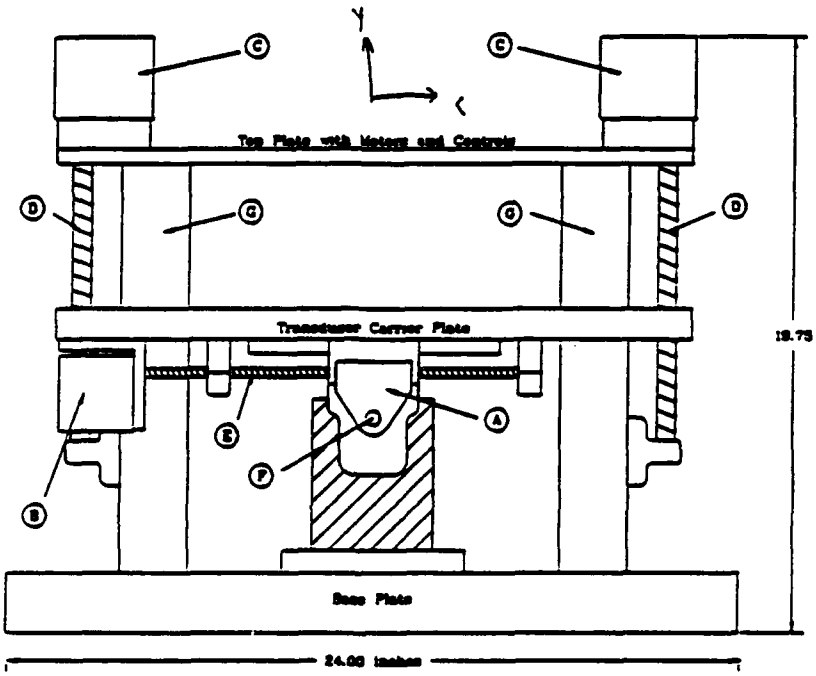

Figure 5.3 System Designed for the Movement of the Transmitting and Receiving Transducer; A: Transducer Housing, B: Stepper Motors for X-Movement (Horizontal), C: Stepper Motors for Y-Movement (Vertical), D: Vertical Motion Screws, E: Horizontal Motion Screws, F: Air Pressure Connections, G: MTS Frame

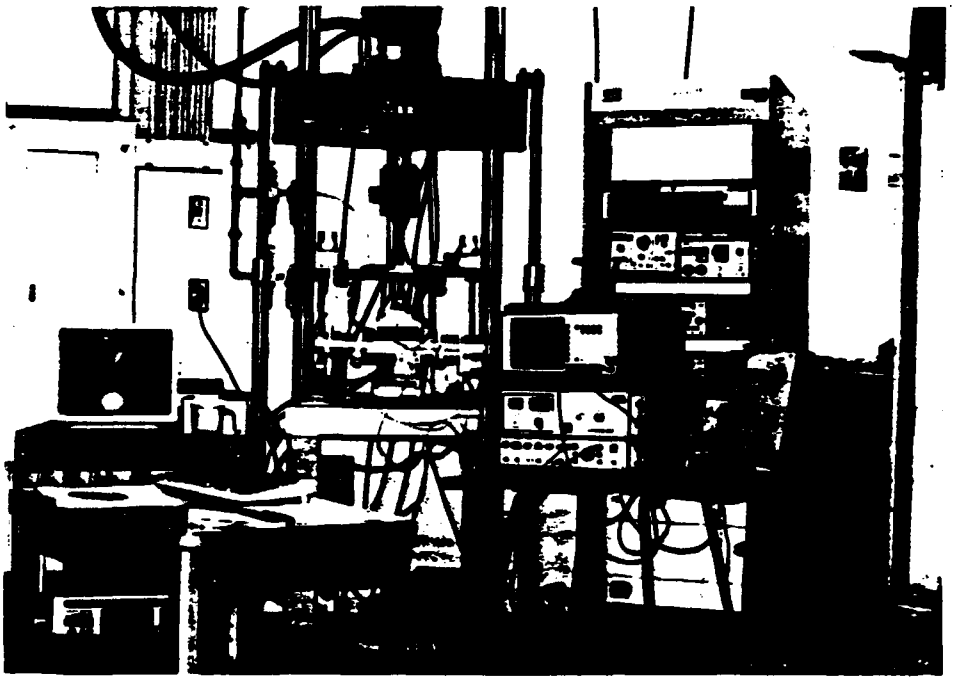

Figure 5.4 Photograph of the Setting-up of Test

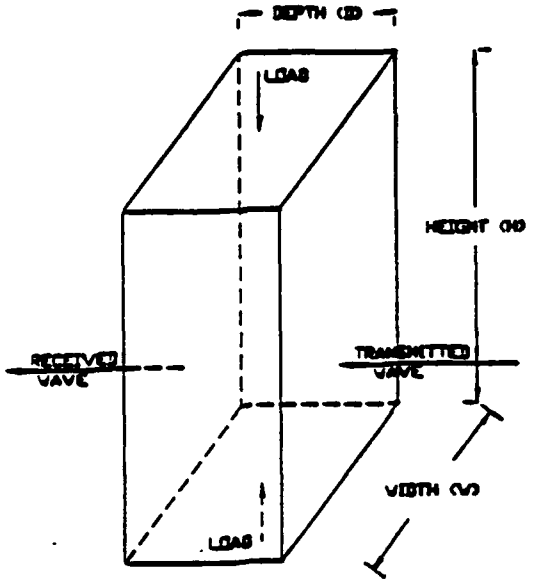

(a)

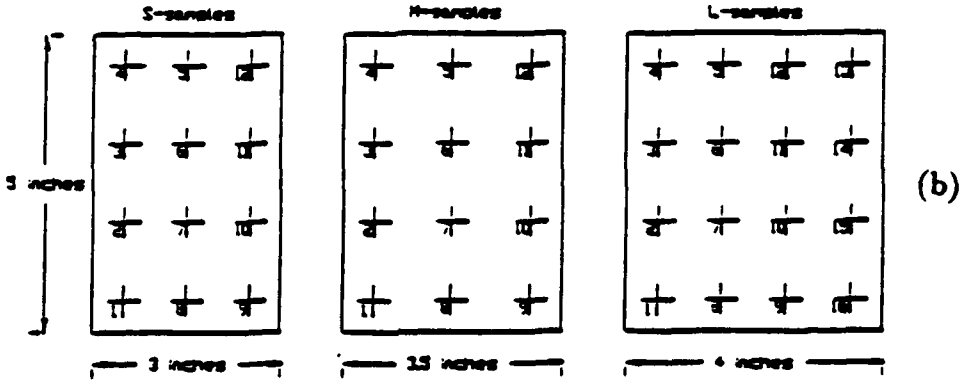

(b)

Figure 5.5 (a) Prismatic Sample $W \times H \times D$ Showing Direction of External Load and of Ultrasonic Wave, (b) Location of Center of Transducers where Measurements Were Taken for the Three Series of Specimens

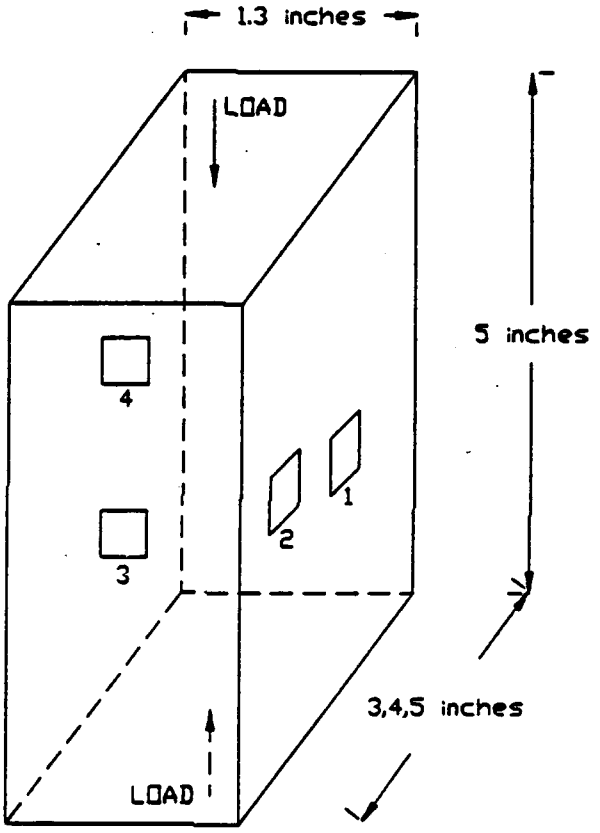

Figure 5.6 Prismatic Sample and Strain Gage Locations for Strain Gage Tests

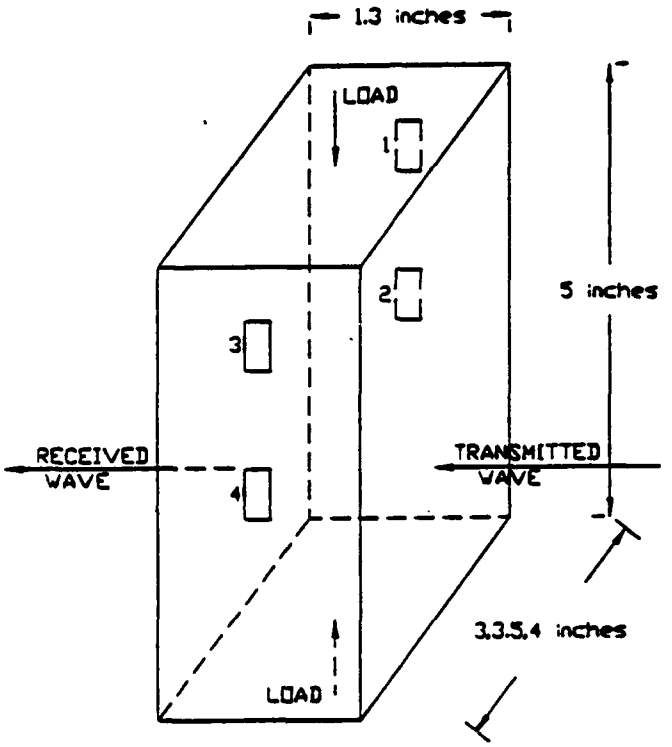

Figure 5.7 Position of Four Strain Gages for Combined Strain and Ultrasonic Scanning Tests

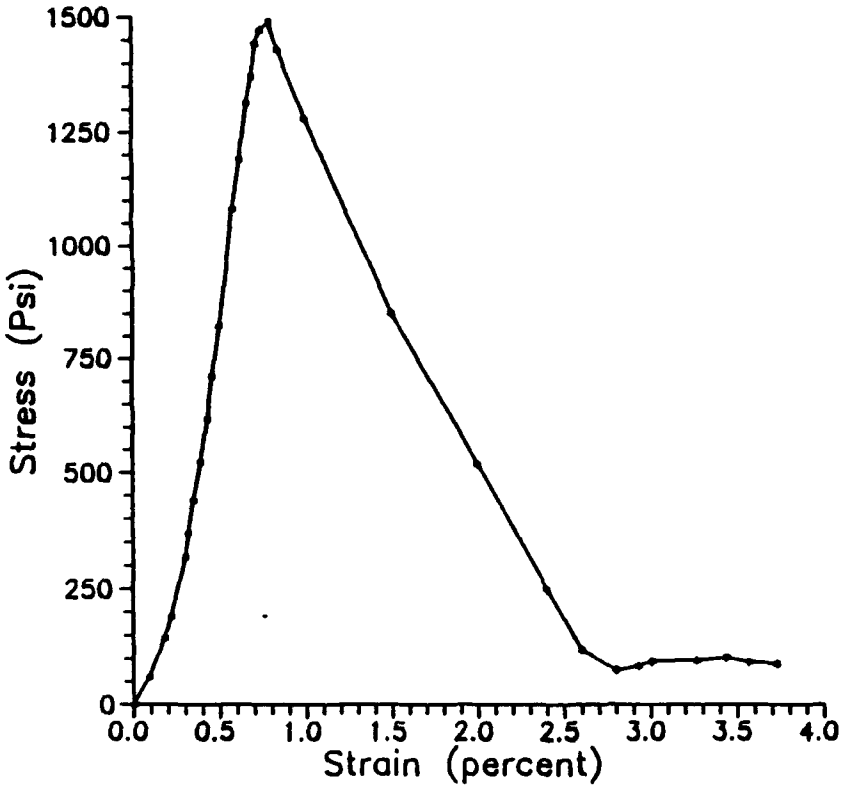

Figure 5.8 Average Measured Stress-Strain Curve

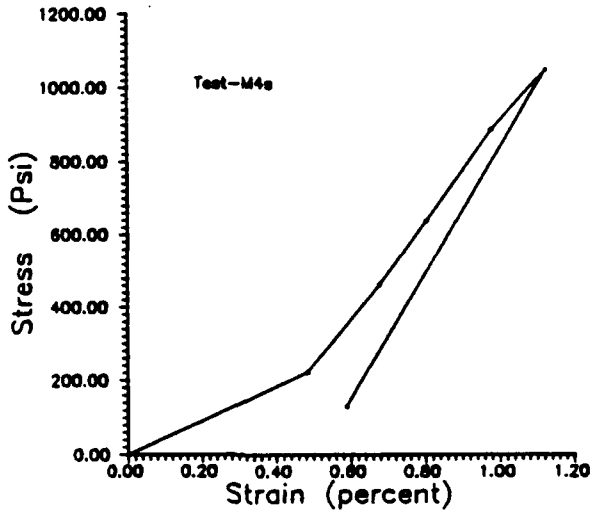

(a)

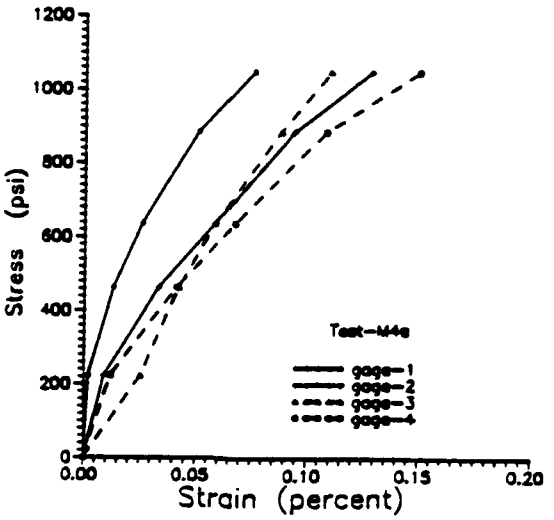

(b)

Figure 5.9 Data from Test-M4s, (a) Average Stress-Strain Response; (b) Strain Gage Readings

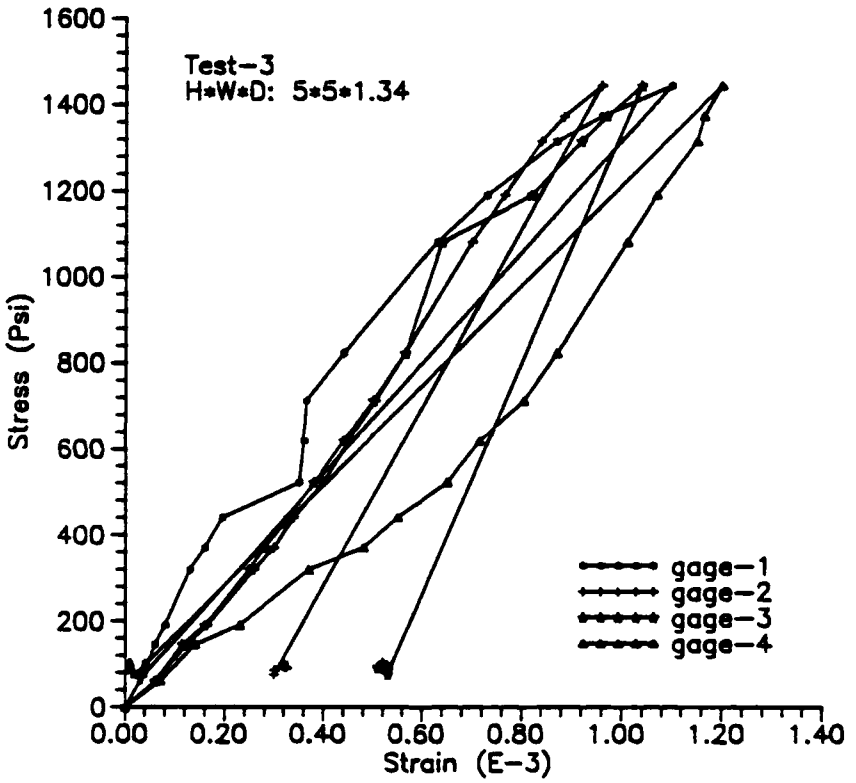

Figure 5.10 Strain Gage Readings for Sample PL1

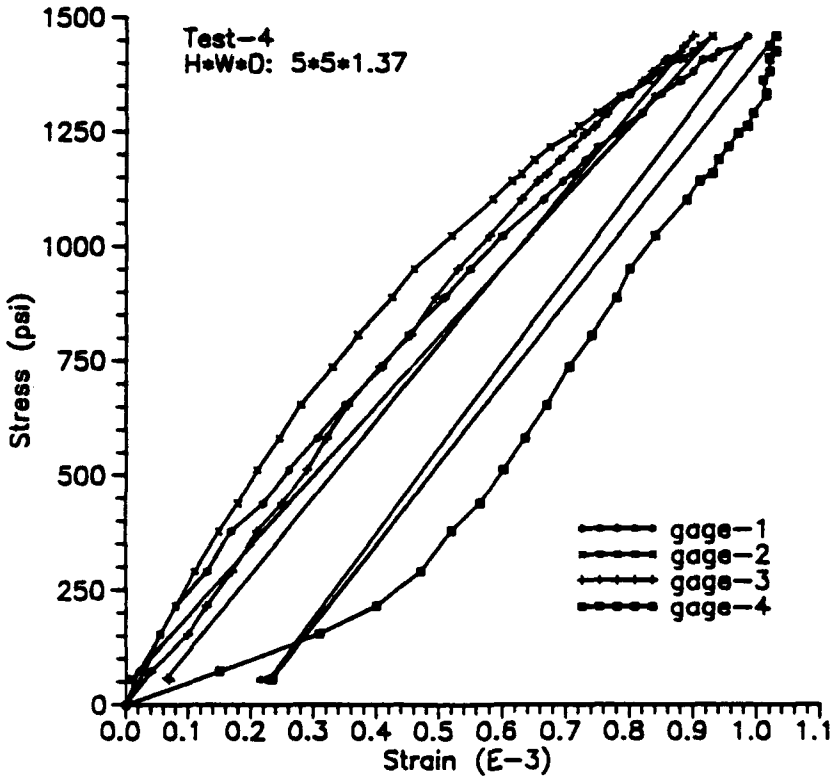

Figure 5.11 Strain Gage Readings for Sample PL2

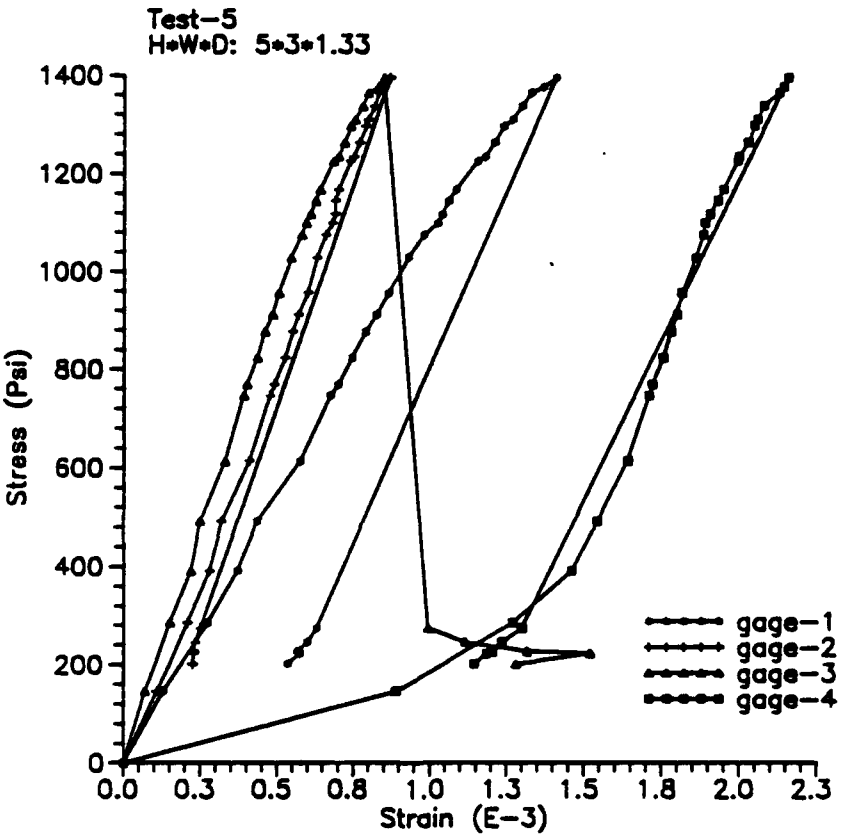

Figure 5.12 Strain Gage Readings for Sample PS1

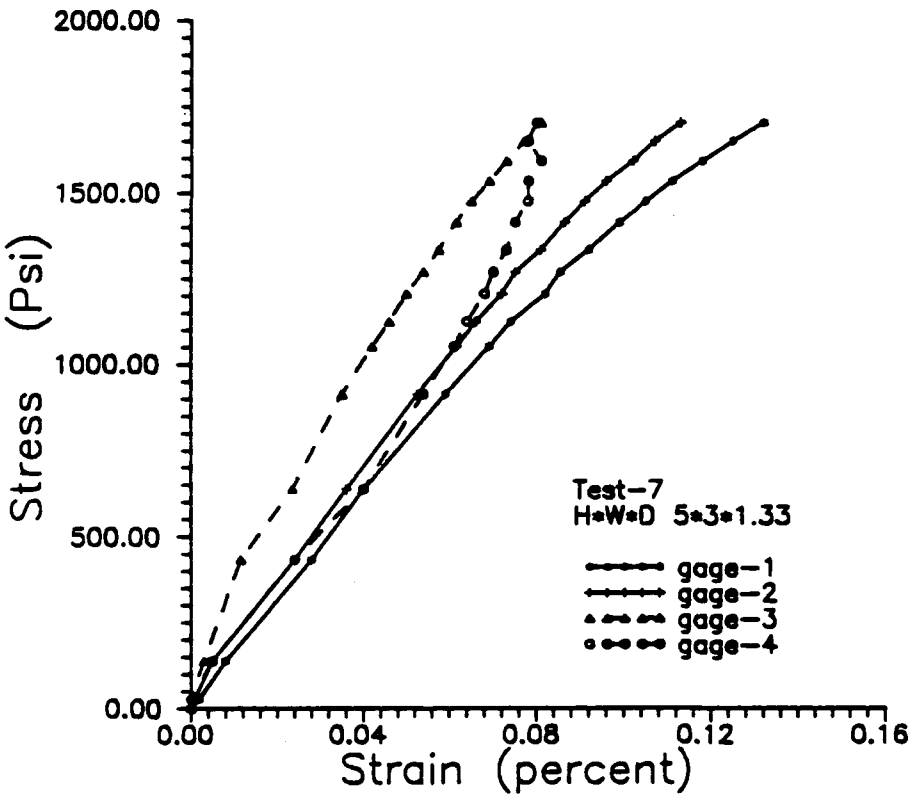

Figure 5.13 Strain Gage Readings for Sample PS2

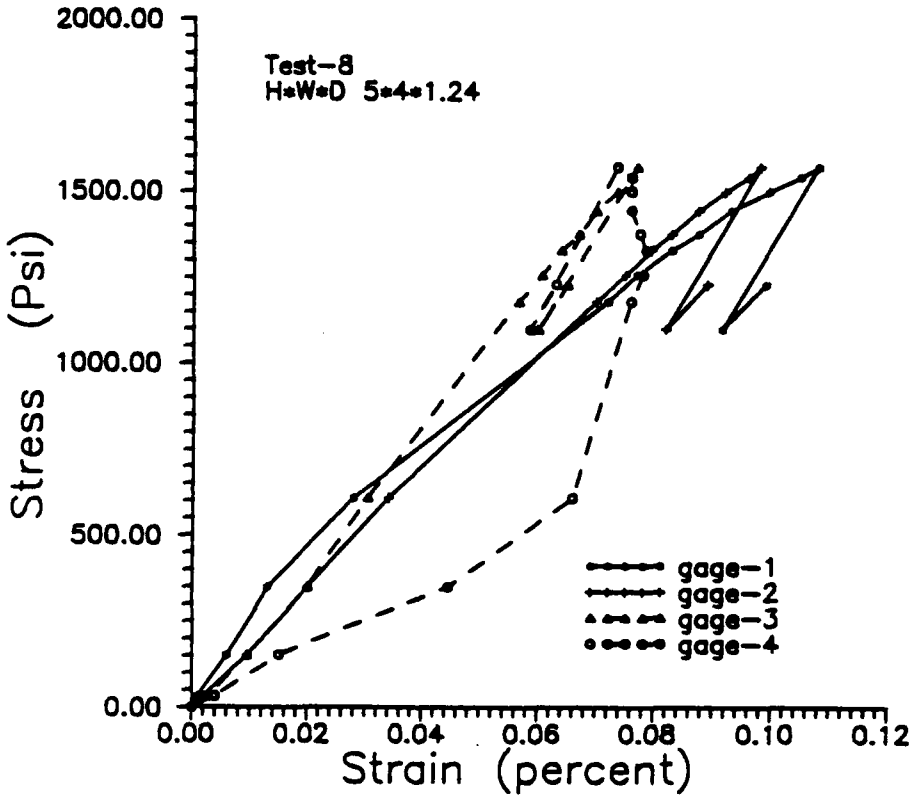

Figure 5.14 Strain Gage Readings for Sample PM1

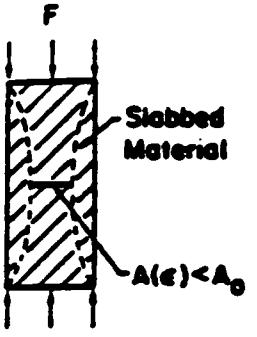

Figure 5.15 Schematic of Surface Slabbing (Spalling)

(a)

(b)

(c)

Figure 5.16I Picture of Three Samples after Failure at Peak; (a) Sample S3, (b) Sample M2, (c) Sample L1

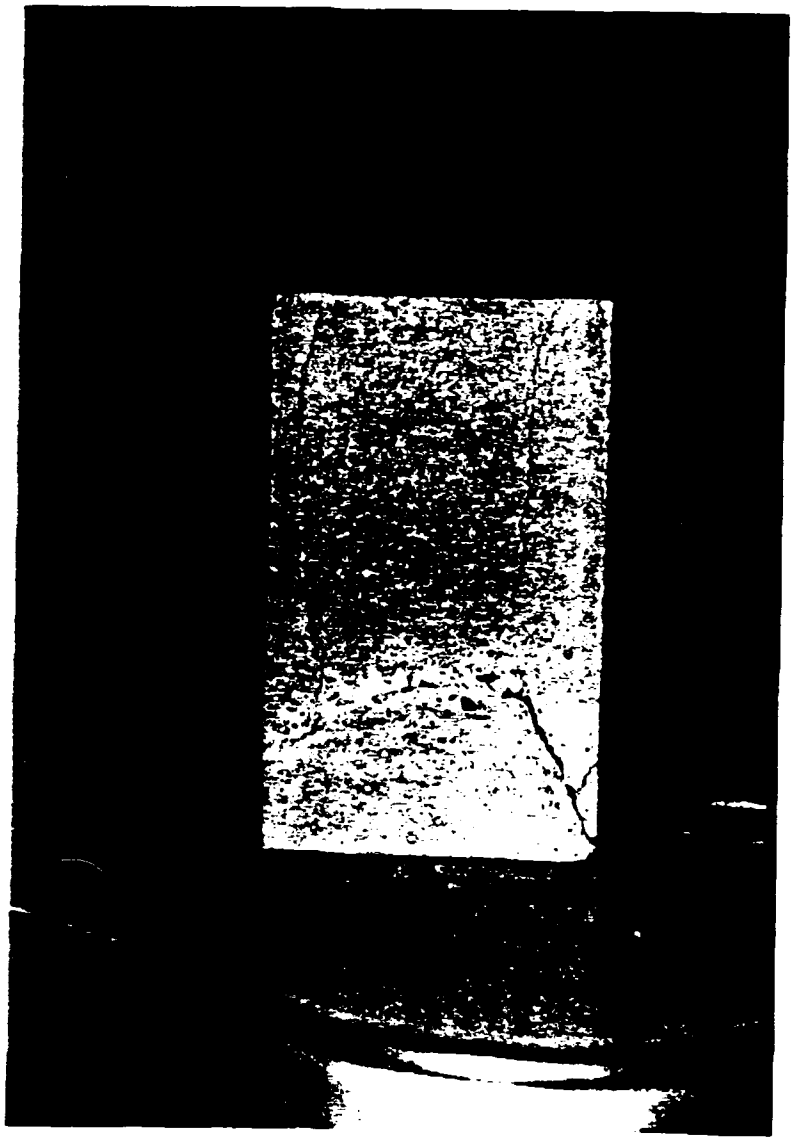

Figure 5.16II Showing of Surface Spalling From Sample PM2

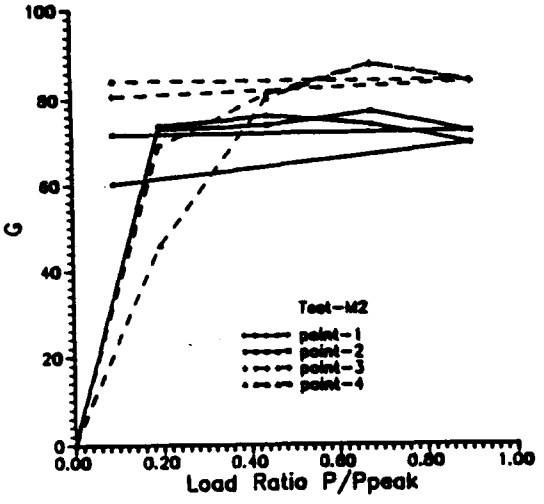

(a)

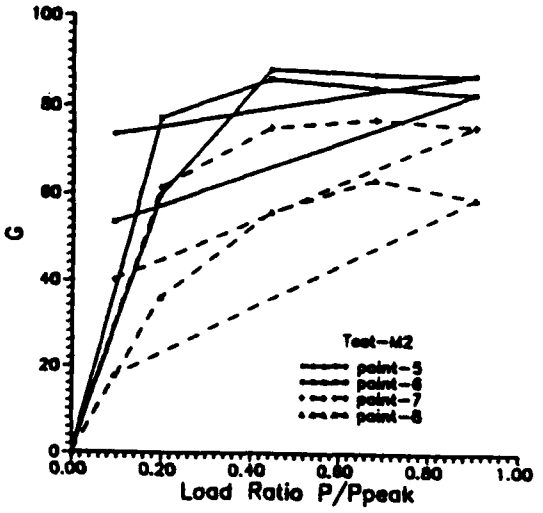

(b)

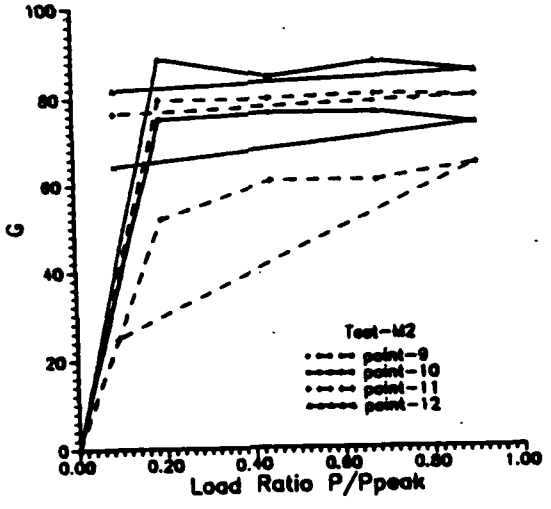

(c)

Figure 5.17 The Change of G with Load Status for Test-M2, (a) for location 1,2,3,4; (b) for location 5,6,7,8; (c) for location 9,10,11,12

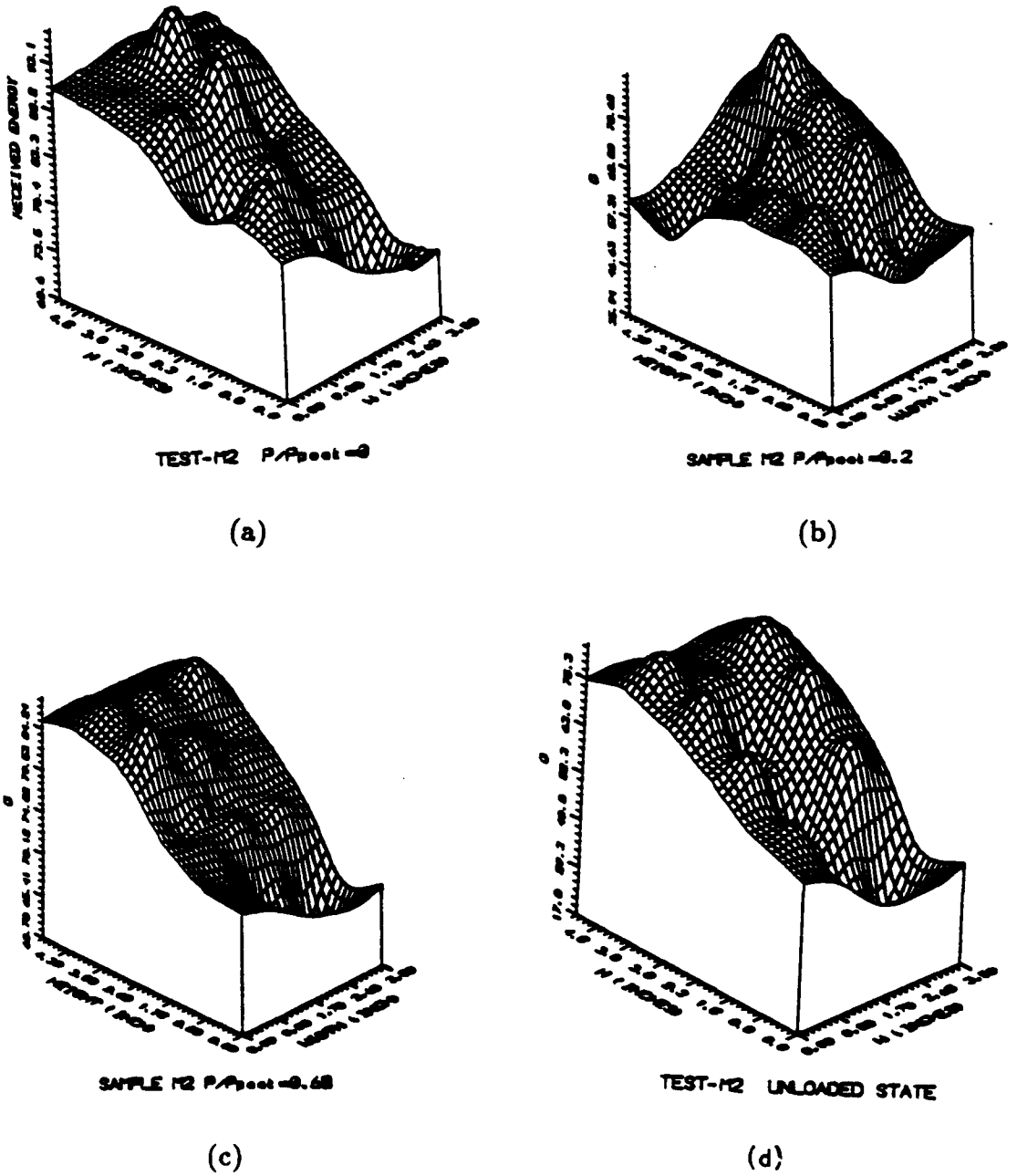

(a) (b)

(c) (d)

Figure 5.18 Spatial Distribution of Initially Received Energy and G for Test-M2

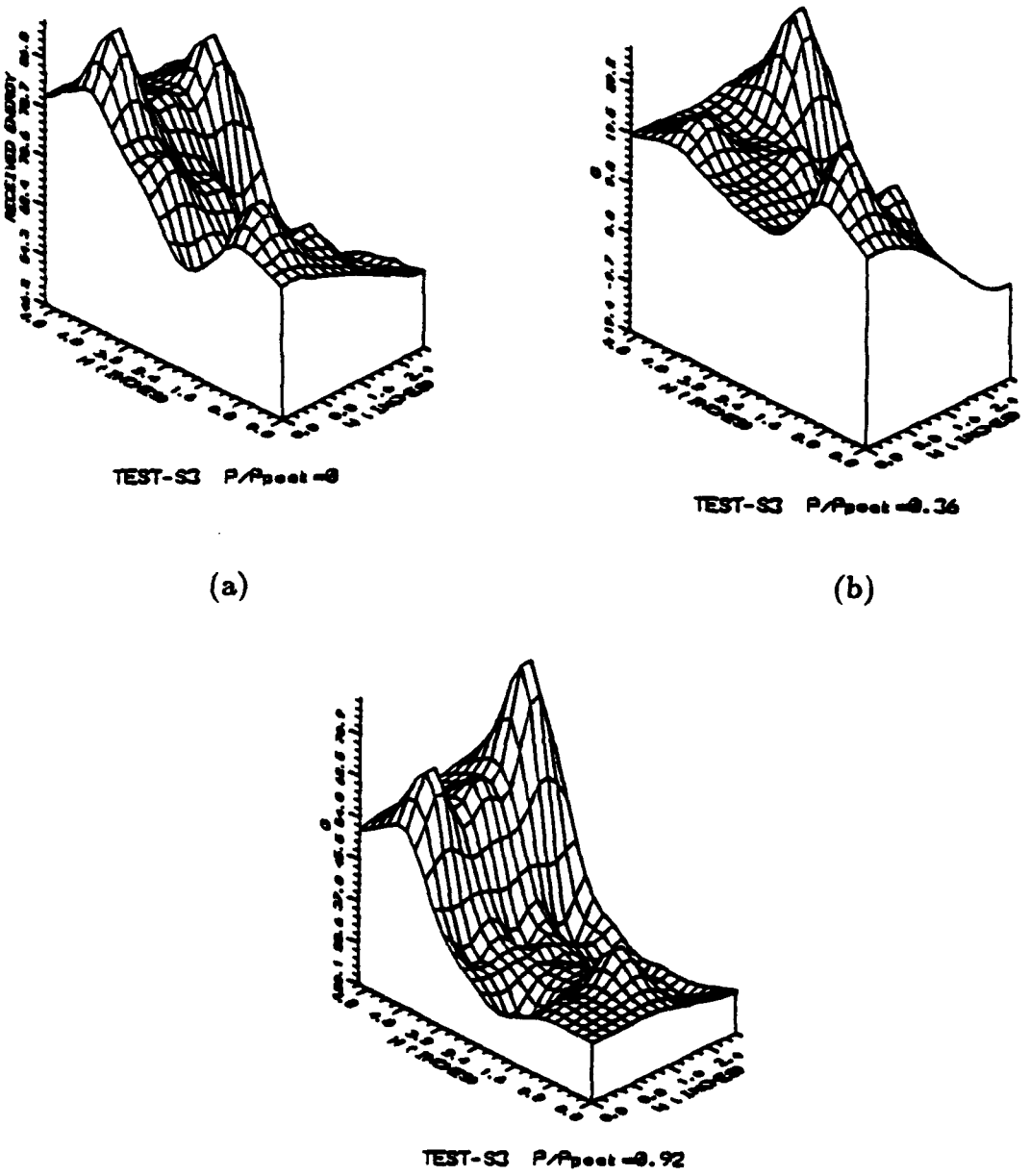

(a)

(b)

(c)

Figure 5.19 Spatial Distribution of Initially Received Energy and G for Test-S3

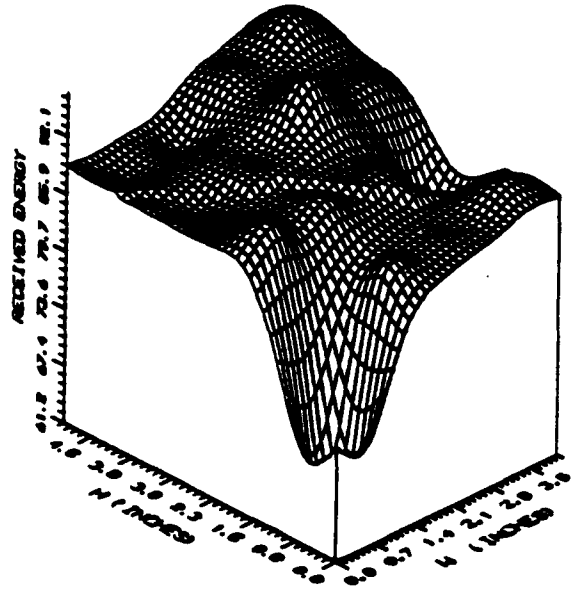

(a)

TEST-L1 P/Pbeat =0

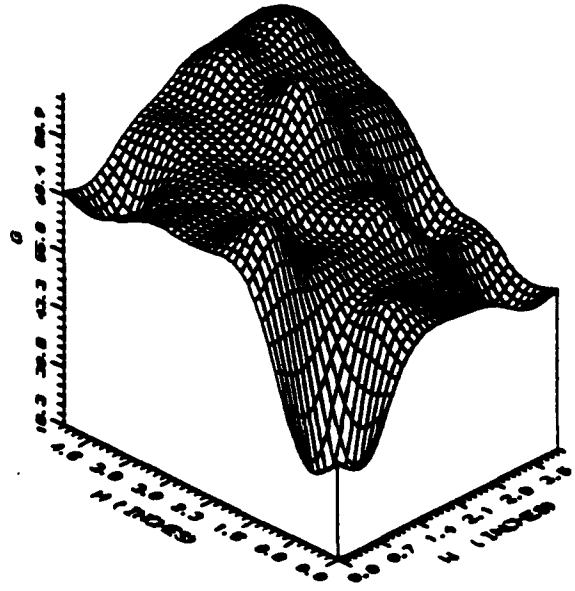

(b)

TEST-L1 P/Pbeat =0.93

Figure 5.20 Spatial Distribution of Initially Received Energy and G for Test-L1

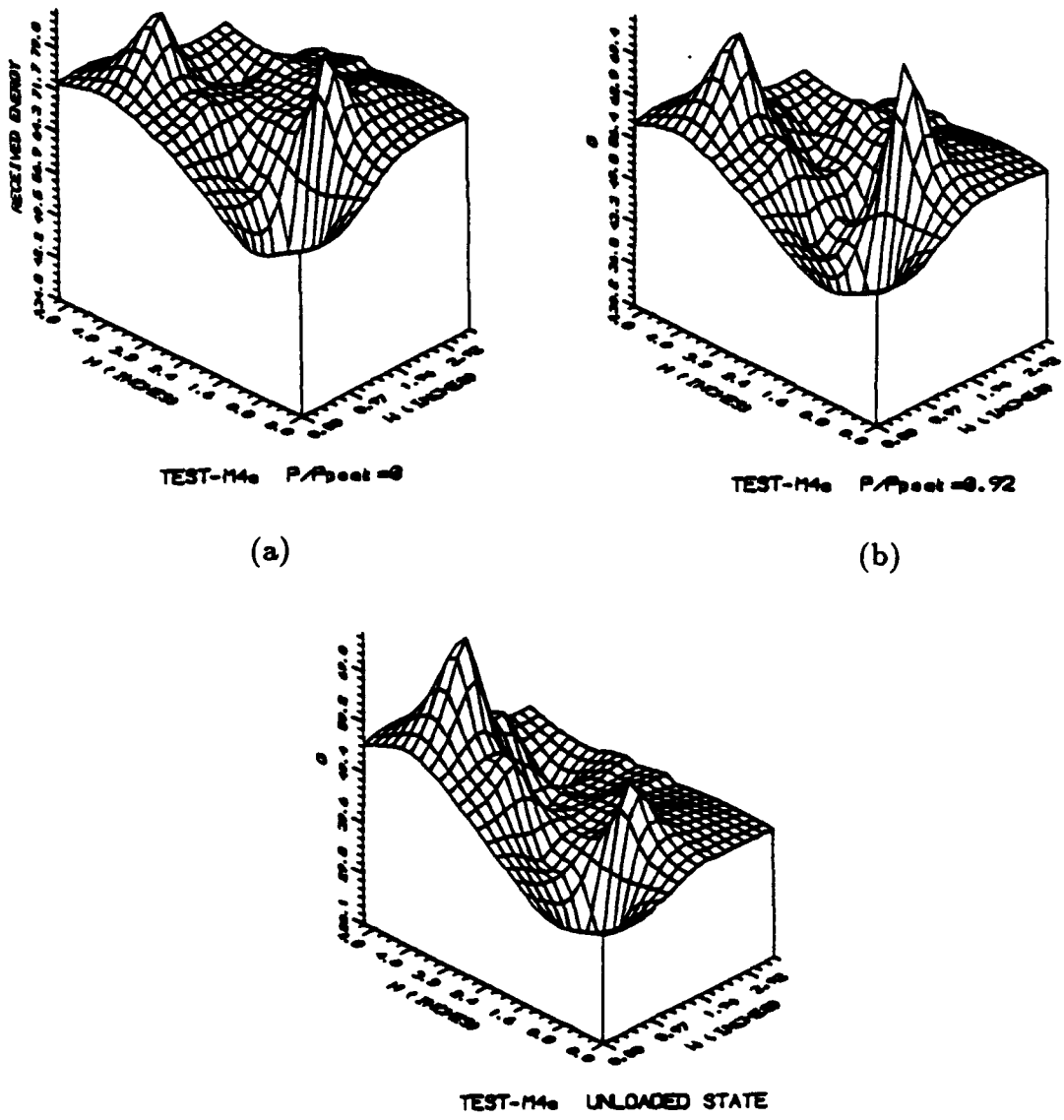

(a) (b)

(c)

Figure 5.21 Spatial Distribution of initially Received Energy and G for Loading and Unloading State (P/Ppeak=0.09) for Test-M4s

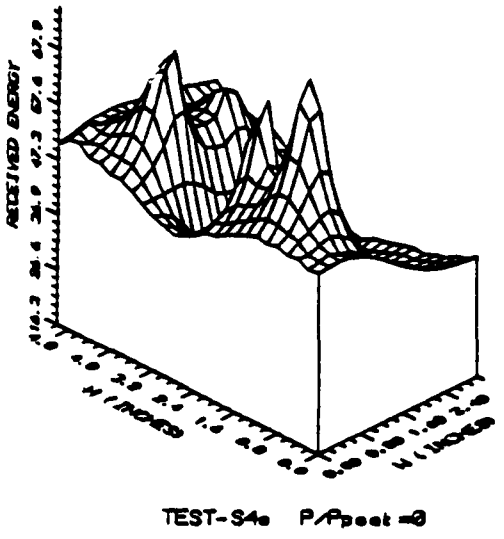

(a)

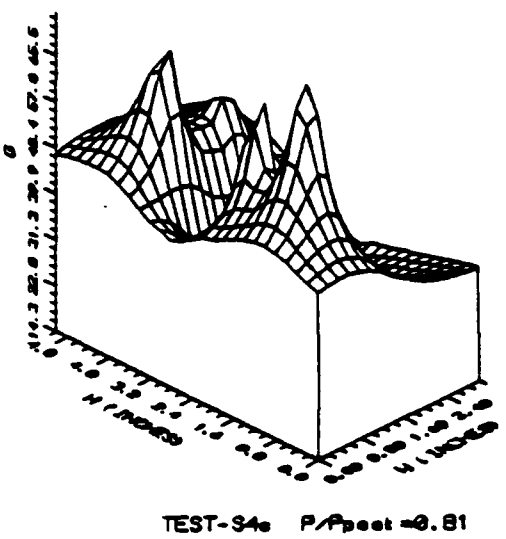

(b)

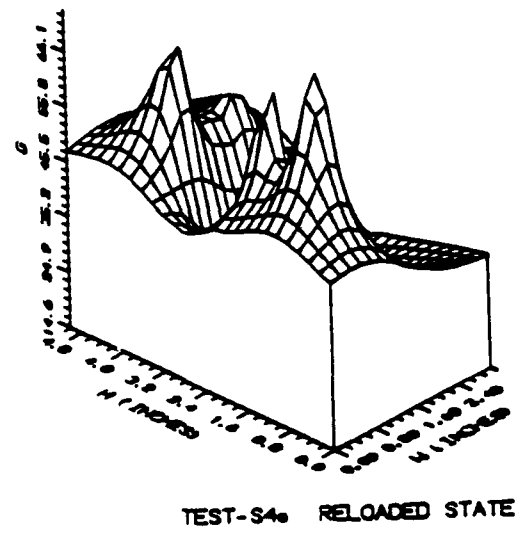

(d)

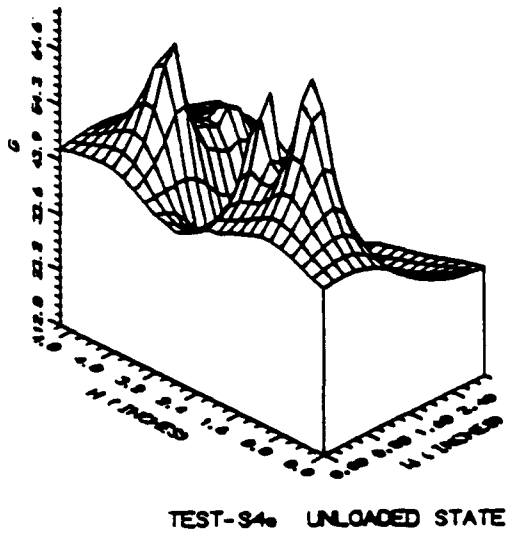

(c)

Figure 5.22 Spatial Distribution of Initially Received Energy and G for Loading, Unloading, and Reloading for Test-S4s

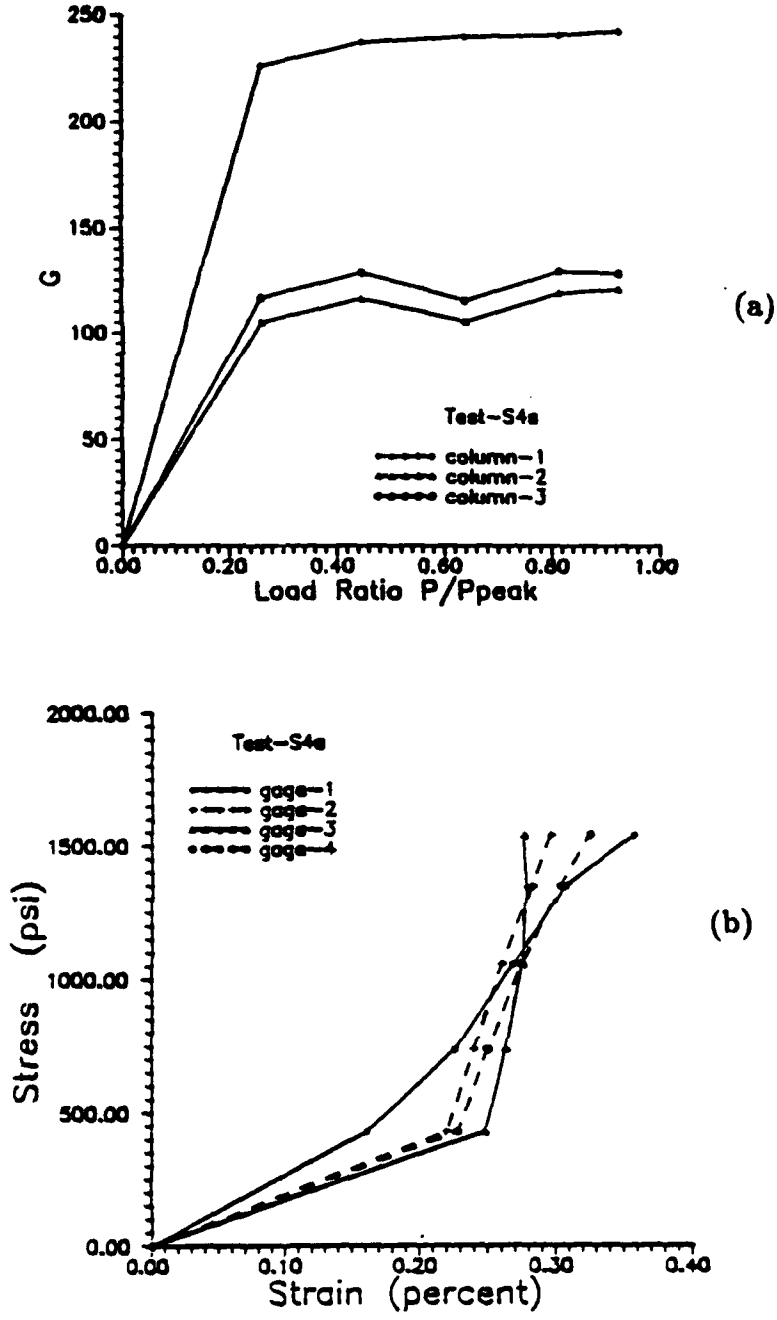

Figure 5.23 For Test-S4s, (a) Changes of G of Different Columns with Loading; (b) Strain Gage Readings

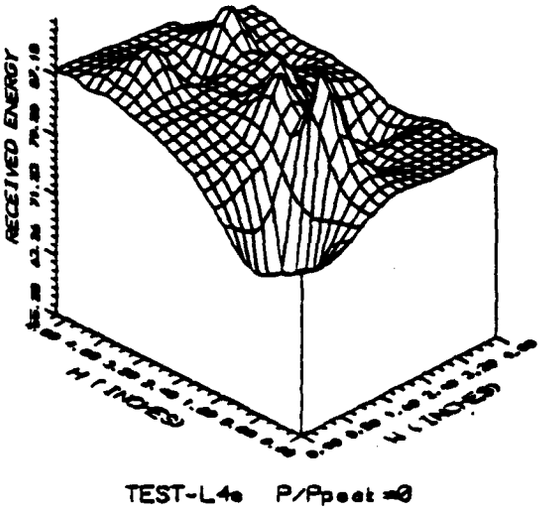

(a)

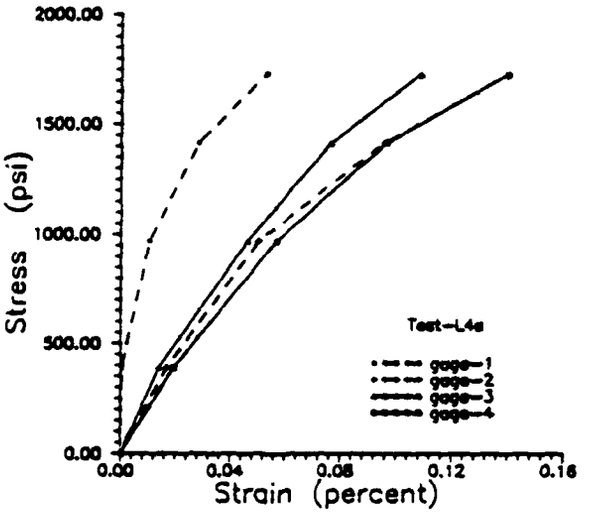

(b)

Figure 5.24 For Test-L4s, (a) Spatial Distribution of Initially Received Energy; (b) Strain Gage Readings

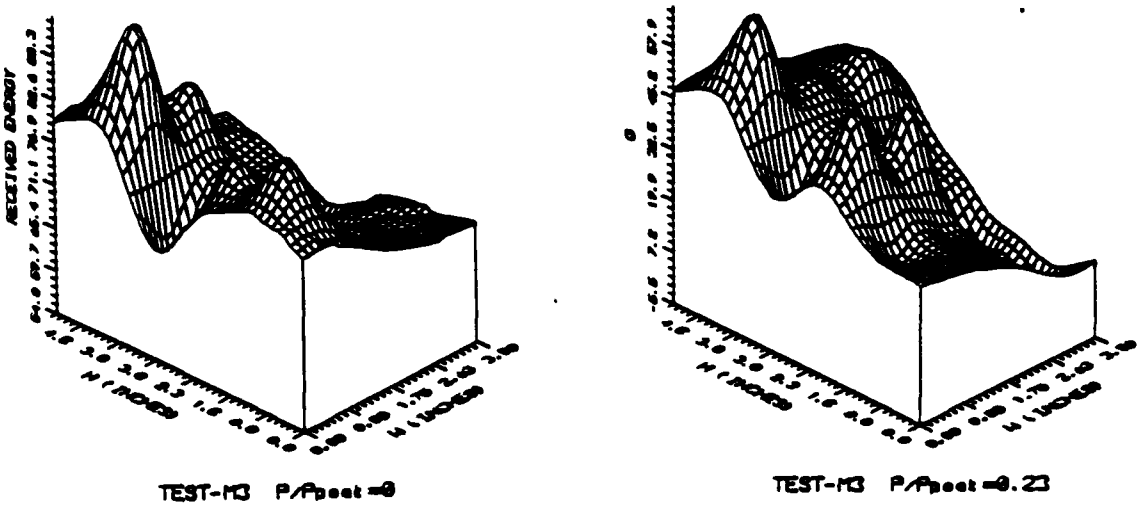

(a) (b)

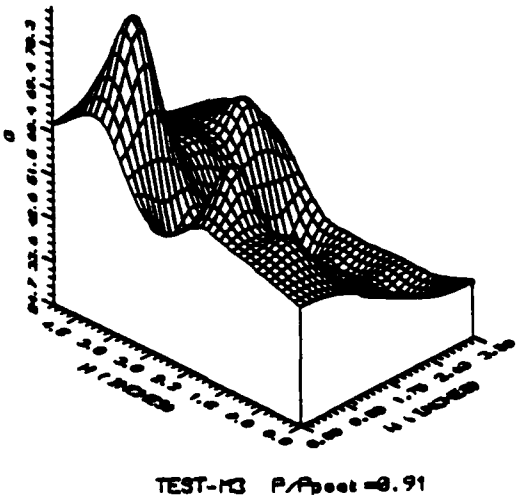

(c)

Figure 5.25 Spatial Distribution of initially Received Energy and G for Test-M3

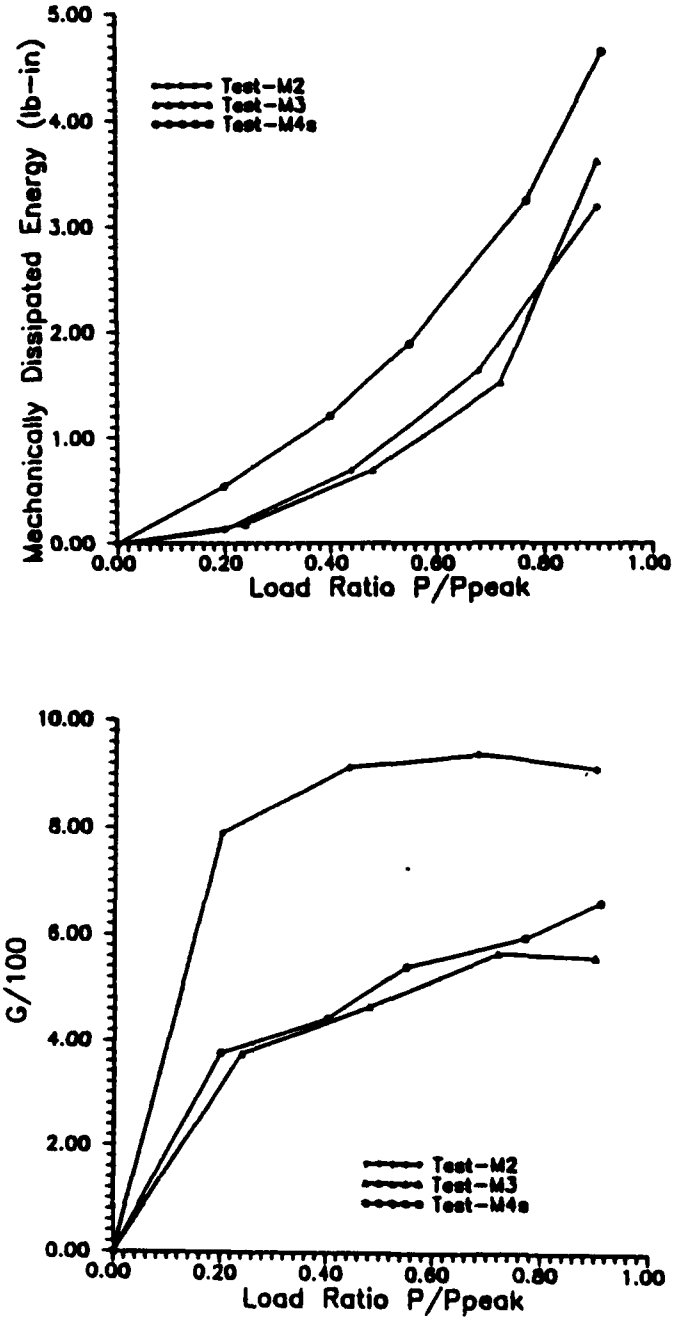

Figure 5.26 For Test-M2, M3, M4s, (a) Change of Mechanically Dissipated Energy with Loading; (b) Change of G with Loading

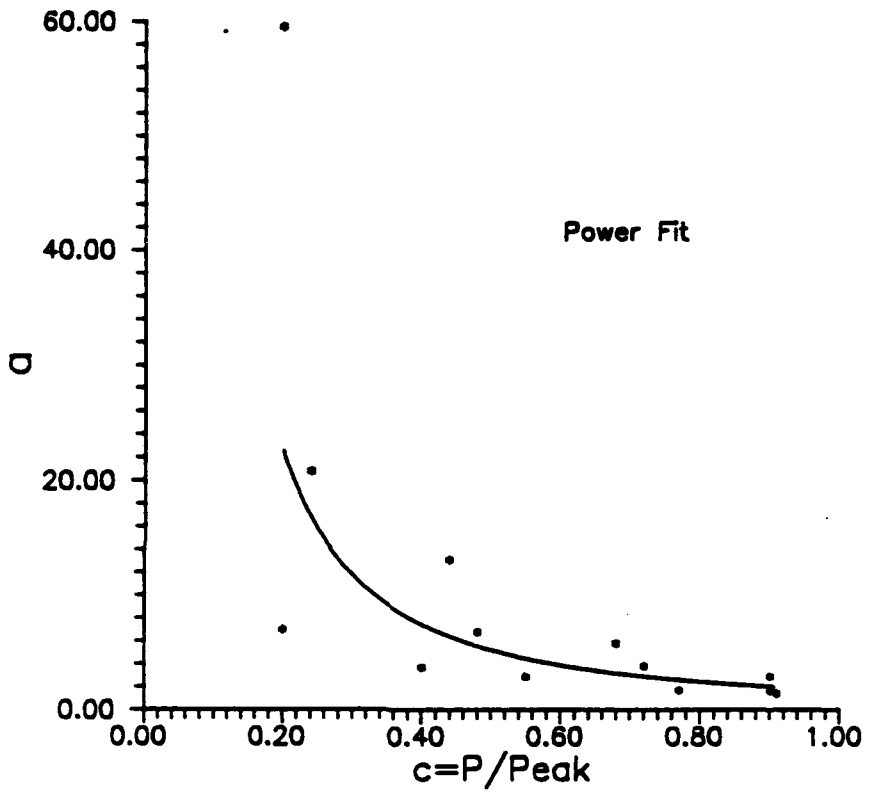

Figure 5.27 a v.s. load level $c = P/P_{peak}$ and power fit curve for Test-M2, M3, M4s

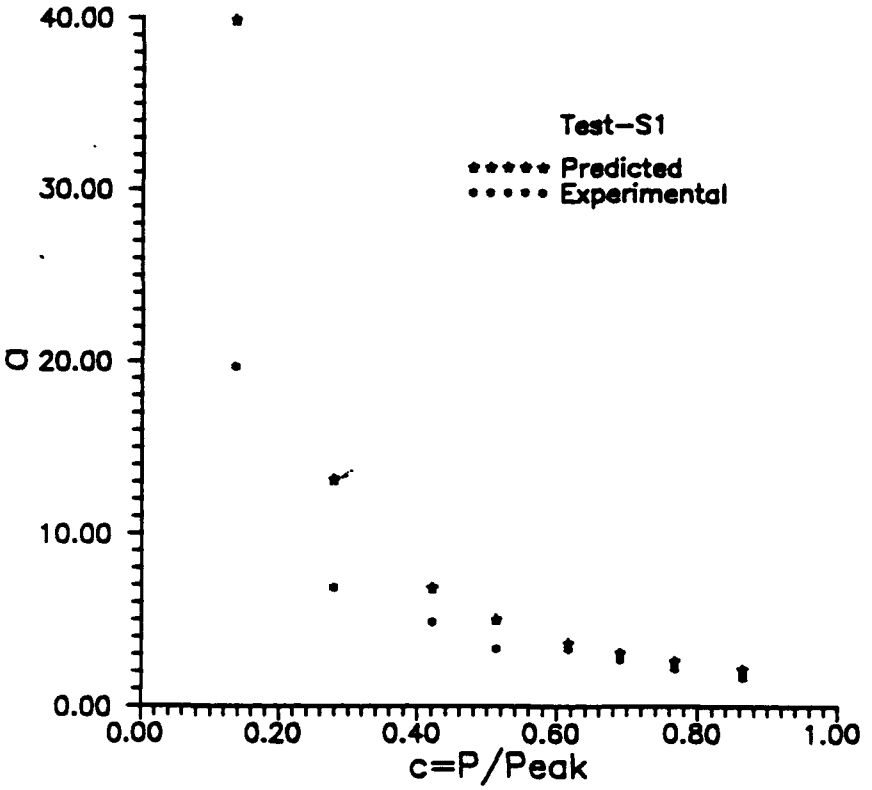

Figure 5.28 a v.s. load level $c = P/P_{peak}$ for Test-S1

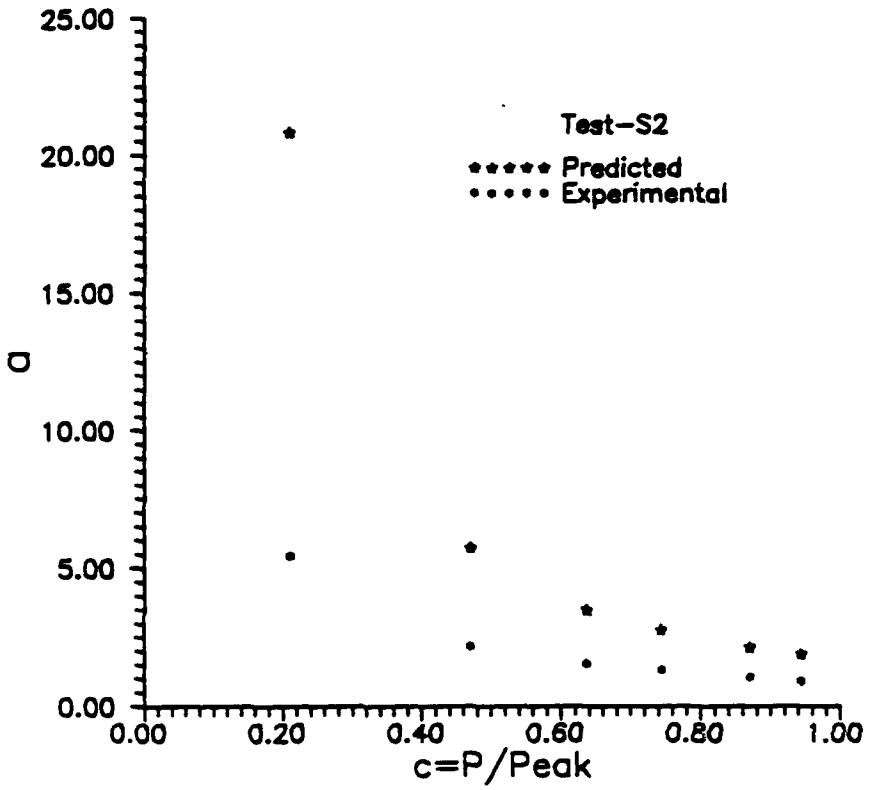

Figure 5.29 a v.s. load level $c = P/P_{peak}$ for Test-S2

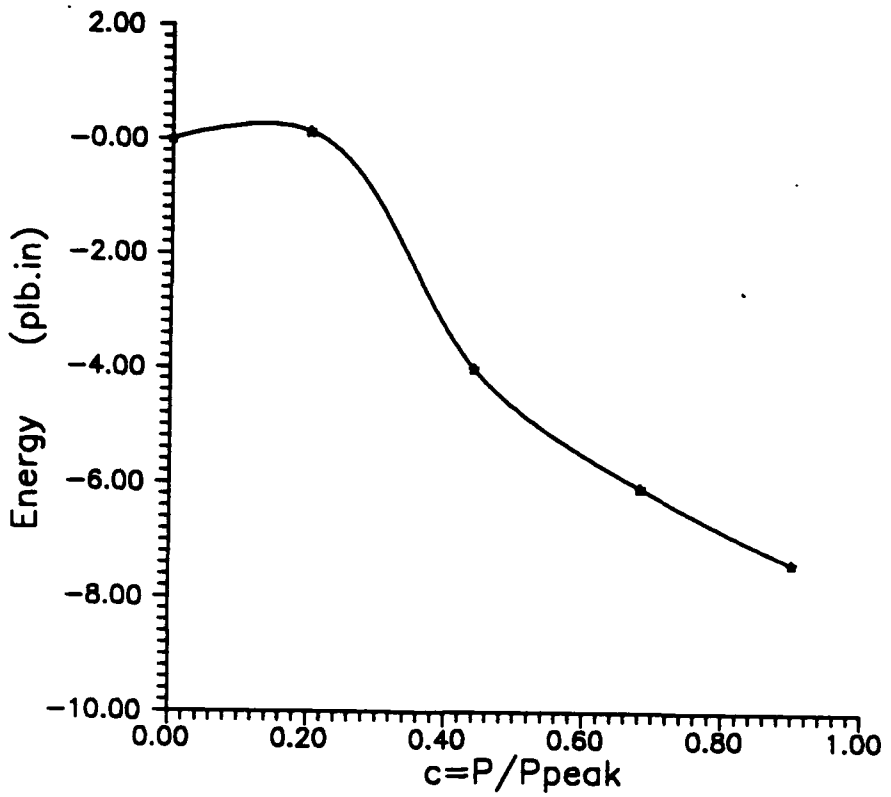

Figure 5.30 Energy ($\Pi + D_m$) v.s. load level $c = P/P_{peak}$ for Test-M2

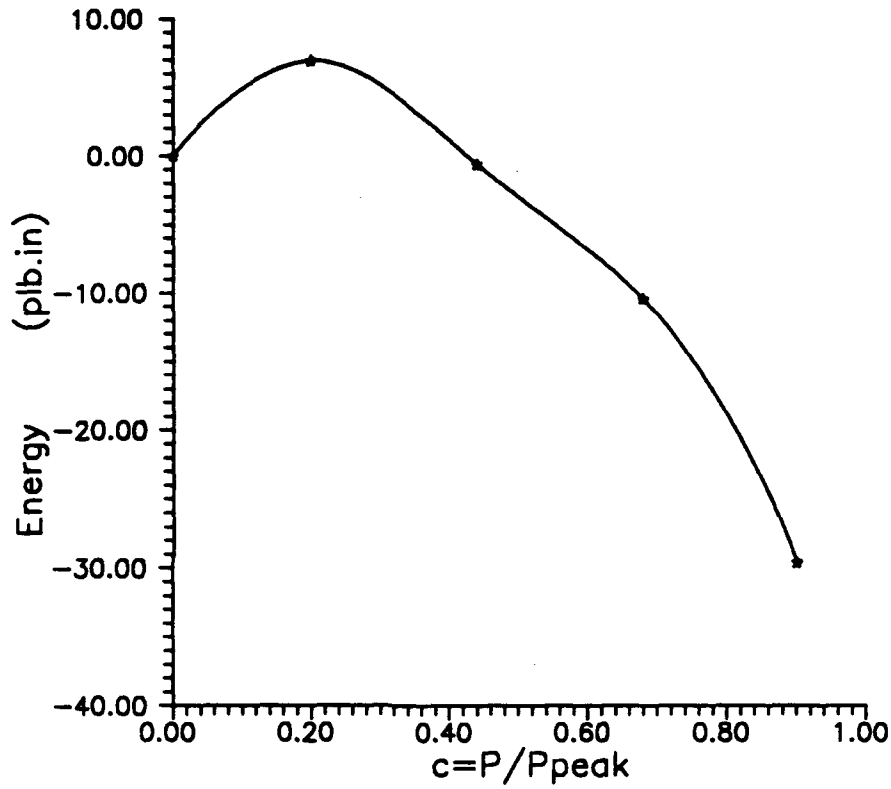

Figure 5.31 Energy ($\Pi + D_u$) v.s. load level $c = P/P_{peak}$ for Test-M2

CHAPTER 6

INITIAL HETEROGENEITY AND DEGRADATION

In this chapter, the concept of state of degradation is employed in order to consider the initial material (structure) inhomogeneity. Then, degradation and its patterning in simulated rock specimens subjected to external load are modeled numerically by implementing the theory for damage and surface degradation with incorporation of the initial state. The theoretical results are compared with experimental observations obtained through ultrasonic scanning tests [Tang et al 1991].

6.1 General

Structures composed of brittle materials, e.g. rock and concrete, experience damage due to microcracking and fracturing when loaded. The term degradation is often associated with damage evolution. Depending on the external load on a structure, the degradation process may become unstable. Physically, when the inflow of energy from the external loading system on a structure exceeds the energy absorbed in the process of degradation and plastic deformations, an instability can ensue, Salamon [1970], Petukhov and Linkov [1979], Zubelewicz and Mroz [1983], Frantziskonis, Tang and Desai [1991].

For decades, laboratory tests on brittle materials sought to achieve a homogeneous state of stress and deformation on samples subjected to, for example, uniaxial load. However, even under ideal testing conditions, the heterogeneous micro-structure of the material yields an inhomogeneous deformation field from the early straining stage, Fairhurst and Cook [1966], Hudson et al [1971], Read and Hegemier [1984], Yukutake [1989], Frantziskonis et al [1991], Chapter 5. The initial heterogeneity significantly influences the spatial variation of degradation in a brittle material structure subjected to mechanical load. This spatial variation may provide an explanation why the experimentally observed failure (or instability) modes are rather random, and why the peak strengths from same size and

shape samples of the same material are diversely distributed, Bazant et al [1990]. The onset of an instability depends on the accumulation of damage. The initial heterogeneity influences the spatial variation of damage or microcracking. Also, microcrack propagation is dependent on the geometric configuration, i.e., different relative locations of aggregates are expected to cause different microcrack propagation patterns even if the external loading conditions are identical.

The influence of initial material heterogeneity on microcrack propagation has been studied recently by Yamaguchi and Chen [1991], in which, the representative volume element of concrete is modeled as a two-phase composite, consisting of a mortar matrix and aggregate inclusions, and two distinct types of microcracks (mortar crack and bond crack) are considered. It is assumed that there are no initial flaws, but the material properties of the inclusions are different from those of the matrix. It is then found that the location of neighboring aggregates do not influence the propagation of bond cracks significantly. However, the relative locations of neighboring aggregates exert a considerable influence on the development of mortar cracks.

In chapter 5, an experimental study of degradation mechanisms and patterning in simulated rock has been performed. The results from both the strain gage tests and ultrasonic scanning tests highlight the surface effects and the influence of initial state on the local deformation and damage evolution. It was found that the ultrasonically dissipated energy from load application follows, in general, the initial non-homogeneity pattern. In this chapter, the initial heterogeneity is considered by virtue of the concept of initial state and the degradation progress is simulated numerically by using the theory for damage and surface degradation growth. The numerical results are compared with the experimental measurements. It is understood that the initial heterogeneity implementation is not random [Yuan et al 1991], but rather inspired and "extracted" from relevant ultrasonic experiments. In Yuan [1991] and Yuan et al [1992], the implications of random initial material inhomogeneity on degradation evolution and material response were studied. It is also noted that the initial heterogeneity considered here is based on the experimental observations and the way to deal with the initial heterogeneity herein

is different from that studied by Yamaguchi and Chen [1991], in the sense that inhomogeneity is considered in the whole structure (specimen) rather than in the representative volume element.

The theory used for the purposes of this chapter, namely, damage and surface degradation growth, has been presented in chapter 3. It is noted that the damage model and the concept of surface degradation consideration were originated by Frantziskonis and Desai [1987,1991], Frantziskonis [1989], Frantziskonis, Tang and Desai [1991]. The used constitutive law for the undamaged part and numerical procedure is referred to appendix-A and chapter 4, separately. In the following section, the considerations for initial damage implementation are discussed. Then, the numerical solutions of demonstration problems and comparison with experimental measurements are presented.

6.2 Implementation of Initial Damage

As presented in the previous chapter, three series (S, M, L) of samples were tested through ultrasonic scanning. For S and M series we have 12 representative measurement points, and for L series we have 16 representative measurement points, Figure 5.5b. For each test, about six load steps were applied up to the peak, and the ultrasonic measurements were obtained at each load step. For each sample tested, the initial ultrasonic measurements (without external load exerted) have been taken as the reference to assess the structural changes of the sample. Shown in Figure 6.1 and 6.2 are some typical initial measurements of received ultrasonic energy. The contour lines are obtained through transforming the maximum absolute voltage of the received wave to ultrasonic energy with the unit of Joule (equation 5.9b). It can be seen that the distribution of the received ultrasonic energy along the sample is not uniform. Because the wave transmitted along all monitoring area has the same intensity, we conclude that the micro-structure of the sample is not initially uniform. In the following, we will discuss how the initial heterogeneity is considered so that the degradation process can be modeled numerically.

The experiments described in chapter 5 showed that the dissipated energy distribution follows, in general, the initial heterogeneity pattern [Frantziskonis et al

1991, Tang et al 1991]. It seems that degradation is more likely to occur within the volume of high material integrity than of low material integrity. This agrees with the theoretical studies of Yamaguchi and Chen [1991] and the random studies of Yuan et al [1992]. Equation (3.8) is plotted in Figure 6.3, for $\kappa = 50$, $R = 0.5$. The present analysis showed no sensitivity (qualitatively) on the values of R and κ. It can be seen that the rate of damage evolution changes with deformation. As noted previously, damage is a relative concept. If we assume that the material points along the sample correspond to different points along the r-ξ_D curve, the initial heterogeneity can be considered, and more accurate simulation of the degradation progress can be achieved.

As shown in Figures 6.1 and 6.2, the initial received ultrasonic energy distribution along the sample shows two extreme numbers, the highest and the lowest ones. Let us consider the point with the highest initial received ultrasonic energy as reference state. Then other material points can be considered as initially damaged with respect to the reference state. The point with the lowest initial (received) ultrasonic energy is most seriously "damaged" initially, and has the maximum initial damage parameter, say r_0^{max}. The initial damage parameter at other points can be obtained by (linear) interpolation. So we have, generally, $0 \leq r_0 \leq r_0^{max}$, $0 \leq r \leq r_u$. Here, r_0 is the initial damage parameter corresponding to different points along the sample; r_u is the ultimate value of damage parameter r. Following this procedure and considering, in a qualitative sense as described previously, $r_0^{max} = 0.2$ (this is discussed further in the following), we get the initial damage distribution for test samples S4 and M2 as shown in Figure 6.4 and Figure 6.5, respectively. This initial damage distribution will be taken as input for the numerical (FEM) simulation in the next section.

6.3 Numerical Solutions

For illustration purposes we consider samples S4 and M2. Consider the problem to be solved as two-dimensional one (idealized as plane strain). The end platens and the faces of the sample subjected to compressive load were lubricated by a thin layer of silicon grease, and additionally, a thin layer of teflon lubricated on

both sides was placed between end platens and sample. So it is reasonable to assume friction free along boundaries of the sample for the FEM computations. It is assumed that the central line along the depth of the bottom surface of the sample is fixed, to avoid singularity for FEM solution.

From the results presented in section 5 at chapter 3, we have $\kappa^s/\kappa^d = 2621$ and $R^s/R^d = 1.53$, where κ and R are material constants associated with damage evolution, the physical meaning of which is defined in equation (3.8); superscript s, d indicates value for the surface degradation zone and pure damage zone respectively. Specifically, the following values are used herein: $\kappa^s = 131050$, $R^s = 0.765$, $\kappa^d = 50$, $R^d = 0.5$, $r_u = 0.8$.

6.3.1 Damage Growth Consideration

Initially, we neglect the surface effects and consider the damage growth only. Figures 6.6 and 6.7 are the FEM meshes for samples S4 and M2, respectively. Eight-node quadrilateral elements and four-point Gaussian integration method are employed. Although coarse meshes were used, as shown subsequently even such meshes can capture the inhomogeneity patterns of such problems. The initial damage parameter r_0 for each integration point is given as input. The external displacement is taken as known in the process of calculation. In order to assess the structural changes and to compare the numerical results with experimental output, the damage growth $\Delta r = r - r_0$ is used in the following plots. For sample S4, the damage growth pattern obtained at $P/P_{peak} = 0.46$ along the force-displacement curve is shown in Figure 6.8a, and, for comparison, the ultrasonically dissipated energy pattern at $P/P_{peak} = 0.45$ is shown in Figure 6.8b; Similarly, the damage growth pattern at $P/P_{peak} = 0.92$ is shown in Figure 6.9a, and the ultrasonically dissipated energy pattern at $P/P_{peak} = 0.93$ is shown in Figure 6.9b. For sample M2, the damage growth pattern at $P/P_{peak} = 0.18$ is shown in Figure 6.10a, and the ultrasonically dissipated energy pattern at $P/P_{peak} = 0.20$ is shown in Figure 6.10b. Similarly, the modelling results (experimental observations) for sample M2 at $P/P_{peak} = 0.70$ ($P/P_{peak} = 0.68$) are shown in Figure 6.11a (6.11b).

As noted previously, the comparison between the numerical results and experimental observations is qualitative. Since the FEM calculation is processed by displacement control, specific values of P/P_{peak} are approximately achieved for comparison purposes.

An important outcome here is that the initially high intensity regions seem to dissipate energy at a (much) higher rate than the low intensity ones. Both experiment and theory clearly depict this behavior. It is noted that higher rate of energy dissipation corresponds to increased change in microstructure or damage. Then we conclude that the microcrack development is more pronounced in and around the initially high intensity regions. This agrees with the theoretical study by Yamaguchi and Chen [1991] and experimental investigation by Hsu et al [1963]. The experimental results of Hsu et al [1963] have shown that bond cracks begin to grow at 30% of the compressive strength, and that mortar cracks start propagating at the critical stress. The theoretical study by Yamaguchi and Chen [1991] concluded that the propagation of bond cracks is not greatly influenced by the stress state and that the development of mortar cracks and the formation of continuous crack patterns are significantly influenced by the stress state.

6.3.2 Damage Growth and Surface Degradation Consideration

Let us take sample M2 as illustration problem for both damage growth and surface degradation consideration. For this problem, equation (3.30) reduces to

$$\rho = \alpha(H - l) \tag{6.1}$$

where $H = 5in$ is the specimen height, α and l are two material constants. In chapter 5, the surface degradation zone was estimated from the ultrasonic data and from surface instability analysis of Frantziskonis and Vardoulakis [1992] and shear band analysis of Vardoulakis and Frantziskonis [1991]. It was found that for the 5 inches (12.7 cm) height specimens ρ = 1 inch (2.54 cm). With this value and from the test results on different size specimens the values $\alpha = 0.21$ and l = 0.24 inches (0.71 cm) were approximated from the ultrasonic measurements (chapter 5) and instability analysis [Frantziskonis and Vardoulakis 1992]. From

shear band analysis the l was found to be approximately 10 times the thickness of the shear band [Vardoulakis and Frantziskonis 1991]. The FEM mesh (Figure 6.7) is changed as shown in Figure 6.12 to consider the surface degradation. The elements along the two free edges are in the surface degradation zone, and the appropriate material parameters are assigned to them as discussed previously. Following the same procedure as in section 6.3.1, the damage growth, $\Delta r = r - r_0$, at the stage $P/P_{peak} = 0.2$ along the force-displacement curve is obtained as shown in Figure 6.10c.

6.3.3 Discussion

As explained in chapter 5, G can be used to monitor the degradation progress of brittle materials subjected to external mechanical load. In order to show how the theory for damage and surface degradation with initial state consideration describe the degradation process of brittle materials subjected to external mechanical load, we presented some experimental results for samples S4 and M2 as shown in Figures 6.8b-6.9b and Figures 6.10b-6.11b, respectively. Comparing Figure 6.8a (6.9a) with Figure 6.8b (6.9b), it can be seen that the degradation mechanism of sample S4, the initial non-uniformity of which showed higher concentration of received pulse energy along the edge(s), as subjected to external load, is modeled satisfactorily. As for sample M2, where the initial non-uniformity showed higher concentration of received pulse energy in the center of the specimen, the degradation mechanism is not well modeled by considering only the damage growth (compare Figure 6.10a (6.11a) with Figure 6.10b (6.11b)). If both the damage growth and surface degradation are considered in the FEM model, the degradation of sample M2 as subjected to external load can be modeled better (compare Figure 6.10b and Figure 6.10c). But the surface effects is over-predicted by the material parameters used. It seems that more accurate material parameters need to be achieved by further study.

In this study we examine the effects of initial inhomogeneity on the material response to mechanical load. Such inhomogeneity is implemented in the theory via the experimental observations described previously. It was found that the relative

spatial distribution of the inhomogeneity variables is of paramount importance. For the quantitative comparison of theory and experiment a parametric study, e.g. an experimentally obtained value of r_0^{max}, together with introduction of random variables would be necessary. This would require further experimental and theoretical studies.

6.4 Conclusions

The material heterogeneity is considered by virtue of the concept of state of degradation. The degradation mechanism and damage growth patterning of simulated rock under uniaxial external load are modeled numerically by implementing the theory for damage and surface degradation with initial state consideration. Comparing the theoretical outputs and experimental measurements, in a qualitative sense, it is found that the damage growth patterning can be satisfactorily modeled if the initial non-uniformity showed higher concentration of received pulse energy along the edge(s) of the sample. Much better results will be achieved by considering the surface degradation, in addition to the theory for damage and initial damage implementation, if the initial non-uniformity showed higher concentration of received pulse energy in the center of the sample. Overall, it may be concluded that the theory for damage and surface degradation, as combined with the concept of initial state, is capable of describing the degradation patterning for brittle materials. The present comparison of theory and experiments is qualitative. The relative spatial distribution of the inhomogeneity variables, rather than their actual value, is of paramount importance. Parametric studies through extensive experimental results and introduction of random variables are needed for the quantitative implementation of the theory.

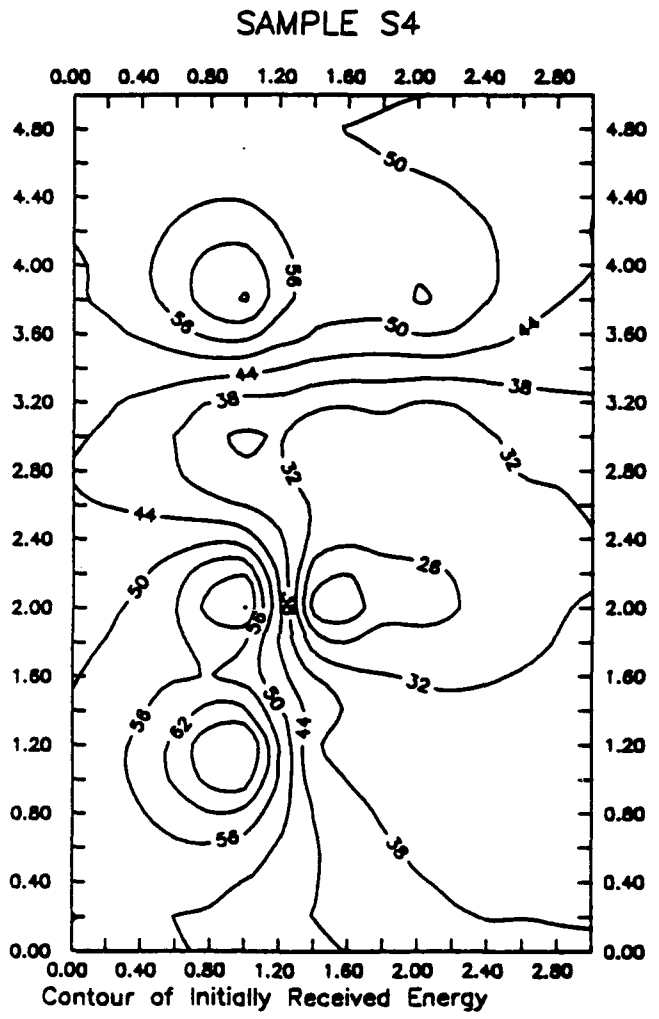

Figure 6.1 Contour of Initially Received Energy for Sample S4

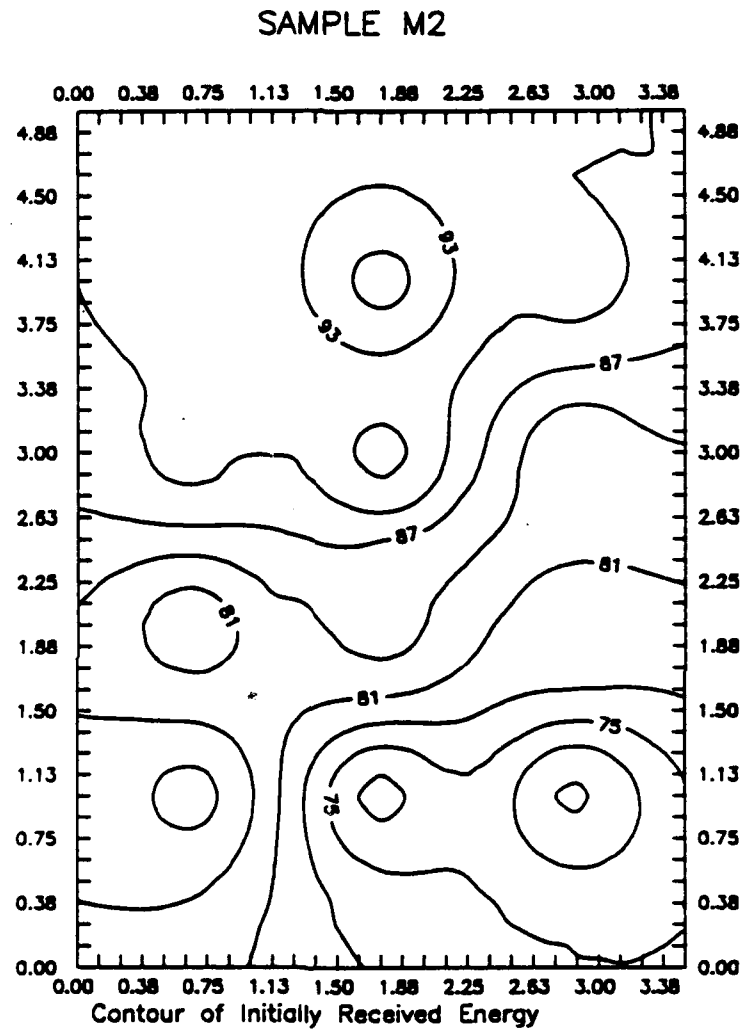

Figure 6.2 Contour of Initially Received Energy for Sample M2

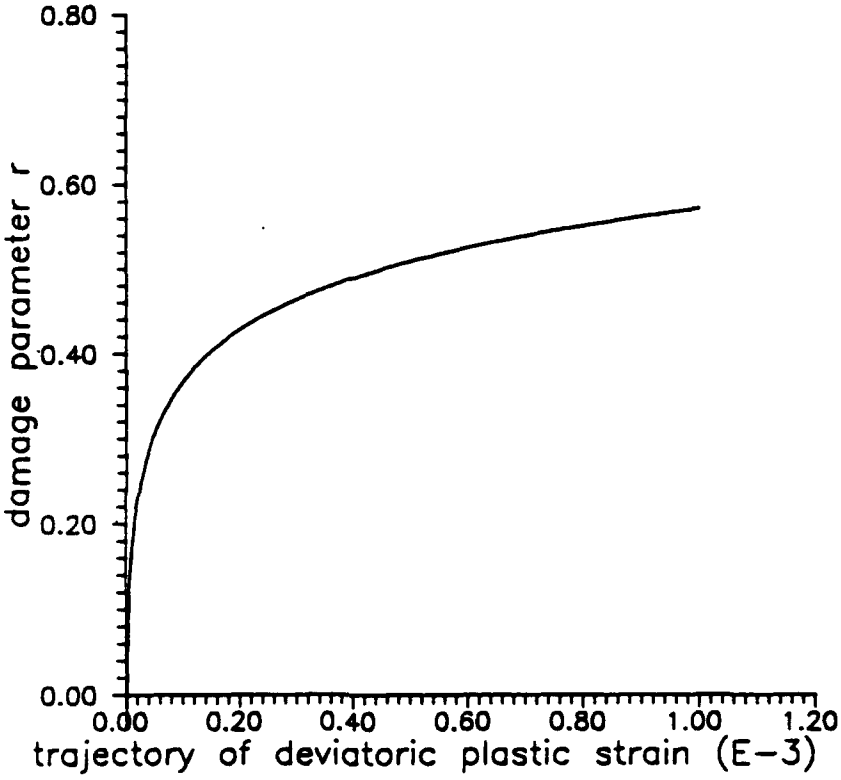

Figure 6.3 Function Plot for $\kappa = 50$, $R = 0.5$

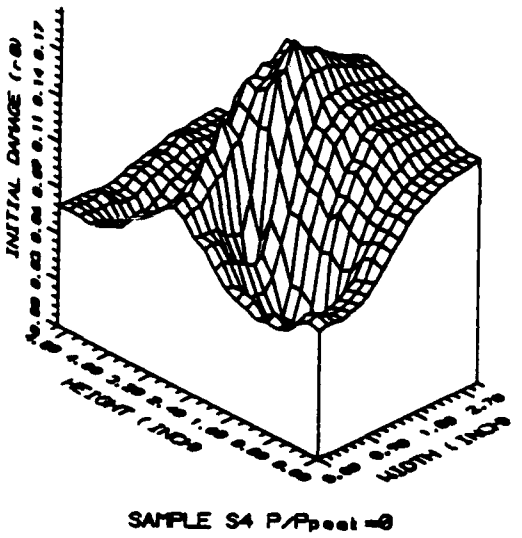

Figure 6.4 Initial Damage Distribution for Sample S4

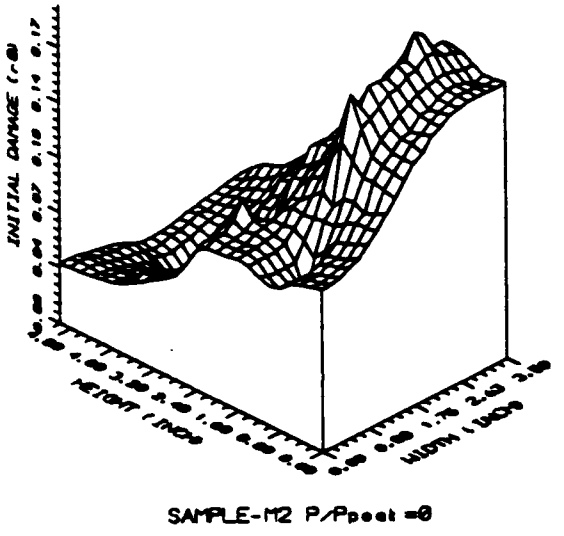

Figure 6.5 Initial Damage Distribution for Sample M2

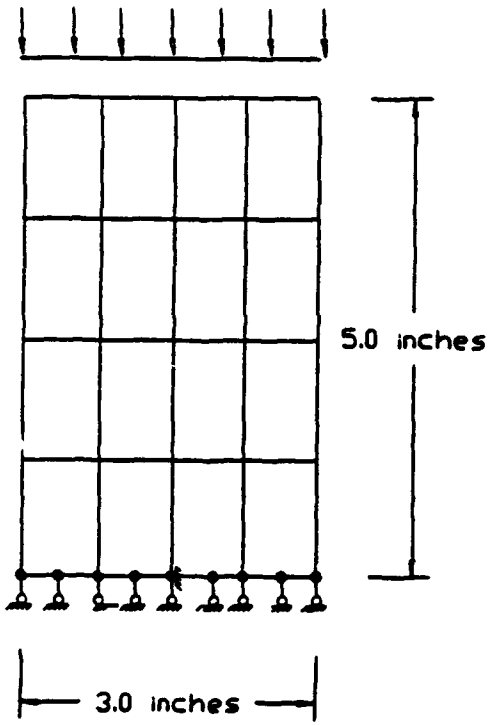

Figure 6.6 Finite Element Mesh for Sample S4

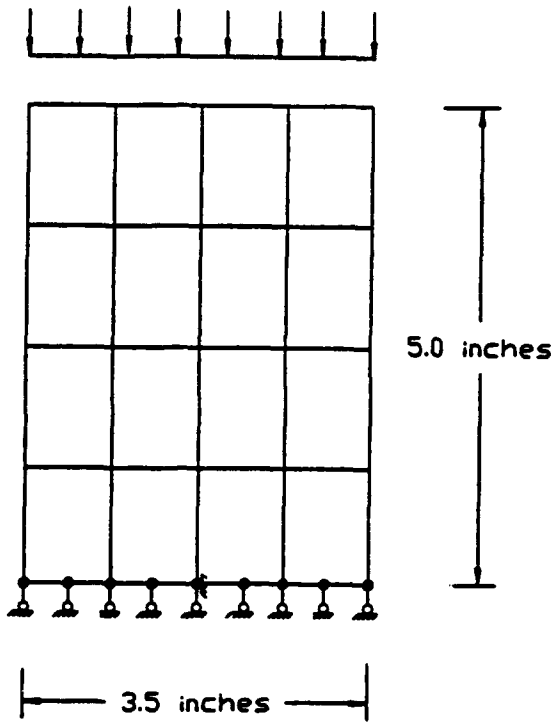

Figure 6.7 Finite Element Mesh for Sample M2

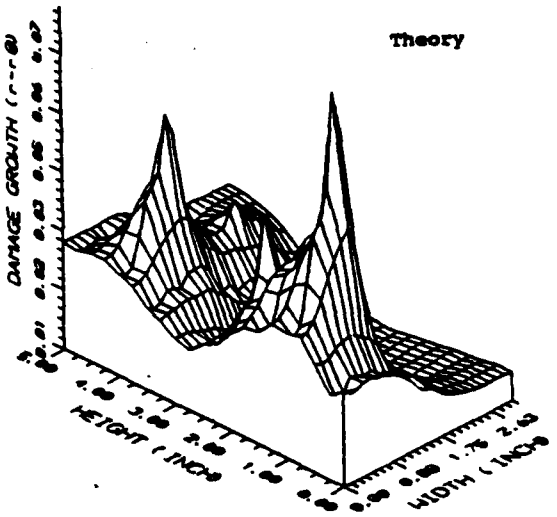

SAMPLE S4 P/Ppeak =0.46

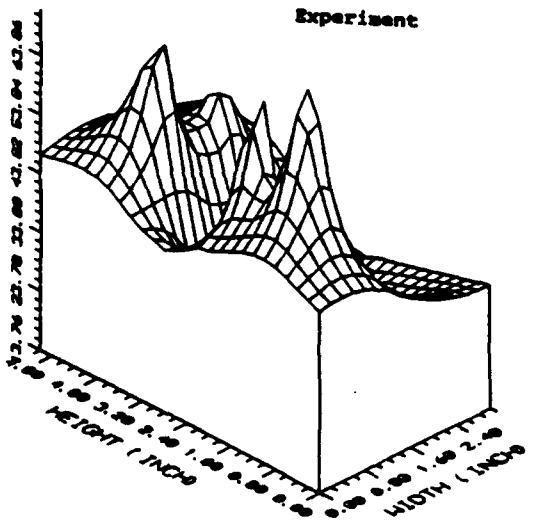

SAMPLE S4 P/Ppeak =0.45

Figure 6.8 Comparison of Theoretical and Experimental Results for Sample S4

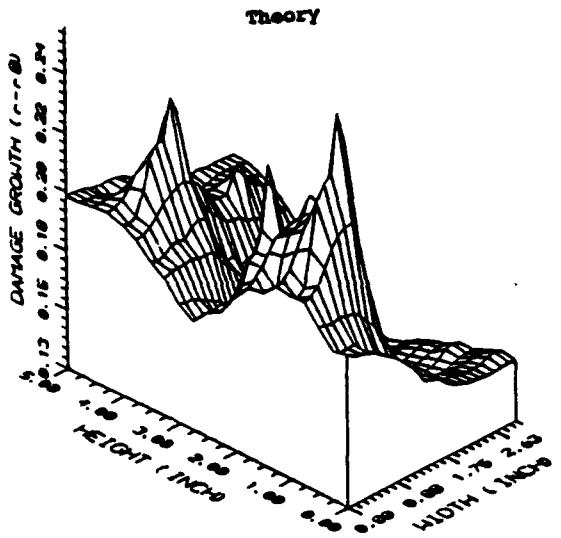

SAMPLE S4 P/Ppeak =0.92

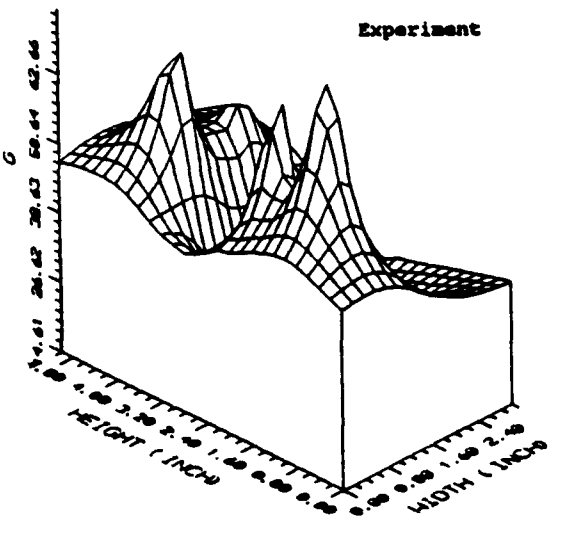

SAMPLE S4 P/Ppeak =0.93

Figure 6.9 Comparison of Theoretical and Experimental Results for Sample S4

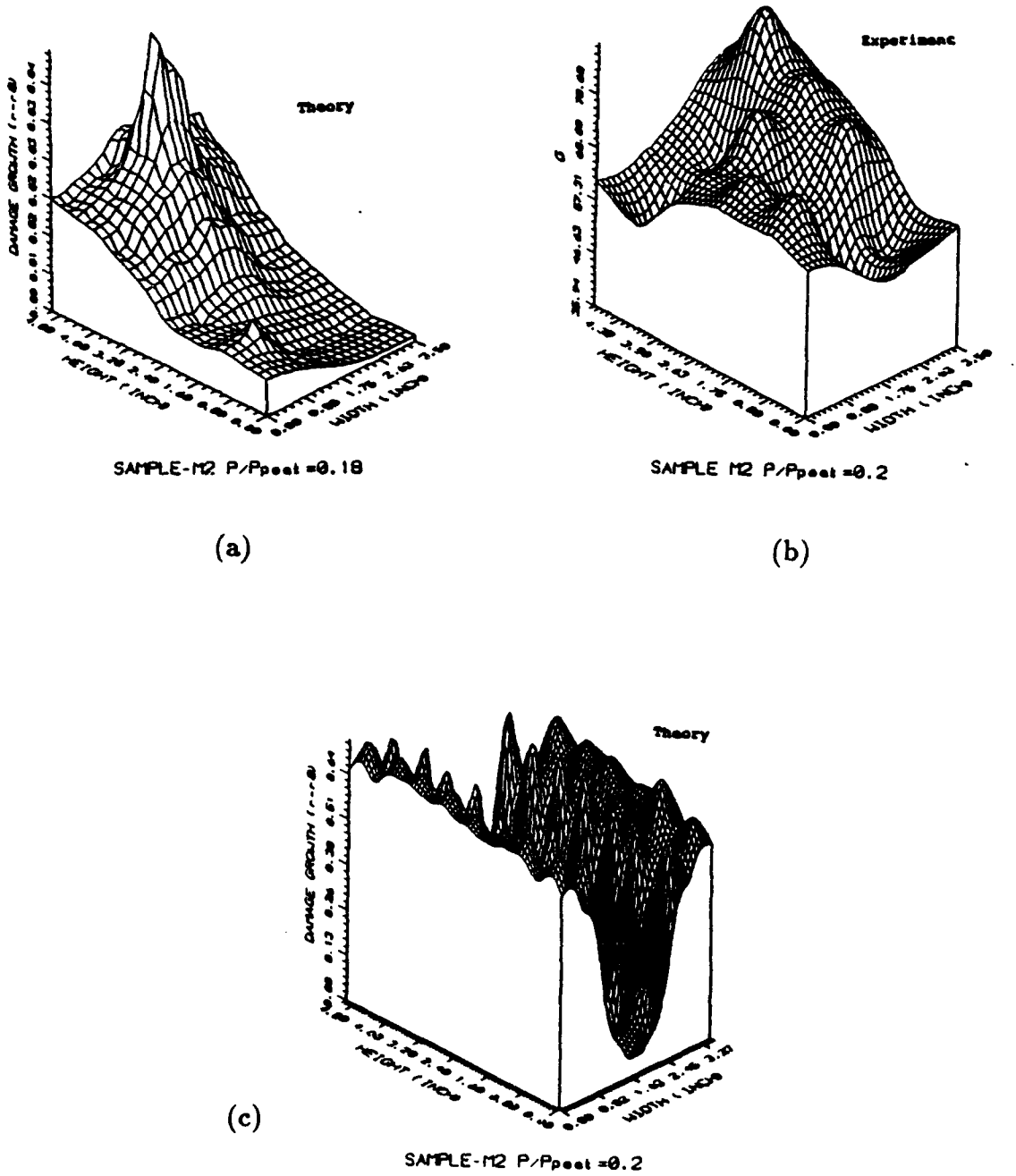

Figure 6.10 Comparison of Theoretical and Experimental Results for Sample M2, (a) Theoretical Results without Surface Degradation Consideration, (b) Experimental Results, (c) Theoretical Results with Surface Degradation Consideration

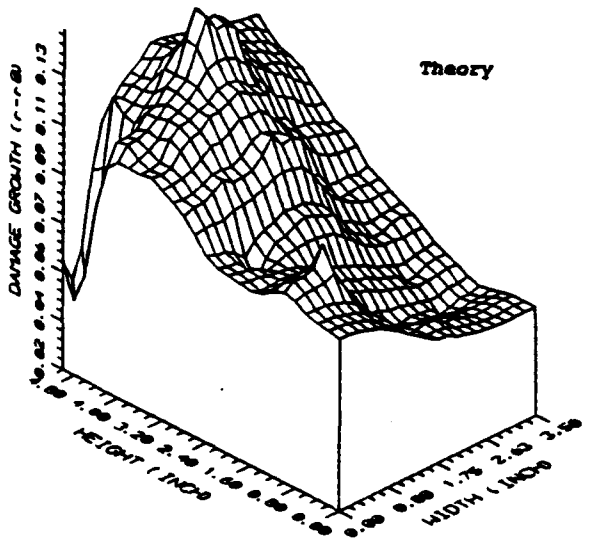

SAMPLE-M2 P/Ppeak =0.70

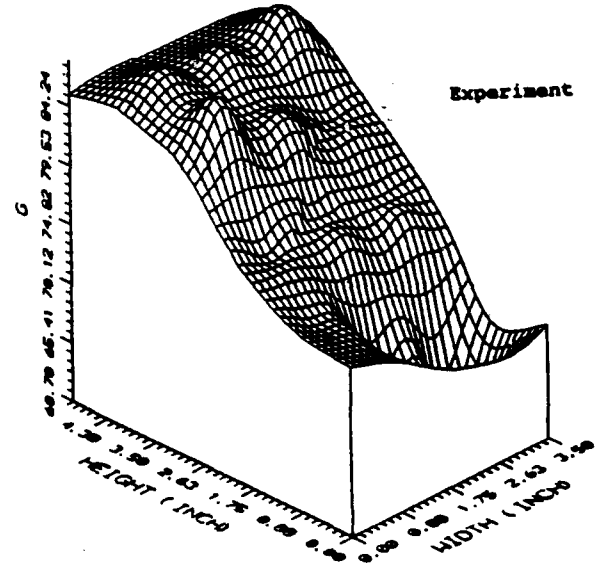

SAMPLE M2 P/Ppeak =0.68

Figure 6.11 Comparison of Theoretical and Experimental Results for Sample M2

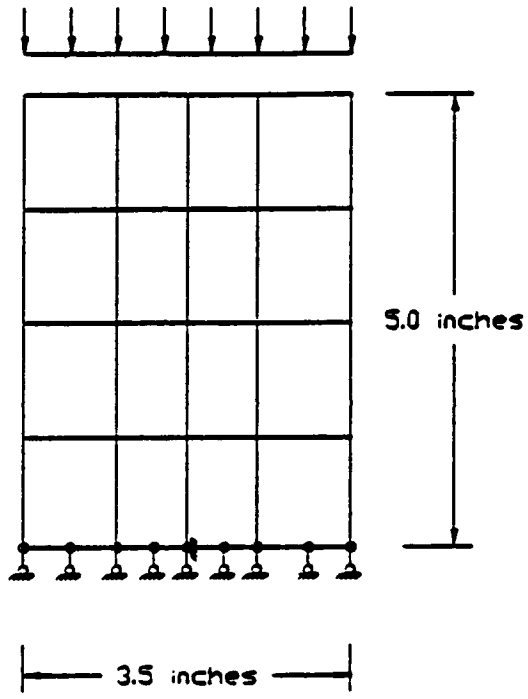

Figure 6.12 Modified Finite Element Mesh to Consider Surface Degradation for Sample M2

CHAPTER 7

EXTENSION TO POST-INSTABILITY STUDY

7.1 General

The instability criteria proposed in this study has been verified through the applications to some typical problems. It is understood that identification of the instability point along the force-displacement curve is by checking the dissipated energy (rate) and elastic potential step by step rather than by checking the stiffness matrix step by step. So, the proposed instability theory is physical model rather than mathematical model such as bifurcation instability theory and localization or shear band analysis. However, we believe that some relationship exists between the physical and mathematical considerations. The establishment of such a relationship will be examined in future effort.

As discussed in Chapter 2, even though the classical continuum theories may describe satisfactorily the onset of instability, they break down in the post-bifurcation regime leading to mathematical problems which are either ill-posed or of changing type. It is clear that classical computations are severely imperfection sensitive. In the damage formulation presented in Chapter 3, the wave-number of the corresponding eigen-mode still depends on mesh size due to the absence of internal length in the flow or constitutive theory. The mesh dependency of the damage model [Frantziskonis and Desai 1987] was investigated by Woo and Desai [1991]. In this chapter, some considerations to eliminate the mesh-dependent problem of various models will be proposed and discussed. The detail solutions will be achieved by future effort.

7.2 Gradient Consideration

7.2.1 Gradient Regularization for A Plasticity Model

For removing the mathematical difficulties of classical constitutive theories, higher order strain gradients have been considered by many researchers. General

review of this topic has been presented in chapter 2. However, for completeness, some basic equations will be presented.

As for the hydrostatic part of the flow-rule or dilatancy condition, Vardoulakis and Aifantis [1991] assume that the volumetric plastic strain-rate $\dot{\epsilon}^p$ at a point x_i depends linearly on the average rate of slip $\dot{\bar{\gamma}}^p$, among the grains contained in a small but finite material volume V surrounding the point x_i and is also a (non-linear) function of the cumulative average slip $\bar{\gamma}_p$ during the considered deformation process at this point. The non-local hypothesis is expressed formally by the relations [Vardoulakis and Aifantis 1991]:

$$\dot{\epsilon}^p = \beta(\bar{\gamma}^p)\dot{\bar{\gamma}}^p, \quad \bar{\gamma}^p = \int \dot{\bar{\gamma}}^p dt \tag{7.1}$$

and

$$\dot{\bar{\gamma}}^p = (1/V)\int \dot{\gamma}^p(x_i + \xi_i)dV \tag{7.2}$$

Assume the region V being a circle of radius R and use the Taylor's expansion of function, then

$$\dot{\bar{\gamma}}^p = \dot{\gamma}^p + l^2 \nabla^2 \dot{\gamma}^p + 0(l^4) \tag{7.3}$$

where $l^2 = R^2/8$. The numerical factor in (7.3) depends on the dimensionality of the problem; e.g. 1/8 is replaced by 1/10 if the calculation is carried on in three dimensions. By assuming for example that l is constant, it follows from (7.1) and (7.3) that the cumulative plastic shear strain is given by a similar expression as $\dot{\gamma}^p$, i.e.

$$\bar{\gamma}^p = \gamma^p + l^2 \nabla^2 \gamma^p + 0(l^4) \tag{7.4}$$

Accordingly, the gradient dependent hydrostatic part of the flow-rule is expressed by the following condition [Vardoulakis and Aifantis 1991]:

$$\dot{\epsilon}^p \approx \beta(\bar{\gamma}^p)(\dot{\gamma}^p + l^2 \nabla^2 \dot{\gamma}^p) \tag{7.5}$$

To show how to modify yield condition, take Coulomb yield condition as example. The Coulomb yield condition is modified as:

$$F = \tau/p - \hat{\mu}(\gamma^p, \nabla^2\gamma^p) = 0 \tag{7.6a}$$

$$\hat{\mu} = \mu(\gamma^p) - c(\gamma^p, \nabla^2\gamma^p)\,\nabla^2\,\gamma^p \tag{7.6b}$$

For reasons to be apparent later the following "initial" condition for the growth of the gradient coefficient c is assumed.

$$c = 0 \quad \text{for} \quad \nabla^2\,\gamma^p = 0 \tag{7.7}$$

To find a more specific form of the function c, the so-called Prager consistency condition is utilized. From (7.6a) we have

$$\dot{\tau} - p\dot{\hat{\mu}} - \dot{p}\hat{\mu} = 0 \tag{7.8}$$

An expression for $\dot{\hat{\mu}}$ can directly be obtained from (7.6b) as

$$\dot{\hat{\mu}} = A\dot{\gamma}^p + B\dot{\delta}^p \tag{7.9}$$

where $\delta^p = \nabla^2\gamma^p$ is set for convenience and the coefficients A and B are defined by the relations

$$A = \frac{\partial\mu}{\partial\gamma^p} - \frac{\partial c}{\partial\gamma^p}\delta^p \tag{7.10a}$$

$$B = -\frac{\partial c}{\partial\delta^p}\delta^p - c \tag{7.10b}$$

An expression for $\dot{p}$ can be determined from the elasticity of the material and the dilatancy condition (7.5) as follows

$$\dot{p} = -K\dot{\epsilon}^e = -K(\dot{\epsilon} - \dot{\epsilon}^p) = -K[\dot{\epsilon} - \beta(\dot{\gamma}^p + l^2\dot{\delta}^p)] \tag{7.11}$$

with K denoting the bulk modulus and $(\dot{\epsilon}^e, \dot{\epsilon})$ the elastic and total volumetric strain rates respectively. In view of (7.9) and (7.11), (7.8) can be written as

$$\dot{\tau} + K\hat{\mu}\dot{\epsilon} - (K\hat{\mu}\beta + Ap)\dot{\gamma}^p - (K\hat{\mu}\beta l^2 + Bp)\dot{\delta}^p = 0 \tag{7.12}$$

To dispense with difficulties in the loading-unloading criteria arising from the explicit presence of $\delta^p = \nabla^2\gamma^p$ in the consistency condition (7.12), a special

non-linear model by requiring that the coefficient of δ^p is identically equal to zero is assumed [Vardoulakis and Aifantis 1991], i.e.

$$K\hat{\mu}\beta l^2 + Bp = 0 \tag{7.13}$$

By substituting in (7.13) the definition (7.6b) for $\hat{\mu}$, and the definition (7.10b) for B, we obtain a first order linear differential equation for $c = c(\delta^p)$, of the form

$$\frac{\partial c}{\partial \delta^p} + f(\delta^p)c = g(\delta^p) \tag{7.14}$$

where

$$f(\delta^p) = 1/\delta^p + \alpha l^2, \quad g(\delta^p) = \alpha \mu l^2/\delta^p \tag{7.15}$$

with

$$\alpha = (K/p)\beta \tag{7.16}$$

The solution of this differential equation is

$$c = e^{-F}[c(0) + \int_0^{\delta^p} g(x)e^F dx], \quad F = \int_0^{\delta^p} f(x)dx \tag{7.17}$$

On recalling (7.7) and carrying out the integration in (7.17), An explicit expression for c of the following form is obtained [Vardoulakis and Aifantis 1991]:

$$c = \frac{\mu}{\delta^p}[1 - exp(-\alpha l^2 \delta^p)] \tag{7.18}$$

This, in turn, in conjunction with (7.6b) gives the following exponential expression for the gradient dependent mobilized friction coefficient $\hat{\mu}$

$$\hat{\mu} = \mu(\gamma^p)exp(-\alpha l^2 \nabla^2 \gamma^p) \approx \mu(\gamma^p)(1 - \alpha l^2 \nabla^2 \gamma^p) \tag{7.19}$$

On returning to the consistency condition (7.12) we obtain, in view of (7.13), the relation

$$\dot{\tau} + K\hat{\mu}\dot{\epsilon} = (K\hat{\mu}\beta + Ap)\dot{\gamma}^p \tag{7.20}$$

From this equation and with definition (7.10a) for A, the desired expression for the rate of the equivalent plastic strain rate $\dot{\gamma}^p$ can be derived [Vardoulakis and Aifantis 1991].

$$\dot{\gamma}^p = \frac{\dot{\tau}/G + \chi\hat{\mu}\dot{\epsilon}}{\hat{h} - \hat{h}_T} \tag{7.21}$$

with

$$\hat{h} = (p/G)\hat{h}_t \tag{7.22a}$$

$$\hat{h}_t = h_t exp(-\alpha l^2 \nabla^2 \gamma^p) \approx h_t(1 - \alpha l^2 \nabla^2 \gamma^p) \tag{7.22b}$$

$$h_t = d\mu/d\gamma^p \tag{7.22c}$$

$$\hat{h}_T = -\chi\hat{\mu}\hat{\beta} \tag{7.23a}$$

$$\hat{\beta} = \beta - (d\beta/d\gamma^p) l^2 \nabla^2 \gamma^p \tag{7.23b}$$

where $\chi = K/G$ is the ratio of the elastic moduli with G being the elastic shear modulus of the material.

Following the standard decomposition of stress tensor σ_{ij} and strain tensor ϵ_{ij} into a spherical part and a deviatoric part, and assuming that deviatoric plastic strain-rates are coaxial with the stress deviator and proportional to the plastic hardening parameter γ^p, the rate-dependent constitutive equation can be derived as [Vardoulakis and Aifantis 1991]:

$$\dot{\sigma}_{ij} = G(L_{ijkl}\dot{\epsilon}_{kl} - N_{ijkl} \nabla^2 \dot{\epsilon}_{kl}) \tag{7.24}$$

where

$$L_{ijkl} = L^e_{ijkl} - L^p_{ijkl} \tag{7.25}$$

L^e_{ijkl} is a tensor concerned with the elastic constants of the material; L^p_{ijkl} and N_{ijkl} are tensors concerned with the plastic behavior of the material.

It is seen that the theory is essentially a second-grade flow theory of plasticity; i.e. a plasticity theory for which the stress-rate depends on the strain-rate as well as on its Laplacian.

Based on Mindlin's elasticity theory with micro-structure, Vardoulakis and Frantziskonis [1991] have recently achieved a gradient regularization of the classical kinematic-hardening plasticity. The outcome is that their Laplacian were introduced into the flow rule, constitutive equation for double force, and incremental stress-incremental strain constitutive equation. Shear-band analysis shows that the theory provides the band thickness, and regularizes the governing equations.

7.2.2 Gradient Regularization for A Specific Model

The model described in section 1 at Chapter 4 [Desai et al 1986] is a constitutive model which is relevant to various yield functions used in the context of plasticity. For reading convenience, let us write down the yield functions as:

$$F = J_{2D} - (-\alpha J_1^n + \gamma J_1^2)(1 - \beta S_r)^m = 0 \tag{7.26}$$

with

$$\alpha = \frac{a_1}{\xi^{n_1}} \tag{7.27}$$

where J_{2d} is the second invariant of the deviatoric stress tensor, S_{ij}, a_1, n_1, n, γ, β, and m are treated as material constants, J_1 is the first invariant of stress tensor, σ_{ij}. S_r is the stress ratio such as $J_{3D}^{\frac{1}{3}}/J_{2D}^{\frac{1}{2}}$ and Lode angle, J_{3D} is the third invariant of S_{ij}, and ξ is plastic strain trajectory defined as

$$\xi = \int (d\epsilon_{ij}^p d\epsilon_{ij}^p)^{1/2} \tag{7.28}$$

To consider the gradient effect, the yield function (7-26) is modified as

$$F' = J_{2D} - (-\alpha' J_1^n + \gamma J_1^2)(1 - \beta S_r)^m = 0 \tag{7.29}$$

with

$$\alpha' = \alpha(\xi, \nabla^2\xi) = \frac{a_1}{\xi^{n_1}} - c(\xi, \nabla^2\xi)\,\nabla^2\,\xi \tag{7.30}$$

The coefficient c can be derived by considering Prager's consistency condition, $\Delta F' = 0$. For simplicity, c may be taken as a constant. However, c can be redefined as a function of damage parameter, r, such that

$$c = f(r, \dot{r}) \tag{7.31}$$

with the principle that c is proportional to $\dot{r}$, and that c reaches its maximum as r approaches its ultimate value r_u. In (7.31), f means function.

Let us decompose the strain rate $\dot{\epsilon}_{ij}$ into elastic $\dot{\epsilon}^e_{ij}$ and plastic $\dot{\epsilon}^p_{ij}$. The standard flow rule requires that

$$\dot{\epsilon}^p_{ij} = k\lambda \frac{\partial Q}{\partial \sigma_{ij}} \tag{7.32}$$

with

$$k = \begin{cases} 1, & \text{if } F = 0 \text{ and } \frac{\partial F}{\partial \sigma_{kl}} \dot{\sigma}_{kl} > 0 \\ 0, & \text{otherwise} \end{cases} \tag{7.33}$$

The expression of λ can be achieved by following the standard plasticity theory (see Appendix A). Now, the flow rule (7.32) is modified as

$$\dot{\epsilon}^p_{ij} = k \frac{\partial Q}{\partial \sigma_{ij}} (\lambda + l^2 \nabla^2 \lambda) \tag{7.34}$$

with l being the 'internal length'. As discussed in (Vardoulakis and Aifantis 1991), prior to localization the coordinates x_i must be non-dimensionalized by some global dimension L of the structure under consideration. Before localization $(l^2/L^2) \ll 1$. However, when the deformation is localized in a narrow zone of intense shear then the spatial coordinates are non-dimensionalized by say the thickness d of the shear band. Accordingly, the gradient effects are not necessarily negligible.

By using the yield function (7.29) and flow rule (7.34), and following the standard plasticity procedure, the following incremental stress-incremental strain relation is expected if associated flow is assumed.

$$\dot{\sigma}_{ij} = C^{ep}_{ijkl} \dot{\epsilon}_{kl} - l^2 C^p_{ijkl} \nabla^2 \dot{\epsilon}_{kl} \tag{7.35}$$

with

$$C^{ep}_{ijkl} = C^{e}_{ijkl} - C^{p}_{ijkl} \tag{7.36}$$

where C^{e}_{ijkl} is a tensor concerned with elasticity, and C^{p}_{ijkl} is a tensor concerned with plasticity.

It is noted that the above modification is processed for undamaged (intact) part of the material if δ_{0+r} model is concerned. For the damaged part, the assumption of perfect rigid plastic behavior with zero shear strength is kept unchanged.

7.3 Non-Local Damage Consideration for A Specific Model

The concept of non-local continuum [Kroner 1967; Krumhanzl 1968; Eringen and Edelen 1972] was formalized [Bazant 1984; Bazant, Belytschko and Chang 1984; Bazant and Pijaudier-Cabot 1988] to overcome the macroscopic strain-softening problem in brittle materials which causes localization instabilities, spurious mesh sensitivity and incorrect convergence. One very effective version of the non-local concept is the nonlocal continuum with local strain [Pijaudier-Cabot and Bazant 1987]. The key idea is to prevent localization of damage to regions of zero volume by a non-local formulation of the stress-strain relation in which only the damage, i.e. strain-softening response is non-local while the elastic response is local. Being stimulated by this idea, we now propose an alternative to eliminate the post-instability mesh-dependent problem for specific damage model. Here, we keep the constitutive descriptions for the two parts (intact part and damaged past) unchanged, and consider the damage parameter r (which measures the structural transformation of the system under external mechanical load) non-local modification. It is noted that the damage description and its function are different from the damage theory utilized by Pijaudier-Cabot and Bazant [1987]. Then, the proposed non-local damage consideration is expected to be different from that used by Bazant and Pijaudier-Cabot [1988].

The damage model was originated by Frantziskonis and Desai [1987]. Discussion about this model has been presented in Chapter 3. The evolution law of

damage parameter r is described by equation (3.8) and (3.9). The damage parameter is used to calculate the average stress and to modify the constitutive tensor. As can be seen from equation (3.4), along localization zone or shear band, the incremental shear stress approaches zero or a very small value (dependent on the material) as r reaches its ultimate value r_u. This may be responsible for the zero energy dissipation along shear band. If the neighboring effects are considered and therefore the local damage parameter is regularized, then the problem of zero energy dissipation may be eliminated.

Let us regularize the local damage parameter as follows. The spatial average of the magnitude of deviatoric plastic trajectory at location x may be defined as

$$\bar{\xi}_D(\mathbf{x}) = \frac{1}{V_r(\mathbf{x})} \int_V \alpha(\mathbf{s}-\mathbf{x})\xi_D(\mathbf{s})dV = \int_V \alpha'(\mathbf{x},\mathbf{s})\xi_D(\mathbf{s})dV \tag{7.37}$$

in which

$$V_r(\mathbf{x}) = \int_V \alpha(\mathbf{s}-\mathbf{x})dV \tag{7.38}$$

$$\alpha'(\mathbf{x}-\mathbf{s}) = \alpha(\mathbf{s}-\mathbf{x})/V_r(\mathbf{x}) \tag{7.39}$$

The above bar denotes the averaging operator, V=volume of the body and $\alpha(\mathbf{x})$ = weighting function which defines the averaging; s is the general co-ordinate vector. The averaging may be specified by a uniform function, $\alpha = 1$, which is non-zero only within a representative volume such as a circle in two dimensions or a sphere in three dimensions. However, the normal distribution function is recommended [Bazant and Lin 1988]:

$$\alpha(\mathbf{x}) = e^{-(k|\mathbf{x}|/l)^2} \tag{7.40}$$

in which, for one, two and three dimensions:

$$1D: \quad |\mathbf{x}|^2 = x^2, \quad k = \sqrt{\pi} = 1.772 \tag{7.41}$$

$$2D: \quad |\mathbf{x}|^2 = x^2 + y^2, \quad k = 2 \tag{7.42}$$

$$3D: \quad |\mathbf{x}|^2 = x^2 + y^2 + z^2, \quad k = (6\sqrt{\pi})^{1/3} = 2.149 \tag{7.43}$$

l is the characteristic length, a material property which defines the diameter of the representative volume. From experiments, Bazant and Pijaudier-Cabot (1988) found that $l = 2.7$ times the maximum aggregate size for concrete.

Now, we can use the averaged $\bar{\xi}_D$ to get the regularized damage parameter $\bar{r}$ as

$$\bar{r} = r_u - r_u exp(-\kappa \bar{\xi}_D^R) \tag{7.44}$$

As defined in chapter 3, r_u, κ, and R are material constants, and they have been identified for a brittle material [Desai, Kundu and Wang 1990]. Then the constitutive tensor $\mathbf{L}$ (3.6) can be modified as

$$\bar{L}_{ijkl} = (1 - \bar{r})C^u_{ijkl} + \bar{r}C^d_{ijkl} \tag{7.45}$$

It is important to note that these modification are processed in load step. If we implement these modification along iteration step, convergency problem may be involved.

7.4 Physical Modification through Diffusion Assumption

The damage model [Frantziskonis and Desai 1987] assumes that there is no diffusion, as in the mixture theory, between the damaged and intact parts of the deforming materials. As a result, the strains in the damaged part and intact part and the observed strains, $d\epsilon^d_{ij}$, $d\epsilon^i_{ij}$ and $d\epsilon^a_{ij}$, respectively, are assumed to be the same. In order to eliminate the mesh-dependent problem in post-instability stage, Desai [1991] proposed a procedure and algorithm to allow the relative motions between the damaged and intact parts of deforming materials. It is suggested that this approach that introduces a physically consistent constraining condition can lead to results similar to those in the foregoing procedures. The Finite-Element implementation and examination of this algorithm is being currently pursued.

CHAPTER 8

SUMMARY AND CONCLUSIONS

In this study, first, the theoretical and experimental view points concerned with instability and bifurcation were reviewed and discussed. In its most general form, bifurcation theory is theory of equilibrium solutions of an nonlinear equation. For brittle materials such as rock and concrete, the non-linearity of the (incremental) equilibrium equation comes from the constitutive description which reflects the unconservative (plastic and/or damage) behavior of the deforming material system. Then, the onset of bifurcation or localization is relevant to the yield function and plastic potential assumed. The occurrence of a bifurcation or limit point in a numerical stress analysis is marked by singularity of the stiffness matrix and negative or complex eigenvalues–conditions that traditionally produce severe numerical instability sufficient to disrupt a conventional finite element program. Classical theories of plasticity, in particular, break down in the post-bifurcation regime where ellipticity is lost. In order to eliminate this mathematical problem, a few non-traditional considerations have been proposed. They are gradient regularization, Cosserat continuum model, non-local theory, and rate-dependent consideration.

Based on energy consideration, an alternative instability criterion has been developed and examined. According to this criterion, a brittle material system may experience unstable damage growth if the rate of decrease of elastic potential per unit damaged volume is higher than that of increase of dissipated energy per unit damaged volume.

The definition of surface degradation zone was discussed and the material constants concerned with surface degradation were identified against experiment results. The damage growth instability criterion was extended to consider the surface degradation instability resulting spalling of material from the stress-free surface(s). The onset of surface degradation instability is influenced by the material behavior, structural geometry, and the external load.

The proposed pure damage growth instability criterion and surface degradation instability criterion are, in some sense, similar to the well-known Griffth's criterion.

The energy-based stability theory was implemented analytically and numerically. It was shown that the onset of both surface degradation instability and global degradation instability occur in the strain hardening stage, that is, before and close to the peak strength. It was also identified that the onset of surface degradation instability occurs before the onset of global degradation instability. The comparison of theoretical prediction and experimental results highlights that the degradation instability theory predicts the global instabilities concerned with non-uniform deformation and the surface degradation instabilities concerned with spalling and size, shape effects for brittle materials like rock and concrete.

Relevant physical experiments were performed to study the degradation mechanism of a brittle material. Ultrasonic energy analysis reported that dissipated energy shows a random distribution and it follows, in general, the initial non-homogeneity pattern. The surface effects of simulated rock under uniaxial external compression were highlighted by both pure strain gage tests and ultrasonic scanning tests. The material internal length associated with surface degradation was estimated. Relatively low external energy is required to produce degradation occurring before the peak load. This implies that from low load levels the specimen may be susceptible to instability, and this may explain the large range of peak load values for specimens of the same shape and size. The relationship between the ultrasonically dissipated energy and mechanically dissipated energy is dependent on deformation and can be approximated by a power function of load level coefficient.

Experiments showed that the simulated rock is initially heterogeneous. The material heterogeneity was considered by virtue of the concept of state of degradation. The degradation mechanism and damage growth patterning of simulated rock under uniaxial external load were modeled numerically by implementing the theory for damage and surface degradation with initial state consideration. It was found that the damage growth patterning can be satisfactorily modeled if the initial non-uniformity showed higher concentration of received pulse energy along the

edge of the sample. Much better results would be achieved by considering the surface degradation, in addition to the theory for damage and initial damage implementation, if the initial non-uniformity showed higher concentration of received pulse energy in the center of the sample. The presented comparison of theory and experiments was qualitative. It is felt that parametric studies through extensive experimental results and introduction of random variables are needed for the quantitative implementation of the theory.

Although it is believed that damage concepts can provide a general and simplified approach for characterizing behavior of (geologic) materials undergoing microcracking and fracture leading to loss of strength and strength softening, the post-instability mesh-dependent problem is involved as far as the Finite Element solution is concerned. Three alternatives were proposed to eliminate the post-instability mesh-dependent problem. They are constitutive gradient regularization, non-local damage consideration, and diffusion assumption. The internal length introduction is crucial and physically meaningful herein.

APPENDIX A

ELASTOPLASTIC CONSTITUTIVE RELATIONS

In this appendix, the details of the derivation of the elastic-plastic relation for the topical part are given. The yield function involved were described in section 1 at Chapter 4. In general, we can write the incremental (rate) constitutive relation for the topical part as

$$\dot{\sigma}^t_{ij} = C^{e-p}_{ijkl}\dot{\epsilon}_{kl} \tag{A.1}$$

In the above relation, C^{e-p}_{ijkl} is termed as the elastoplastic constitutive tensor. In order to derive the expression for this tensor, the relations of elastic-plastic theory are used [Hill 1950; Chen and Han 1988]

$$\dot{\epsilon}_{ij} = \dot{\epsilon}^e_{ij} + \dot{\epsilon}^p_{ij} \tag{A.2}$$

that is, strain rate (increment) are decomposed into elastic $\dot{\epsilon}^e_{ij}$ and plastic $\dot{\epsilon}^p_{ij}$. Also

$$\dot{\epsilon}^p_{ij} = k\lambda\frac{\partial Q}{\partial \sigma^t_{ij}} \tag{A.3}$$

known as the flow rule such that

$$k = \begin{cases} 1, & \text{if } F = 0 \quad \text{and} \quad \frac{\partial F}{\partial \sigma^t_{kl}}\dot{\sigma}^t_{kl} > 0; \\ 0 & \text{otherwise} \end{cases} \tag{A.4}$$

For a hardening material (topical part) $\lambda \geq 0$ and in the present theory the topical behavior is hardening (non-softening); thus, always $\lambda \geq 0$. The elastic strain increments (rates) are related to stress rates

$$\dot{\sigma}^t_{ij} = C^e_{ijkl}\dot{\epsilon}_{ij} \tag{A.5}$$

where C^e_{ijkl} is the elasticity constitutive tensor. In the present case, elasticity is assumed linear and isotropic; thus,

$$C^e_{ijkl} = \frac{1}{2G}\delta_{ik}\delta_{li} - \frac{K}{2G(2G+3K)}\delta_{kl}\delta_{ij} \tag{A.6}$$

where G, K denote the initial elastic shear and bulk moduli, respectively. From (A.2) and (A.5), we have

$$\dot{\sigma}^t_{ij} = C^e_{ijkl}(\dot{\epsilon}_{kl} - \dot{\epsilon}^p_{kl}) \tag{A.7}$$

From the definition of the plastic strain trajectory ξ, we have

$$\dot{\xi} = (\dot{\epsilon}^p_{kl}\dot{\epsilon}^p_{kl})^{1/2} \tag{A.8}$$

It follows from the flow rule, (A.3) and (A.8), that

$$\dot{\xi} = \lambda \left(\frac{\partial Q}{\partial \sigma^t_{kl}} \frac{\partial Q}{\partial \sigma^t_{kl}} \right)^{1/2} \tag{A.9}$$

The consistency condition for the yield function F is expressed as

$$\dot{F} = \frac{\partial F}{\partial \sigma^t_{kl}} \dot{\sigma}^t_{kl} + \frac{\partial F}{\partial \xi} \dot{\xi} = 0 \tag{A.10}$$

Substituting (A.7) and (A.9) into (A.10), we have

$$\lambda \left[\frac{\partial F}{\partial \sigma^t_{ij}} C^e_{ijkl} \frac{\partial Q}{\partial \sigma^t_{kl}} - \frac{\partial F}{\partial \xi} \left(\frac{\partial Q}{\partial \sigma^t_{kl}} \frac{\partial Q}{\partial \sigma^t_{kl}} \right)^{1/2} \right] = \frac{\partial F}{\partial \sigma^t_{kl}} C^e_{ijkl} \dot{\epsilon}_{kl} \tag{A.11}$$

The above equations can be solved for λ so that (A.3), (A.7) and (A.11) yield

$$\dot{\sigma}^t_{ij} = \left[C^e_{ijkl} - \frac{C^e_{ijpq} \frac{\partial Q}{\partial \sigma^t_{pq}} \frac{\partial F}{\partial \sigma^t_{mn}} C^e_{mnkl}}{\frac{\partial F}{\partial \sigma^t_{uv}} C^e_{uvrs} \frac{\partial Q}{\partial \sigma^t_{rs}} - \frac{\partial F}{\partial \xi} \left(\frac{\partial Q}{\partial \sigma^t_{kl}} \frac{\partial Q}{\partial \sigma^t_{kl}} \right)^{1/2}} \right] \dot{\epsilon}_{kl} \tag{A.12}$$

The above relation is the final elastoplastic relation for the topical part. In this study, associative flow ($Q = F$) is assumed.

LIST OF REFERENCES

Aifantis, E.C. (1984), On the Microstructural Origin of Certain Inelastic Models, Transactions of ASME, *J. Mat. Engr. Tech.*, 106, 326-330

Aifantis, E.C. (1987), The Physics of Plastic Deformation, *Int. J. Plasticity*, 3, 211-247

Aifantis, E.C. (1988), on the problem of dislocation patterning and persistent slip bands, In: *Non-linear phenomena in materials science* (Kubin, L. and Martin, G. eds.) 397-406, Trans. Tech. Publ.

Al-Kubaisy, M.A. and Young, A.G. (1975), Failure of Concrete under Sustained Tension, *Mag. Concrete Res.*, 27, 92, 171-178

Bazant. Z.P. (1984), Imbricate Continuum and Its Variational Derivation. *J. Engr. Mech. Div., ASCE.* 110, 1693-1712

Bazant, Z.P. Belytschko, T.B. and Chang, T.-P. (1984), Continuum Theory for Strain-Softening, *J.Engr. Mech. Div., ASCE*, 110, 1666-1692

Bazant, Z.P. and Pijaudier-cabot, G. (1987), Modeling of Distributed Damage by Nonlocal Continuum with Local Strain, In: *4th Int. Conf. on Numerical Methods in Fracture Mechanics* (A.R. Luxmore et al eds.), San Antonio, Texas, 411-432

Bazant, Z.P. and Pijaudier-cabot, G. (1988), Non-Local Continuum Damage and Measurement of Characteristic Length, *Proc. Joint ASME/SES Applied Mechanics and Engr. Sciences Conf.*, (G.J. Dvorak and N. Laws eds.), AMD-Vol.92, 79-85

Bazant, Z.P. and Lin, F.-B. (1988), Non-Local yield Limit Degradation, Int. *J. Numer. Methods. Engr.*, 26, 1805-1823

Bazant, Z.P. (1988), Stable States and Paths of Structures with Plasticity or Damage, *J. Engr. Mech. Div., ASCE*, 114, 2013-2034

Bazant, Z.P., Tabbara, M.R., Kazemi, M.T. and Pijaudier-Cabot, G. (1990), "Random Particle Model for Fracture of Aggregate or Fiber Composites", *J. Engr. Mechs. Div., ASCE*, 116, 1686-1705

Benallal, A. Billardon, R. and Geymonat, G. (1989), Some mathematical aspects of the damage-softening rate problem. In: *Cracking and Damage-strain Localization and Size effects* (J. Mazars and Z.P. Bazant eds.), 247-258. Elsevier, Amsterdam

Ben-Zeitum, A.E. (1986), Use of Pulse Velocity to Predict Compressive Strength of Concrete, *Int. J. Cement Composites and Lightweight Concrete*, 8, 51-59

Bergan, P.G., Horrigmoe, G., Krakeland, B. and Soreide, T.H. (1978), Solution techniques for non-linear finite element problems, *Int. J. Numer. Methods Engr.*, 12, 1677- 1696

Bigoni, D. and Hueckel, T. (1991), Uniqueness and Localization-I. Associative and Non-associative Elastoplasticity, *Int. J. Solids Structures*, 28, No.2, 197-213

Biot, M.A. (1963a), Internal Buckling under Initial Stress in Finite Elasticity. *Proc. R. Soc. London*, A273, 306-328

Biot, M.A. (1963b), Surface Instability in Finite Anisotropic Elasticity under Initial Stress, *Proc. R. Soc. London*, A273, 329-339

Biot, M.A. (1963c), Interfacial Instability in Finite Elasticity under Initial Stress, *Proc. R. Soc. London*, A273, 340-344

Biot, M.A. (1965), *Mechanics of Incremental Deformation*, Wiley, New York

Bowen, R.M. (1975), Theory of Mixtures, in: *Continuum Physics* (Eringen, A.C. ed.), New York: Academic Press, 3, 1

Bowen, R.M. (1969), Thermochemistry of Reacting Materials, *J. Chemical Physics*, 50, 4601-4602

Chen, W.F. and Han, D.J. (1988), *Plasticity for Structural Engineers*, Springer-Verlag

Cook, R.D. (1981), *Concepts and Applications of Finite Element Analysis*, 2nd ed., Wiley, New York

Cosserat, E. and Cosserat, F. (1909), *Theorie des Corps Deformables*, Herman et fils, Paris

Crisfield, M.A. and Wills, J. (1988), Solution Strategies and Softening Materials, *Compt. Meths. Appl. Mech. Engr.*, 66, 267-289

de Borst, R. (1989), Numerical Methods for Bifurcation Analysis in Geomechanics, *Ingenieur-Archiv*, 59, 160-174

Derski, W. (1989), *Rock and Soil Mechanics*, Derski et al ed., Polish Scientific Publishers, Warsaw, Charpter 6

Desai, C.S. and Reese, L.C. (1970), Stress-Deformation and Stability Analysis of Deep Boreholes, *Proc. 2nd Congr. International Soc. for Rock Mechanics*, Belgrade, Yugoslavia

Desai, C.S. and Abel, J.F. (1972), Introduction to the Finite Element Method, Van Nostrand Reinhold, New York

Desai, C.S. (1974), A Consistent Finite Element Technique for Work-Softening Behavior, *Proc. Int. Conf. on Comp. Methods in Nonlinear Mechanics*, J.T. Oden et al eds., Univ. of Texas, Austin, Texas

Desai, C.S. (1980), A General Basis for Yield, Failure and Potential Functions in Plasticity, *Int. J. Num. Anal. Meth. in Geomech.*, 4, 361-375

Desai, C.S. and Siriwardane, H.J. (1983), *Constitutive Laws for Engineering Materials*, Prentice-Hall, Inc., Englewood Cliffs, N.J.

Desai, C.S. and Faruque, M.O. (1984), Constitutive Model for Geological Materials, *J. Eng. Mech. Div., ASCE*, 110, 1391-1408

Desai, C.S., Somasundaram, S. and Frantziskonis, G. (1986), A Hierarchical Approach for Constitutive Modelling of Geologic Materials, *Int. J. Numer. Anal. Methods in Geomechanics*, 10, 225-257

Desai, C.S., Kundu, T. and Wang, G. (1990), Size effect on Damage in Progressive Softening Process for Simulated Rock, *Int. J. Numer. Anal. Methods in Geomechanics*, 14, 509-517

Desai, C.S. (1991), Algorithms to Eliminate Mesh-Dependency for A Damage Model, *Report*, Department of Civil Engineering and Engineering Mechanincs, The University of Arizona, Tucson, Arizona

Desai, C.S. and Woo, L. (1992), Damage Model and Implementation in Nonlinear Dynamic Problems, *Computational Mechanics*, accepted

Drucker, D.C. (1951), A more Fundamental Approach to Stress-Strain Relations, *Proc. 1st U.S. Nat. Cong. Appl. Mech.*, 487-491

Drucker, D.C. (1956), On Uniqueness in the Theory of Plasticity, *Q. Appl. Math.*, 14, 35-42

Drucker, D.C. (1959), A Definition of Stable Inelastic Material, *J. Appl. Mech.*, 26, 101-106

Drucker, D.C. (1991), Constitutive Relations for Solids, Retrospect and Prospect, *Proc. of the Third International Conference on Constitutive Laws for Engineering Materials: Theory and Applications*, Desai et al ed.

Eftis, J. and Liebowitz, H. (1975), *Engineering Fracture Mechanics*, 7, 101-135

Eringen, A.C. and Edelen, D.G.B. (1972), On Nonlocal Elasticity, *Int. J. Engr. Sci.*, No. 10m 233-248

Fairhurst, C. and Cook, N.G.W. (1966), The Phenomenon of Rock Splitting Parallel to the Direction of Maximum Compression in the Neighborhood of a Surface, *Proc. First Int. Congress Rock Mech.*, Leisbon, 1, 687-692

Frantziskonis, G and Desai, C.S. (1987a), Constitutive Model with Strain Softening, *Int. J. Solids Structures*, 23, 733-750

Frantziskonis, G. and Desai, C.S. (1987b), Analysis of A Strain Softening Constitutive Law, *Int. J. of Solids and Structures*, 23, 751-768

Frantziskonis, G. (1989), Damage and Free Edge Effects in Laminated Composites, Energy and Stability Propositions, *Acta Mechanica*, 77, 213-230

Frantziskonis, G. and Desai, C.S. (1991), Surface Degradation Mechanisms in Brittle Material Structural Systems, *Int. J. Fracture*, 48, 231-244

Frantziskonis, G., Tang, F.F. and Desai, C.S. (1991), On Borehole Scale Effects and Related Instabilities, *Engr. Fract. Mechs.*, 39, 2, 373-389

Frantziskonis, G., Desai, C.S., Tang, F.F. and Daniewicz, D. (1991), Degradation Mechanisms in Brittle Materials Investigated by Ultrasonic Scanning, *Engineering Fracture Mechanics*, accepted

Frantziskonis, G. and Vardoulakis, I. (1992), On the Micro-structure of Surface Effects and Related Instabilities, *Europ. J. of Mechanics, A-Solids*, 11. 21-34

Guenot, A. (1987), Stress and Rupture Conditions around Oil Wellbores, *Proc. 6th Int. Congress Rock Mech.*, Vol. 1, 109-118, Montreal, Canada

Germer, L. H., MacRac, A. V. and Hartman, C.D. (1961), Nickel Surface, *J. Appl. Phys.*, 32, 2432-2439

Haimson, B.C. and Herick, C.G. (1989), Borehole Breakouts and In Situ Stress, *Proceedings, Energy Source Technology Conference*, Houston, Tx.

Hallbauer, D.K., Wagner, H. and Cook, N.G.W. (1973), Some Observations Concerning the Microscopic and Mechanical Behavior of Quartzite Specimens in Stiff, Triaxial Compression Tests, *Int. J. Rock Mechanics Min. Sci.*, 10. 713

Hertz, H. (1899), *Principles of Mechanics*, Macmillan, London

Hill, R. (1962), Acceleration Waves in Solids, *J. Mech. Phys. Solids*, 10, 1-16

Hill, R. and Hutchinson, J.W. (1975), Bifurcation Phenomena in the Plane Tensile Test, *J. Mech. Phys. Solids*, 23, 239-264

Hill, R., (1958), A General Theory of Uniqueness and Stability in Elastic-Plastic Solids, *J. Mech. Phys. Solids*, 6, 236-249

Howerton, M.T. (1962), *Engineering Thermodynamics*, D. Van Nostrand Company, Inc., Princeton, New Jersey

Hsu, T.T.C., Slate, F., Sturman, G.M. and Winter, G. (1963), Microcracking of Plain Concrete and the Shape of the Stress-Strain Curve, *Am. Conr. Inst. J.*, 60(2), 209-223

Hudson, J.A., Brown, E.T. and Fairhurst, C. (1971), Shape of Complete Stress-Strain Curve for Rock, *Proc. 13th Symposium, Rock Mechanics*, University of Illinois, Urbana

Hutchinson, J.W. and Tvergaard, V. (1980), Surface Instabilities on Statically Strained Plastic Solids, *Int. J. Mech. Sci.*, 22. 339-354

Jagannath, S.V., Desai, C.S. and Kundu, T. (1990), Correlation Between Mechanical and Ultrasonic Responses for Anisotropic Behavior of Soils, *Report to NSF*, Dept. of Civil Engr. and Engr. Mech., Univ. of Arizona, Tucson, Arizona

Jagannath, S.V., Desai, C.S. and Kundu, T. (1991), Measurements of Material Anisotropy by Ultrasonic Technique, *Proc. 5th Int. Conf. Soil Dynamics and Earthquake Engr.*, Karlshure, Germany

Johnston, D.H. and Toksoz, M.N. (1980), Ultrasonic P and S Wave Attenuation in Dry and Saturated Rocks under Pressure, *J. of Geophysical Research*, Vol. 85, No. B2, pp.925-936

Jones, R.L. (1952), A Method for Studing the Formation of Cracks in A Material Subjected to Stress, ***British J. Appl. Phys.***, 3, 7, 229-232

Kachanov, L.M. (1958), ***The Theory of Creep*** (A.J. Kennedy ed.), Chapter IX and X, National Lending Library, Boston, English Translation

Kemeny, J. and Tang, F.F. (1990), A Numerical Damage Model for Rock Based on Microcrack Growth, Interaction, and Coalescence, in: *Damage Mechanics in Engineering Materials* (Ju et al ed.), AMD-vol. 109, MD-vol. 24

Kitagawa, H. and Matsushita, H. (1987), Flow Localization in Elastic-Plastic Material Developing from Stress-Free Surface, *Int. J. Solids Structures*, 23, 3, 351-368

Kondaurov, V. I., Nikitin, L.V. and Ryzhakk E.I., (1989), Damage and Instability in Geomaterials, *Ingenieur-Archiv*, 59, 245-252

Krautkraumer, J. and Krautkramer, H. (1983), *Ultrasonic Testing of Materials*, Springer-Verlag Berlin Herdelberg, 3rd edition, New York

Kroner, E. (1967), Elasticity Theory of Materials with Long-Range Cohesive Forces, *Int. J. Solids Struct.*, No.3, 731-742

Krumhansl, J.A. (1968), Some Considerations of the Relations between Solid State Physics and Generalized Continuum Mechanics, In: *Mechanics of Generalized Continua* (Kroner, E. ed.), Springer-verlag, Berlin, 298-331

Lade, P.V. (1989), Experimental observations of stability, instability, and shear planes in granular materials, *Ingenieur-Archiv*, 59, 114-123

Langhaar, H. L. (1962), ***Energy Method in Applied Mechanics***, John Willey and Sons, Inc., New York

Loret, B. and Harireche, O. (1991), Acceleration Waves, Flutter Instabilities and Stationary Discontinuities in Inelastic Porous Media, *J. Mech. Phys. Solids*, vol. 39, No.5, 569-606

Macmillan, N.H. and Kelly, A. (1972), *Proc. Roy. Soc. London*, A330, 291

Mandel, J. (1966), Conditions de stabilite et postulat de Drucker, In: *Rheology and soil mechanics* (J.Kravtchenko and P.M. Sirieys eds), P58, Springer, Berlin

Marsden, J.E. and Hughes, T.J.R. (1983), ***Mathematical Foundations of Elasticity***, Prentice-Hall, Englewood Cliffs, New Jersey

Mason, W.P. (1958), ***Physical Acoustics and the Properties of Solids***, New-York: Von Nostrand

Maury, V. (1987), Observation, Researches and Recent Results about Failure Mechanisms around Single Galleries, *Proc. 6th Int. Congress Rock Mech.*, Vol. 2, 1119-1128, Montreal, Canada

Mindess, S. (1982), Acoustic Emission and Ultrasonic Pulse Velocity of Concrete, *Int. J. Cement Composites and Lightweight Concrete*, 4, 3, 173-179

Mindlin, R.C. (1964), Microstructure in linear elasticity, *Arch. Rat. Mech.*, 10, 51-78

Muhlhaus, H. -B. (1985), *Ingenieur Archiv.*, 55, 388

Muhlhaus, H. -B. (1986), *Ingenieur Archiv.*, 56, 389

Muhlhaus, H.-B. and Vardoulakis, I. (1987), The thickness of shear bands in granular materials, *Geotechnique*, 37, 271-238

Muhlhaus, H. -B and Aifantis, E.C. (1991), The influence of microstructure-induced gradients on the localization of deformation in viscoplastic materials. *Acta Mechanica*

Muhlhaus, H.-B. and Aifantis, E.C. (1991), A Variational Principle for Gradient Plasticity, *Int. J. Solids Structures*

Needleman, A. and Rice, J.R. (1978), *Mechanics of sheet Metal Forming*, D.P. Koistinen et al eds., 237

Needleman, A. (1979), Non-normality and bifurcation in plane strain tension and compression, *J. Mech. Phys. Solids*, 27, 231-254

Needleman, A. (1988), Rate Dependence and Mesh Sensitivity in Localization, *Comp. Meth. Appl. Mech. Engr.* 67, 69-85

Needleman, A. (1990), Continuum Mechanics Analysis of Plastic Flow Localization, *J. of the Mechanical Behavior of Metals*, 2, Nos 3-4, 293-313

Needleman, A. and Oritz, M. (1991), Effect of Boundaries and Interfaces on Shear-Band Localization, *Int. J. Solids Structures*, 28, No.7, 859-877

Papanastasiou, P.C. and Vardoulakis, I. (1991), Bifurcation Analysis of Deep Boreholes–II, Scale Effects, *Int. J. Numer. Analy. Meth. Geomechanics*

Petukhov, I.M. and Linkov, A.M. (1979), The Theory of Post-Failure Deformations and the Problem of Stability in Rock Mechanics, *Int. J. Rock Mech. Min. Sci. & Geomech. Abstr.*, 16, 57-76

Pijaudire-Cabot, G. and Bazant, Z.P. (1987), Nonlocal Damage Theory, *J. Engr. Mech. Div. ASCE*, 113, No. 10, 1512-1533

Rabier, P.J. (1989), Some Remarks on Damage Theory, *Int. J. Engr. Sci.*, 27, 29-54

Ramm, E. (1981), Strategies for Tracing the Nonlinear Response Near Limit Points. In: *Nonlinear Finite Element Analysis in Structural Mechanics* (Wunderlich, W., Stein, E. and Bathe, K.J. eds.), Springer, 63-69

Raniecki, B. and Bruhns, O. T. (1981), Bounds to bifurcation stresses in solids with non-associated plastic flow law at finite strain, *J. Mech. Phys. solids*, 29, 153

Read, H.E. Hegemier, G.A. (1984), Strain Softening of Rock, Soil and Concrete - A Review Article, *Mechanics of Materials*, 3, 271-294

Reinhardt, H.W. and Hordijk, D.A. (1988), Various Techniques for the Assessment of the Damage Zone between Two Saw Cuts, in: *Crack and Damage, Strain Localization and Size Effect* (J. Mazars and Z.P. Bazant eds.), Elsevier Applied Science, 3-14

Rheinboldt, W.C. (1981), Numerical Analysis of Continuation Methods for Nonlinear Structural Problems, *Comp. Struct.* 13, 103-113

Riks, E. (1972), The Application of Newton's Method to the Problem of Elastic Stability, *J. Appl. Mech.*, 39, 1060-1066

Riks, E. (1979), An Incremental Approach to the Solution of Snapping and Buckling Problems, *Int. J. Solids Struct.*, 15, 529-551

Rice, J.R. (1970), *J. Appl. Mech.*, 92, 728

Rice, J.R. (1975), On the Stability of Dilatant Hardening of Saturated Rock Masses, *J. Geophy. Res.*, 80, 1531

Rice, J.R. (1977), the Localization of Plastic Deformation, In: *Theoretical and Applied Mechanics* (W.T.Koiter ed.), 207-220, North-Holland, Amsterdam.

Roark, R.J. and Young, J.F. (1989), *Formulas for Stress and Strain*, 5th edition

Robotnov, Y.N. (1969), *Creep Problems in Structural Mechanics*, North-Holland, Amsterdam

Robinson, G.S. (1965), Methods of Detecting the Formation and Propagation of Microcracks in Concrete, *Proc. of the Int. Conf. on the Structure of Concrete, Cement and Concrete Association*, London

Rudnicki, J.W. and Rice, J.R. (1975), Conditions for the Localization of Deformation in Pressure-Sensitive Dilatant Materials, *J. Mech. Phys. Solids*, 23, 371-394

Rudnicki, J.W. (1983), *Proc. Symp. Mechanics of Rocks, soils and Ice*, S. Nemat-Nasser ed., P35, ASME-AMD Vol. 57, New York

Rudnicki, J.W. (1984), *J. Geophys. Res.*, 89, 9259

Salamon, M.D.G. (1970), Stability, Instability and Design of Pillar Workings, *Int. J. Rock Mech. Min Sci.*, 7, 613-631

Sammis, C.G. and Ashby, M.F. (1986), The Failure of Brittle Porous Solids Under Compressive Stress States, *Acta Metall.*, 34, 511-526

Shah, S.P. and Chandra, S. (1970), Mechanical Behavior of Concrete Examined by Ultrasonic Measurements, *J. of Materials*, JMLSA, 5, 3, 550-560

Spooner, D.C. and Dougill, J.W. (1975), A quantitative Assessment of Damage Sustained in Concrete during Compressive Loading, *Mag. Concrete Res.*, 27, 92, 151-160

Stein, E., Lammering, R. and Wagner, W. (1989), Stability Problems in Continuum Mechanics and Their Numerical Computation, *Ingenieur-Archiv*, 59, 89-105

Sturrup, V.R., Vechio, F.J. and Ceratin, H. (1984), Pulse Velocity as A Measure of Concrete Compressive Strength, *In Situ Nondestructive Testing of Concrete*, V.M. Malhotra ed., Detroit, ACI SP-82, 201-228

Tang, F.F., Desai, C.S. and Frantziskonis, G. (1991), Heterogeneity and Degradation in Brittle Materials, *Engineering Fracture Mechanics*, Submitted

Tang, F.F. (1992a), Surface Effects Identification through Strain Gage Tests in Brittle Materials, *J. Mechanical Behavior of Materials*, to be submitted

Tang, F.F. and Desai, C.S. (1992b), Instability and Localization in Geomaterials - An Overview Paper, under preparation

Thomas, T. Y. (1961), *Plastic Flow and Fracture in solids*, Academic Press, New York

Thompson, J. L. (1969), Some existence theorems for the transient boundary value problem of linearized ealstostatics, *Arch. Rat. Mech. Anal.*, 32, 369-399

Thompson, J.M.T. and Shorrock, P.A. (1975), Bifurcational Instability of an Atomic Lattice, *J. Mech. Phys. Solids*, 23, 21-37

Triantafyllidis, N. (1980), Bifurcation Phenomena in Pure Bending, *J. Mech. Phys. solids*, 28, 221-245

Triantaphyllidis, N. and Aifantis, E.C. (1986), A Gradient Approach to Localization of Deformation -I. Hyperelastic Materials, *J. Elasticity*, 16, 225-238

Valanis, K.C. (1985), On the Uniqueness of Solution of the Initial Value Problem in Strain Softening Materials, *J. Appl. Mech.*, Vol. 52, September

VanMier, J.G.M. (1984), Strain Softening of Concrete Under Multiaxial Loading Conditions, *Doctoral Dissertation*, Eindhoven Univ. of Techn., The Netherlands

Vardoulakis, I. (1979), *Acta Mech.*, 32, 35-54

Vardoulakis, I. (1981), Bifurcation Analysis of the Plane Rectilinear Deformation on Dry Sand Samples, *Int. J. Solids Structures*, 17, 1085-1101

Vardoulakis, I. (1984), Rock Bursting as a Surface Instability Phenomenon, *Int. J. Rock Mech. Min. Sci. & Geomech. Abstr.*, 21, 3, 134-144

Vardoulakis, I. (1986), *Int. J. Numer. Anal. Meth. Geomech.* 10, 177

Vardoulakis, I. (1989), Shear-banding and Liquefaction in Granular Materials on the Basis of a Cosserat theory, *Ingenieur-Archiv*, 59, 106-113

Vardoulakis, I. and Aifantis, E.C. (1989), Gradient dependent dilatancy and its implications in shear banding, *Ingenieur Archiv*, 59, 197-208

Vardoulakis, I. and Aifantis, E.C. (1991), A gradient flow theory of plasticity for granular materials, *Acta Mechanica*, 87-197-217

Vardoulakis, I. and Frantziskonis, G. (in press), Micro-Structure in Kinematic Hardening Plasticity, *Europ. J. of Mechanics, A-Solids*

Wagner, W. and Wriggers, P. (1988), A Simple Method for the Calculation of Postcritical Branches, *Engr. Comput.*, 5, 103-109

Warburton, P.M. (1991), A Finite Element Approach to Analysing Localization and Post-Critical Behaviour in Rock, in: *Computer Methods and Advances in Geomechanics* (Beer, Booker and Carter eds.), Balkema, Rotterdam, ISBN, 449-454

Waversik, W.R. and Brace, W.F. (1971), *Rock Mech.*, 3, 61-85

Willam, K.J., Pramono, E. and Sture, S. (1986), Stability and Uniqueness of Strain-Softening Computations, In: *Finite Element Methods for Nonlinear Problems* (Bergan, P.G., Bathe, K.J. & Wunderlich, W. eds.), 119-142, Berlin: Springer-Verlag

Woo, L. and Desai, C.S. (1991), Dynamic Analysis for Nonlinear Materials Including Strain - Softening, *Report to NSF*, Dept. of Civil Engr. and Engr. Mech., Univ. of Arizona, Tucson, Arizona

Wriggers, P., Wagner, W. and Miche, C. (1988), A Quadratically Convergent Procedure for the Calculation of Stability Points in Finite Element Analysis, *Compt. Methods Appl. Mech. Engr.*, 70, 329-347

Wriggers, P. and Simo, J.C. (1990), A General Procedure for the Direct Computation of Turning and Bifuracation Points, *Int. J. Num. Methods in Engr.*, 30, 155-176

Yamaguchi, E. and Chen, W.F. (1991), Microcrack Propagation Study of Concrete Under Compression, *J. Engr. Mech. Div. ASCE*, 117, no.3, 653-673

Yuan, X., Tang, F.F. and Frantziskonis, G. (1992), Random Initial Heterogeneity in Brittle Materials, *Proc. ASCE Speciality Conf.*, Texas A&M Univ.

Yuan, X. (1991), Random Initial Inhomogeneity in Brittle Material Structures, *M.S. Thesis*, Dept. of Civil Engr. and Engr. Mech., Univ. of Arizona, Tucson, Arizona

Yukutake, H. (1989), Fracturing Process of Granite Inferred From Measurements of Spatial Velocities and Temporal Variations in Velocity During Triaxial Deformations, *J. of Geophysical Res.*, 94, 15639-15651

Zbib, H. and Aifantis, E.C. (1988), On the localization and post-localization of plastic deformation, *Res Mechanics*, 23, 261-305 (Special Issue on Material Instabilities, Aifantis, E.C. et al eds.)

Zubelewicz, A. and Mroz, Z. (1983), Numerical Simulation of Rock Burst Processes Treated as Problems of Dynamic Instability, *Rock Mechanics*, 16, 253-274

APPENDIX

ADDITIONAL RELATED PUBLICATIONS

1. G. Frantziskonis and C.S. Desai, 'Degradation Instabilities in Brittle Material Structures,' Mechs. Resear. Commun., 17, 135-141, 1990.
2. G. Frantziskonis and C.S. Desai, 'Surface Degradation Mechanisms in Brittle Material Structural Systems,' Int. J. Fracture, 48, 231-244, 1991.
3. G. Frantziskonis, F.F. Tang and C.S. Desai, 'Borehole Scale Effects and Related Instabilities,' Engr. Fracture Mechs., 39, 377-389, 1991.
4. G. Frantziskonis and I. Vardoulakis, 'On the Micro-Structure of Surface Effects and Related Instabilities,' Europ. J. Mechs., 11, 21-34, 1992.
5. I. Vardoulakis and G. Frantziskonis (1991), 'Micro-Structure in Kinematic-Hardening Plasticity,' Europ. J. Mechs., to appear.
6. G. Frantziskonis, 'Surface Effects In Brittle Materials and Internal Length Estimation,' Appl. Mech. Rev., to appear.
7. G. Frantziskonis, 'Heterogeneity, Microstructural Surface Effects and Internal Length Estimation, Proc. ASCE Specialty Conference, 1992, to appear (also to be submitted to refereed Journal).

MECHANICS RESEARCH COMMUNICATIONS Vol. 17 (3), 135-141, 1990 Printed in the USA
0093-6413/90 $3.00 + .00 Pergamon Press plc

DEGRADATION INSTABILITIES IN BRITTLE MATERIAL STRUCTURES

G. Frantziskonis and C.S. Desai
Department of Civil Engineering and Engineering Mechanics
University of Arizona, Tucson, Arizona 85721

(Received 18 August 1989; accepted for print 11 January 1990)

Introduction

Experimental and theoretical information on degradation mechanisms of brittle material structures is reviewed first. It is concluded that although a considerable amount of research on the subject of damage and, to a much less extent, on surface degradation has been performed in recent years, the related stability problems have not been studied adequately.

The analytical solution of the energy based stability problem shows that surface degradation instability and/or damage progression instability occurs before the peak strength is reached. Thus a homogeneous post-peak state is impossible, since basic energy relations are violated.

Damage and surface degradation are closely related to the well known size and shape effects of brittle materials. It is shown that surface degradation is important for both size and shape dependent properties of such materials. The theoretical developments are compared to the observed behavior of an artificial rock.

1. Background and Review

In constitutive modeling research the material is commonly thought of as a continuum without any cracks or discontinuities. However, in recent years it is realized that a slightly damaged material does not necessarily mean the end of its life, and it is important to understand the behavior of materials containing acceptable levels of damage in it in order to predict its remaining strength. In the light of the information known on the subject of damage growth, a Griffith crack characterization of damage is far from reality. The need for a realistic description of damage guides to the development of a theory that contains the essential features of the known damage mechanisms. Such analytical models have only recently been developed. A great majority of the literature considers uniaxial stress conditions. Damage is so defined that the effect of a developed microcrack network is taken into account. A number of investigators have considered the effects of damage in their models directly or indirectly, a review on this subject can be found in [1,2]

It is interesting to note that the model including damage proposed in [1-8] has been investigated successfully with respect to different materials such as concrete and composites. The material constants have been identified and the proposed theory has been validated through comparison with experimental data. Only slight modifications in the model, while transferring from one material to another, are necessary for the rational description of the above materials. The fact that the constitutive equations can be used, with minor modifications, for apparently different looking materials is being examined towards unification of material modeling for engineering applications. This damage based approach is a branch of a general hierarchical approach to constitutive modeling of engineering materials introduced in [8]. Also, as far as decomposition of material behavior is concerned, we note the model proposed in [9].

2. Damage Development

Let us consider a small volume ΔV of the material. This volume is subdivided into an intact (undamaged) part ΔV_u and into a "fractured" (damaged) part ΔV_d. The first part or fraction represents topical (continuum) behavior and the material in it is intact in the sense that no microcracks exist. Due to the inhomogeneity of the material behavior at the microlevel, weak planes can develop leading to formation and subsequent propagation of micro-cracks. The laws that govern the above structural changes are not fully understood. The effect of an isolated or coupled fracture site is that an influence zone exists around it. This influence zone is of volume ΔV_d. Under continued loading, influence zones increase so that ΔV_d increases. At every instant of time we define the ratio

$$r = \frac{\Delta V_d}{\Delta V} \tag{2.1}$$

called the volume damage ratio. The material point of the two fractions material consists of the superposition of a material point of the undamaged fraction, herein called the u-part, and of a material point of the damaged fraction, herein called the d-part.

The above suggests the use of the theory of mixtures, or theory of interacting continua. As a consequence the following relation is applicable [1-4]

$$\sigma_{ij} = (1 - r)\sigma^u_{ij} + r\sigma^d_{ij} \tag{2.2}$$

where σ^u_{ij}, σ^d_{ij} denote the stress tensors in the u and d-part of the material element respectively and σ_{ij} is the average stress tensor. The general theory of mixtures, [10,11] is simplified considerably if diffusion is absent. In the proposed theory there is no diffusion between the components thus the strains in the two material fractions are considered equal [11].

We now consider a material element. Due to the enforced deformation in the element, damage influence zones have been created but failure has not occurred yet. Such influence zones depict the mechanical influence of a system of microcracks. The constitutive equations for the d-part can be established as [4,6]

$$\sigma^d_{ij} = C^d_{ijkl}\,\epsilon_{kl} \tag{2.3}$$

and C^d_{ijkl} is a function of parameters related to the degrading properties of the material. Since there are no microcracks in the u-part, its constitutive relations can be identified as

$$\sigma^u_{ij} = C^u_{ijkl}\,\epsilon_{kl} \tag{2.4}$$

if the undamaged fraction is linearly elastic (i.e. for composites) C^u_{ijkl} contains the usual linear elasticity constants. If plasticity effects are included then a generalized elastic-plastic model can employed and the above relations are written in rate form.

The irreversible nature of damage implies that the material experiencing it obeys non-holonomic laws. Thus the problem is formulated in rate form of the governing equations and the constitutive relations are established as

$$\dot{\sigma}_{ij} = L_{ijkl}\,\dot{\epsilon}_{kl} - \dot{r}(\sigma^u_{ij} - \sigma^d_{ij}) \tag{2.5}$$

where

$$L_{ijkl} = (1 - r)\,C^u_{ijkl} + rC^d_{ijkl} \tag{2.6}$$

Further an evolution law for $\dot{r}$ is defined and it is directly related to failure. A simple and general law can be written as

$$\dot{r} = f(\epsilon_{ij})\dot{\epsilon}_{ij} \tag{2.7}$$

Based on the physical interpretation of damage and failure criteria the function f can be specified [1,2,4,6].

NOTE: *The damage formulation briefly described above has been examined with respect to its basis on principles of mechanics and physics as well as with respect to its capability to predict the experimentally observed response. Properties such as degradation, induced anisotropy, elastic properties degradation are attributed to damage development. The damage related constants have been identified for different brittle materials such as a concrete. Also, the constants have been evaluated for different composite materials such as graphite-epoxy and boron-epoxy. Test data have been back-predicted (simple ones analytically and more complicated ones numerically). The predictive capability of the theory has proven to be surprisingly good, especially for the material behavior highly deviating from the linear elastic one. Such comparisons can be found in references [1-8].*

Surface Degradation

It has been observed that in many engineering materials (metals, brittle materials, geomaterials, etc.) surface unevenness (roughness) grows with increase in strain, e.g. [12]. Surface roughness is induced by microstructural inhomogeneity and its growth is initially stable. It is important to mention that there is certain evidence that this phenomenon acts as a trigger effect on shear bands appearing in a specimen. The sudden growth of surface roughness results in the occurrence and development of shear band penetrating into the body [12]. Microscopically a heterogeneous structure of the material produces an inhomogeneous deformation field from a very early straining stage. However, irregularity of deformation in the body is not uniform, but there is a part in

which the irregularity is greater than that in other ones, that is, near the surface.

The above observations are also evident in existing extensive experiments on brittle materials, where the following have been identified: as loading increases, e.g. in a uniaxial compression test, the density of microcracks rapidly proliferates, leading to vertically aligned macrocracks which result in gross slabbing of material from the specimens (lateral) surfaces [13,14]. In general, the axial cracks are concentrated in the central portions of the specimen length because lateral restraint caused by friction at the specimen ends inhibits their growth near the specimen-platen interface.

Damage distribution at the edge of a body (specimen) where surface degradation is of importance, and is expected to be significantly different from the damage distribution far from the edge. Here we consider that damage at the edge due to surface effects is additive to the damage accumulation due to deformations far from the surface. So at the edges a small volume, ΔV_r is subdivided into an intact part ΔV_{ri} and into a fractured part ΔV_{rd}. We consider that the above subdivision holds for a distance ρ from the edge, where ρ is a positive real number dependent on the material properties, the geometry and the load on the structure. At an instant of time the edge damage concentration volume ratio is defined as

$$r_e = \frac{\Delta V_{rd}}{\Delta V} \tag{2.8}$$

Here r_e is expected to be maximum at the edge and its value decreases continuously till a minimum value expected to be at a distance ρ from the edge. When $r_e = 1$ holds then complete surface degradation is observed in the sense that material has no strength. Let us consider the following volume average, per unit area in the plane parallel to the stress-free surface.

$$\hat{r} = \frac{1}{\rho} \int_0^{\rho} r_e \, dA \tag{2.9}$$

Also the following average stress can be introduced

$$\hat{\sigma}_{ij} = \frac{1}{\rho} \int_0^{\rho} \sigma_{ij} \, dA \tag{2.10}$$

Based on physical reasoning, it is possible to establish a connection between the average values of damage and stress as defined above and the dimension related parameter ρ. As mentioned in [15] equilibrium transverse to the surface as well as moment equilibrium are to be used in establishing the relation between $\hat{\sigma}_{ij}$ and $\hat{r}$. A the effective surface degradation volume total damage ratio is defined as

$$r_t = r + \hat{r} \tag{2.11}$$

Note that r_t can be grater than r_{cr} since $0 \le r \le r_{cr}$. Here r_{cr} is the value of damage variable r at failure. So, in general

$$0 \le r_t \le r_{cr} + 1 \tag{2.12}$$

NOTE: It has been predicted theoretically that in a body with stress free surfaces, an inhomogeneous deformation with relatively short wavelength is possible near the surfaces at (high) strained

states, which is known as the surface instability phenomenon, [16]. Surface unevenness and degradation as described in this paper may be related to surface instability at its initiation. However, the approach herein is different than surface instability in the sense that progressive degradation is also accounted for.

3. Instability Conditions

Consider a body occupying region R. The rate of work of the external forces acting on a material element of volume ΔV, denoted by $\dot{E}$, is

$$\dot{E} = \frac{1}{\Delta V}\int_{\Delta V} \sigma_{ij}\,\dot{\epsilon}_{ij}\,dV \tag{3.1}$$

Part of this work will be stored as elastic energy in the u-part and part as elastic energy in the d-part

$$\dot{E} = \dot{E}^{R} + \dot{Q} + \dot{S} \tag{3.2}$$

where

$$\dot{E}^{R} = \int_{\Delta V_u} \sigma^{u}_{ij}\,\dot{\epsilon}_{ij}\,dV + \int_{\Delta V_d} \sigma^{d}_{ij}\,\dot{\epsilon}_{ij}\,dV \tag{3.3}$$

and Q, S are the dissipated energy due to damage growth and surface degradation growth respectively. Conditions for unstable damage, surface degradation growth are established as [7]

$$-\frac{\partial^2\Pi}{\partial(V_d)^2} - \frac{\partial^2 D}{\partial(V_d)^2} - \frac{\partial^2 Q}{\partial(V_d)^2} - \frac{\partial^2 S}{\partial(V_d)^2} > 0 \tag{3.4}$$

$$-\frac{\partial^2\Pi}{\partial(V_r)^2} - \frac{\partial^2 D}{\partial(V_r)^2} - \frac{\partial^2 Q}{\partial(V_r)^2} - \frac{\partial^2 S}{\partial(V_r)^2} > 0 \tag{3.5}$$

where Π is the total potential energy and D is the dissipated energy due to plastic deformations. When (3.4) is satisfied first unstable damage growth occurs resulting to the catastrophic failure of the structure. When (3.5) is satisfied surface degradation instability takes place. The physical interpretation of such an instability is that bursting growth close to the surface becomes unstable resulting in spalling of material elements.

4. Analytical Solution of a Simple Problem

For simple problems it is possible to examine the above instability conditions analytically. Irrespective of which of Eqns. (3.4) or (3.5) will be satisfied first, the following conclusions can be made. Brittle materials subjected to uniaxial load show a decrease in strength after a peak load has been reached. It is interesting to examine under what conditions stability at the peak strength is possible. First we examine the case where the two material fractions are assumed linear and elastic. Then the condition for stable behavior at the peak is derived as

$$3\mu_u(1+2\nu^2)a - \frac{3}{2}\lambda_u\left[\frac{1}{\nu}-2\nu-1\right]a^2 + \frac{8\mu_u^2}{\lambda_u}\rho \ldots \tag{4.1}$$

where

$$a = \frac{E_u - E_d}{(1-\nu)E_u + r\,E_d} \tag{4.2}$$

E_u, μ_u, λ_u (E_d, μ_d, λ_d) are the Young modulus and Lame constants for the u-part (for the d-part) and ν is the apparent Poisson ratio for the two material fractions. Analysis of the above equation shows that in order to have stability at the peak, the value of r at that point must be close to unity which is physically unacceptable. Even if such a value of r was acceptable, it would be reached at high value of strains where the material reaches a residual state of stress far beyond the peak. Although this stability analysis is based on the condition that no plastic deformations are present, note that at the peak the plastic energy dissipation curve is convex thus $\frac{\partial^2 D}{(\partial V_d)^2} < 0$. Then as can be seen from relations (3.4) and (3.5) plastic deformation promotes instability. Thus a homogeneous post peak state is impossible since basic energy based stability conditions are violated. If surface degradation instability occurs first, this may not necessarily imply the overall failure of the structure. However, initiation of such an instability dictates the onset of non-uniform deformation close to the surface.

5. Connection to Scale (Size) and Shape Effects

It is well known that the deformational characteristics of brittle materials depend on the size as well as on the shape of a structure (specimen). In a specimen subjected to uniaxial stress, when the ratio of height to width (diameter for cylindrical specimens) of the sample is increased the level of (macroscopic) stress at unstable failure decreases [11,15]. Also for constant width (diameter) and increasing height, peak strength decreases, while for constant height and increasing width, peak strength increases. In the proposed theory the so-called effective surface degradation volume is introduced. For high ratios of height to width this volume occupies a large percentage of the sample volume. On the other hand, for low ratio of height to width the effective surface degradation volume is small as compared to the whole volume of the specimen. As expected when height to width ratio increases, surface degradation becomes the predominant damage mode resulting to an instability at a low stress level. As height to width ratio decreases, the effect of surface degradation decreases and damage growth becomes the predominant instability mode. Distance ρ introduced previously is now defined as

$$\rho = \alpha\left[\int_c W\,dS - l\right] \tag{5.1}$$

where W is a weighting function (W=unity provides satisfactory results), l is the so-called surface degradation length, c is the path of maximum principal compressive stress and α is a constant.

Note that l is a new definition of the material characteristic length; it is defined as that specimen size so that the whole structure is in the surface degradation zone. For a cylindrical specimen of length L and diameter D subjected to uniaxial compression we have

$$\rho = \alpha(L - l) \tag{5.2}$$

where α is constant. The stress at peak is given as

$$\sigma = C_1 + \frac{C_2((L-l)^3)}{D^3} - \frac{8\alpha C_1(L-l)}{D} \tag{5.3}$$

Constants C_1, C_2 and α have been determined from a series of tests on artificial rock [18] and it is verified that the theory (expressed through Eqn. 5.3 for the uniaxial load case) is capable in predicting the size as well as the shape effect of brittle material specimens satisfactorily.

Acknowledgments

A part of the research herein was supported by Grant No. AFOSR 890460 from the Air Force Office of Scientific Research, Bolling AFB.

References

1. Frantziskonis, G., Doctoral Dissertation, Dept. of Civil Engg. and Engg. Mechanics University of Arizona, Tucson (1986).
2. Frantziskonis, G. and Desai, C.S., Int. J. Solids Structures. 23, 733 (1987).
3. Frantziskonis, G. and Desai, C.S., Int. J. Solids Structures, 23, 751 (1987).
4. Frantziskonis, G. and Desai, C.S., Acta Mechanica, 68, 151 (1987).
5. Frantziskonis, G., Comp. Structures, Intl. J., 10, 165 (1988).
6. Frantziskonis, G., Solid Mechs. Archives, 13, 129 (1989).
7. Frantziskonis, G., Acta Mechanica, 77, 213 (1989).
8. Desai, C.S., Somasundaram, S. and Frantziskonis, G., Int. J. Numer. Analyt. Methods in Geomechanics, 10, 225 (1986).
9. Desai, C.S., Proc. Int. Conf. on Comp. Methods in Nonlinear Mech., Univ. of Texas, (1974).
10. Bowen, R.M., "Theory of Mixtures," in: Continuum Physics (Eringen, A. C. ed.) 3, 1, New York: Academic Press, (1975).
11. Bowen, R.M., J. Chem. Phys., 50, 4601 (1969).
12. Kitagawa, H. and Matsushita, H., Intl. J. Solids Struct., 23, 351 (1987).
13. Hudson, J.A., Brown, E.T. and Fairhurst, C., Proc. 13th Symp. Rock Mechanics, University of Illinois, Urbana, (1971).
14. Fairhurst, C. and Cook, N.G.W., Proc. First Intl. Congress Rock Mechanics, Lisbon, 1, 687 (1966).
15. G. Frantziskonis, Report CEEM-88-108, University of Arizona (1988).
16. Biot, M.A., Mechanics of Incremental Deformations, Wiley, New York (1965).
17. Ewy, R.T., Cook, N.G.W., and Myer, L.R., Key Questions in Rock Mechanics, Cundall et al (Eds.) Balkemma, Rotterdam, (1988).
18. Desai, C.S., Kundu, T. and Wang, G., Proc. ASME Technol. Conf., Houston, Texas, (1989).

International Journal of Fracture 48: 231–244, 1991.

Surface degradation mechanisms in brittle material structural systems

G. FRANTZISKONIS and C.S. DESAI
Department of Civil Engineering and Engineering Mechanics, University of Arizona, Tucson, Arizona 85721, USA

Received 15 September 1989; accepted in revised form 16 March 1990

Abstract. A mechanics based theory for surface degradation in brittle material systems is introduced. Surface degradation is directly related to damage progression. For this reason the mechanics of damage evolution is presented first. Subsequently, relations governing surface degradation mechanisms are derived and discussed in detail. It is shown that surface degradation can capture important properties of brittle materials such as scale (size) and shape effects, surface damage growth and subsequent bursting instabilities. Finally, the problem of transferring information from laboratory experiments to large scale problems is discussed; the need for further experimental and theoretical research is pointed out.

1.0. Introduction

In many engineering problems such as underground openings, rock strata tend to move suddenly into the opening. Catastrophic events of this kind are called rock bursts and are the result of rock fracturing by spalling. Much of the research in brittle material (i.e., rock, concrete) mechanics has been concerned with the progressive failure of laboratory specimens under external loads. It is theorized that such failure is analogous to large scale problems such as the stability of wall rock in underground openings. The problem is to carefully simulate and observe the deformation, fracture, and unstable collapse of larger scale (as compared to laboratory specimen size) problems. For such problems related to fracturing and stability close to boundaries, much information can be collected from laboratory experiments i.e. uniaxial compression tests.

For decades, laboratory tests on brittle materials (rock, concrete) sought to achieve a homogeneous state of stress and deformation on a sample subjected to uniaxial load. However, even under ideal testing conditions, the heterogeneous micro-structure of the material produces an inhomogeneous deformation field from the early straining stage, Fairhurst and Cook [1], Hudson et al. [2], Read and Hegemier [3]. In a uniaxial compression test, the density of microcracks rapidly proliferates leading to vertically aligned microcracks resulting in gross slabbing of material from the tractionless surfaces. However, irregularity of deformation in the specimen is not uniform, but there is a part in which the irregularity is greater than in other ones, that is near the tractionless surface. In general, the axial cracks are concentrated in the central portions of the specimen's length because lateral restraint due to friction at the specimen ends inhibits their growth near the specimen-platen interface.

Based on Griffith type crack analysis, buckling failure of an elastic, anisotropic half-space containing co-planar cracks at arbitrary locations and subjected to horizontal compression has been studied recently, Vardoulakis and Papamichos [4]. From this study, the following

important conclusions are made: (a) the critical buckling stress decreases dramatically as the distance between the free surface and the cracks diminishes; (b) the influence of cracks far from the surface has very little or no influence on the buckling stress. This analysis suggests that a surface layer exists for which the presence of cracks has significant influence on the buckling stress. In a gross sense, this layer is the spalling part of the specimen as observed in uniaxial compression tests of brittle materials.

It has been predicted theoretically that in a body with stress free surfaces, an inhomogeneous deformation with relatively short wavelength is possible near the surfaces at (high) strained states, which is known as the surface instability phenomenon, Biot [5], Hill and Hutchinson [6], Vardoulakis [7]. Surface unevenness and degradation as described in this paper may be related to surface instability at its initiation. However, the approach herein is different than surface instability since progressive degradation is accounted for in this paper. Kitagawa and Matsushita [8] reviewed the experimental and theoretical information on such surface effects, herein termed surface degradation. It is concluded that surface roughness is induced by material inhomogeneity at the micro-level and its growth is initially stable. As surface unevenness grows localization develops and it is initiated from the free-surface.

In the following, a theory that accounts for surface degradation mechanisms is presented. The close relation between damage development and surface degradation necessitates a brief description of the damage theory presented in [9–12]. Subsequently, the relation between surface degradation and the well known size and shape effects of brittle materials is emphasized and discussed. Furthermore, the relation between laboratory experiments and catastrophic events of larger scale problems is discussed; the need for further experimental and theoretical research is pointed out. Finally, energy based stability criteria relevant to surface bursting and overall failure of a body are developed and discussed.

2.0. Damage and surface degradation

2.1. Damage development

Analytical models for the influence of microcrack initiation and growth on the constitutive behavior of brittle materials have only recently been studied. A great majority of the literature considers uniaxial stress conditions. Damage is so defined that the effect of the induced microcrack network is taken into account. A number of investigators have considered the effects of damage in their models directly or indirectly, a review on this subject can be found in [9], and the references cited there. Note that the model including damage proposed in [9–12] has been investigated successfully with respect to different materials such as concrete and composites. The material constants have been identified and the proposed theory has been validated through comparison with experimental data. Only minor modifications in the model are necessary for the rational description of different materials. The fact that the constitutive equations can be used, with minor modifications, for apparently different looking materials is now being examined towards unification of material modeling for engineering applications. Also, properties such as degradation, induced anisotropy, elastic properties degradation are attributed to damage development.

2.1.1. Formulation

Let us consider a small volume ΔV of the material. This volume is subdivided into an intact (undamaged) part ΔV_u and into a "fractured" (damaged) part ΔV_d (Fig. 1). The first part or fraction represents topical (continuum) behavior, and the material in it is intact in the sense that no microcracks are contained. Due to inhomogeneity of the material behavior at the microlevel, weak planes are developed leading to crack formation and subsequent propagation. The laws that govern the above structural changes are not fully understood. The effect of an isolated or coupled fracture site is that an influence zone exists around it as shown schematically in Fig. 1. This influence zone has volume ΔV_d. Under continued loading, influence zones increase so that ΔV_d increases. At every instant of time, we define the ratio

$$r = \frac{\Delta V_d}{\Delta V}, \tag{1}$$

called the volume damage ratio. The material point consists of the superposition of a material point of the undamaged fraction, herein called the u-part, and of a material point of the damaged fraction, herein called the d-part. This suggests the use of the theory of mixtures, or theory of interacting continua, Bowen [13]. As a consequence, the following relation is applicable:

$$\sigma_{ij} = (1 - r)\sigma^u_{ij} + r\sigma^d_{ij}, \tag{2}$$

where σ^u_{ij}, σ^d_{ij} denote the stress tensors in the u and d-part of the material element respectively and σ_{ij} is the average (measured) stress tensor. The general theory of mixtures, [13, 14] is simplified considerably if diffusion is absent. In the proposed theory, there is no diffusion between the components thus the strains in the two material fractions are considered equal [14].

We now consider a material element. Due to the enforced deformation in the element, damage influence zones have been created but failure has not yet occurred. Such influence zones depict the mechanical influence of a system of microcracks. The constitutive equations for the d-part can be estabilshed as [10, 12]

$$\sigma^d_{ij} = C^d_{ijkl}\varepsilon_{kl} \tag{3}$$

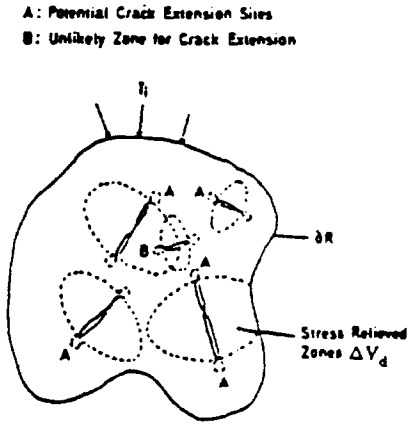

Fig. 1. Schematic of damage influence zones

and C^d_{ijkl} is a function of parameters related to the degraded properties of the material. Since there are no microcracks in the u-part, its constitutive relations can be identified as

$$\sigma^u_{ij} = C^u_{ijkl}\varepsilon_{kl}. \tag{4}$$

If the undamaged fraction is linearly elastic (e.g., for composites), C^u_{ijkl} contains the usual linear elasticity constants. If plasticity effects are included then a generalized elastic-plastic model is employed, Desai et al. [15], and (3) and (4) are expressed in rate form.

The irreversible nature of damage implies that the material experiencing it obeys non-holonomic laws. Thus the problem is formulated in rate form of the governing equations and the constitutive relations are established as

$$\dot{\sigma}_{ij} = L_{ijkl}\dot{\varepsilon}_{kl} - \dot{r}(\sigma^u_{ij} - \sigma^d_{ij}), \tag{5}$$

where

$$L_{ijkl} = (1 - r)C^u_{ijkl} + rC^d_{ijkl}. \tag{6}$$

From (5) it can be seen [12] that although r, $\dot{r}$ are scalars, a tensor namely, $\dot{r}(\sigma^u_{ij} - \sigma^d_{ij})$, is introduced in the formulation. This tensor is responsible for damage induced anisotropy, an obvious property of cracked materials. Further, an evolution law for $\dot{r}$ is defined and it is directly related to failure where r reaches a critical value r_{cr}. A simple law can be written as

$$\dot{r} = f(\varepsilon_{ij})\dot{\varepsilon}_{ij}. \tag{7}$$

Based on the physical interpretation of damage and failure criteria the function f can be specified [9–12]. However for the purposes of this paper specific expression for f need not be specified.

2.2. Surface degradation

As mentioned in the introduction, surface degradation is induced by microstructural inhomogeneity and its growth is initially stable. It is important to mention that there is certain evidence that this phenomenon acts as a trigger effect on the shear band appearing in a specimen. The sudden growth of surface degradation results in the occurrence and developement of shear bands penetrating into the body [8].

The damage distribution, at the edge of a body where surface degradation is of importance, is expected to be significantly different from the damage distribution far from the edge (in the body). Here we consider that damage at the edge due to surface effects is additive to the damage accumulation calculated as if no surface effects were present. So at the edges, a small volume ΔV_e is subdivided into an intact part ΔV_{eu} and into a fractured part ΔV_{ed}. We consider that the above subdivision holds for a distance ρ from the edge, ρ being a positive real number dependent on the material properties, the geometry, and load acting on the body. At every instant of time, the edge damage concentration volume ratio is defined as

$$r_e = \frac{\Delta V_{ed}}{\Delta V}. \tag{8}$$

Here r_e is expected to be maximum at the edge and its value decreases continuously till a minimum value expected to be at a critical distance ρ from the edge. Let us consider the following volume average, for unit area on the plane parallel to the edge:

$$\hat{r} = \frac{1}{\rho}\int_{\rho} r_e \, dA. \tag{9}$$

Also the following stress average can be introduced:

$$\hat{\sigma}_{ij} = \frac{1}{\rho}\int_{\rho} \sigma_{ij} \, dA. \tag{10}$$

Similarly, average partial stresses $\hat{\sigma}^{\mu}_{ij}$, $\hat{\sigma}^{d}_{ij}$ and strains $\hat{\varepsilon}_{ij}$ can be introduced. Since the constitutive equations (3, 4) are linear or incrementally linear, we can write equations similar to (5) and (6) for the average $(\hat{.})$ quantities. At the effective surface degradation volume the total damage ratio is defined as

$$r_t = r + \hat{r}. \tag{11}$$

Note that r_t can be greater than r_{cr} since $0 \leqslant r \leqslant r_{cr}$. So, in general

$$0 \leqslant r_t \leqslant r_{cr} + 1. \tag{12}$$

In general

$$\hat{r} = g(\varepsilon) r, \tag{13}$$

where $g(\varepsilon)$ is the surface degradation amplification function. For the purposes of this paper g need not be specified.

2.2.1. Surface degradation, size and shape effects

It is well known that the deformational characteristics of brittle materials depend on the size of a structure (specimen). In a specimen subjected to uniaxial stress, when the ratio of height to width (diameter for cylindrical specimens) of the sample is increased, the level of (macroscopic) stress at unstable failure decreases, Hudson et al. [2], Desai et al. [16].

In the proposed theory the so-called effective surface degradation volume is introduced. For high ratios of height to width this volume occupies a large percentage of the sample volume. On the other hand, for low ratio of height to width, the effective surface degradation volume is small as compared to the whole volume of the specimen. It is expected that as height to width ratio increases surface degradation becomes the predominant damage mode resulting in an instability at a low stress level. As the height to width ratio decreases, the effect of surface degradation decreases and damage growth becomes the predominant instability mode.

In order to study the effect of stress path on the scale effect the thick wall cylinder tests seem appropriate. Haimson and Herick [17] studied the behaviour of samples with different central hole sizes subjected to external stress (Fig. 2). It was found that small diameter holes

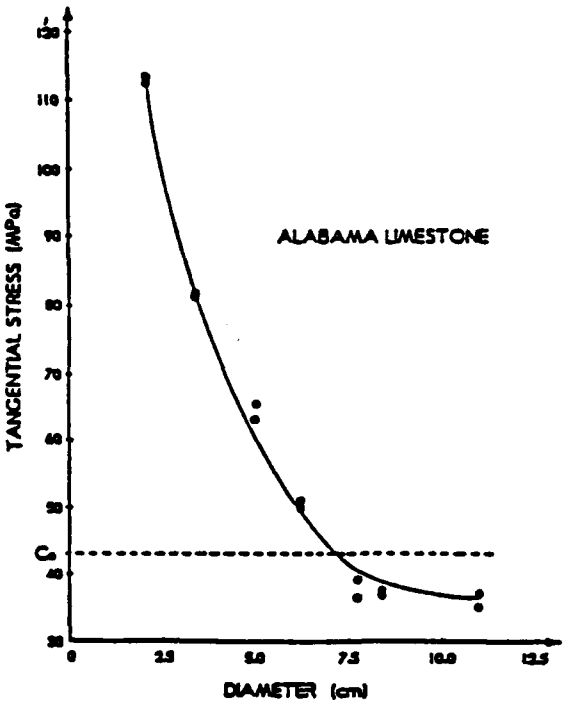

Fig. 2. Relation between hole diameter and hole-wall tangential stress required for breakout initiation in hollow cylinder tests. After [17].

required larger stresses to induce breakouts, as depicted in Fig. 9 in that paper. In the proposed theory, similarly to the problem of different height/width ratio specimens, for small diameter holes the overall effective surface degradation volume is a small percentage of the total volume. Then the effect of surface degradation is reduced for such a case. As the hole size increases surface degradation becomes important. From the above discussion it seems that the proposed theory is capable of capturing the essential features of the scale (size) effects.

Distance ρ introduced previously is defined as

$$\rho = a\left(\int_c W ds - l\right), \tag{14}$$

where W is a weighing function, α is a material constant, l is the so-called surface degradation material length and c is the path of maximum (absolute) principal compressive stress. Material related constant l defines a new characteristic length. It is defined as that specimen size so that the whole specimen is in the surface degradation zone. The simplest case calls for W = unity and as shown subsequently even this provides satisfactory results.

Consider a cylindrical specimen of length L and diameter D subjected to compressive load P, Fig. 3. The load acts parallel to length L and the cylindrical surface is load free. Let σ_{11}, be the uniform stress in the core of the sample and $\hat{\sigma}_{11}$ the average stress (Eqn. 10) in the

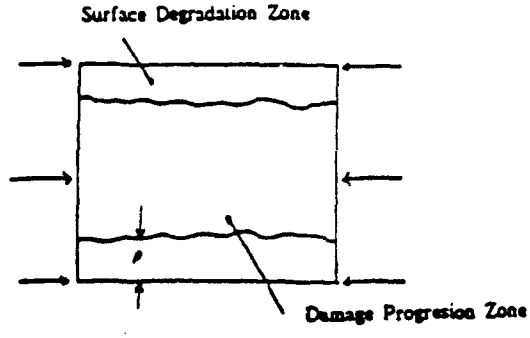

Fig. 3. A uniaxialy loaded cylindrical specimen and surface degradation zones.

surface degradation zone. Then

$$P = \frac{\pi}{4}(D - 2\rho)^2\sigma_{11} + \frac{\pi}{4}[D^2 - (D - 2\rho)^2]\hat{\sigma}_{11}. \tag{15}$$

We consider the simplest possible constitutive equations for the u and d-parts expressed in (3) and (4). Thus we consider C^u_{ijkl} and C^d_{ijkl} to be elastic constitutive tensors. Then, considering the strains in the core and in the surface degradation zone to be equal

$$\sigma_{11} = (1 - r)E^u\varepsilon_{11} + rE^d\varepsilon_{11}, \tag{16}$$

$$\hat{\sigma}_{11} = (1 - \hat{r})E^u\varepsilon_{11} + \hat{r}E^d\varepsilon_{11}, \tag{17}$$

where E^u, E^d are Young's moduli for the u-part and for the d-part, respectively. From (15–17) we obtain

$$P = a_1D^2 + a_2\rho^2 - a_2\rho D, \tag{18}$$

where

$$a_1 = \frac{\pi}{4}[E^u - r(E^u - E^d)]\varepsilon_{11}, \tag{19}$$

$$a_2 = \pi(\hat{r} - r)(E^u - E^d)\varepsilon_{11}. \tag{20}$$

For the uniaxial case, with $W = 1$

$$\rho = \alpha(L - l) \leqslant D/2. \tag{21}$$

From (15) and (21) we obtain

$$\sigma = c_1 + c_2\frac{(L - l)^2}{D^2} - c_3\frac{L - l}{D}. \tag{22}$$

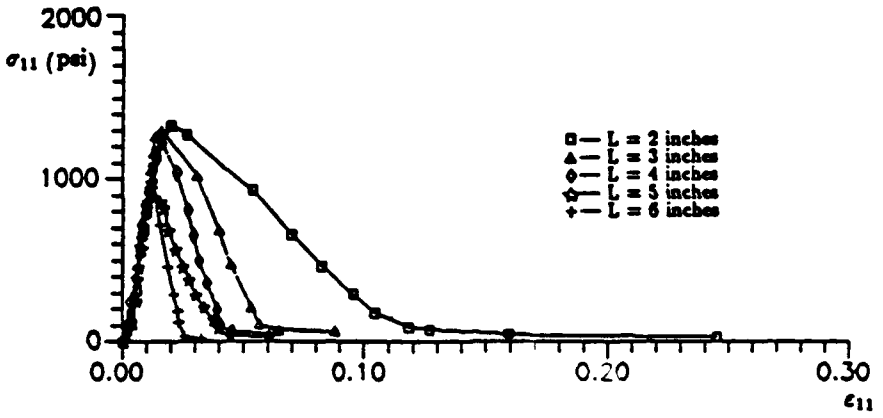

Fig. 4. Experimental results for uniaxial compression of cylindrical specimens of different length L. After [16] (Diameter of samples, D = 3 inches).

where

$$c_1 = 4a_1/\pi, \quad c_2 = 4a_2a^2/\pi, \quad \text{and} \quad c_3 = 4a_2a/\pi. \tag{23}$$

Before we study relation (22) further we discuss results of [16] on experimental studies on scale and shape effects.

2.2.2. *Verification*

A series of uniaxial tests on different size cylindrical specimens of a simulated rock were performed [16]. The simulated rock used consisted of sand, cement, plaster of paris and water in proportions 15:2:3:4 by weight. A wide range of different cylindrical specimens were tested under displacement controlled uniaxial compression. An MTS testing machine with appropriate data acquisition system was used. Both axial and lateral displacements were measured in addition to the axial force. Figure 4 shows typical results reported in [16]. Depending on the specimen size the peak strength and the post peak response vary. Up to peak, the response is rather linear with the elastic modulus being approximately 180 000 psi (1241 MPa). The strain at peak strength varied between 0.01 and 0.02 for different size specimens. The samples tested had different combinations of length L and diameter D. Table 1 shows the dimensions of the samples used as well as the peak strength values.

Table 1. Experimental results for uniaxial compression of different size specimens of artificial rock. (After [16])

Diameter (D) (inches)	Length (L) (inches)	Stress at peak (psi)
3	2	1333
3	3	1303
3	4	1228
3	5	976
3	6	952
1	3	324
1.5	3	650
2	3	918
2.5	3	1130
3	3	1303

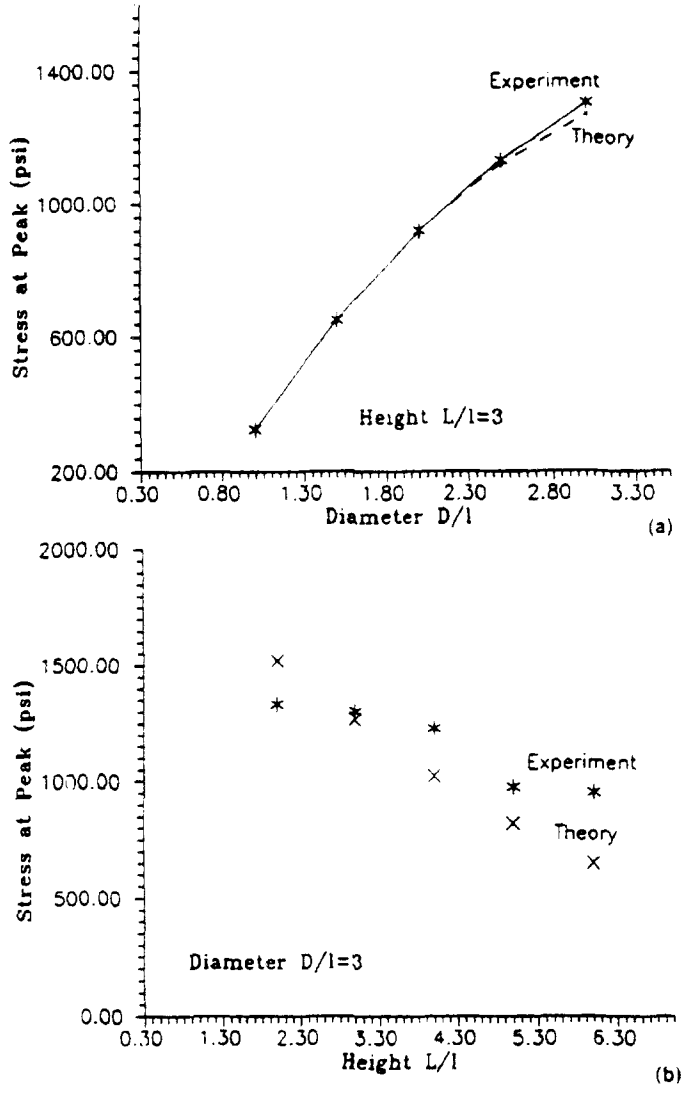

Fig. 5. Comparison of experiment and theory for peak strength of different specimens. Constants c_1, c_2, c_3 determined from first three tests of Table 1.

Assuming that a_1, a_2 are constant at the peak strength, from the series of tests shown in Table 1, the values of c_1, c_2 and c_3 at peak strengths can be determined. A minimum of three tests is required for this purpose. Two different procedures were used for determining c_1, c_2 and c_3. For the first procedure, the first three tests shown in Table 1 were used, while for the second procedure all tests were used and a least square fit was employed. Values of $c_1 = 1408$, $c_2 = -162$, $c_3 = 165$ were obtained from the second procedure. The analysis is rather insensitive to variations of c_1, c_2, c_3. Figures 5, 6 show comparisons between experiment and theoretical predictions from the first and the second procedure respectively. In these figures, the dimensionless ratio D/l or L/l is plotted on the horizontal axis. The average stresses at the peak of different specimens is plotted on the vertical axis. As can be seen for the test series of constant sample diameter and increasing height the peak strength reduces significantly

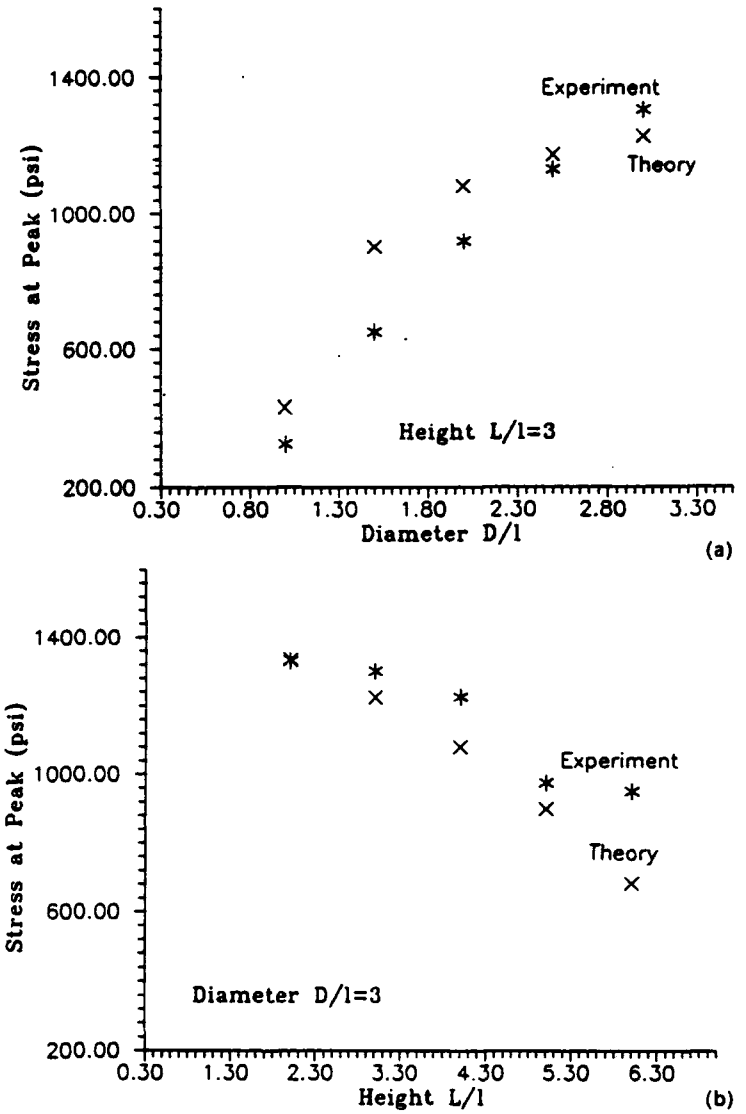

Fig. 6. Comparison of experiment and theory for peak strength of different specimens. Constants c_1, c_2, c_3 determined from all tests of Table 1, by least square procedure.

and a concave curve of peak strength versus height is observed. On the other hand for constant height and increasing diameter peak strength, a convex curve is observed, Figs. 5, 6. As can be seen the theory is able to capture such responses satisfactorily. The above series of tests and back-predictions are part of the shape effects of brittle materials. The so-called size effect is for different responses of specimens of the same shape but different size. For the size effect of cylindrical specimens the height over diameter remains constant. If $d = L/D$ is constant, then for increasing L or D the peak strength decreases, Fig. 7. Bazant, [18, 19]. From the available test results shown in Figs. 5, 6, two different tests of $d = 1/2$ can be back-predicted. In addition, Fig. 7 shows predictions for different lengths L that are not available in test results. However, the shape of this prediction curve is similar to the one shown in [18, 19].

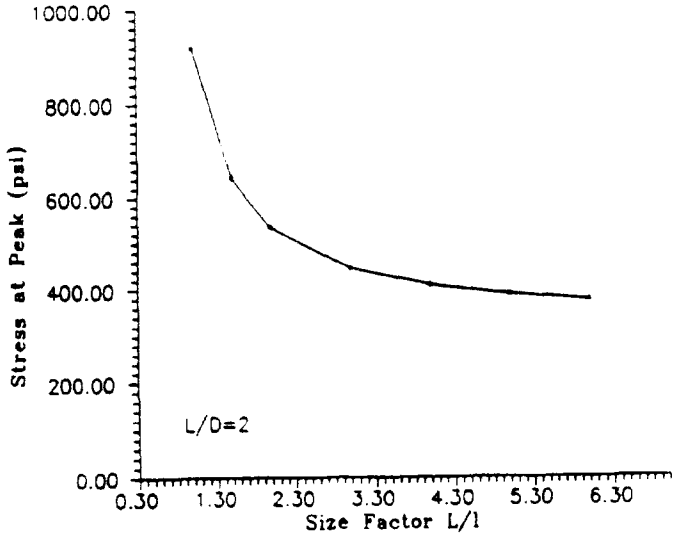

Fig. 7. Size effect predictions ($d = L/D$).

2.2.3. Stress paths and effect of confining pressure

As mentioned previously, it is not easy to simulate and observe the deformation, fracture, and unstable collapse of larger scale (as compared to laboratory specimen size) problems. Towards the solution of this problem, we mention the experimental work of Ewy et al. [20] on thick-walled cylinders on rock with the incorporation of several important features such as the ability to impose several stress paths, "freezing" of the fracture geometry under load, and measurement of the extent of failure and study of its connection to the observed instability modes. From these test results, it is observed that the presence of a surface (boundary) makes the stress conditions in the rock similar to those leading to splitting failure under uniaxial stress. Thus it appears that surface degradation and its connection to unstable collapse is important. Capturing the essential features of a brittle material specimen under uniaxial force is of vital importance. However, the information from the thick walled cylinder tests provides further information such as the effect of stress path on the extent of damage zones and instability modes. For low or zero confinement surface degradation is important; such instabilities lead to splitting close to the opening wall. For high confinement however, damage progresses within the whole specimen leading to a damage progression instability mode. In other words, for low (or zero) confinement surface degragation is predominant resulting in spalling types of instabilities while for high confinement damage progression is predominant leading to a global instability.

In the theory proposed herein, surface degradation is active in the region from the surface up to a distance ρ from it. Such degradation is quantitatively related to stress, so that for high confinement, the rate of surface degradation growth is reduced. It is expected that for low and zero confinement surface degradation instabilities are predominant; as confinement increases surface effects become less effective and damage progression, in a wide range of the structure (specimen) becomes predominant. The different stress paths, as reported in [20] can be simulated numerically and the different instability modes can be analyzed. It is important to note that such an analysis will provide further information on parameter ρ as related to the final unstable instability mode, and it will be presented elsewhere.

2.2.4. Comments on related research

Consider a structure (specimen) occupying region R and subjected to external tractions. Depending on the external load level, the geometry of the structure and the material properties, the following instabilities may develop:

— Surface degradation instability resulting in spalling of material from the surface.
— Damage progression instability resulting in overall failure by shear band formation or other non-homogeneous failure mode.

Note that the surface degradation instability does not necessarily imply overall failure of the structure. In other words "post-spalling" is possible until a global instability develops.

The rate of work of the external forces acting on a material element of volume ΔV, denoted by $\dot{E}$, is

$$\dot{E} = \dot{E}^R + \dot{Q} + \dot{S} = \frac{1}{\Delta V}\int_{\Delta V} \sigma_{ij}\dot{\varepsilon}_{ij}\,\mathrm{d}V + \dot{Q} + \dot{S}, \tag{24}$$

where Q, S denote the dissipated energy due to damage progression and due to surface degradation, respectively. Balance of global energy of the body R requires that

$$\dot{H} = \int_{\partial R} T_i\dot{u}_i\,\mathrm{d}S + \int_R \hat{\rho}f_k\dot{u}_k\,\mathrm{d}V = \int_R \dot{E}\,\mathrm{d}V + \tfrac{1}{2}\int_R \rho\,\frac{\mathrm{d}}{\mathrm{d}t}\,\dot{u}_i\dot{u}_i\,\mathrm{d}V, \tag{25}$$

where the last integral on the right hand side is the rate of kinetic energy, $\hat{\rho}$ denotes density, and f_k are the body forces acting on R. By setting

$$\dot{U} = \int_R \dot{E}^R\,\mathrm{d}V \tag{26}$$

it follows from (24)–(26) that

$$\dot{U} + \dot{Q} + \dot{S} = \dot{H}, \tag{27}$$

where $\dot{Q}$ and $\dot{S}$ are defined in volume V.

The total potential energy is now expressed as

$$\Pi = U - H. \tag{28}$$

The strain energy tranformation rate $G(G^*)$ being the energy required to transform u-volume to d-volume (the energy required so that surface degradation proceeds) is

$$-\frac{\partial\Pi}{\partial V_d} = \frac{\partial Q}{\partial V_d} + \frac{\partial S}{\partial V_d} = G, \tag{29}$$

$$-\frac{\partial\Pi}{\partial V_r} = \frac{\partial Q}{\partial V_r} + \frac{\partial S}{\partial V_r} = G^*. \tag{30}$$

As damage progression is assumed quasi-static

$$-\frac{\partial K}{\partial V_d} = -\frac{\partial K}{\partial V_r} = 0, \tag{31}$$

where K is the total kinetic energy. If damage and surface degradation occur, the kinetic energy is increased so that

$$-\frac{\partial^2 K}{\partial (V_d)^2} > 0, \tag{32}$$

$$-\frac{\partial^2 K}{\partial (V_r)^2} > 0. \tag{33}$$

Here, if only damage occurs then (32) is valid, if only surface degradation occurs then (33) is valid, and if both damage and surface degradation grow then (32) and (33) are valid. From the above relations the conditions for unstable damage and surface degradation growth are established as [12]

$$-\frac{\partial^2 \Pi}{\partial (V_d)^2} - \frac{\partial^2 D}{\partial (V_d)^2} - \frac{\partial^2 Q}{\partial (V_d)^2} - \frac{\partial^2 S}{\partial (V_d)^2} > 0, \tag{34}$$

$$-\frac{\partial^2 \Pi}{\partial (V_r)^2} - \frac{\partial^2 D}{\partial (V_r)^2} - \frac{\partial^2 Q}{\partial (V_r)^2} - \frac{\partial^2 S}{\partial (V_r)^2} > 0. \tag{35}$$

In [21], these inequalities have been examined analytically for the uniaxial compression test. It is concluded that surface degradation instability precedes the damage growth one. In addition, it is shown that such instabilities occur before the peak strength is reached. This implies that a post peak homogeneous state is impossible. Although the analytical solution for the uniaxial test provides important information, further analytical and numerical studies are needed. Numerical results are currently being studied.

Acknowledgements

A part of the research herein was supported by Grant No. AFOSR 890460 from the Air Force Office of Scientific Research, Bolling AFB.

References

1. C. Fairhurst and N.G.W. Cook, in *Proceedings First International Congress, Rock Mechanics*, Lisbon, 1 (1966) 687–692.
2. J.A. Hudson, E.T. Brown and C. Fairhurst, in *Proceedings 13th Symposium, Rock Mechanics*, University of Illinois, Urbana, (1971).
3. H.E. Read and G.A. Hegemier, *Mechanics of Materials* 3 (1984) 271–294.

4. I. Vardoulakis and E. Papamichos, "Surface instabilities in Elastic Anisotropic Media with Surface Parallel Griffith Cracks," *International Journal of Rock Mechanics, Mining Science & Geomechanics Abstracts*, submitted.
5. M.A. Biot, *Mechanics of Incremental Deformations*, Wiley, New York (1965).
6. R. Hill and J.W. Hutchinson, *Journal of the Mechanics and Physics of Solids* 23 (1975) 239–264.
7. I. Vardoulakis, *International Journal of Rock Mechanics, Mining Science & Geomechanics Abstracts* 21 (1984) 137–144.
8. H. Kitagawa and H. Matsushita, *International Journal of Solids and Structures* 23 (1987) 351–368.
9. G. Frantziskonis and C.S. Desai, *International Journal of Solids and Structures* 23 (1987) 733–750.
10. G. Frantziskonis G. and C.S. Desai, *Acta Mechanica* 68 (1987) 151–170.
11. G. Frantziskonis, *Composite Structures, International Journal* 10 (1988) 165–184.
12. G. Frantziskonis, *Acta Mechanica* 77 (1989) 213–230.
13. R.M. Bowen, *Continuum Physics*, A.C. Eringen, (ed.), 3, Academic Press, New York (1975) 1.
14. R.M. Bowen, *Journal of Chemical Physics* 50 (1969) 4601–4602.
15. C.S. Desai, S. Somasundaram and G. Frantziskonis, *International Journal for Numerical and Analytical Methods in Geomechanics* 10 (1986) 225–257.
16. C.S. Desai, T. Kundu and G. Wang, *International Journal for Numerical and Analytical Methods in Geomechanics* 14 (1990) 509–517.
17. B.C. Haimson and C.G. Herrick, "Borehole Breakouts and In Situ Stress," *Proceedings, Energy-Source Technology Conference*, Houston, TX (1989).
18. Z.P. Bazant and P.A. Pfeiffer, *ACI Materials Journal* 84 (1987) 463–480.
19. Z.P. Bazant and Z. Cao, *ACI Materials Journal* 84 (1987) 44–53.
20. R.T. Ewy, N.G.W. Cook and L.R. Myer, "Hollow Cylinder Tests for Studying Fracture Around Underground Openings," *Key Questions in Rock Mechanics*, Cundall et al. (eds.) Balkemma, Rotterdam (1988).
21. G. Frantziskonis and C.S. Desai, *Mechanics Research Communications* 17 (1990) 135–141.

Engineering Fracture Mechanics Vol. 39, No. 2, pp. 377–389, 1991
Printed in Great Britain.

0013-7944/91 $3.00 + 0.00
Pergamon Press plc.

BOREHOLE SCALE EFFECTS AND RELATED INSTABILITIES

G. FRANTZISKONIS, F. F. TANG and C. S. DESAI
Department of Civil Engineering and Engineering Mechanics, University of Arizona, Tucson, AZ 85721, U.S.A.

Abstract—A new mechanics based approach is proposed for scale effects and instabilities on borehole problems. In borehole types of structural systems, two types of instabilities can take place. The first is due to surface degradation growth and results into spalling of layers at the hole wall. The second is due to damage progression, and results into globally unstable response of the structure. The hole size has been found experimentally to be an important parameter in breakout instability initiation. Laboratory size holes may overestimate instability initiation properties by a large factor. At the same time, material properties such as peak stress depend largely on the size and shape of a specimen subjected to uniaxial or triaxial compression. This work attempts to incorporate size and scale effects into the instability initiation conditions. The important task of transferring information from laboratory experiments to actual large scale engineering problems is analysed and discussed. The potential of the theory is demonstrated. The need for further experimental and theoretical work is identified.

1. INTRODUCTION AND REVIEW

Borehole instabilities and breakouts are often characterized by the slabbing mode that affects a portion of the material close to the borehole wall. In addition, it is clear that the borehole size has significant effect on the initiation of breakout, Haimson and Herrick[1]. In general, 'small' holes fail at higher external stresses than 'large' ones. Since laboratory size boreholes are usually smaller than the ones in the field, the importance of hole size and its relation to breakouts is of a basic and quantitative nature. Thus in order to achieve a well-grounded statement about borehole stability that complies with laboratory and field observations, the dependency of borehole stability on its size (scale effect) must also be modeled.

Borehole scale effects is an example of the fact that the deformational characteristics of brittle materials depend on the size as well as on the shape of the structure (specimen). In a specimen subjected to uniaxial compressive stress, when the ratio of height to width (diameter for cylindrical specimens) of the sample is increased, the level of (macroscopic) stress at unstable failure decreases, Hudson *et al.*[2], Desai *et al.*[3]. In ref. [3] a number of uniaxial compressive tests on cylindrical specimens are reported, from which the following conclusions are made. For the series of tests of constant sample diameter and increasing height, the peak stress reduces significantly, and a concave curve of peak strength versus height is observed, Fig. 1(a). On the other hand, for constant height and increasing diameter the peak strength increases and a convex curve is observed, Fig. 1(b). The above test results represent a part of the shape effects in brittle materials. The size effect calls for different response of specimens of the same shape but different size. For cylindrical specimens, size effect is observed if the height over diameter (L/D) remains constant: as the size of the sample increases, the peak strength reduces as shown in Fig. 1(c).

Haimson and Herrick[1] studied the behavior of samples with different central hole sizes subjected to external stress. Square blocks of dry Alabama limestone having different diameters of central holes, ranging from 2 to 12 cm were subjected to uniaxial stress. All blocks had side length to borehole diameter ratio of 5:1. It was found that small diameter holes required larger stresses to induce breakouts, Fig. 2.

The above test results indicate that size and shape effects are significant especially for structures (specimens) of small size. The borehole tests indicate that as the hole size increases (more than 9 cm for Alabama limestone), the size effect becomes less prominent since the applied stress for breakout approaches a constant level. Similarly, the cylindrical specimen tests indicate that the peak stress tends asymptotically to a certain level. However different stress levels are reached depending on size or shape effects as shown in Fig. 1.

Engineering Fracture Mechanics Vol. 39, No. 2, pp. 377–389, 1991
Printed in Great Britain.

0013-7944/91 $3.00 + 0.00
Pergamon Press plc.

BOREHOLE SCALE EFFECTS AND RELATED INSTABILITIES

G. FRANTZISKONIS, F. F. TANG and C. S. DESAI
Department of Civil Engineering and Engineering Mechanics, University of Arizona, Tucson, AZ 85721, U.S.A.

Abstract—A new mechanics based approach is proposed for scale effects and instabilities on borehole problems. In borehole types of structural systems, two types of instabilities can take place. The first is due to surface degradation growth and results into spalling of layers at the hole wall. The second is due to damage progression, and results into globally unstable response of the structure. The hole size has been found experimentally to be an important parameter in breakout instability initiation. Laboratory size holes may overestimate instability initiation properties by a large factor. At the same time, material properties such as peak stress depend largely on the size and shape of a specimen subjected to uniaxial or triaxial compression. This work attempts to incorporate size and scale effects into the instability initiation conditions. The important task of transferring information from laboratory experiments to actual large scale engineering problems is analysed and discussed. The potential of the theory is demonstrated. The need for further experimental and theoretical work is identified.

1. INTRODUCTION AND REVIEW

BOREHOLE instabilities and breakouts are often characterized by the slabbing mode that affects a portion of the material close to the borehole wall. In addition, it is clear that the borehole size has significant effect on the initiation of breakout, Haimson and Herrick[1]. In general, 'small' holes fail at higher external stresses than 'large' ones. Since laboratory size boreholes are usually smaller than the ones in the field, the importance of hole size and its relation to breakouts is of a basic and quantitative nature. Thus in order to achieve a well-grounded statement about borehole stability that complies with laboratory and field observations, the dependency of borehole stability on its size (scale effect) must also be modeled.

Borehole scale effects is an example of the fact that the deformational characteristics of brittle materials depend on the size as well as on the shape of the structure (specimen). In a specimen subjected to uniaxial compressive stress, when the ratio of height to width (diameter for cylindrical specimens) of the sample is increased, the level of (macroscopic) stress at unstable failure decreases, Hudson *et al.*[2], Desai *et al.*[3]. In ref. [3] a number of uniaxial compressive tests on cylindrical specimens are reported, from which the following conclusions are made. For the series of tests of constant sample diameter and increasing height, the peak stress reduces significantly, and a concave curve of peak strength versus height is observed, Fig. 1(a). On the other hand, for constant height and increasing diameter the peak strength increases and a convex curve is observed, Fig. 1(b). The above test results represent a part of the shape effects in brittle materials. The size effect calls for different response of specimens of the same shape but different size. For cylindrical specimens, size effect is observed if the height over diameter (L/D) remains constant as the size of the sample increases, the peak strength reduces as shown in Fig. 1(c).

Haimson and Herrick[1] studied the behavior of samples with different central hole sizes subjected to external stress. Square blocks of dry Alabama limestone having different diameters of central holes, ranging from 2 to 12 cm were subjected to uniaxial stress. All blocks had side length to borehole diameter ratio of 5:1. It was found that small diameter holes required larger stresses to induce breakouts, Fig. 2.

The above test results indicate that size and shape effects are significant especially for structures (specimens) of small size. The borehole tests indicate that as the hole size increases (more than 9 cm for Alabama limestone), the size effect becomes less prominent since the applied stress for breakout approaches a constant level. Similarly, the cylindrical specimen tests indicate that the peak stress tends asymptotically to a certain level. However different stress levels are reached depending on size or shape effects as shown in Fig. 1.

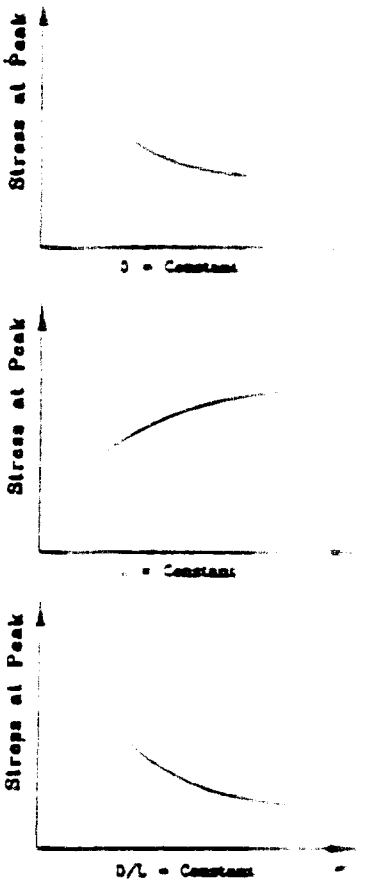

Fig. Schematic of size and shape effects from uniaxial compression [illegible] rock specimens (a) diameter D constant and varying height L, shape effect, (b) L constant and varying D, shape effect, (c) D/L constant, size effect.

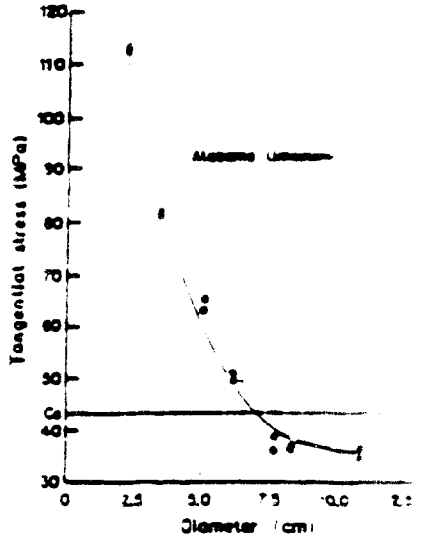

Fig. 2. Experimental data for scale effects for borehole breakout [illegible]

From the above discussion it is clear that size and shape effects in brittle material structures are complicated, and at the same time important to be ignored. For many problems in brittle material mechanics, i.e. borehole stability, analysis is based on simple elastic-perfectly plastic models that are calibrated on test data from conventional triaxial compression experiments. These models lead to irregular stability of the borehole as compared to experimental observations. Reviews, Maury[4], Guenot[5], demonstrate that classical design procedures lead to overestimation of the drilling fluid density by a factor of 2–8. From the test results shown in Fig. 2 it can be seen that breakout of small diameter holes require about three times the stress of large ones. Similar observations hold for tests on cylindrical specimens.

The bifurcation theory is used by Papanastasiou and Vardoulakis[6] to examine the effect of borehole radius on borehole stability. Material behavior is described by the deformation theory of plasticity, and internal length is introduced in the formulation through employment of Cosserat theory. The numerical solutions show an increase of the bifurcation stress with decreasing borehole radius (scale effect). As shown subsequently, the present study is different than the one in ref.[6] in the sense that length is introduced through surface degradation effects in the whole structure rather than in the constitutive equations. Furthermore, instabilities are based on global energy criteria.

In the next section, the relevant theory for damage and surface degradation growth is described. Since this theory has been presented elsewhere[7–12], only the necessary background for completeness of the present paper is presented. In Section 3, in order to demonstrate the scale effects, a simplified solution for a borehole problem is presented first. Subsequently, numerical solutions of borehole problems are presented and discussed.

2. BACKGROUND

2.1. *Damage growth considerations*

A number of investigators have considered the effects of damage in their models directly or indirectly. A review on this subject can be found in ref.[7], and the references cited there. Here, it is not intended to review the analytical models for the influence of microcrack initiation and growth on the constitutive behavior of brittle materials. Only the material directly relevant to the purpose of this study is presented.

The model including damage proposed in refs[7–12] has been investigated successfully with respect to different materials such as concrete and composites. The material constants have been identified and the proposed theory has been validated through comparison with experimental data. Only minor modifications in the model are necessary for the description of different materials. Also, properties such as degradation, induced anisotropy, degradation of elastic properties are attributed to damage development.

2.1.1. *Formulation.* Let us consider a small volume ΔV of the material. This volume is subdivided into an intact (undamaged) part, ΔV_u, and into a 'fractured' (damaged) part, ΔV_d, (Fig. 3). The first part or fraction represents topical behavior, and the material in it is intact in the sense that no microcracks are induced. Due to inhomogeneity of the material behavior at the micro-level, weak planes are developed leading to crack formation and subsequent propagation. The laws that govern the above structural changes are not fully understood. The effect of an isolated or coupled fracture site is that an influence zone exists around it as shown schematically in Fig. 3. This influence zone has volume ΔV_d. Under continued loading, influence zones increase so that ΔV_d increases. At every instant of time, we define the ratio

$$r = \frac{\Delta V_d}{\Delta V} \tag{2.1}$$

called the damage volume ratio. The material point consists of the superposition of a material point of the undamaged fraction, herein called the u-part, and of a material point of the damaged fraction, herein called the d-part. This suggests the use of the theory of mixtures, or theory of interacting continua, Bowen[13]. As a consequence, the following relation is applicable[8]

$$\sigma_{ij} = (1 - r)\,\sigma^u_{ij} + r\sigma^d_{ij} \tag{2.2}$$

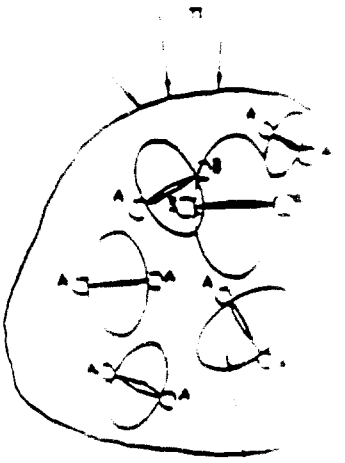

Stress Relieved Zones

A Potential Crack Extension Site

B Unlikely Zone for Crack Extension

Fig. 3. Schematic of damage influence zones

where σ_{ij}^u, σ_{ij}^d denote the stress tensors in the u- and d-part of the material element respectively and σ_{ij} is the average (measured) stress tensor. The general theory of mixtures[13, 14] is simplified considerably if diffusion is absent. In the proposed theory, there is no diffusion between the components thus the strains in the two material fractions are equal. Bowen[14].

We now consider a material element. Due to the enforced deformation in the element, damage influence zones have been created but failure has not occurred yet. Such influence zones depict the mechanical influence of a system of microcracks. The constitutive equations for the d-part can be established as[8, 9]

$$\dot{\sigma}_{ij}^d = C_{ijkl}^d \dot{\epsilon}_{kl} \tag{2.3}$$

where overdot indicates time rate/increment, and C_{ijkl}^d is a function of parameters related to the degraded properties of the material. Since there are no microcracks in the u-part, its constitutive relations can be identified as

$$\dot{\sigma}_{ij}^u = C_{ijkl}^u \dot{\epsilon}_{kl} \tag{2.4}$$

If the undamaged fraction is linearly elastic (e.g. for composites, C_{ijkl}^u contains the usual linear elasticity constants. If plasticity effects are included then a generalized hierarchical elastic–plastic model is employed, Desai *et al.*[15].

The irreversible nature of damage implies that the material experiencing it obeys non-holonomic laws. Thus the problem is formulated in rate form of the governing equations and the constitutive relations are derived from eqs (2.2)–(2.4) as

$$\dot{\sigma}_{ij} = L_{ijkl} \dot{\epsilon}_{kl} - r(\sigma_{ij}^u - \sigma_{ij}^d) \tag{2.5}$$

where

$$L_{ijkl} = (1 - r) C_{ijkl}^u + r C_{ijkl}^d \tag{2.6}$$

From eq. (2.5) it can be seen[8, 9] that although r and $(1 - r)$ are scalars, a tensor namely, $r(\sigma_{ij}^u - \sigma_{ij}^d)$, is introduced in the formulation. This tensor is responsible for damage induced anisotropy, an obvious property of cracked materials. Further, an evolution law for r is defined and it is directly related to failure where r reaches a critical value r_{cr}. A simple and effective law can be written as

$$\dot{r} = f(\epsilon_{ij}) \dot{\epsilon}_{kl} \tag{2.7}$$

Based on the physical interpretation of damage and failure criteria the function f [illegible] specified[7–12]. For the numerical results presented in this paper a specific form of f has been used, and it is given subsequently.

2.2. *Surface degradation*

Surface degradation is induced by microstructural inhomogeneity and its growth is initially stable. It is important to mention that there is certain evidence that this phenomenon acts as a trigger effect on the shear band appearing in a specimen. The sudden growth of surface effects results in the occurrence and development of shear bands penetrating into the body[16, 17].

The damage distribution at the edge of a body where surface degradation is of importance is expected to be significantly different from the damage distribution far from the edge (in the body). We consider that damage at the edge due to surface effects is additive to the damage accumulation calculated as if no surface effects were present. So, at the edges, a small volume ΔV_t is subdivided into an intact part ΔV_{ui} and into a fractured part ΔV_{uf}. We consider that the above subdivision holds for a distance ρ from the edge, ρ being a positive real number dependent on the material properties, the geometry, and load acting on the body. At every instant of time, the edge damage concentration volume ratio is defined as[10–12]

$$r_e = \frac{\Delta V_{uf}}{\Delta V}. \tag{2.8}$$

Here r_e is expected to be maximum at the edge and its value decreases continuously till a minimum value expected to be at a distance ρ from the edge. Let us consider the following volume average, for unit area on the plane parallel to the edge

$$\bar{r} = \frac{1}{\rho}\int_\rho r_e \, dA. \tag{2.9}$$

Also the following stress average can be introduced

$$\bar{\sigma}_{ij} = \frac{1}{\rho}\int_\rho \sigma_{ij} \, dA. \tag{2.10}$$

Similarly, average partial stresses $\bar{\sigma}^u_{ij}$, $\bar{\sigma}^f_{ij}$ and strains $\bar{\epsilon}_{ij}$ can be introduced. Since the constitutive eqs (2.3) and (2.4) are linear or incrementally linear, we can write equations similar to (2.5) and (2.6) for the average $(\bar{\cdot})$ quantities. At the effective surface degradation volume the total damage ratio is defined as

$$r_t = r + \bar{r}. \tag{2.11}$$

In general

$$\bar{r} = g(\epsilon) r \tag{2.12}$$

where $g(\epsilon)$ is the surface degradation amplification function. As shown in ref.[12], g can be specified from test results on different size specimens. Distance ρ is defined as

$$\rho = a\left(\int_c W \, ds - l\right) \tag{2.13}$$

where W is a weighting function (the simplest case calls for W = unity and even this case has been shown to provide satisfactory results), a is a material constant determinable from test results on different size specimens, l is the so-called surface degradation material length, and c is the path of maximum (absolute) principal compressive stress. Material related constant l defines a new characteristic length. It is defined as that specimen size so that the whole specimen is in the surface degradation zone. The surface degradation constants have been determined[12] (from tests on different size specimens) for a material described subsequently.

As discussed in the introduction, the deformational characteristics of brittle materials depend on the size and shape of a structure (specimen). In refs[11, 12] the effect of surface degradation on the scale (size) as well on the shape of a structure is examined, mainly with respect to uniaxial

compression of cylindrical specimens. It is shown that surface degradation can capture important properties of brittle materials such as scale and shape effects, surface degradation growth and subsequent bursting instabilities.

2.3. *Energy considerations*

Consider a structure (specimen) occupying region R and subjected to external tractions. Let ∂R be the boundary of R. From the thermodynamic viewpoint, the state of the material may be characterized by its strain energy density, ψ, defined as

$$\hat{\rho}\psi = \tfrac{1}{2}\sigma_{ij}\epsilon_{ij} \tag{2.14}$$

where $\hat{\rho}$ is mass density. Since damage comprises the creation and propagation of cracks and voids, damage growth dissipates energy. In addition, there is dissipated energy due to plastic deformations. By differentiation of eq. (2.14) with respect to time t, the internal energy density rate is obtained as

$$\dot{W} = \tfrac{1}{2}(\sigma_{ij}\dot{\epsilon}_{ij} + \dot{\sigma}_{ij}\epsilon_{ij}) = \sigma_{ij}\dot{\epsilon}_{ij} - \dot{\phi} \tag{2.15}$$

where $\dot{\phi}$ is the rate of dissipated energy

$$\dot{\phi} = \tfrac{1}{2}(\sigma_{ij}\dot{\epsilon}_{ij} - \dot{\sigma}_{ij}\epsilon_{ij}). \tag{2.16}$$

By integration of eq. (2.16) we obtain the expression for the dissipated energy per unit volume

$$\phi = \int_0^t \sigma_{ij}\dot{\epsilon}_{ij}\,\mathrm{d}t - \tfrac{1}{2}\sigma_{ij}\epsilon_{ij} \tag{2.17}$$

and t denotes time.

Now let D be the energy dissipated from damage growth. In the damage formulation described previously, if the topical (μ-part) response is assumed linearly elastic, eqs (2.3) and (2.4) can be written as

$$\begin{aligned} \sigma_{ij}^{\mu} &= C_{ijkl}^{\mu}\epsilon_{kl} \\ \sigma_{ij}^{d} &= C_{ijkl}^{d}\epsilon_{kl}. \end{aligned} \tag{2.18}$$

In this case, $\phi = D$ and from eqs (2.16) and (2.18) it follows that

$$\dot{D} = \tfrac{1}{2}\epsilon_{ij}(C_{ijkl}^{\mu} - C_{ijkl}^{d})\epsilon_{kl}\dot{r}. \tag{2.19}$$

Region R of a body is defined as $R = R_1 + R_2$ where R_2 is the surface degradation volume bounded from the stress-free boundary surface and extended to a distance ρ from it. Then, R_1 is the rest of R such that $R_1 = R - R_2$. The dissipated energy from damage and surface degradation growth is

$$\int_R \dot{D}\,\mathrm{d}V = \int_{R_1} \dot{Q}\,\mathrm{d}V + \int_{R_2} \dot{S}\,\mathrm{d}V \tag{2.20}$$

where $\dot{Q}$ and $\dot{S}$ represent the energy density dissipated from damage growth, and from surface degradation growth, respectively. Let $\dot{D}_p$ be the rate of dissipated energy from plastic deformation such that $\dot{\phi} = \dot{D} + \dot{D}_p$, (2.18 does not hold in this case). Considering quasi-static loading, in the absence of body forces, rate of energy balance requires

$$\int_{\delta R} T_i\dot{u}_i\,\mathrm{d}S = \int_R \dot{W}\,\mathrm{d}V + \int_{R_1} \dot{Q}\,\mathrm{d}V + \int_{R_2} \dot{S}\,\mathrm{d}V + \int_R \dot{D}_p, \tag{2.21}$$

where T_i is the external load applied on δR, and u_i denote displacements.

Depending on the external load level, the geometry of the structure and the material properties, the following instabilities may develop:

—Surface degradation instability resulting in spalling of material from the surface.
—Damage progression instability resulting in overall failure by shear band formation or other failure mode.

Note that surface degradation instability does not necessarily imply overall failure of the structure. In other words 'post-spalling' is possible until a global instability develops.

The total potential energy is expressed as[8, 9]

$$\Pi = \int_R W \, dV - \int_{\partial R} T_i \cdot u_i \, dS. \tag{2.22}$$

From the above relations the conditions for unstable damage and surface degradation growth are established as[8, 9]

$$-\frac{\partial^2 \Pi}{\partial (V_d)^2} - \frac{\partial^2 D_s}{\partial (V_d)^2} - \frac{\partial^2 Q}{\partial (V_d)^2} - \frac{\partial^2 S}{\partial (V_d)^2} > 0 \tag{2.23}$$

$$-\frac{\partial^2 \Pi}{\partial (V_m)^2} - \frac{\partial^2 D_s}{\partial (V_m)^2} - \frac{\partial^2 Q}{\partial (V_m)^2} - \frac{\partial^2 S}{\partial (V_m)^2} > 0. \tag{2.24}$$

In refs [10, 11], these inequalities have been discussed with respect to the instability of typical problems with emphasis on uniaxial load conditions. In the next section relations (2.23) and (2.24) are examined for borehole type of problems, and the connection to scale effects is studied.

3. ANALYTICAL AND NUMERICAL SOLUTIONS

3.1. *Simple analysis of a borehole problem*

Let us consider the following problem depicted in Fig. 4. The borehole structure of length and width D contains a central circular hole of radius R. The ratio D/R is considered constant such that $D/2R = 5$. Uniaxial compressive external stress σ is applied externally. If the material is considered linear, isotropic and elastic, then the σ_{max} occurs at point A and, Roark and Young[18]

$$\sigma_{max} = \sigma_A = k\sigma_{nom} \tag{3.1}$$

where

$$\sigma_{nom} = \frac{\sigma D}{D - 2R} \tag{3.2}$$

$$k = 3.00 - 3.13\left(\frac{2R}{D}\right) + 3.66\left(\frac{2R}{D}\right)^2 - 1.53\left(\frac{2R}{D}\right)^3. \tag{3.3}$$

In order to demonstrate the capability of the theory to capture the scale effects of this problem we make (for the time being) the following simplifying assumptions. We consider that the material is linear elastic and isotropic. This, of course represents a 'stiffer' material than actual rocks.

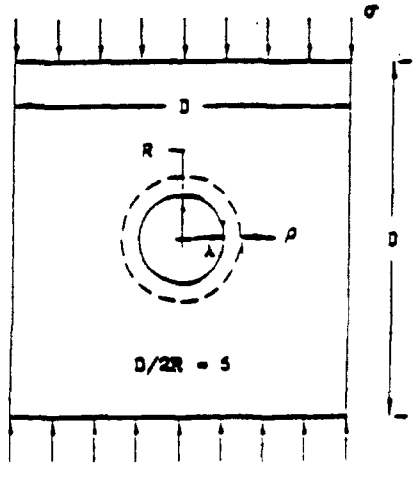

Fig. 4. Geometry of a borehole problem structure under uniaxial compressive external load.

In addition we assume that for the external stress levels at breakout the material in the surface degradation zone has zero stiffness. Thus at breakout initiation this problem can be analysed by using the solution presented in eqs (3.1)–(3.3) but now the radius of the hole is $R+\rho$. For this problem eq. (2.13) reduces to

$$\rho = \alpha(2\pi R - l) \tag{3.4}$$

and

$$\sigma_{max} = k\frac{\sigma D}{D - 2(R+\rho)} \tag{3.5}$$

and k is given from eq. (3.3) where $R+\rho$ is substituted instead of R. For the material discussed later it was found that $\alpha = 0.21$ and l was considered to be one inch[12]. If we consider that at breakout, σ_{max} in (3.5) assumes a constant value we can obtain solutions for different R where always $D/2R = 5$. The curve in Fig. 5 is obtained where the diameter ($2R$) is plotted on the horizontal axis and the external stress at breakout is plotted on the vertical one. Clearly, the shape and trend of this curve is similar to the experimental one given in Fig. 2.

3.2. *Numerical solutions*

In the above problem, certain simplifying assumptions were made to illustrate the potential of the theory analytically. However, if the two fractions are considered to be elastic plastic, it is difficult to obtain an analytical solution even for the uniaxial load case. Herein, the scale effects and the instability inequalities are analyzed numerically for typical borehole problems.

The principle of virtual work leads to the following incremental equations where matrix notation is adopted[19]

$$\int_V \mathbf{B}^T \, d\sigma \, dV = dQ \tag{3.6}$$

where B is the strain–displacement matrix, d(.) denotes increment, dQ is the increment of the external force, superscript T denotes transpose matrix, and V is the volume. The constitutive relations (2.5) and (2.6) are written as

$$d\sigma = \mathbf{L}\, d\varepsilon - dr\ \mathbf{T}. \tag{3.7}$$

From eqs (3.6) and (3.7) and the incremental strain–displacement relations, it follows that

$$\mathbf{k}\, dq = dQ + dQ^{\varepsilon} \tag{3.8}$$

where

$$\mathbf{k} = \int_V \mathbf{B}^T \mathbf{L} \mathbf{B} \, dV \tag{3.9}$$

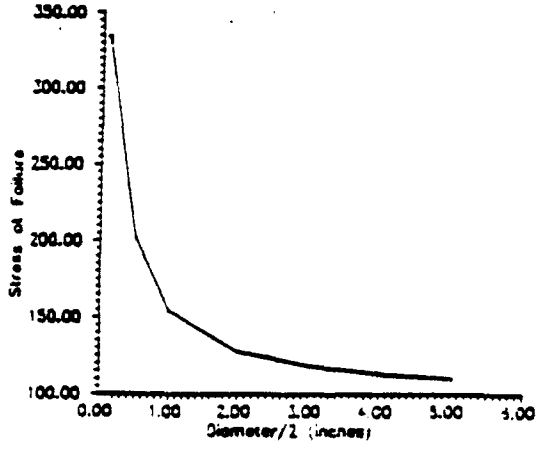

Fig. 5. Scale effect predicted through the simplified analysis.

is the incremental stiffness matrix for the u-part, and

$$dQ^d = \int_V B^T \, dr \, T \, dV \tag{3.10}$$

is termed as the 'damage force'.

In order to evaluate the second partial derivatives appearing in the instability inequalities (2.23), (2.24) numerically, the three-point method is employed, thus for example

$$\frac{\partial^2 D}{\partial V_d^2} = \frac{\left(\frac{\partial D}{\partial V_d}\right)_3 - \left(\frac{\partial D}{\partial V_d}\right)_1}{(V_d)_3 - (V_d)_1} \tag{3.11}$$

where subscripts 1, 2, 3 denote values at three consecutive increments of load.

3.2.1. *Constitutive relations for the elastic–plastic undamaged fraction.* The following brief description of the plasticity model used for the u-fraction is adopted from ref.[15]. As mentioned already, the material behavior is decomposed in two parts, namely the u and the d-part. The undamaged part is assumed to obey an elastic–plastic constitutive law. Since the damaged part 'follows' the deformations of the u-part (2.3) and since it has no shear resistance, the damage constitutive relations (2.4) may be termed as rigid perfectly plastic with zero yield strength. The effect of damage evolution on the volumetric response of a structure is discussed in ref.[12]. The elastic–plastic constitutive relations for the u-part (2.3) are written as

$$\dot{\sigma}_{ij} = C^{ep}_{ijkl} \dot{\epsilon}_{kl} \tag{3.12}$$

for loading, and as

$$\dot{\sigma}_{ij} = C^{e}_{ijkl} \dot{\epsilon}_{kl} \tag{3.13}$$

for unloading.

A general hierarchical single surface modeling procedure for developing elastic–plastic models for isotropic and anisotropic hardening, nonassociative responses and applications for soils, rocks and concrete are described in ref.[15] and the references cited there. This approach is used here to describe the u-part with basic isotropic hardening and associative behavior. The yield function is given by[15]

$$F = J_{2D}^n - \left\{ -\frac{\alpha_1}{\xi^{n_1}} J_1^n + \gamma J_1^2 \right\} (1 - \beta S_r)^{-n/2} \tag{3.14}$$

where $J_1 = J_1 - b$, and b is a material constant representing the distance from the stress origin to the intersection of the surface with the tensile hydrostatic axis $J_1 = \sigma^u_{kk}$ is the first invariant of σ^u_{ij} stress, $S_r = (J^n_{3D})^{1/3}/(J^n_{2D})^{1/2}$ is a stress ratio, J^n_{3D}, (J^n_{2D}) is the third (the second) invariant of the deviatoric part of σ^u_{ij}, β, γ, n are assumed to be material constants related to the shape of the yield function, α_1, n_1 are material constants related to hardening and $d\xi = (d\epsilon^p_{ij} \, d\epsilon^p_{ij})^{1/2}$, superscript p indicating plastic. In order to derive the C^{ep}_{ijkl} tensor, the usual relations of elastic–plastic theory are used.

In general, eq. (2.7) holds. In the present numerical procedure the following evolution function for r is employed[7, 8]

$$r = r_u - r_u \exp(-\kappa \xi^p_D) \tag{3.15}$$

where r_u, κ, R are damage related material constants. A procedure for determining the elasticity, plasticity, and damage constants is given in ref.[7]. The values of the constants used for the present analysis are also given in ref.[7]. These constants were determined from test results for concrete[22], where cubical specimens of 100 mm size were tested under multiaxial load.

A natural question is how to determine the amplification function g shown in eq. (2.12). An effective procedure is by utilizing the stress–strain curves of different size specimens[12]. Damage constants κ and R appearing in eq. (3.15) are expected to be different in the surface degradation zones than in the damage zones. From the test results on different size specimens reported in ref.[2] the following values of κ and R were obtained and are used in the present analysis: $\kappa_1 = 1.75 \times 10^4$.

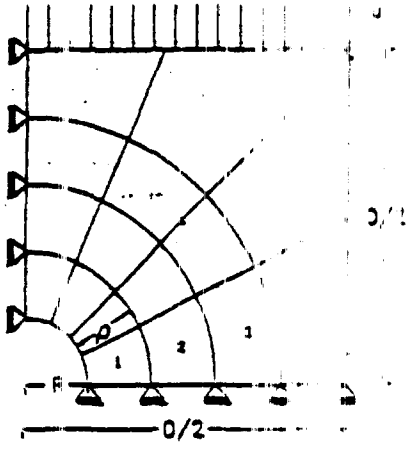

Fig. 6. Finite element mesh for the numerical analysis of the borehole problem depicted in Fig. 4

$\kappa_2 = 668$, $R_1 = 2.305$, $R_2 = 1.502$, where subscripts 1, 2 indicate values for the surface degradation zone and damage zone respectively.

3.2.2. *Example problems.* The finite element method has been used, long ago, for the stress-deformation and stability analysis of borehole problems. Initial works in this area, Desai and Reese[20], considered nonlinear elastic material response and the Mohr envelope was used as the criterion for development of plastic zones. It was found that plastic zones advance close to the borehole at a certain distance depended on the geostatic loading. The extent of plastic zone may be related to the surface degradation zone discussed in this study. However, since the surface degradation zones are depended on the geometry of the structure, such a relation would be based on fixed radius of the borehole.

The problem shown in Fig. 4 was investigated numerically for six different values of the central hole radius. For all problems the ratio of D over R was constant such that $D/2R = 5$. The finite element mesh used is shown in Fig. 6. Eight node quadrilateral elements were used. For the six problems studied the hole radii were 0.5, 1, 2.5, 5, 7.5 and 0 cm. For each problem the surface degradation distance ρ was calculated (eq. 3.4). The elements next to the central hole extend for a distance ρ as shown in Fig. 6. The material properties assigned for these elements are the surface degradation ones. The purpose of this analysis is to study the surface degradation instabilities close to the hole. Thus no surface degradation was considered close to the lateral surfaces of length D, since the surface degradation growth at these points is much slower than the growth close to the hole.

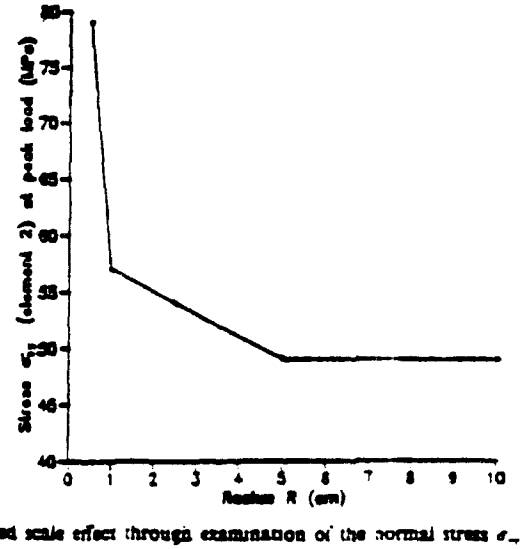

Fig. 7. Predicted scale effect through examination of the normal stress σ_{rr} at element 2

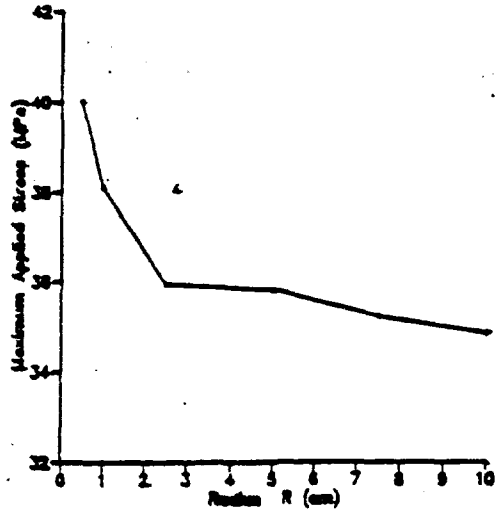

Fig. 8. Predicted scale effect through examination of the maximum external applied stress.

The calculated load–deformation curve for these problems monotonically increases until a peak load is reached. Beyond the peak load, softening response was calculated. In Fig. 7 radius R is plotted on the horizontal axis and the normal stress $\sigma_{\theta\theta}$ at the peak load for the lower left Gauss point of element 2 is plotted on the vertical axis. Here $\sigma_{\theta\theta}$ represents the so called tangential stress at the end of the surface degradation zone. A simple criterion for spalling of the surface degradation zone calls for $\sigma_{\theta\theta}$ reaching a critical value. In this case, Fig. 7 shows the capability of the theory to represent the scale effect. The shape of this curve is similar to the one shown in Fig. 2. Since the material constants for Alabama limestone are not available, no quantitative comparison can be made. Figure 8 is similar to Fig. 7, but the maximum (peak) stress is plotted on the vertical axis.

At every increment of load the instability inequalities (2.23) and (2.24) were examined. Surface degradation growth showed the following interesting characteristics, for these problems. Surface degradation showed an initial unstable region from the beginning of the external load application. Subsequently the response became stable until a second instability was initiated. This trend is similar to the crack propagation problem studied by Sammis and Ashby[21]. In that ref.[21] the crack propagation problem of a notched specimen with a central hole is studied theoretically and experimentally. The geometry of the problem is similar to the one shown in Fig. 4 and the

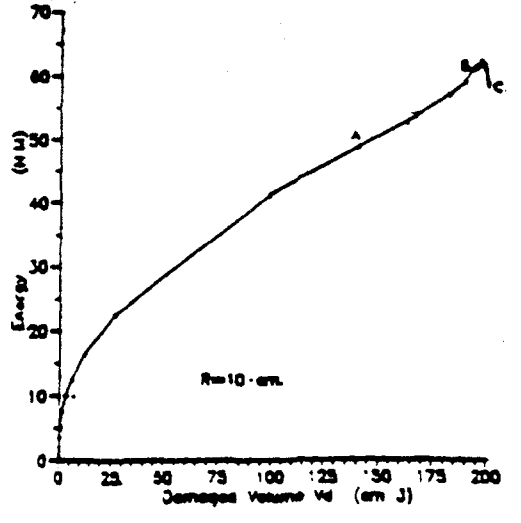

Fig. 9. Damaged volume V_d vs energy ϵ for the borehole problem of $R = 10$ cm, $D = 100$ cm.

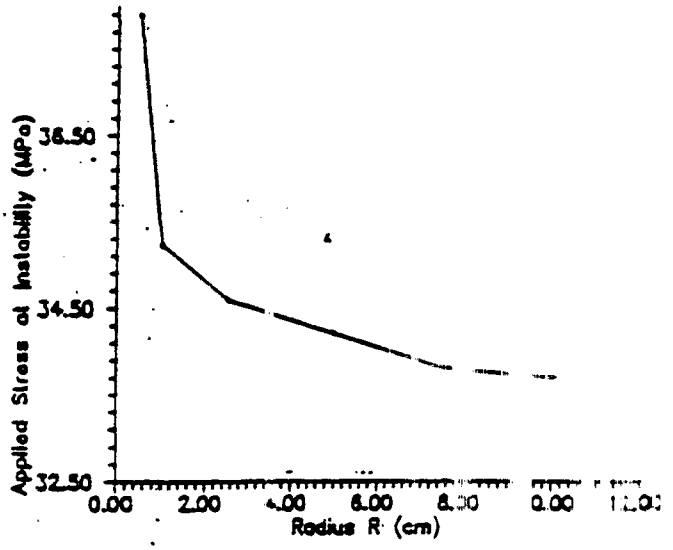

Fig. 10. Predicted scale effect through examination of surface degradation instability

propagation of initial surface cracks parallel to the external compressive load is studied. Crack propagation was found (theoretically and experimentally) to be initially unstable (from the beginning of the load application) then stable and then unstable again. Here we note that the instability inequalities (2.23) and (2.24) are necessary but not sufficient conditions for instability initiation. Let

$$e = \Pi + D, + Q + S. \tag{3.6}$$

In Fig. 9, e is plotted with respect to the surface degradation volume V_s for the case $R = 10$ cm and $D = 100$ cm. Similar curves were obtained for the other five cases considered. When this curve is convex, surface degradation instability is possible. The curve shown in Fig. 9 is initially convex implying possible unstable growth, up to point A. After point A the surface degradation growth is stable up to point B. After point B the curve is convex again. Note that the convexity after B increases rapidly. Point C on this curve is at peak load. This analysis is similar, in trend, to the crack propagation problem studied in ref.[20]. It implies that the material is susceptible to surface degradation instability from the beginning of the load application. After a certain amount of surface damage has been achieved, the damage growth response is stable for a rather small range of external load. Then surface damage instability is expected to occur, after point B. The scale effect shown in Fig. 10 corresponds to instability initiation at point B, where radius R is plotted on the horizontal axis and the externally applied stress at surface instability is plotted on the vertical axis.

4. CONCLUSIONS

Surface degradation growth is shown to play an important role for phenomena observed in borehole problems such as scale effects and surface damage instabilities. Analytical and numerical results show the capability of the theory to predict such phenomena. At this time, only qualitative comparison of observed and predicted responses is possible. Further experimental work related to growth of damage and resulting instability close to borehole walls is needed.

Acknowledgement—A part of the research herein was supported by Grant No. AFOSR 890460 from the Air Force Office of Scientific Research, Bolling AFB.

REFERENCES

[1] B. C. Haimson and C. G. Herick. Borehole breakouts and *in situ* stress. *Proc. Energy-Source Technol. Conf.* Houston, Texas (1989).
[2] J. A. Hudson, E. T. Brown and C. Fairhurst. Shape of the complete stress–strain curve for rock. *Proc. 13th Symp. Rock Mechanics*, University of Illinois, Urbana (1971).

[3] C. S. Desai, T. Kundu and G. Wang, Size effect on damage in progressive softening process for simulated rock. *Int. J. numer. anal. Meth. Geomechanics* 14, 509–517 (1990).
[4] V. Maury, Observations, researches and recent results about failure mechanisms around single galleries. *Proc. 6th Int. Congress Rock Mech.* (Vol. 2, pp 1119–1128). Montreal, Canada (1987).
[5] A. Gomot, Stress and rupture conditions around oil wellbores. *Proc. 6th Int. Congress Rock Mech.* (Vol. 1, 109–118). Montreal, Canada (1987).
[6] P. C. Papanastasiou and I. G. Vardoulakis, Bifurcation analysis of deep boreholes—II. Scale effect. *Int. J. numer. anal. Meth. Geomechanics* (in press).
[7] G. Frantziskonis and C. S. Desai, Constitutive model with strain softening. *Int. J. Solids Structures* 23, 733–750 (1987).
[8] G. Frantziskonis and C. S. Desai, Elastoplastic model with damage for strain softening geomaterials. *Acta Mechanica* 68, 151–170 (1987).
[9] G. Frantziskonis, Damage and free edge effects in laminated composites. Energy and stability propositions. *Acta Mechanica* 77, 213–230 (1989).
[10] G. Frantziskonis and C. S. Desai, Degradation instabilities in brittle material structures. *Mech. Res. Comm.* 17, 135–141 (1990).
[11] G. Frantziskonis and C. S. Desai, Surface degradation mechanisms in brittle material structural systems. *Int. J. Fracture* submitted.
[12] G. Frantziskonis, F. F. Tang and C. S. Desai, Degradation instabilities in brittle material structural systems (in progress).
[13] R. M. Bowen, Theory of mixtures, in *Continuum Physics* (Edited by A. C. Eringen) Vol. 3, p. 1. Academic Press, New York (1975).
[14] R. M. Bowen, Thermochemistry of reacting materials. *J. Chemical Physics* 50, 4601–4602 (1969).
[15] C. S. Desai, S. Somasundaram and G. Frantziskonis, A hierarchical approach for constitutive modelling of geologic materials. *Int. J. numer. Anal. Meth. Geomechanics* 10, 225–257 (1986).
[16] H. Kitagawa and H. Matsuhisa, Flow localization in elastic-plastic material developing from the stress-free surface. *Int. J. Solids Structures* 23, 351–368 (1987).
[17] H. Yukutake, Fracturing process of granite inferred from measurements of spatial velocities and temporal variations in velocity during triaxial deformations. *J. Geophysical Res.* 94, 15639–15651 (1989).
[18] R. J. Roark and W. C. Young, *Formulas for Stress and Strain*, 5th edn (1989).
[19] C. S. Desai and J. F. Abel, *Introduction to the Finite Element Method*. Van Nostrand Reinhold, New York (1972).
[20] C. S. Desai and L. C. Reese, Stress-deformation and stability analysis of deep boreholes. *Proc. 2nd Compr. Intl. Soc. Rock Mechs.* Belgrade, Yugoslavia (1970).
[21] C. G. Sammis and M. F. Ashby, The failure of brittle porous solids under compressive stress states. *Acta Metall.* 34, 511–526 (1986).
[22] J. G. M. VanMier, Strain softening of concrete under multiaxial loading conditions. Doctoral Dissertation. Eindhoven Univ. of Techn., The Netherlands (1984).

(*Received* 10 *May* 1990)

Eur. J. Mech., A/Solids, 11, n° 1, 21-34, 1992

On the micro-structure of surface effects and related instabilities

G. FRANTZISKONIS * and I. VARDOULAKIS **

ABSTRACT. – Based on Mindlin's theory for material micro-structure interesting surface effects under conditions of equilibrium are studied in this paper. The governing field equations for uniaxial plane deformations are established; surface instability analysis shows non uniform deformations for a layer of specified distance from the surface. Experimental as well as fracture mechanics based considerations show that this surface-layer is extremely thin for metals while for brittle materials its magnitude is of the order of 1 cm. Material micro-structure introduces a singular perturbation to the original Hill and Hutchinson problem; here we introduce a single perturbation parameter and we obtain a "dispersion" law for the surface buckling load. It is found that surface degradation and skin effects can be attributed to localized surface buckling instabilities. Experimental information on skin effects can provide an estimation of the internal material length.

1. Introduction

About three decades ago Germer *et al.* [1961] observed surface irregularities in homogeneously strained metal solids. Based on electron diffraction measurements it was concluded that displacements of a superficial layer toward the interior of the metal solid is five times as large as that of the next layer. Based on exponential decay considerations Mindlin [1965] concluded that such an effect is confined to an extremely thin surface-layer in metallic materials. Recently, Kitagawa & Matsushita [1987] reviewed the experimental and theoretical information on such surface effects herein termed as surface degradation effects. Further in [K & M, 1987] it is shown how unevenness of the surface grows and localization develops from an initial random inhomogeneous deformation field. As concluded in [K & M, 1987] and in the references cited there surface roughness is induced by micro-structural inhomogeneity and its growth is initially stable. Microscopically the heterogeneous structure of the material produces an inhomogeneous deformation field from the very early straining stage. However, irregularity of deformation in the body is not uniform, but there is a part in which the irregularity is greater than in other ones, that is near the boundary surface.

* Department of Civil Engineering and Engineering Mechanics, University of Arizona, Tucson, Arizona 85721 U.S.A.

** Department of Civil and Mineral Engineering, University of Minnesota, Minneapolis, Minnesota 55455 U.S.A. and Department of Engineering Science, National Technical University of Athens, 5 Heroes of Polytechnion Avenue, Zographou, Athens, Greece, GR-15773.

EUROPEAN JOURNAL OF MECHANICS, A/SOLIDS, VOL. 11, N° 1, 1992
0997-7538/92/01 21 14/$ 3.40/ © Gauthier-Villars

The above observations are also evidenced from extensive experiments on brittle materials. The following have been identified: as loading increases, e. g. in a uniaxial compression test, the density of microcracks rapidly proliferates leading to vertically aligned microcracks which result in gross slabbing of material from the specimens lateral surfaces [Hudson *et al.*, 1971]; [Fairhurst & Cook, 1966]). In general, the axial cracks are concentrated in the central portion of the specimens length because lateral restraint at the specimen ends, due to friction, inhibits their growth near the specimen-platen interface.

Theoretically, it has been predicted that a homogeneously strained body with tractionless surfaces develops surface undulations or waves. This phenomenon is known as surface instability ([Biot, 1965]; [Hill & Hutchinson, 1975]; [Vardoulakis, 1984]). In a more general formulation, conditions for the so-called complementary condition, [Benallal *et al.*, 1989], for governing instabilities at the boundary of a solid have been established. Since there are not physical length quantities in the continuum formulation of the problem, the wavelength of the surface instability mode remains arbitrarily short or long. The exponential decay beneath the surface is also arbitrary since it depends on the surface wavelength variation.

Buckling under plane strain conditions due to horizontal compression of an elastic, anisotropic half-space containing co-planar cracks at arbitrary locations has been analyzed recently by Vardoulakis & Papamichos [1991]. It is demonstrated that the critical buckling stress decreases dramatically as the distance between the free surface and the cracks diminishes. Further the influence of cracks far from the surface has very little or no influence on the buckling stress. From these results it can be seen that a surface layer exists for which the presence of cracks influences the buckling stress significantly. In a *grosso modo* sense this layer is the nonhomogeneous, bursting part of the material. In a recent paper, [Papamichos *et al.*, 1990] have demonstrated, using a newly developed apparatus and a micromechanical model of surface parallel cracks, that surface instabilities lead to exfoliation in Indiana limestone.

The formulation introduced in ([Frantziskonis, 1989]; [Frantziskonis & Desai, 1987; 1990; 1991]) accounts for homogeneous damage development in a homogeneously strained brittle material structure and inhomogeneous surface degradation development close to the tractionless surface(s). Based on energy dissipation considerations it is shown that surface degradation instability (spalling) will occur before the final global one (e. g. shear band formation). Also it is shown that surface degradation mechanisms can explain the well known size and shape effects on the constitutive and strength behavior of brittle materials. This is in continuation of previous vork on damage and surface effects (for composites), and the related energy based instability problems, e. g. [F, 1989].

In the following, Mindlin's theory for microstructure is employed as a tool to explain important surface related phenomena. In this context, a restricted continuum formulation is achieved. First, the theory is formulated and the governing equations for uniaxial plane deformations are solved. The solution is compared to classical instability analysis. Finally, a parameter analysis is performed and the properties that influence surface instability are discussed.

2. Micro-structure considerations

In [M, 1964] Mindlin formulated a general and extremely powerful theory for micro-structure in linear elasticity. Although the theory is very general, the number of constants involved in the general theory is very large (903 independent constants are involved in the simplest general case) and their physical interpretation is rather impossible. However, if one is interested in surface effects under conditions of equilibrium, specific higher order terms of the general theory can be identified. Then a simplified theory results which gives light to important surface related phenomena. For completeness some of the definitions introduced by Mindlin are repeated herein. However, for compactness only the definitions relevant to this paper appear in the following. The physical interpretation of the higher order kinematic and static variables is given in [M, 1964].

Kinematic variables

Consider a material volume V, with boundary surface S, with x_i, $i=1, 2, 3$ the rectangular components of the material position vector. The displacement of a material particle is u_i. Embedded in each material particle there is assumed to be a micro-volume V′ with micro-displacement u_i'. The displacement gradient of the micro-medium is

$$\psi_{ij} = u'_{i,j} \tag{1}$$

where a comma denotes spatial derivative. The macro-strain is defined as usual

$$\varepsilon_{ij} = \frac{1}{2}(u_{i,j} + u_{j,i}) \tag{2}$$

and also a relative deformation is

$$\gamma_{ij} = u_{j,i} - \psi_{ij} \tag{3}$$

and a micro-deformation gradient is

$$\kappa_{ijk} = \psi_{jk,i}. \tag{4}$$

Typical components of ε_{ij}, γ_{ij} and κ_{ijk} are illustrated in Figure 1.

Static variables and field equations

Utilizing the principle of virtual work, dynamic quantities dual to the above kinematic ones are defined

$$\delta W = \tau_{ij}\,\delta\varepsilon_{ij} + \sigma_{ij}\,\delta\gamma_{ij} + \mu_{ijk}\,\delta\kappa_{ijk} \tag{5}$$

$$\int_V \delta W\, dV = \int_V f_i\,\delta u_i\, dV + \int_V \Phi_{ij}\,\delta\psi_{ij}\, dV + \int_S t_i\,\delta u_i\, dS + \int_S T_{ij}\,\delta\psi_{ij}\, dS \tag{6}$$

where τ_{ij} is the Cauchy stress σ_{ij} is the relative stress and μ_{ijk} is double stress. The first index of μ_{ijk} designates the normal to the plane across which the component jk acts. For example μ_{111} is a double force per unit area (tensile or compressive) acting on a unit

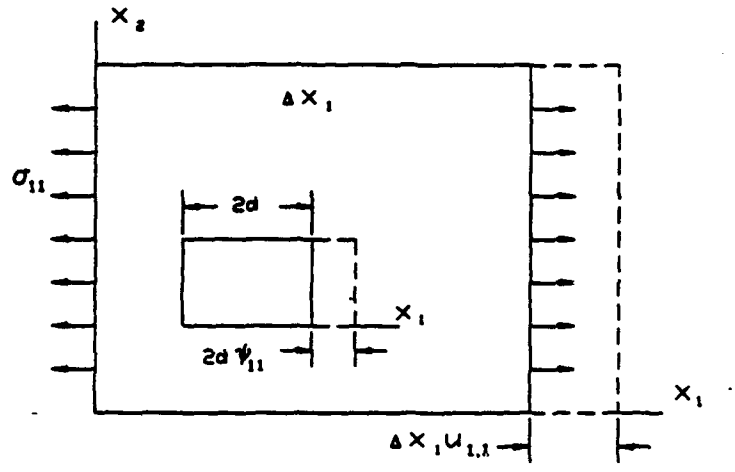

Fig. 1. – Relative Stress σ_{11}, Displacement Gradient $u_{1,1}$, Micro-Deformation ψ_{11}, Relative Deformation $\gamma_{11} = u_{1,1} - \psi_{11}$.

$$\kappa_{111} = \psi_{11,1}$$

Fig. 2. – Double Stress μ_{111} and Gradient of Micro-Deformation κ_{111}.

area on the plane transverse to axis 1. Typical components of μ_{ijk} are shown in Figure 2. The variational equation of motion is established as [M, 1964]

$$(7)\quad \int_V (\tau_{ij,i} + \sigma_{ij,i} + f_j)\,\delta u_j\,dV + \int_V (\mu_{ijk,i} + \sigma_{jk} + \Phi_{jk})\,\delta\psi_{jk}\,dV + \int_S [t_j - n_i(\tau_{ij} + \sigma_{ij})]\,\delta u_j\,dS + \int_S (T_{jk} - n_i\mu_{ijk})\,\delta\psi_{jk}\,dS = 0.$$

The twelve general equilibrium equations, follow from (7) and in the absence of body forces and body double forces can be written, in rate form

$$(8)\quad \dot{\tau}_{ij,i} + \dot{\sigma}_{ij,i} = 0$$

$$(9)\quad \dot{\mu}_{ijk,i} + \dot{\sigma}_{jk} = 0.$$

Then the relative stress can be eliminated from the rate-equilibrium equations

$$(10)\quad \dot{\sigma}_{jk} = -\dot{\mu}_{kij,i}.$$

We define the equilibrium stress as

$$(11)\quad \dot{\pi}_{ij} = \dot{\tau}_{ij} + \dot{\sigma}_{ij} = \dot{\tau}_{ij} - \dot{\mu}_{kij,k}.$$

The twelve traction boundary conditions are

$$\dot{t}_i = n_i(\dot{\tau}_{ij} + \dot{\sigma}_{ij}) \tag{12}$$

$$\dot{\mathbf{T}}_{jk} = n_i \dot{\mu}_{ijk} \tag{13}$$

where n_i is the outward normal to the boundary surface, t_i is the external force on the boundary and $\mathbf{T}_{ij}$ is the boundary couple force. It is interesting to note that the Cosserat continuum [Scheefer, 1962] can be obtained by imposing certain restrictions on the static and kinematic variables described above.

Restricted continuum

A particular case of Mindlin's continuum is the so-called restricted continuum; *i.e.* a micro-homogeneous material for which the macroscopic strain coincides with the micro-deformation. This leads to a vanishing relative deformation rate, and, accordingly to a rate of micro-deformation gradient that coincides with the strain-rate gradient.

The weak formulation of the balance law of linear momentum together with the appropriate set of boundary conditions is achieved through the principle of virtual work. In accordance with [M, 1964] we first define the virtual work of internal forces $\delta W^{(i)}$, *i.e.*

$$\delta W^{(i)} = \tau_{ij}\,\delta\varepsilon_{ij} + \mu_{ijk}\,\delta\kappa_{ijk}. \tag{14}$$

This work equation postulates that the Cauchy stress is dual in energy to the macroscopic strain and that the double stress is dual in energy to the gradient of the strain. Since there is no relative deformation rate, the relative stress is workless. The virtual strain and its gradients are computed straight forward from a virtual displacement field.

With expression (14) for the local variation of the virtual internal work done by the stress, we can compute the corresponding variation for a material volume V from the relation

$$\Delta W^{(i)} = \int_V \delta W^{(i)}\, dV. \tag{15}$$

The surface S of the considered volume V is divided into two complementary parts S_u and S_σ such that on S_u kinematic data whereas on S_σ static data are prescribed. In classical continua these are constraints on displacements and tractions, respectively. Since second-grade models introduce second strain gradients into the constitutive description, additional kinematic data must be prescribed on S_u. With the displacement already given in S_u, only its normal derivative with respect to that boundary is unrestricted. This means that on S_u the normal derivative of the displacement should also be given; *i.e.*

$$u_i = w_i \quad \text{and} \quad \mathrm{D}v_i = r_i \text{ on } S_u \tag{16}$$

where $\mathrm{D} = n_{k,k}$ is the derivative in the direction normal to the (smooth) boundary with local unit normal n_k.

For the computation of the virtual work of external forces $\Delta W^{(e)}$ we have to consider not only the surface tractions but also the work of the double forces. Following these

considerations, the virtual work of external forces becomes

$$\Delta W^{(e)} = \int_S (t_i \delta u_i + R_i D \delta u_i) \, dS \tag{17}$$

where t_i and R_i are surface tractions and double forces, respectively. From (14), (15), and (17) the virtual work equation $\Delta W^{(i)} = \Delta W^{(e)}$ becomes

$$\int_V (\tau_{ij} \delta \varepsilon_{ij} + \mu_{ijk} \kappa_{ijk}) \, dV = \int_S (t_i \delta u_i + R_i D \delta u_i) \, dS \tag{18}$$

From this virtual work equation we finally derive field equations

$$\tau_{jk,j} - \mu_{ijk,ij} = 0 \tag{19}$$

and the corresponding boundary conditions

$$n_j \tau_{jk} - n_i n_j D \mu_{ijk} - (n_i D_j + n_j D_i) \mu_{ijk} + (n_i n_j D_l n_l - D_j n_i) \mu_{ijk} = t_k \tag{20}$$

$$n_i n_j \mu_{ijk} = R_k \tag{21}$$

where $D_j = (\delta_{jl} - n_j n_l)_{,l}$. Constraint (20) comes in place of the classical boundary condition for surface tractions. Constraint (22) means that on some part of the boundary S the flux of the plastic shear strain might be given, *i.e.* on S_σ.

In order to solve the boundary value problem defined above, additional equations relating the stresses and double stresses to the strain, relative deformation and to the micro-deformation gradient must be included. These are specific to the material and are the constitutive equations.

3. Surface instabilities

In this paper, only plane-strain surface instabilities under initial stress will be discussed. It should be noted, however, that three-dimensional surface instabilities in the sense of Hutchinson & Tvergaard [1980] are also possible. These surface instabilities will not be discussed here. Consider the problem depicted in Figure 3. Starting from a stress-free state C_0, the structure is stressed uniaxially, under plain strain conditions. Let C be the resultant configuration. In order to study the stability of continued equilibrium in C, the existence of non-homogeneous infinitesimal transition, $C \to C'$, is investigated, with C being the reference configuration. The equilibrium in C is unstable if an unbounded,

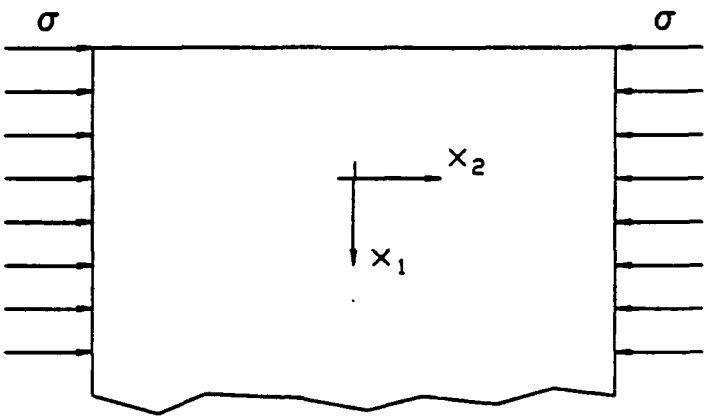

Fig. 3. – Half Space Under Compressive Load.

non-periodic solution exists. Further discussion on the types of instabilities can be found in the papers by Needleman [1979] and Vardoulakis [1984]. The equilibrium stress tensor, $\dot{\pi}_{ij}$ can be written as a function of co-rotational stress $\dot{\pi}^{R}_{ij}$

$$\dot{\pi}_{ij} = \dot{\pi}^{R}_{ij} + \dot{\omega}_{ik}\pi_{kj} - \pi_{ik}\dot{\omega}_{kj} \tag{22}$$

where $\dot{\omega}_{ij}$ is the rate of rotation tensor

$$\dot{\omega}_{ij} = \frac{1}{2}(\dot{u}_{i,j} - \dot{u}_{j,i}) \tag{23}$$

For the plain-strain problem of Figure 3 we assume incrementally linear constitutive equations for the Cauchy stress-rate

$$\begin{cases} \dot{\tau}_{11} = 2\mu^* \dot{\varepsilon}_{11} + (1 - \sin\varphi)\dot{p} \\ \dot{\tau}_{22} = 2\mu^* \dot{\varepsilon}_{22} + (1 + \sin\varphi)\dot{p} \\ \dot{\tau}_{12} = 2\mu \dot{\varepsilon}_{12} \end{cases} \tag{24}$$

where

$$\dot{\varepsilon}_{ij} = \frac{1}{2}(v_{i,j} + v_{j,i}), \qquad v_i = \dot{u}_i \tag{25}$$

and p is the hydrostatic stress. The quantity $4\mu^*$ is the instantaneous tangent modulus and μ is the instantaenous shear modulus for shearing parallel to the coordinate axes, and φ is the mobilized friction angle. Material parameters μ, μ^* and φ are, in general, dependent on the histories of deformation. For the purposes of this paper the particular dependence is specified later. However, the range of these parameters is important for specifying the solution regime for the surface instability problem.

The constitutive equation for the double stress rate is written as

$$\dot{\mu}_{111} = \mu l^2 \dot{\varepsilon}_{11,1}. \tag{26}$$

A dimensional analysis shows that l has dimension of length and as shown subsequently this quantity is important for the surface instability problem.

Equilibrium can be expressed in terms of the equilibrium stress rate

$$\begin{cases} \dot{\pi}_{11,1}+\dot{\pi}_{12,2}-\tau_{22}\dot{\omega}_{21,2}=0 \\ \dot{\pi}_{21,1}+\dot{\pi}_{22,2}-\tau_{22}\dot{\omega}_{21,1}=0 \end{cases} \tag{27}$$

and $\tau_{22}=\sigma$, σ being the external applied stress, Figure 3. From (22) and (24) and considering μ_{111} to be, in general, non zero and all other components of μ_{ijk} being zero for this specific problem, it follows that

$$\begin{cases} \dot{\pi}_{11}=\dot{\tau}_{11}-\dot{\mu}_{111,1}=2\mu^*\dot{\varepsilon}_{11}+(1-\sin\varphi)\dot{p}-\mu l^2\dot{\varepsilon}_{11,11} \\ \dot{\pi}_{22}=\dot{\tau}_{22},\ \dot{\pi}_{12}=\dot{\pi}_{21}=\dot{\tau}_{12}=\dot{\tau}_{21}, \end{cases} \tag{28}$$

Then, the two equilibrium Equations (27) are expressed as

$$\begin{cases} -(1-\sin\varphi)\dot{p}_{,1}=-\mu l^2 v_{1,1111}+2\mu^* v_{1,11}+\left(\mu+\dfrac{\sigma}{2}\right)v_{1,22}+\left(\mu+\dfrac{\sigma}{2}\right)v_{2,12} \\ -(1+\sin\varphi)\dot{p}_{,2}=2\mu^* v_{2,22}+\left(\mu+\dfrac{\sigma}{2}\right)v_{1,21}+\left(\mu-\dfrac{\sigma}{2}\right)v_{2,11}, \end{cases} \tag{29}$$

Introducing a stream function Ψ such that

$$v_1=\Psi_{,2}, \qquad v_2=-\Psi_{,1} \tag{30}$$

we satisfy material incompressibility constraint, and eliminating $\dot{p}$ from (29) gives

$$-L^2\Psi_{,221111}+\Psi_{,1111}+b\Psi_{,1122}+c\Psi_{,2222}=0 \tag{31}$$

where

$$\begin{cases} b=[(\lambda^2+1)(1-\xi_2)-(\lambda^2-1)\xi_1]/(\xi_1+\xi_2) \\ c=\lambda^2(\xi_2-\xi_1)/(\xi_1+\xi_2) \\ \lambda=\tan(\pi/4+\varphi/2) \\ \xi_1=-\dfrac{\sigma}{4\mu^*},\ (\tau_{22}<0), \qquad \xi_2=\dfrac{\mu}{2\mu^*} \\ L^2=\dfrac{\xi_2}{\xi_1+\xi_2}l^2. \end{cases} \tag{32}$$

Differential Equation (31) is a singular perturbation of the original (resulting without micro-structure considerations) as discussed by Hill and Hutchinson [1975] and others. This is discussed further subsequently. Following [B, 1965], plane strain surface instabilities can be analyzed by setting

$$\begin{cases} \Psi=\dfrac{H}{m\pi}\hat{u}(x)\sin y \\ x=\dfrac{x_1}{H}, \qquad y=m\pi\dfrac{x_2}{H}, \qquad m=1,2,\ldots \end{cases} \tag{33}$$

Here, $2\pi H$ represents wavelength. From the above and (30) it follows that

$$\begin{cases} v_1 = \hat{u}(x)\cos y \\ v_2 = -\dfrac{1}{m\pi}\hat{u}'(x)\sin y \end{cases} \tag{34}$$

where $(.)' = d/dx$. Substituting Ψ from (33) into (31) yields the governing equation for the stability problem

$$\{1+(m\pi)^2(L/H)^2\}\hat{u}^{IV} - (m\pi)^2 b\hat{u}'' + (m\pi)^4 c\hat{u} = 0. \tag{35}$$

The solution of (35) is

$$\hat{u}(x) = \sum_{j=1}^{4} c_j \exp(m\pi\alpha_j x) \tag{36}$$

where c_j are integration constants and a_j satisfy the characteristic equation

$$\alpha_j^4 - \frac{b}{1+n}\alpha_j^2 + \frac{c}{1+n} = 0 \tag{37}$$

where

$$n = (m\pi)^2(L/H)^2, \qquad \bar{n} = (m\pi)^2(l/H)^2, \qquad 0 < \bar{n} \ll 1 \quad \text{for } l \ll H. \tag{38}$$

Introducing

$$D = \frac{b^2}{(1+n)^2} - \frac{4c}{1+n} \tag{39}$$

the possibilities for solving the above equation are classified as follows, depending on whether there are 4, 2, or 0 real values of α.

(H) hyperbolic regime: 4 real solutions α

$$\begin{cases} b/(1+n) > 0, \quad c/(1+n) > 0, \quad D > 0 \\ \text{or} \\ b/(1+n) > 0, \quad c/(1+n) = 0 \\ \text{or} \\ b/(1+n) > 0, \quad D = 0 \end{cases} \tag{40}$$

(P) parabolic regime: 2 real solutions α

$$c/(1+n) < 0, \quad \text{or} \quad b/(1+n) < 0, \quad c/(1+n) = 0 \tag{41}$$

(EC) elliptic-complex regime: 4 complex solutions α

$$D < 0 \tag{42}$$

(EI) elliptic-imaginary regime: 4 imaginary solutions α

$$b/(1+n)>0, \qquad c/(1+n)>0, \qquad D>0. \tag{43}$$

The notion of surface instability means that the deformation is confined close to the surface; *i.e.* the displacement field is fading exponentially with x, being zero at infinite x, thus

$$\lim_{x\to\infty} \hat{u}_i = 0 \qquad \text{or} \qquad \mathrm{Re}\{\alpha_j\}<0. \tag{44}$$

In the hyperbolic regime, the solution is of the form $u=\exp(\mathrm{im}\,\pi\alpha x)$ where α is real. This solution can not satisfy the boundness condition (44), thus surface instabilities in (H) are not possible.

The solution in the various subregimes of (E) are

(EC)-subregime

$$\begin{cases} \hat{u}^1 = \exp(-m\pi A x)\cos(m\pi B x) \\ \hat{u}^2 = \exp(-m\pi A x)\sin(m\pi B x) \end{cases} \tag{45}$$

where

$$A=\sqrt{(\sqrt{c/(1+n)}+b/2(1+n))/2}, \qquad B=\sqrt{(\sqrt{c/(1+n)}-b/2(1+n))/2} \tag{46}$$

(EI)-subregime

$$\begin{cases} \hat{u}^1 = \exp(-m\pi a_1 x) \\ \hat{u}^2 = \exp(-m\pi a_2 x) \end{cases} \tag{47}$$

where

$$a_1=\sqrt{(-b/(1+n)+\sqrt{D})/2}, \qquad a_2=\sqrt{(-b/(1+n)-\sqrt{D})/2}. \tag{48}$$

Introducing the representation

$$\dot{p}=\hat{p}(x)\cos y \tag{49}$$

from (29), (33) and (34) it follows that

$$\hat{p}=\left[-\left(\mu-\frac{\sigma}{2}\right)\frac{1}{H(m\pi)^2}\hat{u}''' + \frac{1}{H}\left(2\mu^*-\mu-\frac{\sigma}{2}\right)\hat{u}'\right]\Big/(1+\sin\varphi). \tag{50}$$

Using constitutive equations (24), (26) and the above relation (47) the boundary condition $\dot{\pi}_{11}=0$ for $x=0$ yields

$$\begin{cases} (1+n)\,\hat{u}''' - (m\pi)^2 P\,\hat{u}' = 0 \\ P=\dfrac{\lambda^2+1+\xi_1-\xi_2}{\xi_1+\xi_2} \end{cases} \tag{51}$$

Boundary condition $\dot{\pi}_{12}=0$ at $x=0$ yields, from (24), (28), (30), and (31)

$$\hat{u}''+(m\pi)^2\hat{u}=0. \tag{52}$$

The boundary condition for the double stresses (13) is discussed in the following. Introducing $\hat{u}^i$ from (45) or (47) into the boundary conditions (51) and (52) the following homogeneous equations are obtained

$$\begin{cases} (a_1^3 + \mathrm{P}a_1)c_1 + (a_2^3 + \mathrm{P}a_2)c_2 = 0 \\ (a_1^2 + 1)c_1 + (a_2^2 + 1)c_2 = 0 \end{cases} \tag{53}$$

for the (EI) sub-regime, and

$$\begin{cases} (\mathrm{A}^2 - \mathrm{B}^2 + 1)c_1 - 2\mathrm{AB}c_2 = 0 \\ [(1+n)(3\mathrm{AB}^2 - \mathrm{A}^3) + \mathrm{PA}]c_1 + [(1+n)(3\mathrm{A}^2\mathrm{B} - \mathrm{B}^3) - \mathrm{PB}]c_2 = 0 \end{cases} \tag{54}$$

for the (EC) sub regime. For non trivial solution [$c_j \neq 0$ in (36)] the eigenvalue equation resulting from (53) can be solved in terms of the critical stress σ. As can be seen clearly, the final instability condition is a perturbation of the original Hill and Hutchinson problem. We introduced a single pertrubation parameter, denoted by n, and we expect to obtain a "dispersion" law for the surface buckling load.

In order to solve the eigenvalue Eq. (53) the expressions for μ and μ^* must be specified. In order to perform a relatively simple parametric study, we will discuss here only a one parameter family of stress-strain curves of the power law type. It is assumed that the stress-strain curve from a plain strain uniaxial compression is given by

$$\frac{\tau}{\tau_0} = \left(\frac{\gamma}{\gamma_0}\right)^{\mathrm{N}} \tag{55}$$

where N is a constant between zero and one, τ_0 and γ_0 are arbitrary reference values of τ and γ respectively, γ is the second is the second invariant of the deviator tensor of ε_{ij}, and τ is the second invariant of the deviator tensor of σ_{ij}. For this kind of hardening function the shear moduli μ and μ^* are expressed as

$$\mu = \frac{\tau}{\gamma}, \qquad \mu^* = \mathrm{N}\mu. \tag{56}$$

The mobilized friction angle φ is expressed as [V, 1984]

$$\sin\varphi = \frac{\mathrm{M}(\gamma/\gamma_c)^{\mathrm{N}}}{1 + \mathrm{M}(\gamma/\gamma_c)^{\mathrm{N}}} \tag{57}$$

where subscript c denotes value at failure and M is a constant related to the strength ratio (uniaxial strength in tension over uniaxial strength in compression).

For $n = 0$ the analysis coincides with the one presented in [V, 1984]. Let γ_s be the strain at surface instability for $n = 0$ and γ_t the one for $n \neq 0$. Let

$$\mathrm{R} = \frac{\gamma_t}{\gamma_s} = \left(\frac{\tau_t}{\tau_s}\right)^{1/\mathrm{N}}. \tag{58}$$

Obviously for $\bar{n} = 0$ we obtain $\mathrm{R} = 1$. For the solution of the eigenvalue problem (53) four different values of N, namely 0.2, 0.4, 0.6 and 0.8, were considered. The value of n

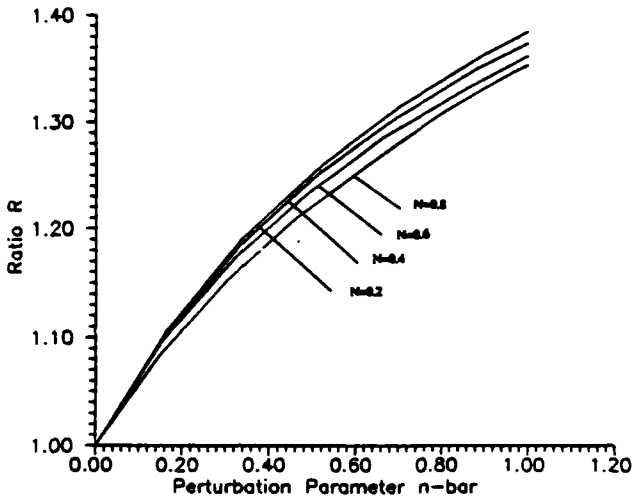

Fig. 4. – Perturbation parameter $\bar{n}$ versus $R = \gamma_n/\gamma_s$.

was varied between 0 and 1. Figure 4 shows the influence of $\bar{n}$ on the surface instability analysis. As can be seen such influence is practically insensitive to the value of material constant N. Since $\bar{n}=0$ corresponds to the long wave limit it also corresponds to the first buckling load. Also, since higher values of $\bar{n}$ indicate surface effects to a grater depth, it seems appropriate that the surface instability stress increases with increasing n. On the other hand $\bar{n}=1$ corresponds to the lowest physically meaningful wavelength limit which depicts the so-called skin-effect that is localized surface buckling strain. Figure 5 shows the eigenstrain field for $N=0.2$, $n=1$ and $M=0$ (non-frictional material).

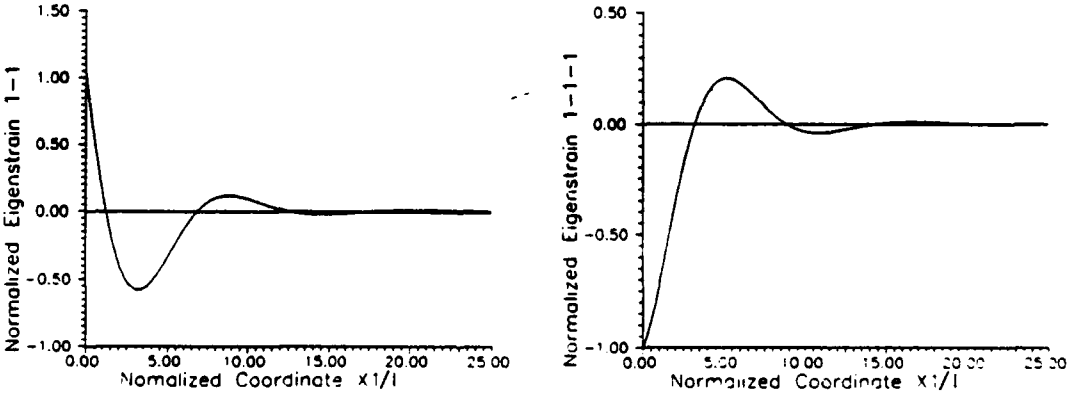

Fig. 5. – Normalized Depth X_1/l versus eigenstrain.
$N=0.2$, $\bar{n}=1$, $M=0$. (*a*) X_1/l vs ε_{11}, (*b*) X_1/l vs ε_{111}.

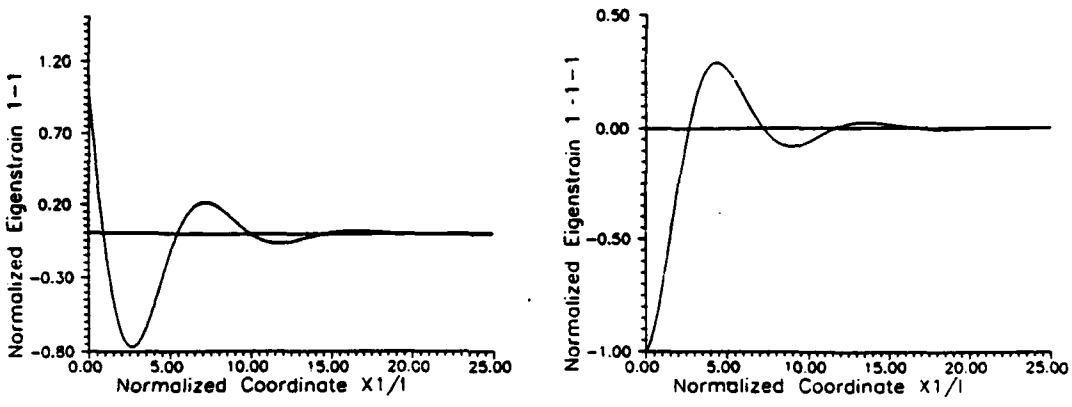

(*a*) (*b*)

Fig. 6. – Normalized Depth X_1/l versus eigenstrain.
$N=0.2$, $\bar{n}=1$, $M=0.43$. (*a*) X_1/l vs ε_{11}, (*b*) X_1/l vs ε_{111}.

Figure 6 shows the eigenstrain field for $N=0.2$, $n=1$ and $M=0.43$ (frictional material). According to Eqs. (45) or (47) the attenuation of the various eigenfields is governed by the coefficients a_1, a_2 or A, B respectively. Note that the slope of the curve in Figures 5 b and 6 *b* is proportional to R_1 appearing in Eq. (21). For the example of Figure 5 we recognize that a significant % of attenuation is obtained at a depth of $5l$. From experiments ([G *et al.*, 1961]; [M, 1965]; [K & M, 1987]) for metals, [Yukutake, 1989] for brittle frictional materials) in various materials the depth of the surface degradation zone can be obtained which then provides l. Such a calibration of the internal material length l is paramount if one wishes to solve problems with eigenstresses in laminated materials by using constitutive equations of the present type. Notice that these equations constitute the simplest possible generalization of elastoplastic relations for such media.

Conclusions

The present analysis shows that micro-structure considerations highlight surface (skin) effects. Such effects can be attributed to localized surface buckling instabilities. The single introduced new parameter is the internal length l. We have provided in principle a method for estimating l. Here we used the simplest possible generalization of elastoplastic constitutive relations, applicable for monotonous loading cases. However, other types of constitutive equations can be employed to include for example fatigue, and its effects on surface degradation and buckling. Potential applications for problems prone to surface buckling, *i.e.* borehole wall stability, have been demonstrated through the presented analytical solution. Numerical solutions for such problems will be presented elsewhere. Such solutions together with experimental observations and parametric analysis for the estimation of l are expected to provide a tool for the analysis of structures prone to surface buckling.

Acknowledgements

This paper is a partial result of research supported by the Air Force Office of Scientific Research (AFOSR 890460, Bolling AFB for G.F.) and the National Science Foundation (CES-8800381 for I.V.).

REFERENCES

GERMER L. H., MACRAE A. U., HARTMAN C. D., 1961, Nickel surface, *J. Appl. Phys.*, 32, 2432-2439.

MINDLIN R. D., 1965, Second gradient of strain and surface-tension in linear elasticity, *Int. J. Solids Struct.*, 1, 417-438.

KITAGAWA H., MATSUSHITA H., 1987, Flow localization in elastic-plastic material developing from stress-free surface, *Intl. J. Solids Struct.*., 23, 351-368.

HUDSON J. A., BROWN E. T., FAIRHURST C., 1971, Shape of the complete stress strain curve for rock, *Proc. 13th Symp. Rock Mech.*, University of Illinois, Urbana.

FAIRHURST C., COOK N. G. W., 1986, The phenomenon of rock splitting parallel to the direction of maximum compression in the neighborhood of a surface, *Proc. First Intl. Congress Rock Mech.*, Lisbon, 1, 687-692.

BIOT M. A., 1965, *Mechanics of Incremental Deformations*, Wiley, New York.

HILL R., HUTCHINSON J. W., 1975, Bifurcation phenomena in the plane tension test, *J. Mech. Phys. Solids*, 23, 239-264.

VARDOULAKIS I., 1984, Rock bursting as a surface instability phenomenon, *Int. J. Rock Mech. Sci. & Geomech. Abstr.*, 21, 137-144.

BENALLAL A., BILLARDON R., GEYMONAT G., 1989, Some mathematical aspects of the damage softening rate problem, *In Cracking and Damage*, MAZARS J. and BAZANT Z. P. Eds., 247-258.

VARDOULAKIS I., PAPAMICHOS E., 1991, Surface instabilities in elastic anisotropic media with surface parallel Griffith cracks, *Int. J. Rock Ech. Min. Sci. & Geomech. Abstr.*, submitted.

PAPAMICHOS E., LABUZ J. F., VARDOULAKIS I., 1990, Surface Instabilities in Brittle Rock, *Int. Conf. on Micromech. of Failure of Quasi-brittle Matls.*, Albuquerque, New Mexico, June 6-8.

FRANTZISKONIS G., 1989, Damage and free edge effects in laminated composites. Energy and stability propositions, *Acta Mechanica*, 77, 213-230.

FRANTZISKONIS G., DESAI C. S., 1987, Elastoplastic model with damage for strain softening geomaterials, *Acta Mechanica*, 68, 151-170.

FRANTZISKONIS G., DESAI C. S., 1991, Surface degradation mechanics in brittle material structures, *Int. J. Fracture*, 48, 231-244.

FRANTZISKONIS G., DESAI C. S., 1990, Degradation instabilities in brittle material structures, *Mechs. Research Comm.*, 17, 135-141.

MINDLIN R. D., 1964, Micro-structure in linear elasticity, *Arch. Rational Mech. Anal.*, 4, 50-78.

SCHEEFER H., 1962, Das Cosserat-kuntinuum, *Zeit. Argew. Math. Mech.*, 47, 485-498.

HUTCHINSON J. W., TVERGAARD V., 1980, Surface instabilities on statically strained plastic solids, *Int. J. Mech. Sci.*, 22, 339-354.

NEEDLEMAN A., 1979, Non-normality and bifurcation in plane strain tension and compression, *J. mech. Phys. Solids*, 27, 231-254.

YUKUTAKE H., 1989, Fracturing process of granite inferred from measurements of spatial velocities and temporal variations in velocity duing triaxial deformations, *J. Geophys. Res.*, 94, 15639-15651.

(Manuscript received July 10, 1990;
in revised form March 4, 1991;
accepted March 6, 1991.)

Eur. J. Mech., A/Solids, 11, n° 2, 1- , 1992

Micro-structure in kinematic-hardening plasticity

I. VARDOULAKIS * and G. FRANTZISKONIS **

ABSTRACT. — A gradient regularization of the classical kinematic-hardening plasticity is presented. The underlying continuum model is formally related to Mindlin's elasticity theory with micro-structure. The evolution law for the back stress is identical to Mindlin's higher order equilibrium equation. For consistency reasons the flow rule of classical plasticity is modified by incorporating the Laplacian of the plastic multiplier. The variational formulation of the problem with appropriate boundary conditions is given and an expression for the dissipated energy is established. Shear-band analysis shows that the theory provides the band thickness, and regularizes the governing equations. Micro-structure introduces a singular perturbation to the classical surface instability analysis, and the internal length l is the perturbation parameter. In addition, micro-structure effects tend to reduce the wavelength at onset of surface instability.

1. Introduction

Vardoulakis & Aifantis [1991] developed a second grade isotropic hardening (I-H) plasticity theory, and demonstrated that in this case the constitutive equations are singular perturbations of the original ones and that the introduced internal length is the single perturbation parameter. The motivation for this type of work was the fact that classical theories of plasticity are inadequate for addressing problems such as strain localization and deformation patterning (shear band thickness and spacings), estimate of wavelength in surface instability problems, and mesh-size-independent numerical solution of large scale problems. It is known that resorting to non standard continuum models such mathematical and physical difficulties can be overcome. The term "regularization" of the original mathematical problem is associated with such procedures. Non standard continuum formulations include non-local, Cosserat, and strain-gradient dependent constitutive theories. An extensive review on this subject is given in [V & A, 1991] and is not repeated herein.

In this paper we address the problem of constitutive regularization for the particular case of kinematic-hardening (K-H) plasticity theory. Most applications of the K-H model refer to cyclic plasticity of ductile metals and cohesive soils, which can not be addressed

* Department of Civil and Mineral Engineering University of Minnesota Minneapolis, Minnesota 55455 USA, and Department of Engineering Science National Technical University of Athens 5 Heroes of Polytechnion Avenue Zographou, Athens, Greece, GR-15773.

** Department of Civil Engineering and Engineering Mechanics University of Arizona Tucson, Arizona 85721 USA.

EUROPEAN JOURNAL OF MECHANICS, A SOLIDS, VOL. 11, N° 2, 1992
0997-7538/92/02 1 00/$ 0.00/

properly by the J-H theory. In this paper, however, the emphasis does not lie on cyclic plasticity but rather on modeling brittle, pressure sensitive materials which undergo cohesion hardening and softening. This type of behavior is typical for ultra high strength concretes and high strength rocks. It is demonstrated here that Prager's formalism of K-H plasticity applies for modeling brittle solids. The term "kinematic-hardening" is kept here for easy reference purposes but could be replaced by the term "cohesion-hardening".

Micro-structure based formulation does not only regularize the classical K-H theory but it also provides physical insight into the back stress evolution law. Mindlin [M, 1964] was among the first to introduce higher order gradients in the context of linear elasticity. It turns out that there is a connection between the modified K-H theory and the micro-structure theory of Mindlin since a "complete balance law" for the back-stress is given here in connection to Mindlin's structure. Namely, it turns out that the evolution law for the back-stress is identical to the higher order equilibrium equation of Mindlin. The classical part of the back-stress evolution law (without higher order gradients) is interpreted as a double body force. This is exactly what has been suggested by Aifantis [A, 1978; A, 1985] for media with micro-structures where the back stress is identified as an internal stress associated with the evolving micro-structures. In addition, the divergence of the back stress is identified here as a configurational, higher order, self equilibrating stress, which is required to equilibrate the back stress.

The paper is organized as follows: in Section 2 the constitutive equations of the classical K-H plasticity model in relation to cohesion-hardening, pressure-sensitive material modeling are briefly outlined. Section 3 is devoted to microstructural considerations in elastoplasticity, the variational formulation and the complete set of equilibrium equations. Section 4 deals with the gradient modification of the K-H plasticity. The flow rule is modified by including the Laplacian of the plastic multiplier $\dot{\lambda}$ and the Laplacian of the plastic strain rate tensor $\dot{\varepsilon}^p_{ij}$. Prager's consistency condition is discussed and the incremental form of the constitutive equations is derived. The resultant stress-strain relations are singular perturbations of the ones of classical K-H theory. The single perturbation parameter l is called the internal length of the material. In order to give an insight to the physical meaning and possible experimental determination of l, shear-band and surface instability analysis are presented in Sections 5 and 6. The issues of shear band thickness and surface skin effect are also discussed.

2. Classical K-H plasticity

For easy reference purposes and clarity in notation we present here the basic assumptions and constitutive equations of K-H plasticity, described in detail in many textbooks on plasticity. We start with the decomposition of the strain rate $\dot{\varepsilon}_{ij}$ into an elastic and a plastic part, *i.e.*

$$\dot{\varepsilon}_{ij} = \dot{\varepsilon}^e_{ij} + \dot{\varepsilon}^p_{ij} \tag{2.1}$$

The yield function is expressed in terms of the stress σ_{ij} and the back stress α_{ij}

$$F(\tau_{ij}, \lambda) = 0 \qquad \text{where} \tag{2.2}$$

$$\tau_{ij} = \sigma_{ij} - \alpha_{ij} \tag{2.3}$$

is called hereafter the Cauchy stress tensor; see Section 3 in connection to [M, 1964]. Prager's consistency condition dictates that, for loading $\dot{F} = 0$ or, due to (2.2) and (2.3)

$$\frac{\partial F}{\partial \tau_{ij}}(\dot{\sigma}_{ij} - \dot{\alpha}_{ij}) + \frac{\partial F}{\partial \lambda}\dot{\lambda} = 0 \tag{2.4}$$

For demonstration purposes, we shall restrict ourselves in this section to associate flow-rule, which is written as

$$\dot{\varepsilon}^p_{ij} = \dot{\lambda}\frac{\partial F}{\partial \tau_{ij}} \tag{2.5}$$

The expression for the rate parameter $\dot{\lambda}$ can be derived from the consistency condition (2.4), the flow rule (2.5), and the elasticity relation

$$\dot{\sigma}_{ij} = C^e_{ijkl}\dot{\varepsilon}^e_{kl} \qquad \text{where} \tag{2.6}$$

$$C^e_{ijkl} = G\left(\delta_{ik}\delta_{jl} + \delta_{il}\delta_{jk} + \frac{2\nu}{1-2\nu}\delta_{ij}\delta_{kl}\right) \tag{2.7}$$

is the elastic constitutive tensor, G is the shear modulus and ν is the Poisson's ratio.

In order that the formulation of the constitutive model is complete, an evolution law for the back stress must be specified. Commonly used such laws are the Prager

$$\dot{\alpha}_{ij} = C\,\dot{\varepsilon}^p_{ij} \tag{2.8}$$

and the Ziegler

$$\dot{\alpha}_{ij} = \dot{\xi}(\sigma_{ij} - \alpha_{ij}) \tag{2.9}$$

and c, ξ are material related parameters.

From the consistency condition (2.4), the elasticity relation (2.6), the flow rule (2.5) and the back-stress evolution law *e.g.* (2.8) we obtain

$$\dot{\lambda} = \frac{1}{H}(B_{kl}\dot{\varepsilon}_{kl}) \tag{2.10}$$

where we have set

$$A_{ij} = \frac{\partial F}{\partial \tau_{ij}} = \frac{\partial F}{\partial \sigma_{ij}} \tag{2.11}$$

$$B_{ij} = A_{kl}C^e_{klij} = A_{kl}C^e_{ijkl} \tag{2.12}$$

$$H = B_{kl}A_{kl} + c\,A_{kl}A_{kl} - (\partial F/\partial \lambda) \tag{2.13}$$

and from (2.6), (2.5) and (2.10) we obtain the constitutive equations of K-H plasticity in terms of stress and strain-rates

$$\dot{\sigma}_{ij} = C^{ep}_{ijkl}\,\dot{\varepsilon}_{kl} \qquad \text{where} \tag{2.14}$$

$$C^{ep}_{ijkl} = C^{e}_{ijkl} - C^{p}_{ijkl} \tag{2.15}$$

$$C^{p}_{ijkl} = \frac{\langle 1 \rangle}{H} B_{ij} B_{kl} \tag{2.16}$$

$$\langle 1 \rangle = \begin{cases} 1 & \text{if } F = 0,\ \lambda > 0 \\ 0 & \text{else} \end{cases} \tag{2.17}$$

As an example we mention the Drucker-Prager K-H plasticity for which

$$F = \bar{\tau} - \mu (q - \bar{p}) = 0 \tag{2.18}$$

where μ is the friction coefficient and q is a parameter related to the cohesion of the material. In particular, we will restrict ourselves here to the special case where both μ and $q = q_0$ are constant; see Figure 1. In (2.18) $\bar{p} = (1/3)\tau_{kk}$ and $\bar{\tau} = \sqrt{(1/2)\, t_{ij} t_{ij}}$ are the first and second invariant, respectively, of the Cauchy stress tensor $\tau_{ij} = t_{ij} + \bar{p}\delta_{ij}$. In

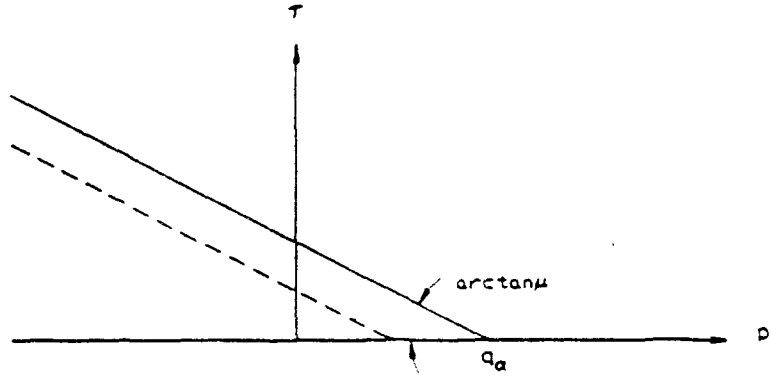

Fig. 1. – Plot of the yield surface in $p - \tau$ space and schematic representation of cohesion hardening.

particular, for the yield function (2.18) we have

$$A_{ij} = \frac{t_{ij}}{2\bar{\tau}} + \frac{1}{3}\mu\,\delta_{ij} \tag{2.19}$$

Similarly, we define the first and second invariant of the plastic strain-rate $\dot{\varepsilon}^p = \dot{\varepsilon}^p_{kk}$ and $\dot{\gamma}^p = \sqrt{2\, \dot{e}^p_{ij} \dot{e}^p_{ij}}$ and $\dot{e}^p_{ij}$ is the deviator tensor of $\dot{\varepsilon}^p_{ij}$; then, the flow rule (2.5) and Eq. (2.19) yield $\dot{\varepsilon}^p = \mu\dot{\lambda}$ and $\dot{\gamma}^p = \dot{\lambda}$. For illustration purposes we consider triaxial axisymmetric

extensions,

$$(\tau_{ij}) = \begin{pmatrix} \tau_{11} & 0 & 0 \\ 0 & \tau_{22} & 0 \\ 0 & 0 & \tau_{33} \end{pmatrix} \tag{2.20}$$

and $\tau_{11} = \tau_{22} < \tau_{33}$. For this state, equation (2.18) yields

$$\frac{\tau}{q_a - p} = \mu \quad \text{where} \tag{2.21}$$

$$q_a = q_0 + \frac{1}{\mu}(\tau_a + \mu p_a)$$

$$\tau = \frac{1}{\sqrt{3}}(\sigma_{33} - \sigma_{11}); \; \tau_a = \frac{1}{\sqrt{3}}(\alpha_{33} - \alpha_{11}) \tag{2.22}$$

$$\bar{\tau} = \tau - \tau_a$$

$$p = \frac{1}{3}(2\sigma_{11} + \sigma_{33}); \; p_a = \frac{1}{3}(2\alpha_{11} + \alpha_{33})$$

$$\bar{p} = p - p_a$$

Eq. (2.21) indicates that the Drucker-Prager K-H plasticity model is in fact a cohesion hardening/softening model, whenever we set $\mu = \text{const.}$, $q = \text{const.}$ and since $q_a = q_a(\varepsilon^p_{ij})$. figure 1. From (2.8) and (2.22) we obtain

$$\dot{\tau}_a = \frac{c}{2}\dot{\gamma}^p$$

$$\dot{p}_a = \frac{c}{3}\mu\dot{\gamma}^p \tag{2.23}$$

$$\dot{q}_a = \frac{1}{\mu}\left(\frac{1}{2} + \frac{1}{3}\mu^2\right)c\dot{\gamma}^p$$

thus the back stress evolution parameter c is expressed as, from $(2.23)_3$

$$c = \frac{\mu}{(1/2) + (1/3)\mu^2}\frac{dq_a}{d\gamma^p} \tag{2.24}$$

For the special case of uniaxial tension ($\sigma_{33} = \sigma \neq 0$, $\sigma_{11} = \sigma_{22} = 0$) we obtain

$$c = \frac{2(\sqrt{3} + \mu}{1 + \mu^2}\frac{d\sigma}{d\gamma^p} \tag{2.25}$$

and $\dot{\gamma}^p = 2(\dot{\varepsilon}^p_{33} - \dot{\varepsilon}^p_{11})$. Thus c is proportional to the slope of the $\sigma(\gamma^p)$-curve. observed in uniaxial tension tests.

If, for simplicity, we adopt a 2-D representation of the state of stress so that

$$(\sigma_{ij}) = \begin{bmatrix} \sigma_{11} & \sigma_{13} \\ \sigma_{31} & \sigma_{33} \end{bmatrix}$$

the yield function F in (2.18) is expressed as

(2.26) $$\left(\frac{\sigma_{33}-\sigma_{11}}{2} - \frac{\alpha_{33}-\alpha_{11}}{2}\right)^2 + (\sigma_{13}-\alpha_{13})^2 = R^2 \quad \text{where}$$

$$R = \mu q - \mu\left(\frac{\sigma_{33}+\sigma_{11}}{2} - \frac{\alpha_{33}+\alpha_{11}}{2}\right)$$

Eq. (2.26) represents a circle in the deviator plane as shown in Figure 2. This representation reveals that the considered model has the character of a kinematic/isotropic hardening model. It is purely kinematic when $\dot{p}_n = 0$ which implies that $\dot{\alpha}_{kk} = 0$ or $\dot{\varepsilon}^p = 0$. This means that the purely kinematic case is valid only when we deal with the special case of non-associativeness with plastic volume incompressibility.

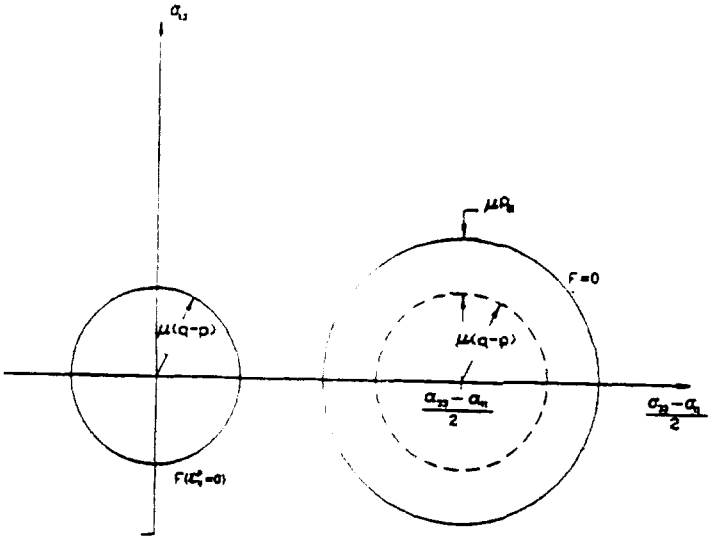

Fig. 2. – Plot of initial and subsequent yield surfaces in $(\sigma_{33}-\sigma_{11})/2$ vs σ_{13} space.

3. Micro-structure in elastoplasticity

In [M, 1964] Mindlin formulated a general and powerful theory for micro-structure in linear elasticity. As shown in this section Mindlin's continuum formalism can be successfully applied in the formulation of the gradient-dependent K-H plasticity theory. This

procedure provides a new interpretation for the back stress evolution law and for the dissipated energy.

In deviation from Mindlin's original paper, we introduce here a different micro-structure, which is more suitable for describing elastoplasticity as will be shown below. In order to motivate our choice of appropriate kinematic variables we start from mass balance considerations in a two-phase medium consisting of solids and voids. Let $v_i(x_i, t)$ be the velocity of the solid phase, where x_i $(i=1,2,3)$ are Cartesian coordinates of space and t denotes time. With ρ_s being the density of the solid phase and $n(x,t)$ the porosity of the medium, conservation of mass requires that

$$\partial_i v_i = -\frac{1}{\rho_s}\partial_t \rho_s + \frac{1}{1-n}\partial_t n \tag{3.1}$$

where $\partial_i = \partial/\partial x_i$ denotes spatial derivative and $\partial_t = \partial/\partial t$ denotes time derivative. We identify the macroscopic volumetric strain-rate as

$$\dot{\varepsilon}_{ii} = \partial_i v_i \tag{3.2}$$

and the microscopic volumetric strain-rate as

$$\dot{\psi}_{ii} = \frac{1}{1-n}\partial_t n \tag{3.3}$$

The quantity

$$\dot{\gamma}_{ii} = -\frac{1}{\rho_s}\partial_t \rho_s \tag{3.4}$$

is then the relative volumetric strain-rate.

If we consider that porosity in brittle solids (rocks, concretes) changes are practically inelastic, we identify the plastic volume changes as the microscopic volumetric strain rate,

$$\dot{\varepsilon}^p_{kk} = \dot{\psi}_{kk} \tag{3.5}$$

If we additionally consider the classical strain-rate decomposition of elastoplasticity, *i.e*

$$\dot{\varepsilon}_{ij} = \dot{\varepsilon}^e_{ij} + \dot{\varepsilon}^p_{ij} \tag{3.6}$$

then we identify the elastic volume changes as the relative volumetric strain-rate

$$\dot{\varepsilon}^e_{kk} = \dot{\gamma}_{kk} \tag{3.7}$$

The above scheme is generalized as follows: the symmetric part of the macro-velocity gradient is defined as the macroscopic strain-rate

$$\dot{\varepsilon}_{ij} = \frac{1}{2}(\partial_i v_j + \partial_j v_i) \tag{3.8}$$

The microscopic strain-rate is set equal to the plastic strain-rate

$$\dot{\psi}_{ij} = \dot{\varepsilon}^p_{ij} \tag{3.9}$$

Eq. (3.9) implicates vanishing anti-symmetric part of micro-deformation. Consequently, micro-rotation is not taken into account here, meaning that Cosserat effects are suppresed. The relative strain-rate coincides then with the elastic strain rate

$$\dot{\gamma}_{ij} = \dot{\varepsilon}_{ij} - \dot{\psi}_{ij} = \dot{\varepsilon}^e_{ij} \tag{3.10}$$

Finally, the micro-deformation gradient is given by the gradient of the plastic strain-rate

$$\dot{\kappa}_{ijk} = \hat{c}_i \dot{\psi}_{jk} = \hat{c}_i \dot{\varepsilon}^p_{jk} \tag{3.11}$$

The above definitions illustrate the fundamental difference between micro-structure in elasticity [M, 1964] and elastoplasticity. In elasticity micro-deformation derives from a potential field, namely the velocity field in the micro-medium. However, in elastoplasticity, where (3.9) holds, such a potential field for the plastic strain-rates does not exist. Similar observations apply also for the micro-deformation gradient. On the basis of these kinematic quantities we introduce the following dynamic ones: *a*) The Cauchy stress-rate $\dot{\tau}_{ij}$ which is dual in energy to $\dot{\varepsilon}_{ij}$. *b*) the relative stress-rate $\dot{\alpha}_{ij}$ which is dual in energy to $\dot{\gamma}_{ij}$ and *c*) the double stress-rate $\dot{\mu}_{ijk}$ which is dual in energy to $\dot{\kappa}_{ijk}$. The total stress-rate is defined by

$$\dot{\sigma}_{ij} = \dot{\tau}_{ij} + \dot{\alpha}_{ij} \tag{3.12}$$

Following the above definitions, the second order virtual work of internal forces is

$$\delta W^i = \dot{\tau}_{ij}\,\delta\dot{\varepsilon}_{ij} + \dot{\alpha}_{ij}\,\delta\dot{\gamma}_{ij} + \dot{\mu}_{ijk}\,\delta\dot{\kappa}_{ijk} = \dot{\sigma}_{ij}\,\delta\dot{\varepsilon}_{ij} - \dot{\alpha}_{ij}\,\delta\dot{\varepsilon}^p_{ij} + \dot{\mu}_{ijk}\,\hat{c}_i\,\delta\dot{\varepsilon}^p_{jk} \tag{3.13}$$

From (3.13) it is clear that the dissipated second order work of internal forces is expressed as

$$\delta\dot{W}^p = (\dot{\sigma}_{ij} - \dot{\alpha}_{ij})\,\dot{\varepsilon}^p_{ij} - \mu_{ijk}\,\hat{c}_i\,\dot{\varepsilon}^p_{jk} \tag{3.14}$$

If the plastic strain rates are constant in space (or if the plastic strain rate gradients are negligible) we obtain that

$$\delta\dot{W}^p = (\dot{\sigma}_{ij} - \dot{\alpha}_{ij})\,\dot{\varepsilon}^p_{ij} \tag{3.15}$$

If we identify the relative stress with the back-stress, (3.15) is exactly the expression for dissipated second order energy of classical K-H plasticity, that has to be always positive [Eisenberg, 1970].

With the expression (3.13) for the local variation of the virtual internal work done by the stress rates, we can compute the corresponding variation for a body of volume V from

$$\Delta W^i = \int_V \delta W^i\, dV \tag{3.16}$$

In the expression for the virtual work of external forces ΔW^e we have to include not only the rate of surface tractions and double forces but also the work of the body forces [M, 1964]. Then

$$\Delta W^e = \int_S \dot{t}_i \delta v_i \, dS + \int_S \dot{T}_{ij} \delta \dot{\psi}_{ij} \, dS + \int_V \dot{f}_i \delta \tau_i \, dV + \int_V \dot{\Phi}_{ij} \delta \dot{\psi}_{ij} \, dV \tag{3.17}$$

where $\dot{f}_i$ is the rate of body force per unit volume, $\dot{t}_i$ the rate of surface traction per unit surface, $\dot{\Phi}_{ij}$ the rate of body double-force per unit volume, and $\dot{T}_{jk}$ the rate of surface double-traction per unit area. Notice that it is not possible to have a direct geometric visualization of $\dot{\Phi}_{ij}$ and $\dot{T}_{ij}$. From (3.13), (3.16) and (3.17) the virtual work equation $\Delta W^i = \Delta W^e$ becomes

$$\int_V (\dot{\sigma}_{ij} \delta \dot{\varepsilon}_{ij} - \dot{\alpha}_{ij} \delta \dot{\psi}_{ij} + \dot{\mu}_{ijk} \partial_i \delta \dot{\psi}_{jk}) \, dV = \int_S \dot{t}_i \delta \tau_i \, dS + \int_S \dot{T}_{ij} \delta \dot{\psi}_{ij} \, dS + \int_V \dot{f}_i \delta \tau_i \, dV + \int_V \dot{\Phi}_{ij} \delta \dot{\psi}_{ij} \, dV \quad \text{or} \tag{3.18}$$

$$\int_V (\dot{\sigma}_{ij} \delta \dot{\varepsilon}_{ij} - \dot{f}_j \delta \tau_j) \, dV + \int_V (\dot{\mu}_{ijk} \partial_i \delta \dot{\psi}_{jk} - \dot{\alpha}_{ij} \delta \dot{\psi}_{ij} - \dot{\Phi}_{ij} \delta \dot{\psi}_{ij}) \, dV = \int_S \dot{t}_i \delta \tau_i \, dS + \int_S \dot{T}_{ij} \delta \dot{\psi}_{ij} \, dS \tag{3.19}$$

We consider that $\delta \tau_i$ and $\delta \dot{\psi}_{ij}$ are independent variations and that the boundary S of the volume V is subdivided as follows: *a*) into two complementary parts S_τ and S_σ such that τ_i is prescribed on S_τ, thus $\delta \tau_i = 0$ on S_τ, and *b*) into two complementary parts S_ψ and S_μ, such that $\dot{\psi}_{ij}$ is prescribed on S_ψ, thus $\delta \dot{\psi}_{ij} = 0$ on S_ψ. Accordingly, equation (3.19) splits into two independent integral equations

$$\int_V (\dot{\sigma}_{ij} \delta \dot{\varepsilon}_{ij} - \dot{f}_j \delta \tau_j) \, dV = \int_S \dot{t}_i \delta \tau_i \, dS \tag{3.20}$$

$$\int_V (\dot{\mu}_{ijk} \partial_i \delta \dot{\psi}_{jk} - \dot{\alpha}_{ij} \delta \dot{\psi}_{ij} - \dot{\Phi}_{ij} \delta \dot{\psi}_{ij}) \, dV = \int_S \dot{T}_{ij} \delta \dot{\psi}_{ij} \, dS \tag{3.21}$$

The above two equations constitute the basis of any week formulation of the rate boundary value problem. Moreover, from (3.20) we obtain

$$\int_V [\partial_i (\dot{\sigma}_{ij} \delta \tau_j) - \partial_i \dot{\sigma}_{ij} \delta \tau_j - \dot{f}_j \delta \tau_j] \, dV = \int_S \dot{t}_i \delta \tau_i \, dS \tag{3.22}$$

Applying the divergence theorem, the above equation becomes

$$\int_S \dot{\sigma}_{ij} \delta \tau_j n_i \, dS - \int_V (\partial_i \dot{\sigma}_{ij} + \dot{f}_j) \delta \tau_j \, dV = \int_S \dot{t}_i \delta \tau_i \, dS \tag{3.23}$$

which in turn yields

$$\begin{cases} \partial_i \dot{\sigma}_{ij} + \dot{f}_j = 0 & \text{in } V \\ \dot{\sigma}_{ij} n_j = \dot{t}_j & \text{on } S_\sigma \end{cases} \tag{3.24}$$

On the other hand from (3.21) we obtain, by applying the divergence theorem

$$\int_V [\partial_i (\dot{\mu}_{ijk} \delta\dot{\psi}_{jk}) - \partial_i \dot{\mu}_{ijk} \delta\dot{\psi}_{jk} - \dot{\alpha}_{ij} \delta\dot{\psi}_{ij} - \dot{\Phi}_{ij} \delta\dot{\psi}_{ij}] dV \tag{3.25}$$

$$= \int_S \dot{\mu}_{ijk} \delta\dot{\psi}_{jk} n_i dS - \int_V (\partial_i \dot{\mu}_{ijk} + \dot{\alpha}_{jk} + \dot{\Phi}_{jk}) \delta\dot{\psi}_{jk}) dV = \int_S \dot{\tau}_{ij} \delta\dot{\psi}_{ij} dS$$

which yields

$$\begin{cases} \partial_i \dot{\mu}_{ijk} + \dot{\alpha}_{jk} + \dot{\Phi}_{jk} = 0 & \text{in } V \\ \dot{\mu}_{ijk} n_i = \dot{\tau}_{jk} & \text{on } S_\mu \end{cases} \tag{3.26}$$

Eq. $(3.24)_1$ is the classical equilibrium equation; we identify σ_{ij} defined by (3.12) as the equilibrium stress tensor. Equation $(3.26)_1$ is higher order equilibrium equation which relates the back stress to double volume forces and to the divergence of double stresses. In the classical continuum $(3.26)_1$ is encountered in the form of an evolution law for the back stress, e.g. Prager's rule (2.8). From this point of view Prager's rule is reinterpreted as a constitutive equation for the double force

$$\dot{\Phi}_{ij} = -c\,\dot{\psi}_{ij} \tag{3.27}$$

Thus plastic strain-rates introduce self-equilibrating double body forces.

It should be noted that derivation of $(3.26)_1$ can be seen as a rigorous approach to what is usually termed in the literature as "complete balance law for the back stress" in references [A. 1978; A. 1985]. Further, we note that the present formulation reduces to the gradient flow theory of isotropic plasticity discussed in [V & A. 1991] if we set $\dot{\Phi}_{ij} = 0$, and $\dot{\psi}_{ij} = \dot{\varepsilon}^p_{kk} \delta_{ij}$.

Finally, we remark that Eq. $(3.24)_2$ expresses the boundary condition for the surface tractions, while $(3.26)_2$ expresses the boundary condition for the double force per unit area.

4. Gradient modification of K-H plasticity

The classical flow-rule for non-associative plasticity reads

$$\dot{\varepsilon}^p_{ij} = A^Q_{ij} \dot{\lambda} \qquad \text{where} \tag{4.1}$$

$$A^Q_{ij} = \frac{t_{ij}}{2\tau} + \frac{1}{3} \beta \delta_{ij} \tag{4.2}$$

and the plastic potential Q is expressed as, for Drucker-Prager K-H plasticity

$$Q = \bar{\tau} = \beta(\bar{q} - \bar{p}) \tag{4.3}$$

In the above equations t_{ij} is the deviator tensor of τ_{ij}, β is the dilatancy coefficient and $\bar{q}$ is an appropriate constant necessary to shift the plastic potential surface to the stress point in consideration.

Utilizing a non-local argument [Bazant, 1984; V & A, 1991] we generalize the flow rule (4.1) as

$$\dot{\varepsilon}^p_{ij} = A^Q_{ij}(\dot{\lambda} + l^2 \nabla^2 \dot{\lambda}) \tag{4.4}$$

It should be noticed that in references [Shreyer & Chen, 1986; Shreyer, 1990] instead of the Laplacian, non-linear gradient effects are introduced for modeling one dimensional softening and localization; the analytical solutions obtained in [S, 1990] give an insight to non-linear, non-local plasticity. We restrict ourselves here, however, to linear non-local models.

In order to generalize Prager's rule we modify the constitutive Eq. (3.27) for the double force and introduce a simple constitutive equation for the double stresses, which is motivated from the work presented in [V & A, 1991].

$$\Phi_{ij} = -c(\dot{\psi}_{ij} + l^2 \nabla^2 \dot{\psi}_{ij}) \tag{4.5}$$

$$\dot{\mu}_{rij} = M_{ijkl}\, \dot{\kappa}_{rkl} \tag{4.6}$$

or following (3.9) and (3.11) we obtain

$$\Phi_{ij} = -c(\dot{\varepsilon}^p_{ij} + l^2 \nabla^2 \dot{\varepsilon}^p_{ij}) \tag{4.5a}$$

$$\dot{\mu}_{rij} = M_{ijkl}\, \partial_r \dot{\varepsilon}^p_{kl} \tag{4.6a}$$

Similar simple constitutive equations for the double stress are used in [V & A, 1991; Frantziskonis & Vardoulakis, 1991].

We summarize the set of constitutive assumptions made so far

– Stress-rate decomposition	(3.12)	$\dot{\sigma}_{ij} = \dot{\tau}_{ij} + \dot{\alpha}_i$
– Strain-rate decomposition	(2.1)	$\dot{\varepsilon}_{ij} = \dot{\varepsilon}^e_{ij} + \dot{\varepsilon}^p_{ij}$
– Flow rule	(4.5)	$\dot{\varepsilon}^p_{ij} = A^Q_{ij}(\dot{\lambda} + l^2 \nabla^2 \dot{\lambda})$
– Consistency condition	(2.4)	$A^Q_{ij}\, \dot{\tau}_{ij} = 0$
– Balance law for $\dot{\alpha}_{ij}$	$(3.26)_1$	$\dot{\alpha}_{jk} = \partial_i\, \dot{\mu}_{ijk} - \Phi_{jk}$
– Constitutive Eq. for $\dot{\sigma}_{ij}$	(2.6)	$\dot{\sigma}_{ij} = C^e_{ijkl}\, \dot{\varepsilon}^e_{kl}$
– Constitutive Eq. for Φ_{ij}	(4.5a)	$\Phi_{ij} = -c(\dot{\varepsilon}^p_{ij} + l_1^2 \nabla^2 \dot{\varepsilon}^p_{ij})$
– Constitutive Eq. for $\dot{\mu}_{ijk}$	(4.6a)	$\dot{\mu}_{rij} = M_{ijkl}\, \partial_r \dot{\varepsilon}^p_{kl}$

Further differences between micro-structure in elasticity and elastoplasticity follow from the above constitutive equations: in elastoplasticity the total stress-rates are determined from the elastic (relative) strain-rates, whereas in elasticity both back (relative) stress and Cauchy stress derive from corresponding potentials. Double stresses and body forces in elastoplasticity derive from plastic (micro-) strain rates, whereas in elasticity the corresponding potentials are independent of micro-strain

A simple dimensional analysis reveals that l, appearing in the above expressions (4.4) and (4.5) has the dimension of length and is called "internal length". As mentioned in [V & A, 1991], prior to localization the coordinates x_i must be non-dimensionalized by some global dimension L of the structure under consideration. Since $(l^2/L^2) \ll 1$ we say that $\dot{\alpha}_{ij}$ varies slowly in space and that gradient effects are insignificant. However, when the deformation is localized in a narrow zone of intense shear then the spatial coordinates are non-dimensionalized by say the thickness d of the shear band, which is found to be a small multiple of l [V & A, 1991]. $\nabla^2 \dot{\varepsilon}_{ij}$ is multiplied by a number $(l/d)^2 = O(1)$, and accordingly gradient effects are not necessarily negligible.

It should be noticed that, as demonstrated by Muhlhaus and Aifantis [Muhlhaus & Aifantis, 1991], the consistency condition of gradient plasticity is in general a differential equation and not an algebraic one as in classical plasticity; cf. Eq. (2.10). However, as shown in [V & A, 1991], one can choose the constitutive tensor M_{ijkl} for the double stresses in such a way that the consistency condition assumes an algebraic form. If we choose

$$M_{ijkl} = l^2 C^e_{ijkl} \tag{4.7}$$

from (2.6) and $(3.6)_1$ the consistency condition (2.4) is written as

$$B_{kl}\dot{\varepsilon}_{kl} - (B_{kl} + c A_{kl})(A^Q_{kl} - l^2 \nabla^2 A^Q_{kl})\dot{\lambda} + l^4 A_{kl}(B^Q_{kl} + c A^Q_{kl})\nabla^4 \dot{\lambda} = 0 \tag{4.8}$$

where we have set

$$B^Q_{kl} = \frac{\partial Q}{\partial \sigma_{ij}} C^e_{ijkl} \tag{4.9}$$

Thus the consistency condition becomes a fourth order differential equation for the plastic multiplier $\dot{\lambda}$. If, for consistency with (4.5), we neglect the fourth order terms in (4.9) we obtain

$$\dot{\lambda} = \frac{1}{H} B_{kl}\dot{\varepsilon}_{kl} + O(l^4) \tag{4.10}$$

where by keeping $O(l^2)$-terms we have set

$$H = (B_{kl} + c A_{kl})(A^Q_{kl} - l^2 \nabla^2 A^Q_{kl}) \tag{4.11}$$

This means that the consistency condition is a $O(l^4)$ algebraic equation for the plastic multiplier. Thus from $(3.26)_1$, (4.5a) and (4.7) the following "evolution" law for the back stress is derived

$$\dot{\alpha}_{ij} = c\dot{\varepsilon}^p_{ij} - (C^e_{ijkl} + c\,\delta_{ik}\delta_{jl}) l^2 \nabla^2 \dot{\varepsilon}^p_{ij} \tag{4.12}$$

From (4.10) we derive the expression for $\nabla^2 \dot{\lambda}$

$$\nabla^2 \dot{\lambda} \simeq \frac{1}{H} B_{kl} \nabla^2 \dot{\varepsilon}_{kl} + \nabla^2 \left(\frac{B_{kl}}{H}\right) \dot{\varepsilon}_{kl} \qquad \text{and} \tag{4.13}$$

(4.14) $$\nabla^2\left(\frac{B_{kl}}{H}\right)\simeq\frac{1}{H}\left(\nabla^2 B_{kl}-\frac{1}{H}B_{kl}\nabla^2 H\right)$$

where we have neglected nonlinear terms. From (2.6), (4.4), (4.10), (4.11), (4.13) and (4.14) we finally obtain

(4.15) $$\dot\sigma_{ij}=L_{ijkl}\dot\varepsilon_{kl}-l^2 N_{ijkl}\nabla^2\dot\varepsilon_{kl}\qquad\text{where}$$

(4.16) $$L_{ijkl}=C^e_{ijkl}-\frac{\langle 1\rangle}{p}B^Q_{ij}\left[B_{kl}-l^2\left(\nabla^2 B_{kl}-\frac{1}{p}B_{kl}\nabla^2 p\right)\right]$$

(4.17) $$N_{ijkl}=\frac{\langle 1\rangle}{p}B^G_{ij}B_{kl}$$

Neglecting $O(l^2)$-terms in the stiffness tensor we finally obtain

(4.18) $$\dot\sigma_{ij}=C^{ep}_{ijkl}\dot\varepsilon_{kl}-l^2 C^p_{ijkl}\nabla^2\dot\varepsilon_{kl}\qquad\text{where}$$

(4.19) $$C^{ep}_{ijkl}=C^e_{ijkl}-C^p_{ijkl}$$

(4.20) $$C^p_{ijkl}=\frac{\langle 1\rangle}{H}B^Q_{ij}B_{kl}$$

Thus the present theory is a second grade rate constitutive theory, *i.e.* a theory for which the stress-rate depends on the strain-rate and on its Laplacian. Eqs. (4.18) can be seen as a singular perturbation of the classical ones, with l being the perturbation parameter. More importantly, besides the internal length l no new material parameter is introduced here.

5. Shear band analysis

Here we consider the Drucker-Prager K-H, then the expression for the yield surface is given in (2.18). For this specific function.

(5.1) $$\frac{\partial F}{\partial\tau_{ij}}=\frac{\partial F}{\partial\sigma_{ij}}=\frac{1}{3}\mu\delta_{ij}+\frac{1}{2\bar\tau}\bar t_{ij}$$

For simplicity and for the sake of illustration we consider a 2-D problem and write the constitutive Eqs. (4.18) in the coordinate system of the principal axes of τ_{ij}, under loading conditions. Let $\kappa=K/G$, K being the bulk modulus and G the shear modulus. For simplicity in notation stiffness tensors non-dimensionalized by G keep the same symbol, e.g.

(5.2) $$C^e_{ijkl}=(\kappa-1)\delta_{ij}\delta_{kl}+\delta_{ik}\delta_{jl}+\delta_{il}\delta_{jk}$$

Then (4.18) are written as

$$\dot{\sigma}_{11} = G(C^{ep}_{1111}\dot{\varepsilon}_{11} + C^{ep}_{1122}\dot{\varepsilon}_{22} - l_{11}^2\nabla^2\dot{\varepsilon}_{11} - l_{12}^2\nabla^2\dot{\varepsilon}_{22})$$

(5.3)
$$\dot{\sigma}_{22} = G(C^{ep}_{2211}\dot{\varepsilon}_{11} + C^{ep}_{2222}\dot{\varepsilon}_{22} - l_{21}^2\nabla^2\dot{\varepsilon}_{11} - l_{22}^2\nabla^2\dot{\varepsilon}_{22})$$

$$\dot{\sigma}_{12} = \dot{\sigma}_{21} = 2G\dot{\varepsilon}_{12} \qquad \text{where}$$

(5.4)
$$C^{ep}_{1111} = (\kappa+1) - \frac{G}{H}(\mu\kappa+1)(\beta\kappa+1)$$

$$C^{ep}_{2222} = (\kappa+1) - \frac{G}{H}(\mu\kappa-1)(\mu\kappa-1)$$

$$C^{ep}_{1122} = (\kappa-1) - \frac{G}{H}(\mu\kappa+1)(\beta\kappa-1)$$

$$C^{ep}_{2211} = (\kappa-1) - \frac{G}{H}(\mu\kappa-1)(\beta\kappa+1) \qquad \text{and}$$

(5.5)
$$l_{11}^2 = l^2 C^{p}_{1111} = l^2\frac{G}{H}(\mu\kappa+1)(\beta\kappa+1)$$

$$l_{22}^2 = l^2 C^{p}_{2222} = l^2\frac{G}{H}(\mu\kappa-1)(\beta\kappa-1)$$

$$l_{12}^2 = l^2 C^{p}_{1122} = l^2\frac{G}{H}(\mu\kappa+1)(\beta\kappa-1)$$

$$l_{21}^2 = l^2 C^{p}_{2211} = l^2\frac{G}{H}(\mu\kappa-1)(\beta\kappa+1)$$

(5.6)
$$H = G(\mu\kappa\beta+2) + c(\mu\beta/2+2)$$

The above expressions are introduced in the equilibrium Eqs. $(3.24)_1$, which in the absence of body forces read

(5.7)
$$\partial_1\dot{\sigma}_{11} + \partial_2\dot{\sigma}_{21} = 0$$

(5.8)
$$\partial_1\dot{\sigma}_{12} + \partial_2\dot{\sigma}_{22} = 0$$

We consider that a shear band is forming and is inclined with respect to the x_1 axis at an angle θ (*Fig.* 3). By introducing a new coordinate system $(x, y) = (n_2 x_1 + n_1 x_2,\ -n_1 x_1 + n_2 x_2)$ with axes parallel and normal to the shear band, $(n_1, n_2) = (-\sin\theta, \cos\theta)$, Eqs. (5.7) and (5.8) reduce to the following system of ordinary differential equations [V & A, 1991]

(5.9)
$$-l_{11}^2 n_1^2 v_1^{4} + a_{11} v_1'' - l_{12}^2 n_1 v_2^{4} + a_{12} v_2'' = 0$$

(5.10)
$$-l_{21}^2 n_1 n_2 v_1^{4} + a_{21} v_1'' - l_{22}^2 n_2^2 v_2^{4} + a_{22} v_2'' = 0$$

where v_i are the components of the velocity, $(.)' = \partial/\partial x$ and

(5.11)
$$[a_{ij}] = \begin{bmatrix} C^{ep}_{1111} n_1^2 + n_2^2 (C^{ep}_{1122}+1) n_1 n_2 \\ (C^{ep}_{1122}+1) n_1 n_2 b_1^2 + C^{ep}_{2222} n_2^2 \end{bmatrix}$$

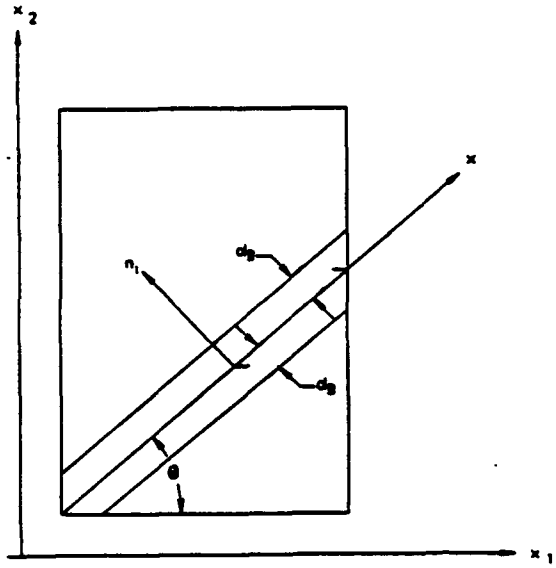

Fig. 3. – Shear band orientation within a specimen.

By seeking periodic solutions of the type $v_i = c_i \cos(qy)$, we obtain

(5.2) $$[b_{ij}]\{c_j\} = \{0\} \quad \text{where}$$

(5.13) $$[b_{ij}] = \begin{bmatrix} -l_{11}^2 n_1^2 q^4 - a_{11} q^2 & -l_{12}^2 n_1 n_2 q^4 - a_{12} q^2 \\ -l_{21}^2 n_1 n_2 q^4 - a_{21} q^2 & -l_{22}^2 n_2^2 q^4 - a_{22} q^2 \end{bmatrix} \quad \text{and}$$

(5.14) $$\{c_j\} = \begin{Bmatrix} c_1 \\ c_2 \end{Bmatrix}$$

c_i being constants. For non-trivial solution, the matrix Eq. (5.12) yields the following condition

(5.15) $$(ql)^2 = -\frac{Q(n_1, n_2)}{R(n_1, n_2)} \quad \text{where}$$

(5.16) $$Q = \det(a_{ij})$$

(5.17) $$R = g_{22} a_{11} n_2^2 + g_{11} a_{22} n_1^2 - (g_{12} a_{21} + g_{21} a_{12}) n_1 n_2; g_{ij} = (l_{ij}/l)^2$$

and q is related to the shear band thickness d_B, $d_B = \pi/q$. The condition $Q = 0$ coincides with the classical bifurcation condition

(5.18) $$C^{ep}_{1111} n_1^4 + (C^{ep}_{1111} C^{ep}_{2222} - C^{ep}_{1122} C^{ep}_{2211} - C^{ep}_{1122} - C^{ep}_{2211}) n_1^2 n_2^2 + C^{ep}_{2222} n_2^4 = 0$$

Before the occurrence of classical bifurcation and for any (n_1, n_2), $Q(n_1, n_2) > 0$. For any state past the classical bifurcation $Q < 0$. However, $R(n_1, n_2)$ is a quadratic form of the orientation cosines. It turns out that always $R > 0$ which means that the system of governing differential equations is always elliptic, as opposed to the classical system of

governing equations which is of changing type, from elliptic to hyperbolic at the point of classical bifurcation. As can be seen from (5.15) prior to classical bifurcation there is no real solution for the shear band thickness. At the classical bifurcation point d_B is infinite as compared to the internal length l, rapidly decreasing in the post-bifurcation regime. This well established qualitative result is discussed in [V & A, 1991].

Estimation of the internal length through shear-band analysis

Since for a 2-D model $\kappa = K/G = 1/(1-2\nu)$, if we assume that Poisson ratio is $\nu = 0.1$, then $\kappa = 1.25$. For a geologic material (rock, concrete) if we consider that the yield stress in uniaxial compression is ten times the yield strength in uniaxial tension, then for the 2D case $\mu = 0.818$. For the associative plasticity case $\beta = \mu$ and for the limit case that plastic incompressibility is assumed $\beta = 0$. Material parameter c is considered as a variable; however, for the purpose of this estimation the evolution law for c need not be specified: Let $c' = c/G$. Then the classical bifurcation condition (5.18) yields, at bifurcation onset, for the associative case $c' = -0.429$, $\theta = 73.2°$ and for the plastic incompressible case $c' = -0.389$, $\theta = 57.2°$. Thus differences in the flow-rule affect mainly the shear-band orientation angle. For the associative case and for the corresponding value of θ the dimensionless shear-band thickness d_B/l is plotted against $-c'$ in Figure 4. According to this figure the shear band thickness decreases rapidly after the onset of bifurcation. assuming a stationary value of $(d_B/l)_\infty \simeq 3$. Obviously, the solution for $(d_B/l)_\infty$ depends on

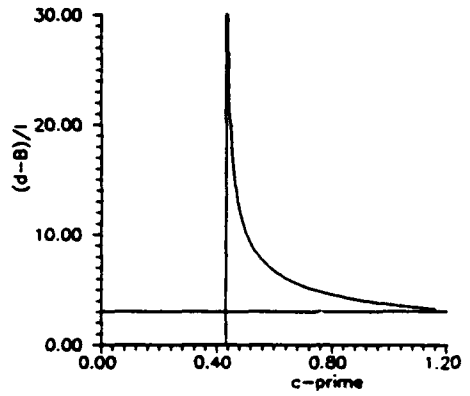

Fig. 4. – Shear band thickness d_B/l versus c'.

the values of constants such as ν, μ, β. For the specific values chosen herein, the value of c' at classical bifurcation is negative which implies that it occurs in the post peak regime. Note that the Prager evolution for the back stress was used herein. However, any other type of evolution law can be used. For example if the Ziegler evolution law is used then classical bifurcation occurs in the pre-peak regime [Tvergaard. 1978; Hutchinson & Tvergaard. 1981].

6. Surface instability analysis

The problem considered in this section is plane strain surface instabilities under initial stress, Figure 5. Analysis of these types of instabilities can be found in the papers by

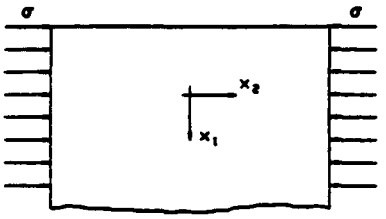

Fig. 5. – Problem considered for surface instability analysis.

Needleman [Needleman, 1979] and [Vardoulakis, 1984]. In reference [F & V, 1991] the effects of micro-structure on the so-called skin or surface degradation effects are studied.

Substituting the constitutive Eqs. (4.18) into the equilibrium Eqs. $(3.22)_1$ we obtain, for the problem depicted in Figure 5

$$\begin{aligned} &-l_{11}^2\nabla^2(\partial_{11}^2 v_1)-l_{12}^2\nabla^2(\partial_{21}^2 v_2)+C^{ep}_{1111}\partial_{11}^2 v_1+\partial_{22}^2 v_1+(C^{ep}_{1122}+1)\partial_{12}^2 v_2=0\\ &-l_{21}^2\nabla^2(\partial_{12}^2 v_1)-l_{22}^2\nabla^2(\partial_{22}^2 v_2)+C^{ep}_{2222}\partial_{22}^2 v_2+\partial_{11}^2 v_2+(C^{ep}_{2211}+1)\partial_{12}^2 v_1=0 \end{aligned} \tag{6.1}$$

For surface buckling modes, the velocity field is expressed in terms of two unknown amplitude functions

$$v_1=U(x)\sin(qy);\qquad v_2=V(x)\cos(qy) \tag{6.2}$$

$$\lim_{x\to\infty} U(x)\quad \lim_{x\to\infty} V(x) \tag{6.3}$$

and $x=x_1/L$, $y=x_2/L$, L is a reference length associated with the wavelength W of the deformation and q is again a dimensionless wavenumber. The wavelength W is inversely proportional to q such that $W=2\pi L/q$. Substituting the velocity field (6.2) in (6.1) and assuming that the two functions in (6.2) have the exponential form

$$\begin{cases} U(y)=A\,e^{\gamma x} \\ V(y)=B\,e^{\gamma x} \end{cases} \qquad \text{we obtain} \tag{6.4}$$

$$\begin{cases} A[z^2-C^{ep}_{1111}-q^2C^{p}_{1111}(1-z^2)]+B[-z(1+C^{ep}_{1122})-q^2C^{p}_{1122}z(1-z^2)]=0\\ A[z(1+C^{ep}_{2211})+q^2C^{p}_{2211}z(1-z^2)]+B[z(C^{ep}_{2222}+1)+q^2C^{p}_{2222}z^2(1-z^2)]=0 \end{cases} \tag{6.5}$$

where we have set

$$z=\frac{\gamma}{q} \tag{6.6}$$

For non-trivial solution in terms of A, B, the determinant of the system (6.5) must vanish. This leads to

$$\bar{q}^2=(ql/L)^2=\frac{S(z)}{T(z)} \quad \text{where} \tag{6.7}$$

$$S(z)=(z^2-C^{ep}_{1111})(C^{ep}_{2222}z^2-1)+z^2(1+C^{ep}_{1122})(1+C^{ep}_{2211}) \tag{6.8}$$

$$\begin{aligned} T(z)=&C^{p}_{1111}(1-z^2)(C^{ep}_{2222}z^2-1)-C^{p}_{2222}z^2(1-z^2)(z^2-C^{ep}_{1111})\\ &-z^2(1-z^2)[C^{p}_{2211}(1+C^{ep}_{1122})+C^{p}_{1122}(1+C^{ep}_{2211})] \end{aligned} \tag{6.9}$$

For the case where gradients effects are negligible or $l=0$, equation (6.7) reduces to the classical biquadratic equation for z. For $l\neq 0$ Eq. (6.7) is written as

$$Pz^6+Qz^4+Rz^2+S=0 \quad \text{where} \tag{6.10}$$

$$\begin{aligned} P&=\bar{q}^2 C^{p}_{2222}\\ Q&=\bar{q}^2(-C^{p}_{1111}C^{ep}_{2222}-C^{p}_{2222}-C^{p}_{2222}C^{ep}_{1111}+C^{p}_{1122}\\ &\quad +C^{p}_{2211}+C^{p}_{1122}C^{ep}_{2211}+C^{p}_{2211}C^{ep}_{1122})-C^{ep}_{2222}\\ R&=\bar{q}^2(C^{p}_{1111}C^{ep}_{2222}+C^{p}_{2222}C^{ep}_{1111}-C^{p}_{1122}-C^{p}_{2211}+C^{p}_{1111}-C^{p}_{1122}C^{ep}_{2211}\\ &\quad -C^{p}_{2211}C^{ep}_{1122})+C^{ep}_{1111}C^{ep}_{2222}-C^{ep}_{1122}C^{ep}_{2211}-C^{ep}_{1122}-C^{ep}_{2211}\\ S&=\bar{q}^2(-C^{p}_{1111})+C^{ep}_{1111} \end{aligned} \tag{6.11}$$

Eq. (6.10) has six roots $\pm z_1$, $\pm z_2$, $\pm z_3$. The notion of surface instabilities means that the deformation is confined close to the surface (6.3), *i.e.* the displacement field is fading exponentially with x, being zero at infinite x, thus $\mathrm{Re}\{z_i\}<0$. Thus if there is a real negative solution for the reduced cubic Eq. (6.10) there is no solution to the surface instability problem. Let z_1, z_2, and z_3 correspond to solutions whose real part is positive. The velocity field then becomes

$$\begin{aligned} v_1&=(A_1e^{-qz_1x}+A_2e^{-qz_2x}+A_3e^{-qz_3x})\sin(qy)\\ v_2&=(K_1A_1e^{-qz_1x}+K_2A_2e^{-qz_2x}+K_3A_3e^{-qz_3x})\cos(qy) \quad \text{where} \end{aligned} \tag{6.12}$$

$$K_i=\frac{\bar{q}^2 C^{p}_{1111}(l-z_i^2)+(z_i^2-C^{ep}_{1111})}{\bar{q}^2 C^{p}_{2211}z_i(1-z_i^2)+(1+C^{ep}_{1122})z_i} \qquad i=1,2,3 \tag{6.13}$$

The boundary condition $\dot{\sigma}_{12}=0$ at $x=0$ yields

$$A_1(K_1+z_1)+A_2(K_2+z_2)+A_3(K_3+z_3)=0 \tag{6.14}$$

The boundary condition $\dot{\sigma}_{22}=0$ at $x=0$ yields

$$\begin{aligned} &(A_1+A_2+A_3)C^{ep}_{2211}-(K_1z_1A_1+K_2z_2A_2\\ &\quad +K_3z_3A_3)C^{ep}_{2222}-l^2_{21}(-A_1-A_2-A_3\\ &\quad +A_1z_1^2+A_2z_2^2+A_3z_3^2)b^2/L^2-l^2_{22}(K_1z_1A_1+K_2z_2A_2+K_3z_3A_3\\ &\quad -K_1A_1z_1^3-K_2A_2z_2^3-K_3A_3z_3^3)b^2/L^2=0 \end{aligned} \tag{6.15}$$

Finally, the boundary condition for the double traction $\dagger_{22}=0$ at $x=0$ yields

$$A_1 K_1 z_1^2 + A_2 K_2 z_2^2 + A_3 K_3 z_3^2 = 0 \tag{6.16}$$

Eqs. (6.14)-(6.16) form a homogeneous system of equations in terms of the constants A_1, A_2 and A_3. To arrive at non-trivial solutions, the determinant of the system must vanish. This provides the surface instability condition.

Estimation of internal length through surface instability analysis

The critical value of c' is the lowest one that satisfies the above bifurcation condition. It is interesting to note that the critical c' is a function of the internal length l and the wave number q or the wavelength W. Thus different critical values of c' are obtained for different values of the dimensionless wave number $\bar{q}^2$. Obviously, $\bar{q}^2=0$ corresponds to long wave length and $\bar{q}^2=1$ corresponds to the shortest physically meaningful wavelength. Figure 6 shows values of critical c' as a function of $\bar{q}^2$ for the associative K-H case. Since surface instabilities are only possible prior to shear-banding the results of Figures

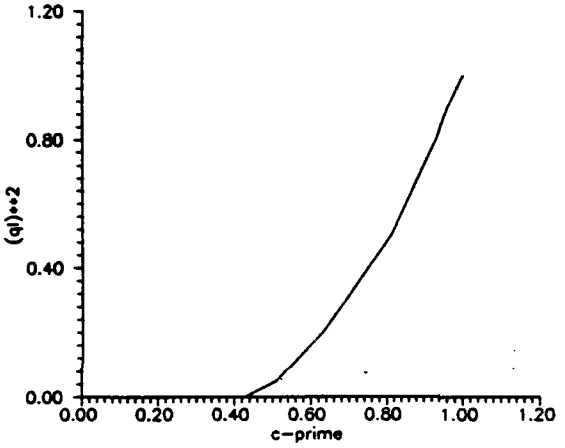

Fig. 6. – Influence of micro-structure on surface instability.

5 and 6 are then only physically meaningful if the post-peak stress-strain curve is concave. as is typical for brittle materials like concrete [Willam *et al.*, 1985]. Accordingly the internal length l can be determined if one considers the eigen-strain field ε_{22} for $\bar{q}=1$ as shown in Figure 7 [F & V, 1991]. From this figure it follows that a significant % of attenuation is obtained at a depth of approximately 51. From experiments, the depth of the surface degradation zone can be determined, e. g. spalling depth for brittle materials, which then provides l.

Conclusion

The gradient modification of the K-H plasticity presented herein regularizes the classical one and this could be used for post-failure computations in brittle material structures.

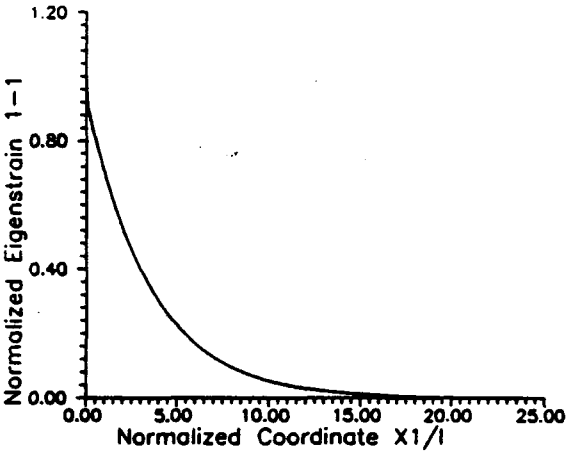

Fig. 7. – Normalized depth X_1/l versus eigenstrain ε_{11}, $\bar{q}=1$.

The single introduced new parameter is the internal length l. We have provided here in principle two independent methods for estimating l. Thus the present theory is amendable to a callibration/verification procedure. This could be done by Non Destructive techniques as explained in [Frantziskonis, 1991].

Acknowledgements

This paper is a partial result of research supported by the National Science Foundation (CES-8800381 for I.V.) and the Air Force Office of Scientific Research (AFOSR 890460, Bolling AFB for G.F.).

REFERENCES

AIFANTIS E. C., 1978. A Proposal for Continuum With Microstructure, *Mech. Res. Comm.*, 5, 139-145.

AIFANTIS E. C., 1985, Mechanics of Microstructures-I. Continuum Mechanics, Thermodynamics, and Microstructures, *Proc. Intl. Centre Theor. Phys.*, Trieste, Italy, V. Balakrishnan and C. E. Botani Eds., 314-346.

BAZANT Z. P., 1984, The Impricate Continuum and its Variational Formulation, *J. Engr. Mech. Div.*, ASCE, 110, 1693-1712.

EISENBERG M. A., 1970. On the Relation Between Continuum Plasticity and Dislocation Theories, *Int. J. Engng. Sci.*, 8, 261-271.

FRANTZISKONIS G., 1991, work in progress.

FRANTZISKONIS G., VARDOULAKIS I., 1991, On the Micro-Structure of Surface Effects and Related Instabilities, *Eur. J. Mech., A Solids*, submitted.

HUTCHINSON J. W., TVERGAARD V., 1981, Shear Band Formation in Plane Strain, *Int. J. Solids Struct.*, 17, 451-470.

MINDLIN R. D., 1964, Micro-Structure in Linear Elasticity, *Arch. Rational Mech. Anal.*, 4, 50-78.

MUHLHAUS H. B., AIFANTIS E. C., 1991, *A Variational Prnciple for Gradient Plasticity*, submitted for publication.

NEEDLEMAN A., 1979, non-normality and Bifurcation in Plane Strain Tension and Compression, *J. Mech. Phys. Solids*, 27, 231-254.

SHREYER H. L., 1990, Analytical Solutions for Nonlinear Strain-Gradient Softening and localization. *J. Appl. Mech.*, ASME, 57, 522-528.

SCHREYER H. L., CHEN Z., 1986, One-Dimensional Softening With Localization, *J. Appl. Mech.*, ASME, 53, 791-797.

TVERGAARD V., 1978, Effect of Kinematic Hardening on Localized Necking in Biaxially Stretched Sheets. *Int. J. Mech. Sci.*, 20, 651-658.

VARDOULAKIS I., 1984, Rock Bursting as a Surface Instability Phenomenon, *Int. J. Rock Mech. Min. Sci. Geomech. Abstr.*, 21, 137-144.

VARDOULAKIS I., AIFANTIS E. C., 1991, A Gradient Flow Theory of Plasticity for Granular Materials, *Acta Mechanica*, in press.

WILLAM K., HURLBUT B., STURE S., 1985, Experimental and Constitutive Aspects of Concrete Failure, *Finite Elements Analysis of Reinforced Concrete Structures*, Proc. of Seminar, Tokyo, Japan May 21-24, 1985, 226-254.

(Manuscript received February 8, 1991;
accepted September 16, 1991.)

Surface Effects in Brittle Materials and Internal Length Estimation

by

G. Frantziskonis
Department of Civil Engineering and Engineering Mechanics
University of Arizona
Tucson, Arizona 85721

The concept of state of degradation is employed as a tool to study the effect of initial material (structure) inhomogeneity and the implications of surface (skin) effects on brittle material response. The initial heterogeneity pattern and its growth under external load is studied experimentally via ultrasonic scanning measurements on prismatic simulated rock samples subjected to mechanical load. Numerical solutions are compared with the experimental results. The skin effects are also studied experimentally through the spatial variation of dissipated energy within the samples tested. In addition, microstructure considerations highlight the skin effect and its implications. The material length for the simulated rock is estimated (for load levels up to peak load) through the experimental observations which yielded l≈0.24 inches (0.61 cm). The analytical solution of a simple problem including microstructure considerations for the same material yielded l≈0.21 inches (0.53 cm). This paper integrates and extends the recent work of the author and co-workers.

INTRODUCTION

Structures composed of brittle materials such as rock and concrete are observed to damage when loaded towards failure. The term degradation is often associated with damage evolution. The effect of degradation on material response has recently received intensive attention. Ultrasonic measurements have been used successfully as indicators of such internal degradation. Unfortunately, it is very difficult to detect and characterize individual microcracks using non-destructive techniques. However, it is feasible to measure the effect of distributed microcracks, since microcracks affect the attenuation of ultrasonic pulses and the velocity of the transmitted wave. In the light of appropriate modeling, attenuation measurements can provide an average quantitative measure of degradation. Here, average is considered with respect to the material volume that the ultrasonic wave passes through.

For decades, laboratory tests on brittle materials sought to achieve a homogeneous state of stress and deformation on samples subjected to uniaxial load. However, even under ideal testing conditions, the heterogeneous micro-structure of the material yields an inhomogeneous deformation field from the early straining stage, Fairhurst and Cook [1], Hudson et al [2], Read and Hegemier [3], Yukutake [4]. In a uniaxial compression test the density of microcracks rapidly proliferates, leading to vertically aligned microcracks resulting in gross slabbing of material from the tractionless surfaces. The development of microcracks is more pronounced near the free surface, because the constraints to crack development are smaller than those in the interior. In addition, near surface microcracks have a greater tendency towards crack propagation, for the simple reason that the stress intensity factor for such a crack is higher than for a same size or even bigger crack in the interior.

It is difficult to observe and/or simulate the spatial pattern of material heterogeneity at the microscale. Undoubtedly, important information can be extracted from models simulating the material microstructure and spatial randomness of heterogeneity. In a recent such study, Bazant et al [5], micromechanics based conclusions are relevant to the findings in this study.

ULTRASONIC MEASUREMENTS

The purpose of the ultrasonic tests [6] was to study the spatial variation of degradation mechanisms in brittle material subjected to mechanical load. For this purpose ultrasonic measurements were taken at several locations of each sample in the direction transverse to the applied compressive load. Thus the spatial variation of internal microcracking was studied.

Figure 1 shows the schematic of the test system

for ultrasonic measurements on specimens subjected to external mechanical load. The ultrasonic measurement procedure is described first. The pulser section of the instrument generates short, high-amplitude repetitive voltage pulses of controlled energy. The pulse is applied to an ultrasonic transducer, which by virtue of its piezoelectricity vibrates mechanically at its resonant frequency. The transmitted pulses are received either by the transmitting transducer after partial or total reflection (pulse-echo method), or by a separate receiving transducer (through-transmission method). The voltage signals produced by the receiving transducer are amplified by the receiver section. The amplified signal is available, on the oscilloscope, as an output for direct measurements.

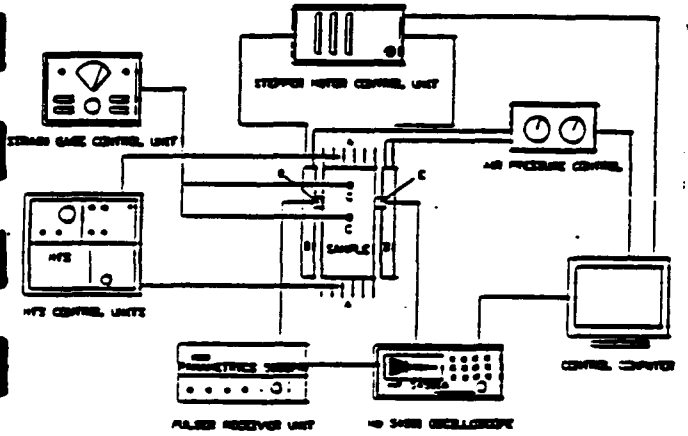

FIG 1. Schematic of the Test System for Ultrasonic Measurements while Samples are Subjected to Mechanical Load; A: External Load Applied Through MTS Frame, B: Device for Movement of Transducers, C: Strain Gages, D: Transmitting Transducer, E: Receiving Transducer.

The ultrasonic transducers used (D, E in Fig. 1) were the P/N Z-10016-3, Zevex Inc., Salt Lake City, Utah, resonant frequency of 50 Khz. The diameter of each transducer is 1.5 inches (1 inch = 2.54 cm). With these characteristics, the waves produced are appropriate for transmission through brittle attenuating materials like the one tested. In order to take ultrasonic measurements at several locations in a sample subjected to mechanical load, it was necessary to develop an automated scanning system. Appropriate computer controlled devices were developed for the automated movement of the transducers. Data at various locations of the samples were extracted from the oscilloscope and the pulser-receiver.

The system for the movement of the transducers described above was mounted on an MTS testing machine, figure 1. This allowed acquisition of ultrasonic measurements while the sample was subjected to external mechanical load from the MTS frame. Three series of prismatic samples were tested. For all samples the hight (H) was 5 inches (12.7 cm) and the depth (D) was 1.3 inches (3.302 cm). For the three series, the width (W) of the samples was 3.0, 3.5 and 4.0 inches (7.62, 8.89 and 10.16 cm), respectively. The ultrasonic pulse was transmitted through the depth (D) at different locations of the sample. Load was applied parallel to the height (H). The material specimens were made of simulated rock and were cast in aluminum molds with casting direction parallel to the height. This material was developed [7] through a parametric variation of various components such as sand, cement and plaster of Paris, and air entraining agent. The following combination was used: sand:cement:plaster of Paris:water = 15:2:3:4, by volume.

Energy Considerations

Consider a structure (specimen) subjected to external mechanical load, figure 2. As load increases, the sample experiences degradation. Within the volume V of the structure we identify an elementary volume dV_i with cross-sectional area dF_i perpendicular to the direction of the ultrasonic wave transmission. For piezoelectric ultrasonic transducers of diameter d, $dF_i = \pi d^2/4$. Let Q_i be the dissipated energy due to degradation progression in dV_i. We can write, in general

$$Q_i = \gamma R_i^n \qquad (1)$$

where R_i is a measure of degradation within dV_i and γ is the dissipated energy per unit of R_i. As an initial estimation, for simplicity, we consider n=1.

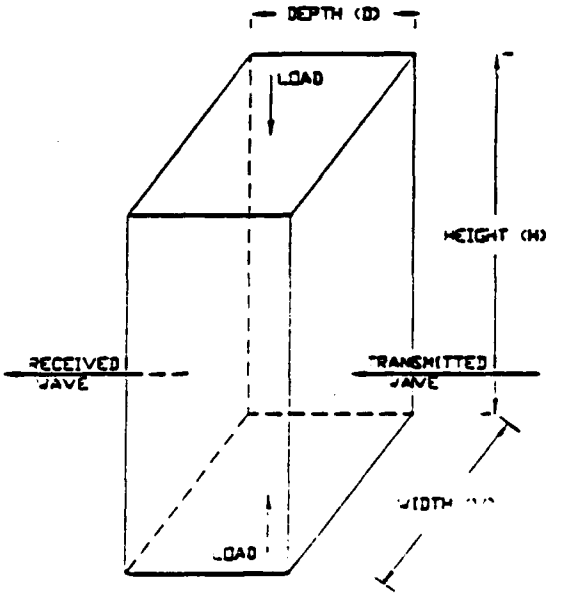

FIG 2. Prismatic Samples WxHxD Showing Direction of external Load and of Ultrasonic Wave.

Let an ultrasonic pulse be transmi

dV_i. Let zero (0) denote the state of the sample where no external load is applied. Let the energy of the received (after transmission through dV_i) ultrasonic wave at zero state be E_{0i}. Let the energy of the received wave at a deformed state be E_i. Due to the degradation progression in dV_i the attenuation of the transmitted wave changes. We can write, in general

$$\Delta E_i = E_{0i} - E_i = c\, R_i \tag{2}$$

where c is the transformation coefficient relating degradation R_i to ultrasonic wave attenuation ΔE_i. From (1) and (2) we obtain

$$\Delta E_i = \frac{c}{\gamma} Q_i = a\, Q_i \tag{3}$$

Equation (3) indicates that the local (within dV_i) ultrasonic attenuation is proportional to the local degradation dissipated energy; here local pertains to the fact that the ultrasonic wave passes through volume dV_i. For the specimens tested, volume dV_i is of cylindrical shape of diameter d=1.5 inches (3.81 cm) and depth D=1.3 inches (3.302 cm).

The speed of an ultrasonic P-wave in an elastic material can be related to the Young's modulus E and Poisson's ratio ν as

$$c_l = \sqrt{\frac{E}{\rho} \frac{1-\nu}{(1+\nu)(1-2\nu)}} \tag{4}$$

where c_l is the ultrasonic wave speed and ρ is the material density. The material examined in [6] shows inelastic response from the early straining stages. For strains up to the peak the Young' modulus (from the unloading/reloading slope) was found [6, 7] to be approximately 180,000 psi (1240 MPa) and ν=0.3. The initial density of all samples tested was 0.066 lbm/in^3 (1.825 g/cm^3). For these values, if for the time being we assume that Eq. (4) is valid, we obtain c_l = 37,664 in/s (957 m/s), thus for a sample depth of 1.3 inches (3.302 cm) the transit time is 33.8 μs. The transit time measured in the experiments was initially 34 μs with 0.5 μs accuracy of the time measurement. The pulse velocity remained constant while the sample was loaded and changed only when the external load was close to the peak. This is consistent with results obtained for hardened paste and mortar specimens [8], and for concrete specimens [9]. However, as discussed subsequently, the attenuation of the pulse showed significant changes from the early straining stages.

The average energy, E_i, of a received ultrasonic wave is proportional to the square of its maximum amplitude. Mathematically, we can write

$$E_i = \beta A_i^2 \tag{5}$$

$$E_{0i} = \beta A_{0i}^2 \tag{6}$$

where A is the maximum absolute voltage of the received wave while the sample is under external load, A_{0i} is the maximum absolute voltage of the received wave before any external load is applied, and β is a constant relevant to the electromechanical characteristics of the receiving transducer. From Eqs. (2) and (6), it follows that

$$\Delta E_i = \beta (A_{0i}^2 - A_i^2) = \beta G \tag{7}$$

From equations (3) and (7) we conclude that the dissipated energy Q_i is proportional to the difference $G = A_{0i}^2 - A_i^2$. For this reason, in all measurements presented in the following, from [6, 10], by the term dissipated energy we imply the difference $G = A_{0i}^2 - A_i^2$. However this term could be replaced by "ultrasonic pulse attenuation," or "intensity reduction."

Before we present typical results from the ultrasonic experiments we present the theory for damage and surface degradation growth; the goal is to compare the experimental results with theoretical ones based on material degradation considerations. Since this theory has been presented elsewhere, Frantziskonis and Desai [11-13], only the necessary background for completeness of this paper is presented.

DAMAGE AND SURFACE DEGRADATION

Adopting the notation used in [11-13] the constitutive equations are written, in incremental form as

$$\dot{\sigma}_{ij} = L_{ijkl}\, \dot{\epsilon}_{kl} - \dot{r}(\sigma_{ij}^u - \sigma_{ij}^d) \tag{8}$$

where

$$L_{ijkl} = (1 - r)\, C_{ijkl}^u + r C_{ijkl}^d$$

r is a scalar representing the ratio of damaged to intact volume, C_{ijkl}^u, C_{ijkl}^d is the constitutive tensor for the intact (topical) and for the damaged part respectively. Further, an evolution law for $\dot{r}$ is defined and it is directly related to failure where r reaches a critical value r_{cr}. A simple and effective law can be written as

$$\dot{r} = f(\epsilon_{ij})\dot{\epsilon}_{ij} \tag{9}$$

Based on the physical interpretation of damage and failure criteria the function f can be specified. For the numerical results presented a specific form of f has been used, and it is given subsequently.

Surface degradation is induced by microstructural

inhomogeneity and its growth is initially stable. It is important to mention that there is certain evidence that this phenomenon acts as a trigger effect on the shear band appearing in a specimen. The sudden growth of surface degradation results in the occurrence and development of shear bands penetrating into the body. In the remaining of this section a brief description of the theory for surface degradation is given. Details of this theory have been presented in [11-13], so here we only provide the background necessary for the numerical results. Damage distribution at the edge of a body where surface degradation is of importance, is expected to be significantly different from the damage distribution far from the edge (in the body). Here we consider that damage at the edge due to surface effects is additive to the damage accumulation calculated as if no surface effects were present. So at the edges, a small volume ΔV_e is subdivided into an intact part ΔV_{ei} and into a fractured part ΔV_{ed}. We consider that the above subdivision holds for a distance ρ from the edge, ρ being a positive real number dependent on the material properties, the geometry, and load acting on the body. Distance ρ is defined as

$$\rho = a\left[\int_c W ds - l\right] \tag{10}$$

where W is a weighting function (the simplest case calls for W=unity and even this case has been shown to provide satisfactory results), a is a material constant determinable from test results on different size specimens, l is the so-called material length, and c is the path of maximum (absolute) principal compressive stress. Material related parameter ρ defines a new characteristic length. It is defined as that specimen size so that the whole specimen is in the surface degradation zone.

MICRO-STRUCTURE OF SURFACE EFFECTS

In this section, as described in details in [14], based on Mindlin's theory for material micro-structure interesting surface effects under conditions of equilibrium are studied. The governing field equations for uniaxial plane deformations are considered. Then, surface instability analysis shows non uniform deformations for a layer of specified distance from the surface. Material micro-structure introduces a singular perturbation to the original Hill and Hutchinson problem; here we introduce a single perturbation parameter and we obtain a "dispersion" law for the surface buckling load. It is found that surface degradation and skin effects can be attributed to localized surface buckling instabilities. Experimental information on skin effects can provide an estimation of the internal material length.

Theoretically, it has been predicted that a homogeneously strained body with tractionless surfaces develops surface undulations or waves. This phenomenon is known as surface instability Biot [15], Hill & Hutchinson [16], Vardoulakis [17]. In a more general formulation, conditions for the so-called complementary condition, Benallal et al, [18], for governing instabilities at the boundary of a solid have been established. Since there are not physical length quantities in the continuum formulation of the problem, the wavelength of the surface instability mode remains arbitrarily short or long. The exponential decay beneath the surface is also arbitrary since it depends on the surface wavelength variation.

Buckling under plane strain conditions due to horizontal compression of an elastic, anisotropic half-space containing co-planar cracks at arbitrary locations has been analyzed recently by Vardoulakis and Papamichos [19]. It is demonstrated that the critical buckling stress decreases dramatically as the distance between the free surface and the cracks diminishes. Further the influence of cracks far from the surface has very little or no influence on the buckling stress. From these results it can be seen that a surface layer exists for which the presence of cracks influences the buckling stress significantly. In a sense this layer is the nonhomogeneous, bursting part of the material. In a recent paper, Papamichos et al [20] have demonstrated, using a newly developed apparatus and a micromechanical model of surface parallel cracks, that surface instabilities lead to exfoliation in Indiana limestone.

Mindlin's theory for microstructure is employed as a tool to explain important surface related phenomena. In this context, a restricted continuum formulation is achieved. The theory is formulated and the governing equations for uniaxial plane deformations are solved. The solution is compared to classical surface instability analysis. Finally, a parameter analysis is performed and the properties that influence surface instability are discussed.

In [21] Mindlin formulated a general and extremely powerful theory for micro-structure in linear elasticity. If one is interested in surface effects under conditions of equilibrium, specific higher order terms of the general theory can be identified. Then a simplified theory results which gives light to important surface related phenomena.

Consider a material volume V, with boundary surface S, with x_i, i=1,2,3 the rectangular components of the material position vector. The displacement of a material particle is u_i. Embedded in each material particle there is assumed to be a micro-volume V' with micro-displacement u_i. The

placement gradient of the micro-medium is

$$\psi_{ij} = u_{i,j} \tag{11}$$

where a comma denotes spatial derivative. The macro-strain is defined as usual

$$\epsilon_{ij} = \frac{1}{2}(u_{i,j} + u_{j,i}) \tag{12}$$

and also a relative deformation is

$$\gamma_{ij} = u_{j,i} - \psi_{ij} \tag{13}$$

and a micro-deformation gradient is

$$\kappa_{ijk} = \psi_{jk,i} \tag{14}$$

Utilizing the principle of virtual work, dynamic quantities dual to the above kinematic ones are defined

$$\delta W = \tau_{ij}\,\delta\epsilon_{ij} + \sigma_{ij}\,\delta\gamma_{ij} + \mu_{ijk}\,\delta\kappa_{ijk} \tag{15}$$

where τ_{ij} is the Cauchy stress σ_{ij} is the relative stress and μ_{ijk} is double stress. The first index of μ_{ijk} designates the normal to the plane across which the component jk acts. For example μ_{111} is a double force per unit area (tensile or compressive) acting on a unit area on the plane transverse to axis 1. The variational equation of motion is established [21] and the twelve general equilibrium equations follow from it and can be written, in rate form

$$\dot{\tau}_{ij,i} + \dot{\sigma}_{ij,i} = 0 \tag{16}$$

$$\dot{\mu}_{ijk,i} + \dot{\sigma}_{jk} = 0 \tag{17}$$

Then the relative stress can be eliminated from the rate-equilibrium equations

$$\dot{\sigma}_{jk} = -\dot{\mu}_{kij,i} \tag{18}$$

We define the equilibrium stress as

$$\dot{\pi}_{ij} = \dot{\tau}_{ij} + \dot{\sigma}_{ij} = \dot{\tau}_{ij} - \dot{\mu}_{kij,k} \tag{19}$$

The twelve traction boundary conditions are

$$\dot{t}_i = n_i\,(\dot{\tau}_{ij} + \dot{\sigma}_{ij}) \tag{20}$$

$$\dot{T}_{jk} = n_i\,\dot{\mu}_{ijk} \tag{21}$$

where n_i is the outward normal to the boundary surface, t_i is external force on the boundary and T_{ij} is the boundary couple force.

A particular case of Mindlin's continuum is the so-called restricted continuum; i.e. a micro-homogeneous material for which the macroscopic strain coincides with the micro-deformation. This leads to a vanishing relative deformation rate, and, accordingly to a rate of micro-deformation gradient that coincides with the strain-rate gradient.

The weak formulation of the balance law of linear momentum together with the appropriate set of boundary conditions is achieved through the principle of virtual work. In accordance with [21] we first define the virtual work of internal forces $\delta W^{(i)}$, i.e.

$$\delta W^{(i)} = \tau_{ij}\,\delta\epsilon_{ij} + \mu_{ijk}\,\delta\kappa_{ijk} \tag{22}$$

This work equation postulates that the Cauchy stress is dual in energy to the macroscopic strain and that the double stress is dual in energy to the gradient of the strain. Since there is no relative deformation rate, the relative stress is workless. The virtual strain and its gradients are computed straight forward from a virtual displacement field.

With expression (22) for the local variation of the virtual internal work done by the stress, we can compute the corresponding variation for a material volume V from the relation

$$\Delta W^{(i)} = \int_V \delta W^{(i)}\,dV \tag{23}$$

The surface S of the considered volume V is divided into two complementary parts S_u and S_σ such that on S_u kinematic data whereas on S_σ static data are prescribed. In classical continua these are constraints on displacements and tractions, respectively. Since second-grade models introduce second strain gradients into the constitutive description, additional kinematic data must be prescribed on S_u. With the displacement already given in S_u, only its normal derivative with respect to that boundary is unrestricted. This means that on S_u the normal derivative of the displacement should also be given; i.e.

$$u_i = w_i \text{ and } Dv_i = r_i \text{ on } S_u \tag{24}$$

where $D=n_{k,k}$ is the derivative in the direction normal to the (smooth) boundary with local unit normal n_k.

For the computation of the virtual work of external forces $\Delta W^{(e)}$ we have to consider not only the surface tractions but also the work of the double forces. Following these considerations, the virtual work of external forces becomes

$$\Delta W^{(e)} = \int_S (t_i\,\delta u_i + R_i\,D\,\delta u_i)\,dS$$

where t_i and R_i are surface tractions and double forces, respectively. From the virtual work equation $\Delta W^{(i)} = \Delta W^{(e)}$ we finally derive field equations

$$\tau_{jk,j} - \mu_{ijk,ij} = 0 \tag{26}$$

and the corresponding boundary conditions

In order to solve the boundary value problem defined above, additional equations relating the stresses and double stresses to the strain, relative deformation and to the micro-deformation gradient must be included. These are specific to the material and are the constitutive equations.

Surface Instabilities

Consider the problem depicted in figure 3 [14].

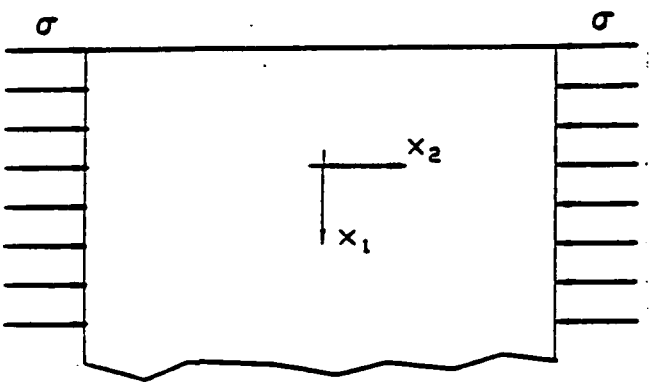

FIG 3. Half Space Under Compressive Load.

Starting from a stress-free state C_0, the structure is stressed uniaxially, under plain strain conditions. Let C be the resultant configuration. In order to study the stability of continued equilibrium in C, the existence of non-homogeneous infinitesimal transition, C→C', is investigated, with C being the reference configuration. The equilibrium in C is unstable if an unbounded, non-periodic solution exists. The equilibrium stress tensor, π_{ij} can be written as a function of co-rotational stress $\dot{\pi}^R_{ij}$

$$\dot{\pi}_{ij} = \dot{\pi}^R_{ij} + \dot{\omega}_{ik}\,\pi_{kj} - \pi_{ik}\,\dot{\omega}_{kj} \tag{27}$$

where $\dot{\omega}_{ij}$ is the rate of rotation tensor

$$\dot{\omega}_{ij} = \frac{1}{2}\,(\dot{u}_{i,j} - \dot{u}_{j,i}) \tag{28}$$

For the plain-strain problem of figure 3 we assume incrementally linear constitutive equations for the Cauchy stress-rate

$$\begin{aligned} \dot{\tau}_{11} &= 2\mu^{*}\,\dot{\epsilon}_{11} + (1-\sin\phi)\dot{p} \\ \dot{\tau}_{22} &= 2\mu^{*}\,\dot{\epsilon}_{22} + (1+\sin\phi)\dot{p} \end{aligned} \tag{29}$$

$$\dot{\tau}_{12} = 2\mu\,\dot{\epsilon}_{12}$$

where

$$\dot{\epsilon}_{ij} = \frac{1}{2}\,(v_{i,j} + v_{j,i}),\ v_i = \dot{u}_i \tag{30}$$

and p is the hydrostatic stress. The quantity $4\mu^{*}$ is the instantaneous tangent modulus and μ is the instantaneous shear modulus for shearing parallel to the coordinate axes, and ϕ is the mobilized friction angle. Material parameters μ, μ^{*} and ϕ are, in general, dependent on the histories of deformation. The particular dependence is specified later. However, the range of these parameters is important for specifying the solution regime for the surface instability problem [14].

The constitutive equation for the double stress rate is written as

$$\dot{\mu}_{111} = \mu l^2 \dot{\epsilon}_{11,1} \tag{31}$$

A dimensional analysis shows that l has dimension of length and as shown subsequently this quantity is important for the surface instability problem.

Equilibrium can be expressed in terms of the equilibrium stress rate

$$\begin{aligned} \dot{\pi}_{11,1} + \dot{\pi}_{12,2} - \tau_{22}\,\dot{\omega}_{21,2} &= 0 \\ \dot{\pi}_{21,1} + \dot{\pi}_{22,2} - \tau_{22}\,\dot{\omega}_{21,1} &= 0 \end{aligned} \tag{32}$$

ant $\tau_{22} = \sigma$, σ being the external applied stress, figure 3. From the two equilibrium equations (32) by introducing a stream function Ψ such that

$$v_1 = \Psi_{,2} \quad v_2 = -\Psi_{,1} \tag{33}$$

we obtain

$$-L^2\Psi_{,221111} + \Psi_{,1111} + b\Psi_{,1122} + c\Psi_{,2222} = 0 \tag{34}$$

where the expressions for b, c, L^2 are given in [14]. Differential equation (34) is a singular perturbation of the original (resulting without micro-structure considerations) as discussed by Hill and Hutchinson [16] and others. Following Biot [15], plane strain surface instabilities can be analyzed [14]. From the solution of (34) it is concluded that the integration constants must satisfy the corresponding characteristic equation, which together with the boundary conditions provides solution to the eigenvalue problem. For such a solution the expressions for μ and must be specified. A one parameter family stress-strain curves of the power law type is assumed, thus the stress-strain curve from a plain strain uniaxial compression is given by

$$\frac{\tau}{\tau_0} = \left[\frac{\gamma}{\gamma_0}\right]^N \tag{35}$$

where N is a constant between zero and one, τ_0 and γ_0 are arbitrary reference values of τ and γ respectively, γ is the second is the second invariant of the deviator tensor of ϵ_{ij}, and τ is the second invariant of the deviator tensor of σ_{ij}. For this kind of hardening function the shear moduli μ and $\overset{*}{\mu}$ are expressed as

$$\mu = \frac{\tau}{\gamma} \qquad \overset{*}{\mu} = N\mu \tag{36}$$

The mobilized friction angle ϕ is expressed as [17]

$$\sin\phi = \frac{M\left[\frac{\gamma}{\gamma_c}\right]^N}{1+M\left[\frac{\gamma}{\gamma_c}\right]^N} \tag{37}$$

where subscript c denotes value at failure and M is a constant related to the strength ratio (uniaxial strength in tension over uniaxial strength in compression). Figure 4 shows the eigenstrain field for N=0.2, n=1 and M=0 (non-frictional material). Similar eigenstrain field was obtained for N=0.2, n=1 and M=0.43 (frictional material). For the example of figure 4 we recognize that a significant % of attenuation is obtained at a depth of $5l$.

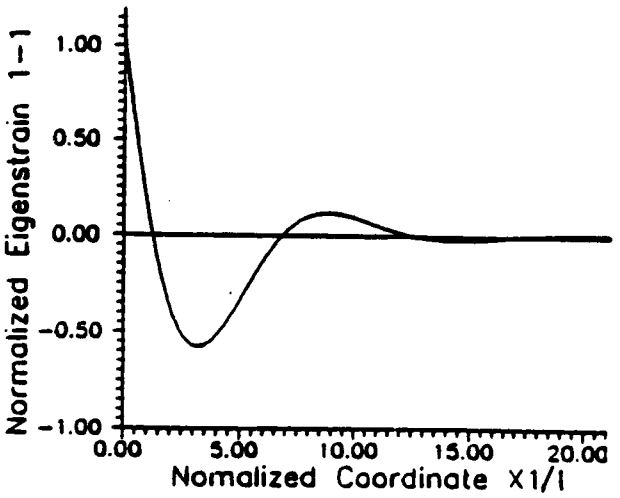

FIG 4. Normalized Depth X_1/l versus eigenstrain. N=0.2 n=1 M=0. (a) X_1/l vs ϵ_{11}, (b) X_1/l vs ϵ_{111}

From experiments in various materials the depth of the surface degradation zone can be obtained which then provides l. Such a calibration of the internal material length l is paramount if one wishes to solve problems with eigenstresses in laminated materials by using constitutive equations of the present type. Notice that these equations constitute the simplest possible generalization of elastoplastic relations for such media.

MATERIAL LENGTH ESTIMATION AND INITIAL HETEROGENEITY

From references [12,13] the value of α=0.21 was estimated. For the specimens tested [6], equation (10) reduces to

$$\rho = \alpha\,(H - l) \tag{38}$$

where H is the specimen height. From the test results reported in [6], distance ρ can be estimated from the dissipated energy distribution within the samples tested. From the test results it seems that the concentration of G close to the free surfaces is distinguishable and can be approximated to about one inch. Then, from Eq. (9) l≈0.24 inches.

Surface instability analysis shows nonuniform deformation for a layer of specified distance from the surface. It was identified that a significant percentage of the nonuniform deformation is obtained at a depth of $5l$. Then if we consider that the nonuniform deformation, in an average nonstatistical sense is about one inch, the internal length l is estimated to be 0.21 inches.

Initial heterogeneity is considered herein via the concept of state of degradation. In order to show how theoretical results can be compared to the experimental ones from ultrasonic scanning we consider the following. Figure 5 shows the contour of initially (without any external load) received ultrasonic energy for sample S4.

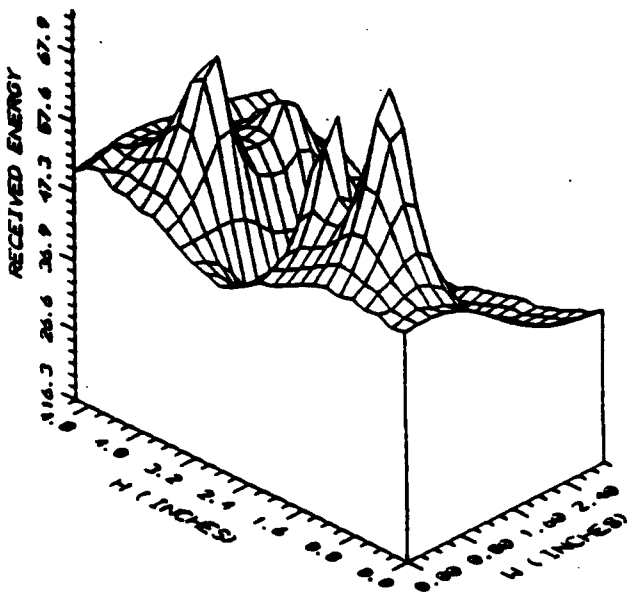

FIG 5. Contour of Initially Received Ultrasonic Energy (Joules) for Sample S4.

A similar pattern is assigned for the initial val[illegible]

the damage variable r. Then the finite element method is used to model the response of the specimen under external load. For sample S4, the damage growth pattern obtained at load P such that $P/P_{peak} = 0.46$ is shown in figure 6a, and, for comparison, the ultrasonically dissipated energy at $P/P_{peak} = 0.45$ is shown in figure 6b.

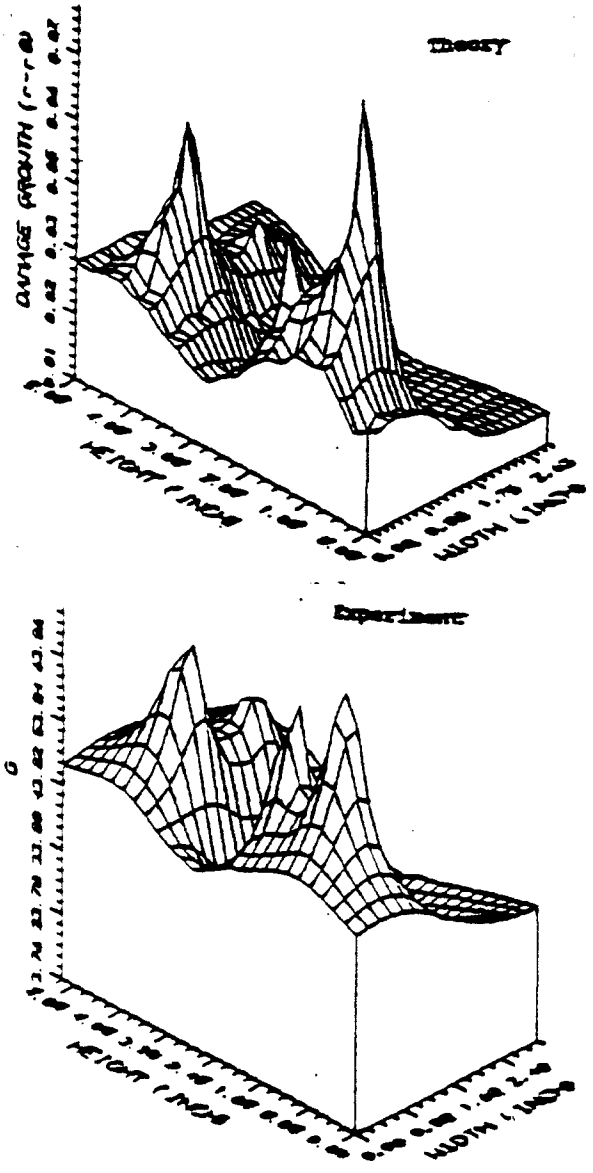

Figure 6: (a)Damage Growth Distribution for Sample S4 at $P/P_{peak} = 0.46$, (b) Distribution of G for Sample S4 at $P/P_{peak} = 0.45$.

An important outcome here is that the initially high intensity regions seem to dissipate energy at a (much) higher rate than the low intensity ones. Both experiment and theory clearly depict this behavior. Similar results were obtained for the rest of the specimens tested and typical results are presented in [10].

ACKNOWLEDGMENTS

A part of the research herein was supported by Grant No. AFOSR-890460 from the Air Force Office of Scientific Research, Bolling AFB. and Grant N0. MSS-9157237 from the National Science Foundation. The help and discussion of Mr. F.F. Tang and Dr. C.S. Desai is gratefully acknowledged.

REFERENCES

1. Fairhurst, C. and Cook, N.G.W., "The Phenomenon of Rock Splitting Parallel to the Direction of maximum Compression in the Neighborhood of a Surface," *Proc. First Intl. Congress Rock Mech.*, Lisbon, 1, 687-692, (19660.
2. Hudson, J.A., Brown, E.T. and Fairhurst, C., "Shape of the Complete Stress-Strain Curve for Rock," *Proceedings 13th Symposium. Rock Mechanics* University of Illinois, Urbana, (1971).
3. Read, H.E. and Hegemier, G.A., "Strain Softening of Rock Soil and Concrete - A Review Article," *Mechanics of Materials*, 3, 271-294, (1984).
4. Yukutake, H., "Fracturing Process of Granite Inferred From Measurements of Spatial Velocities and Temporal Variations in Velocity During Triaxial Deformations," *J. of Geophysical Res.*, 94, 15639-15651, (1989).
5. Bazant, Z.P., Tabbara, M.R., Kazemi, M.T. and Pijaudier-Cabot, G., "Random Particle Model for Fracture of Aggregate or Fiber Composites," *J. Engr. Mechs. Div.*, ASCE, 116, 1686-1705, (1990).
6. Frantziskonis, G. Desai, C.S., Tang, F.F. and Daniewicz, D., "Degradation Mechanisms in Brittle Materials Investigated By Ultrasonic Scanning," *Engr. Fract. Mechs.*, Submitted.
7. Desai, C.S., Kundu, T. and Wang, G., "Size effect on damage in Progressive Softening Process for Simulated Rock," *International Journal for Numerical and Analytical Methods in Geomechanics*, 14, 509-517, (1990).
8. Shah, S.P. and Chandra, S., " Mechanical Behavior of Concrete Examined by Ultrasonic Measurements," *Journal of Materials*, 5, 550-563, (1970).
9. Spooner, D.C. and Dougill, J.W., "A Quantitative Assessment of Damage Sustained in Concrete During Compressive Loading," *Mag. Concrete Research*. 27, 171-178, (1975).
10. Tang, F.F., Frantziskonis, G. and Desai, C.S., "Heterogeneity and Degradation in Brittle Materials," to be submitted.
11. Frantziskonis, G., "Damage and Free Edge Effects in Laminated Composites. Energy and Stability Propositions," *Acta Mechanica*, 77, 213-230, (1989).
12. Frantziskonis, G. and Desai, C.S., 1991, "Surface Degradation Mechanisms in Brittle Material Structures, *Intl J. Fracture*, 48, 231-[illegible]

(1991).
13. Frantziskonis, G., Tang, F.F. and Desai, C.S., "Borehole Scale Effects and Related Instabilities," *Engr. Fracture Mechanics*, 39, 377-389, (1991).
14. Frantziskonis, G. and Vardoulakis, I., "On the Micro-structure of Surface Effects and Related Instabilities," *Europ. J. of Mechanics*, to appear.
15. Biot, M.A., 1965, *Mechanics of Incremental Deformations*, Wiley, New York.
16. Hill, R. and Hutchinson, J.W., "Bifurcation Phenomena in the Plane Tension Test," *J. Mech. Phys. Solids*, 23, 239-264, (1975).
17. Vardoulakis, I., "Rock Bursting as a Surface Instability Phenomenon," *Int. J. Rock Mech. Sci. & Geomech. Abstr.*, 21, 137-144, (1984).
18. Benallal, A., Billardon, R. and Geymonat, G., "Some Mathematical Aspects of the Damage Softening Rate Problem," In Cracking and Damage, J. Mazars and Z.P. Bazant Edts., 247-258, (1989).
19. Vardoulakis, I. and Papamichos, E., 1991, "Surface Instabilities in Elastic Anisotropic Media with Surface Parallel Griffith Cracks," *Int. J. Rock ech. Min. Sci. & Geomech. Abstr.*, submitted
20. Papamichos, E., Labuz, J.F. and Vardoulakis, I., "Surface Instabilities in Brittle Rock," *Int. Conf. on Micromech. of Failure of Quasi-brittle Matls.*, Albuquerque, New Mexico, June 6-8, (1990).
21. Mindlin, R.D., "Micro-Structure in Linear Elasticity," *Arch. Rational Mech. Anal.*, 4, 50-78, (1964).

HETEROGENEITY, MICROSTRUCTURAL SURFACE EFFECTS AND INTERNAL LENGTH ESTIMATION

G. Frantziskonis
Department of Civil Engineering and Engineering Mechanics
University of Arizona
Tucson, Arizona 85721

ABSTRACT

Recently, the concept of state of degradation has been employed by the author in order to study the effect of initial material (structure) inhomogeneity and the implications of surface (skin) effects on brittle material response. The analysis has revealed the importance of the internal material length, e.g. for assigning the initial random variables according to a material dependent fluctuation scale. Different possibilities for its estimation and/or evolution have been suggested. Here, symbolic computations by computer that resulted in the analytical solution of an instability problem are presented. Such analytical solution without computer had not been obtained in the past because the analytical work is tedious and error prone making it very difficult to pursue. The analytical solution, made possible through symbolic computations, provides significant insight into the problem of skin effects in brittle materials and internal length estimation. This paper summarizes the previous work of the author and co-workers, presents the results of symbolic computations of an instability problem, and interprets the results with respect to material length estimation.

INTRODUCTION

The effect of degradation on brittle material response has received intensive attention. Non-destructive techniques have been (and are being) used as indicators of such internal degradation. Unfortunately, it is very difficult to detect and characterize individual microcracks using non-destructive techniques. However, it is feasible to measure the effect of distributed microcracks through wave techniques such as ultrasonic since microcracks affect the attenuation of ultrasonic pulses and the velocity of the transmitted wave. In the light of appropriate modeling, attenuation measurements can provide an average quantitative measure of degradation. Here, average is considered with respect to the material volume that the ultrasonic wave passes through.

It is difficult to observe and/or simulate the spatial pattern of material heterogeneity at the microscale. Undoubtedly, important information can be extracted from models simulating the material microstructure and spatial randomness of heterogeneity. In a recent such study, [Bazant

et al, 1990], micromechanics based conclusions are important with respect to the problem of material heterogeneity and degradation patterning. In a different approach, the initial heterogeneity and its evolution are studied through random degradation variables and/or heterogeneity data as observed from ultrasonic scanning tests [Yuan 1991, Frantziskonis 1991, Frantziskonis et al 1991]. In [Frantziskonis et al, 1991] the purpose of the ultrasonic tests was to study the spatial variation of degradation mechanisms in a brittle material subjected to mechanical load. For this purpose ultrasonic measurements were taken at several locations of each sample in the direction transverse to the applied compressive load. Thus the spatial variation of internal degradation was studied.

Initial heterogeneity was considered in the dissertation of F.F. Tang [Tang, 1991, Tang and Frantziskonis, 1991, Tang et al 1991], via the concept of state of degradation. In order to show how theoretical results can be compared to the experimental ones from ultrasonic scanning we show (figure 1) the contour of initially (without any external load) assigned state mapped

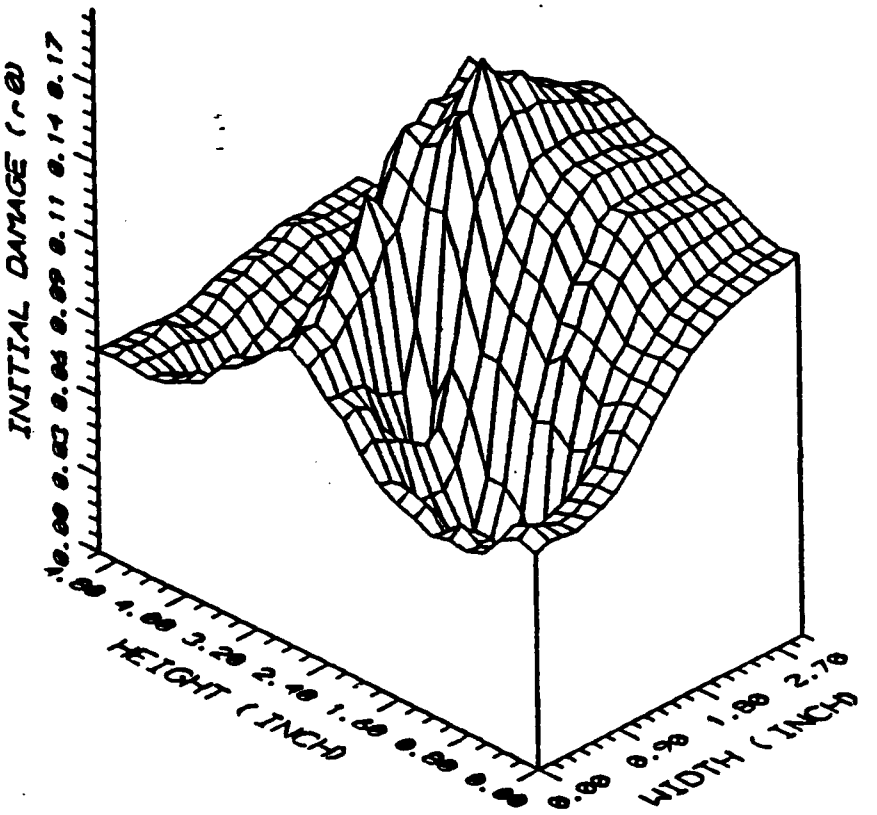

FIG 1: Contour of Initially Assigned State (from Ultrasonic Data) for Sample S4.

from the received ultrasonic energy for a specific sample.

A similar pattern is assigned for the initial value of a damage variable r. Then the finite element method is used to model the response of the specimen under external load. For this sample (S4), the damage growth pattern obtained at load P such that $P/P_{peak}=0.46$ is shown in figure 2a, and, for comparison, the ultrasonically dissipated energy at $P/P_{peak}=0.45$ is shown in figure 2b.

An important outcome of the ultrasonic tests and the FEM solution is that the initially high intensity regions seem to dissipate energy at a (much) higher rate than the low intensity ones. Both experiment and theory clearly depict this behavior. Similar results were obtained for the rest of the specimens tested and further results are presented in [Tang, 1991].

These results, briefly discussed above, have clearly depicted the importance of the internal material length. This is especially true if random variables are used for the description of the initial heterogeneous state of the material. Unfortunately, it ia difficult to identify the initial state

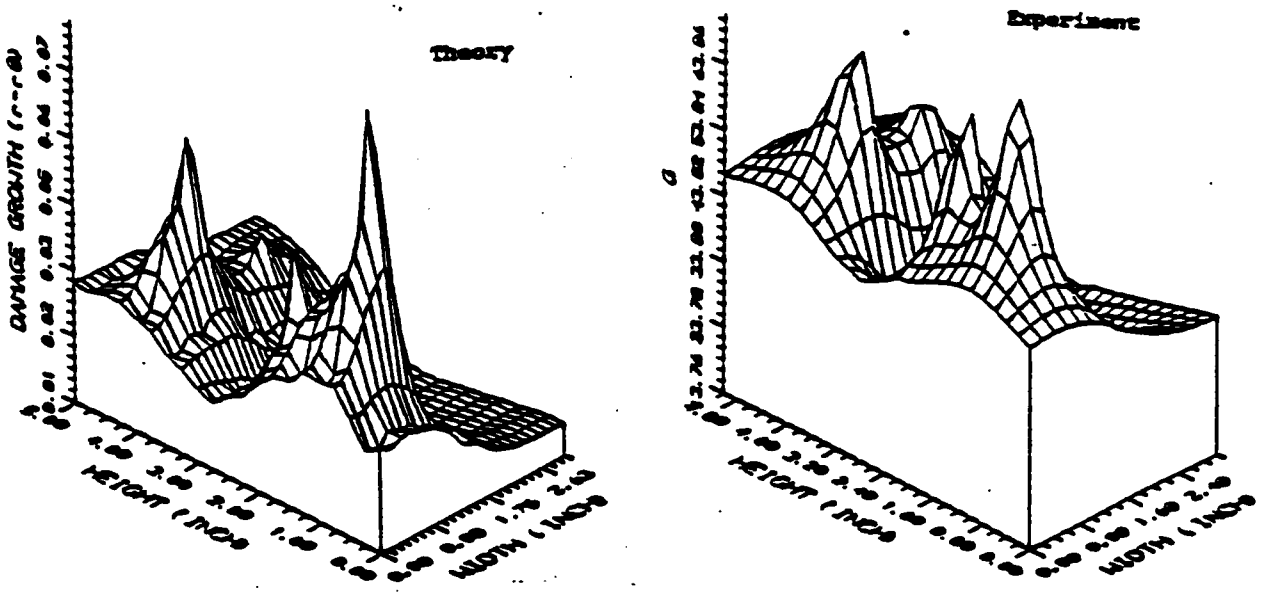

FIG 2: (a) Damage Growth Distribution for Sample S4 at P/P_{peak} = 0.46, (b) Distribution of Dissipated Energy for Sample S4 at P/P_{peak} = 0.45.

of a brittle material structural system. Experimental evidence shows that the initial state of specimens is heterogeneous [Frantziskonis et al, 1991]. Obviously, the heterogeneity fluctuation is scale dependent. The heterogeneity fluctuation length is important and must be identified. It may be appropriate to define the internal material length as the scale fluctuation of material heterogeneity. Then, if "correct" random initial state variables are to be assigned, the scale of fluctuation (material length) must be identified. Since, as shown in [Frantziskonis and Vardoulakis, 1991] surface effects and internal length are closely related, analytical solution of a relevant free-surface problem is presented in the following. Although the homogeneous case is examined (no spatial random variables in the instability problem) the analytical solution provides significant insight into the problem of material length estimation.

SURFACE INSTABILITY ANALYSIS - ANALYTICAL SOLUTION THROUGH SYMBOLIC COMPUTATIONS BY COMPUTER

Surface instability analysis examines the problem of development of surface undulations in a homogeneously strained body with tractionless surfaces [Biot, 1965, Hill and Hutchinson, 1975, Vardoulakis, 1984]. In a more general formulation [Benallal et al, 1989], conditions for the so-called complementary instability at the boundary of a solid have been established. Since there are not physical length quantities in the continuum formulation of the problem, the wavelength of the surface instability mode remains arbitrarily short or long. The exponential decay beneath the surface is also arbitrary since it depends on the surface wavelength variation. Analytical solutions for surface instability are difficult to obtain. Usually, semi-analytical procedures are used. The analytical procedure is brought up to a point beyond which the solution is sought through numerical techniques. In [Vardoulakis, 1984] the instability criterion is formulated in terms of the ratio of the strengths of the material in uniaxial extension and compression, and in terms of an appropriate hardening parameter. Despite the significance of the relevant material properties, the semi-analytical solution does not allow one to study the influence of material properties on surface instability. In addition, the problem of material parameter evaluation through surface instability analysis becomes difficult. However, as demonstrated herein, symbolic computations by computer made the analytical solution of the problem possible. This together with the graphics capabilities of the software used provide significant insight into the surface instability problem, its implications, and the influence and significance of the material parameters.

Before presenting the results from the symbolic computations we present a formulation for material micro-structure and the accompanied instability analysis. As shown below, microstructure introduces a singular perturbation to the original surface instability problem, and the single perturbation parameter is the internal length l. By setting $l = 0$ the analysis reduces to classical surface instability analysis [Vardoulakis, 1984]. Thus quantitative information about skin effects can be obtained from such analysis, as compared to the "classical" surface instability one.

MICRO-STRUCTURE CONSIDERATIONS - ANALYTICAL SOLUTION THROUGH SYMBOLIC COMPUTATIONS BY COMPUTER

As described in details in [Frantziskonis and Vardoulakis, 1991] based on Mindlin's theory for material micro-structure interesting surface effects under conditions of equilibrium can be studied. The governing field equations for uniaxial plane deformations are considered. Then, surface instability analysis shows non uniform deformations for a layer of specified distance from the surface. Material micro-structure introduces a singular perturbation to the original Hill and Hutchinson problem; here a single perturbation parameter is introduced and a "dispersion" law for the surface buckling load is obtained. It is found that surface degradation and skin effects can be attributed to localized surface buckling instabilities. Experimental information on skin effects can provide an estimation of the internal material length l.

Mindlin's theory for microstructure is employed as a tool to explain important surface related phenomena. In this context, a restricted continuum formulation is achieved. The theory is formulated and the governing equations for uniaxial plane deformations are solved. The solution is compared to classical surface instability analysis. It turns out that when $l=0$ the analysis reduces to the "classical" surface instability one. Finally, a parameter analysis is performed and the properties that influence surface instability are discussed.

Mindlin, 1964, formulated a general and extremely powerful theory for micro-structure in linear elasticity. If one is interested in surface effects under conditions of equilibrium, specific higher order terms of the general theory can be identified. Then a simplified theory results which gives light to important surface related phenomena.

Consider a material volume V, with boundary surface S, with $x_i, i=1,2,3$ the rectangular components of the material position vector. The displacement of a material particle is u_i. Embedded in each material particle there is assumed to be a micro-volume V' with micro-displacement u_i'. The displacement gradient of the micro-medium is

$$\psi_{ij} = u_{ij}' \tag{1}$$

where a comma denotes spatial derivative. The macro-strain is defined as usual

$$\varepsilon_{ij} = \frac{1}{2}(u_{i,j} + u_{j,i}) \tag{2}$$

and also a relative deformation is

$$\gamma_{ij} = u_{i,j} - \psi_{ij} \tag{3}$$

and a micro-deformation gradient is

$$\kappa_{ijk} = \psi_{jk,i} \quad . \tag{4}$$

Utilizing the principle of virtual work, dynamic quantities dual to the above kinematic ones are defined

$$\delta W = \tau_{ij}\delta\varepsilon_{ij} + \sigma_{ij}\delta\gamma_{ij} + \mu_{ijk}\delta\kappa_{ijk} \tag{5}$$

where τ_{ij} is the Cauchy stress, σ_{ij} is the relative stress and μ_{ijk} is double stress. The first index of μ_{ijk} designates the normal to the plane across which the component jk acts. For example μ_{111} is a double force per unit area (tensile or compressive) acting on a unit area on the plane transverse to axis 1. The variational equation of motion is established [Frantziskonis and Verdoulakis, 1991] and the twelve general equilibrium equations follow from it and can be written, in rate form

$$\dot{\tau}_{ij,j} + \dot{\sigma}_{ij,j} = 0 \tag{6}$$

$$\dot{\mu}_{ijk,j} + \dot{\sigma}_{jk} = 0 \tag{7}$$

Then the relative stress can be eliminated from the rate-equilibrium equations

$$\dot{\sigma}_{jk} = -\dot{\mu}_{kij,i} \tag{8}$$

We define the equilibrium stress as

$$\dot{\pi}_{ij} = \dot{\tau}_{ij} + \dot{\sigma}_{ij} = \dot{\tau}_{ij} - \dot{\mu}_{kij,k} \tag{9}$$

The twelve traction boundary conditions are

$$\dot{t}_i = n_j(\dot{\tau}_{ij} + \dot{\sigma}_{ij}) \tag{10}$$

$$\dot{T}_{jk} = n_i\dot{\mu}_{ijk} \tag{11}$$

where n_i is the outward normal to the boundary surface, t_i is external force on the boundary and T_{ij} is the boundary couple force.

A particular case of Mindlin's continuum is the so-called restricted continuum; i.e. a micro-homogeneous material for which the macroscopic strain coincides with the micro-deformation. This leads to a vanishing relative deformation rate, and, accordingly to a rate of micro-deformation gradient that coincides with the strain-rate gradient.

The weak formulation of the balance law of linear momentum together with the appropriate set of boundary conditions is achieved through the principle of virtual work. In accordance with [Mindlin, 1964] the virtual work of internal forces $\delta W^{(i)}$ is defined, i.e.

$$\delta W^{(i)} = \tau_{ij}\delta\varepsilon_{ij} + \mu_{ijk}\delta\kappa_{ijk} \tag{12}$$

This work equation postulates that the Cauchy stress is dual in energy to the macroscopic strain and that the double stress is dual in energy to the gradient of the strain. Since there is no relative deformation rate, the relative stress is workless. The virtual strain and its gradients are computed straight forward from a virtual displacement field.

With expression (12) for the local variation of the virtual internal work done by the stress, we can compute the corresponding variation for a material volume V from the relation

$$\Delta W^{(i)} = \int_V \delta W^{(i)} dV \tag{13}$$

The surface S of the considered volume V is divided into two complementary parts S_u and S_σ such that on S_u kinematic data whereas on S_σ static data are prescribed. In classical continua these are constraints on displacements and tractions, respectively. Since second-grade models introduce second strain gradients into the constitutive description, additional kinematic data must be prescribed on S_u. With the displacement already given in S_u, only its normal derivative with respect to that boundary is unrestricted. This means that on S_u the normal derivative of the displacement may also be given; i.e.

$$u_i = w_i \quad and \quad Dv_i = r_i \ on \ S_u \tag{14}$$

where $D=n_k\partial_k$ is the derivative in the direction normal to the (smooth) boundary with local unit normal n_k.

For the computation of the virtual work of external forces $\Delta W^{(e)}$ we have to consider not only the surface tractions but also the work of the double forces. Following these considerations, the virtual work of external forces becomes

$$\Delta W^{(e)} = \int_S (t_i\delta u_i + R_i D\,\delta u_i)\, dS \tag{15}$$

where t_i and R_i are surface tractions and double forces, respectively. From the virtual work equation $\Delta W^{(i)} = \Delta W^{(e)}$ we finally derive field equations

$$\tau_{jkj} - \mu_{ijkij} = 0 \tag{16}$$

and the corresponding boundary conditions [Frantziskonis and Vardoulakis, 1991].

In order to solve the boundary value problem defined above, additional equations relating the stresses and double stresses to the strain, relative deformation and to the micro-deformation gradient must be included. These are specific to the material and are the constitutive equations.

Surface Instabilities

Consider the problem depicted in figure 3. Starting from a stress-free state C_0, the structure is stressed uniaxially, under plain strain conditions. Let C be the resultant configuration. In order to study the stability of continued equilibrium in C, the existence of non-homogeneous

infinitesimal transition, $C \rightarrow C'$, is investigated, with C being the reference configuration. The equilibrium in C is unstable if an unbounded, non-periodic solution exists. The equilibrium stress tensor, $\mathring{t}_{ij}$ can be written as a function of co-rotational stress $\mathring{t}^{R}_{ij}$

$$\mathring{t}_{ij} = \mathring{t}^{R}_{ij} + \omega_{ik}\pi_{kj} - \pi_{ik}\omega_{kj} \tag{17}$$

where ω_{ij} is the rate of rotation tensor

$$\omega_{ij} = \frac{1}{2}(\dot{u}_{i,j} - \dot{u}_{j,i}) \tag{18}$$

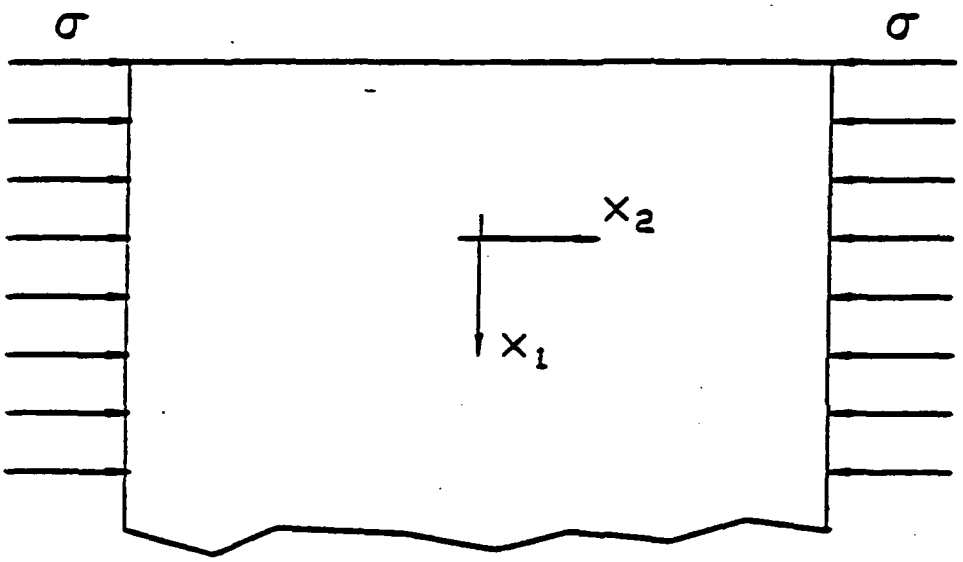

FIG 3: Half Space Under Compressive Load

For the plain-strain problem of figure 3 we assume incrementally linear constitutive equations for the Cauchy stress-rate

$$\begin{aligned} \mathring{t}_{11} &= 2\mu^{*}\dot{\varepsilon}_{11} + (1 - \sin\phi)\dot{p} \\ \mathring{t}_{22} &= 2\mu^{*}\dot{\varepsilon}_{22} + (1 + \sin\phi)\dot{p} \\ \mathring{t}_{12} &= 2\mu\dot{\varepsilon}_{12} \end{aligned} \tag{19}$$

where

$$\dot{\varepsilon}_{ij} = \frac{1}{2}(v_{i,j} + v_{j,i}),\ v_i = \dot{u}_i \tag{20}$$

and p is the hydrostatic stress. The quantity $4\mu^*$ is the instantaneous tangent modulus and μ is the instantaneous shear modulus for shearing parallel to the coordinate axes, and ϕ is the mobilized friction angle. Material parameters μ, μ^* and ϕ are, in general, dependent on the histories of deformation. The particular dependence is specified in the sequence. However, the range of these parameters is important for specifying the solution for the surface instability problem.

The constitutive equation for the double stress rate is written as

$$\dot{\mu}_{111} = \mu l^2 \dot{e}_{11,1} \tag{21}$$

A dimensional analysis shows that l has dimension of length and as shown subsequently this quantity is important for the surface instability problem.

Equilibrium can be expressed in terms of the equilibrium stress rate

$$\begin{aligned} \dot{\pi}_{11,1} + \dot{\pi}_{12,2} - \tau_{22}\dot{\omega}_{21,2} &= 0 \\ \dot{\pi}_{21,1} + \dot{\pi}_{22,2} - \tau_{22}\dot{\omega}_{21,1} &= 0 \end{aligned} \tag{22}$$

and $\tau_{22} = \sigma$, σ being the external applied stress, figure 3. From the two equilibrium equations (22) by introducing a stream function Ψ such that

$$v_1 = \Psi_{,2} \qquad v_2 = -\Psi_{,1} \tag{23}$$

we obtain

$$-L^2\Psi_{,2211} + \Psi_{,1111} + b\Psi_{,1122} + c\Psi_{,2222} = 0 \tag{24}$$

where

$$b = [(\lambda^2+1)(1-\xi_2) - (\lambda^2-1)\xi_1]/(\xi_1+\xi_2)$$

$$c = \lambda^2(\xi_2-\xi_1)/(\xi_1+\xi_2)$$

$$\lambda = \tan(\pi/4+\phi/2), \quad \xi_1 = -\sigma/4\mu^*, \quad \xi_2 = \mu/4\mu$$

$$L^2 = \xi_2 l^2/(\xi_1+\xi_2), \quad n = (m\pi)^2(L/H)^2, \quad \bar{n} = (m\pi)^2(l/H)^2$$

Differential equation (24) is a singular perturbation of the original (resulting without micro-structure considerations) one. Following [Biot, 1965] plane strain surface instabilities can be analyzed. The problem finally reduces to the solution of differential equation (25)

$$(1+n)\hat{u}^{IV} - (m\pi)^2\hat{u}'' + (m\pi)^4 c\hat{u} = 0 \tag{25}$$

subject to the boundary conditions

$$(1+n)\hat{u}''' - (m\pi)^2 P\hat{u}' = 0$$

$$\hat{u}'' + (m\pi)^2\hat{u} = 0 \tag{26}$$

For solution of the above problem the expressions for μ and μ^* must be specified. A one parameter family of stress-strain curves of the power law type is assumed, thus the stress-strain curve from a plain strain uniaxial compression is given by

$$\frac{\tau}{\tau_0} = \left(\frac{\gamma}{\gamma_0}\right)^N \tag{27}$$

where N is a constant between zero and one, τ_0 and γ_0 are arbitrary reference values of τ and γ respectively, γ is the second invariant of the deviator tensor of ε_{ij}, and τ is the second invariant of the deviator tensor of σ_{ij}. For this kind of hardening function the shear moduli μ and μ^* are expressed as

$$\mu = \frac{\tau}{\gamma} \qquad \mu^* = N\mu \tag{28}$$

The mobilized friction angle ϕ is expressed as

$$\sin\phi = \frac{M\left(\frac{\gamma}{\gamma_c}\right)^N}{1+M\left(\frac{\gamma}{\gamma_c}\right)^N} \tag{29}$$

where subscript c denotes value at failure and M is a constant related to the strength ratio (uniaxial strength in tension over uniaxial strength in compression). The above problem is solved through computer symbolic computations. The program <<Mathematica>> [Wolfram Res., 1991] was used and the whole solution procedure is shown in the appendix. In the appendix the total mathematica session has been condensed for compactness. All the input data are given, however. The print out of the uncondensed session is 20 pages long! The length and complication of the procedure as observed from the computer showed clearly why no solution had been obtained before (without computer).

The final solution for the instability problem us obtained from mathematica is as shown in the appendix

$$\gamma^3[8(1+n)M\gamma^N+8(1+n)-n^2]+\gamma^2[8(1+n)M\gamma^N+4n+16N+8nN]-$$

$$\gamma[16N(1-N)+4n+n^2]-n^2-8nN-16N^2=0 \tag{30}$$

and for the case where the internal length $l=0 \rightarrow n=0$ the formulation yields the final solution for the classical surface instability analysis

$$\gamma^3(1+M\gamma^N)+\gamma^2(2N+M\gamma^N)-2\gamma(N-2N^2)-2N^2=0 \tag{31}$$

For the special case of non-frictional material ($M=0$) equation (31) reduces to

$$\gamma^3+2N\gamma^2-2N(1-N)\gamma-2N=0 \tag{32}$$

With the above final form of the surface instability analysis (31)-(32) an overall view of the problem can be obtained.

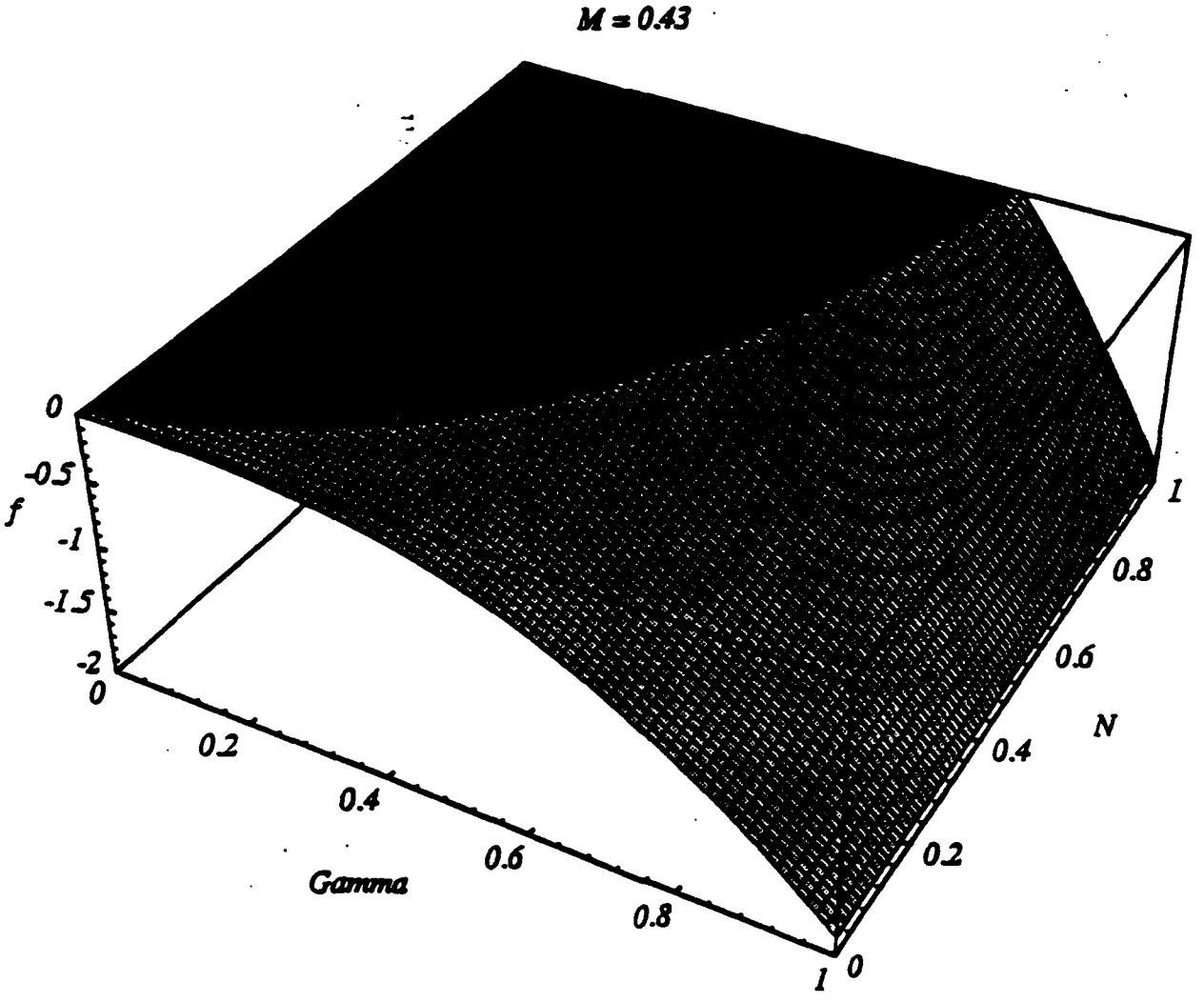

FIG 4a: Influence of N on Instability (f=0)

Figure 4a shows the influence of N on classical instability ($l=n=0$) for a fixed value of $M=0.43$. Here f denotes the left hand side of equation (31). We see clearly that as N increases the strain γ (gamma) at instability increases. The linear case ($N=1$) predicts very high strain at instability ($\gamma=0.81$). The limit case of $N=0$ corresponds to rigid-plastic behavior and instability occurs as soon as the plastic regime is reached. Figure 4b shows an animation of the previous figure where the value of M changes. As can be seen from this figure and equation (31) parameter M influences the strain at instability in a linear fashion. Note that in order to obtain figure 4b (resolution is 80x80 in each figure) by semi-analytical means [Frantziskonis and Vardoulakis,

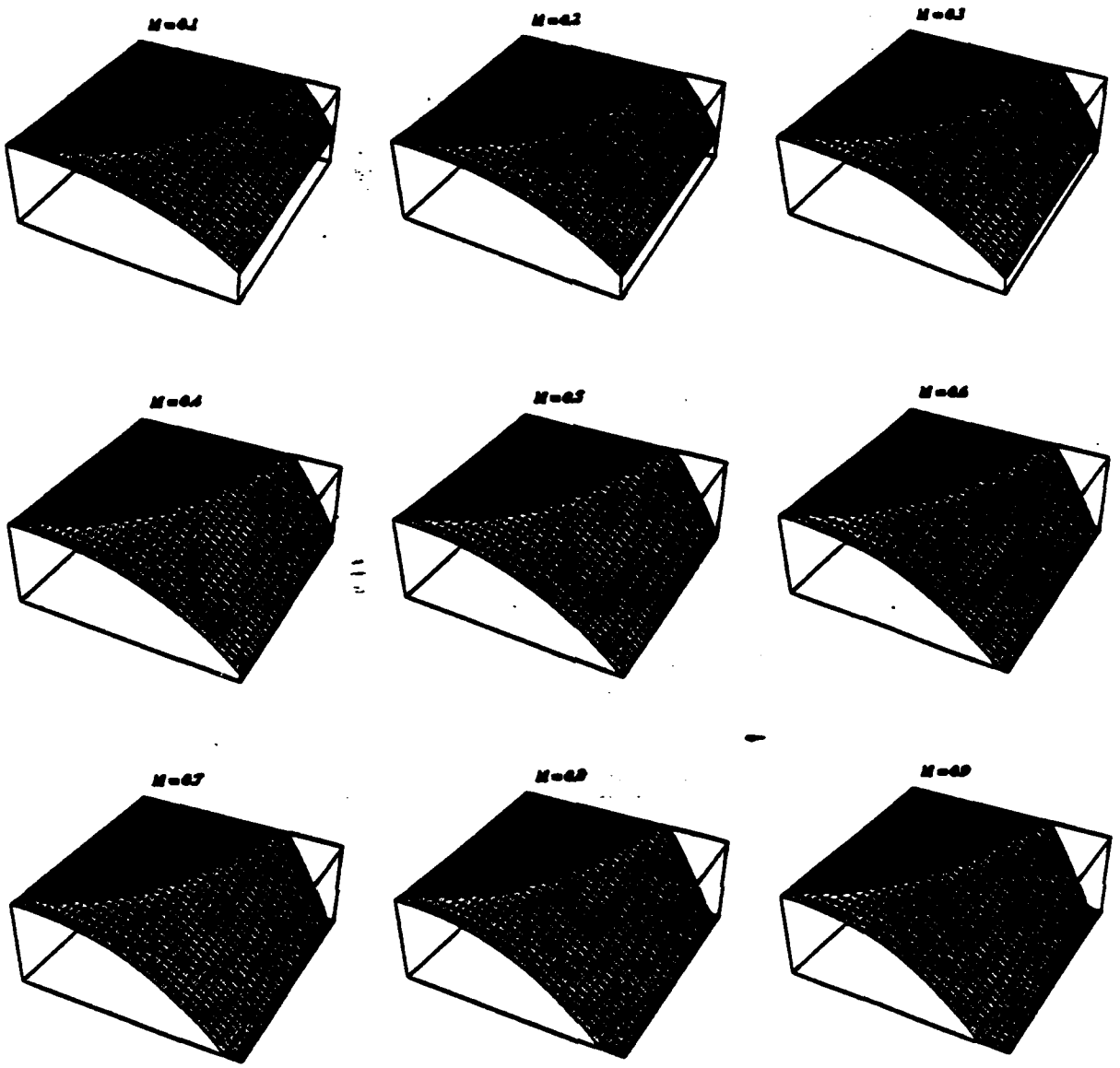

FIG 4b: Animation of Figure 4a

1991] one would need to solve the problem 9x80x80=57,600 times (semi-analytically) or perform 57,600 finite element simulations of the problem!

For the surface instability analysis with micro-structure considerations the problem is more difficult since the value of l is not known appriori. However the final form of the solution (equation (30)) allows us to investigate the influence of all the variables. Figure 5a shows the influence of exponent N on instability, for a specific value of $\bar{n}$ (n-bar). Here, g designates the left hand side of equation (31). Figure 5b shows an animation of figure 5a where the value of n changes.

In order to study the effect of l on instability, we can look at the decay of the strain field, as shown in figure 6. Figure 6b is an animation of figure 6a where the value of $\bar{n}$ changes. We see that if we consider that splitting parallel to the surface will occur at the first peak of the strain field from the free surface, then the distance to the crack varies between l and $3l$. If splitting is considered to occur at that distance from the free surface that significant percent of attenuation occurs, then splitting occurs at about $4l$ to $5l$. The wavelength of the instability problem is difficult to specify, unless detailed experimental data on different size specimens are available. In a series of tests, for example, of varying height of specimen h, it is well known that the stress/strain at instability decreases as h increases. Then, according to figure 5b, the value of $\bar{n}$

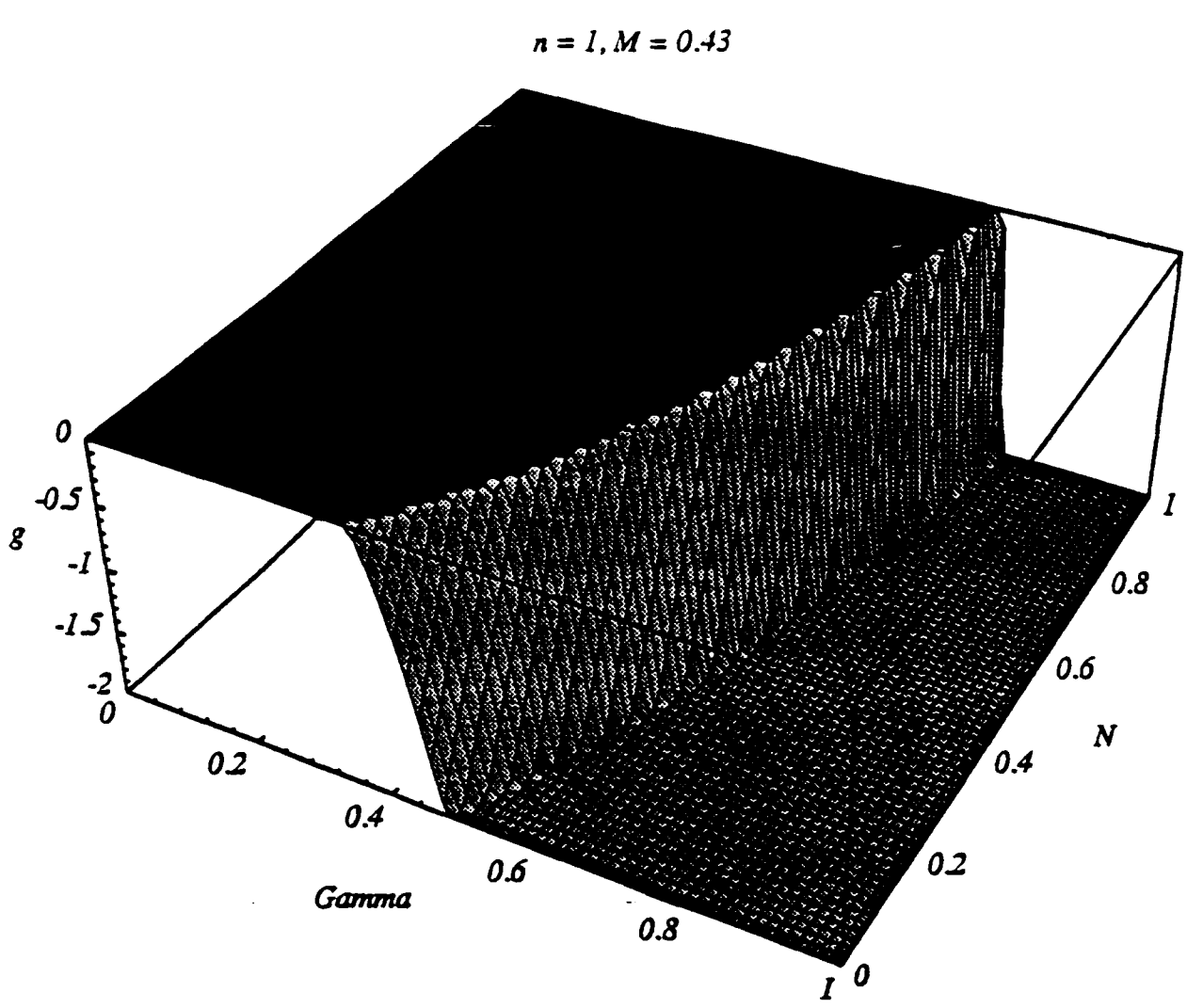

FIG 5a: Influence of N on Instability (f=0) for n-bar=1

decreases as h increases. Then, if we assume that very short specimens will develop a splitting crack at distance l from the free surface, and very long ones at $3l$, by interpolation the value of H for given specimen height h can be specified.

CONCLUSIONS

Symbolic computations by computer have made the analytical solution of an instability problem feasible. The solution, together with the graphics capabilities of the software used provide significant insight into the problem of instability, surface (skin) effects and material length estimation.

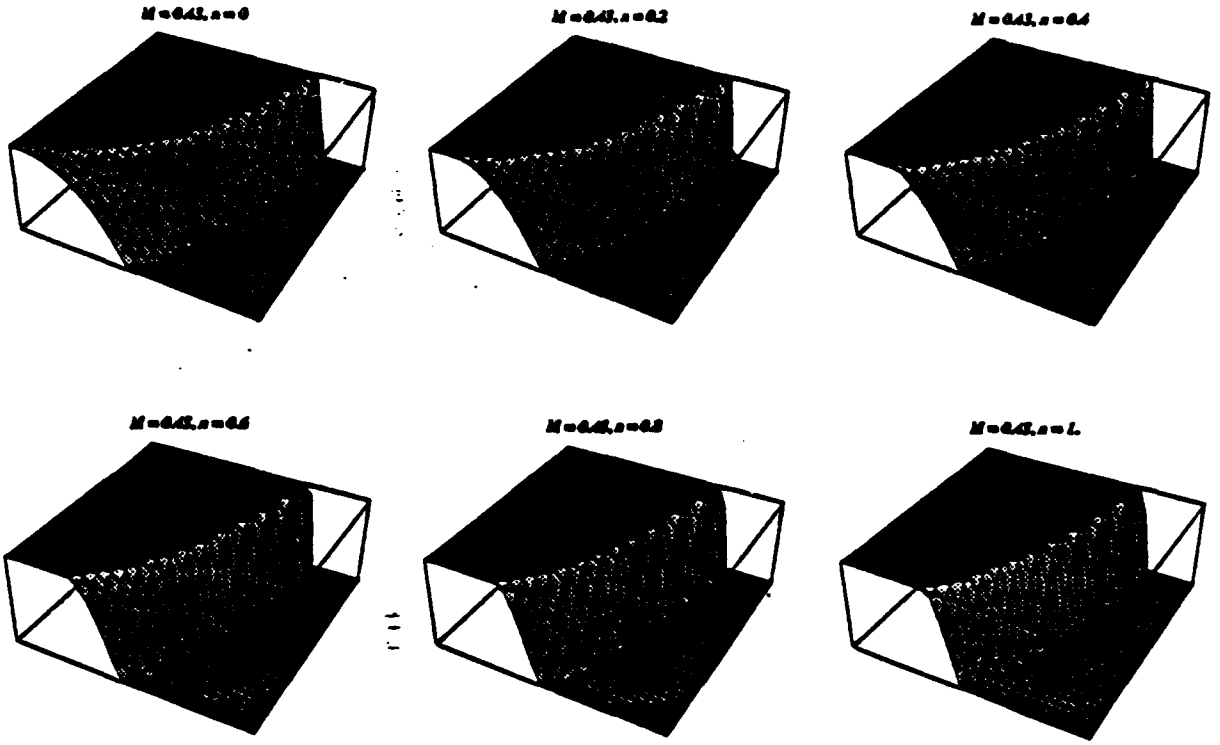

FIG 5b: Animation of Figure 5a

ACKNOWLEDGMENTS

A part of the research herein was supported by Grant No. AFOSR-890460 from the Air Force Office of Scientific Research, Bolling AFB. and Grant N0. MSS-9157237 from the National Science Foundation.

REFERENCES

Bazant, Z.P., Tabbara, M.R., Kazemi, M.T. and Pijaudier-Cabot, G., 1990, "Random Particle Model for Fracture of Aggregate or Fiber Composites," *J. Engr. Mechs. Div.*, ASCE, 116, 1686-1705.

Benallal, A., Billardon, R. and Geymonat, G., 1989, "Some Mathematical Aspects of the Damage Softening Rate Problem," *In Cracking and Damage*, J. Mazars and Z.P. Bazant Edts., 247-258.

Biot, M.A., 1965, *Mechanics of Incremental Deformations*, Wiley, New York.

Frantziskonis, G., 1989,"Damage and Free Edge Effects in Laminated Composites. Energy and Stability Propositions," *Acta Mechanica*, 77, 213-230.

Frantziskonis, G. and Vardoulakis, I., 1991, "On the Micro-structure of Surface Effects and Related Instabilities," *Europ. J. of Mechanics*, 11, 21-34, 1992.

Frantziskonis, G., 1991, "Surface Effects in Brittle Materials and Internal Length Estimation", *Appl. Mech. Rev.*, to appear.

Frantziskonis, G. Desai, C.S., Tang, F.F. and Daniewicz, D.,1991 "Degradation Mechanisms in Brittle Materials Investigated By Ultrasonic Scanning," *Engr. Fract. Mechs.*, in press.

Hill, R. and Hutchinson, J.W., 1975, "Bifurcation Phenomena in the Plane Tension Test," *J. Mech. Phys. Solids*, 23, 239-264.

Mindlin, R.D., 1964, "Micro-Structure in Linear Elasticity," *Arch. Rational Mech. Anal.*, 4, 50-78.

Tang, F.F., 1991, Degradation Instabilities and Heterogeneity in Brittle Materials, *PhD Dissertation*, University of Arizona, Under Preparation

Tang, F.F. and Frantziskonis, 1991, G., paper under preparation.

Tang, F.F., Frantziskonis, G. and Desai, C.S., (1991),"Heterogeneity and Degradation in Brittle Materials," to be submitted.

Vardoulakis, I., 1984, "Rock Bursting as a Surface Instability Phenomenon," *Int. J. Rock Mech. Sci. & Geomech. Abstr.*, 21, 137-144.

Wolfram Research Inc., *Mathematica*, 1991, P.O. Box 6059, Champaign, Illinois 61821-9902.

Yuan, X., 1991, "Random Initial Inhomogeneity in Brittle Materials," *MSc Thesis*, University of Arizona, June 1991.

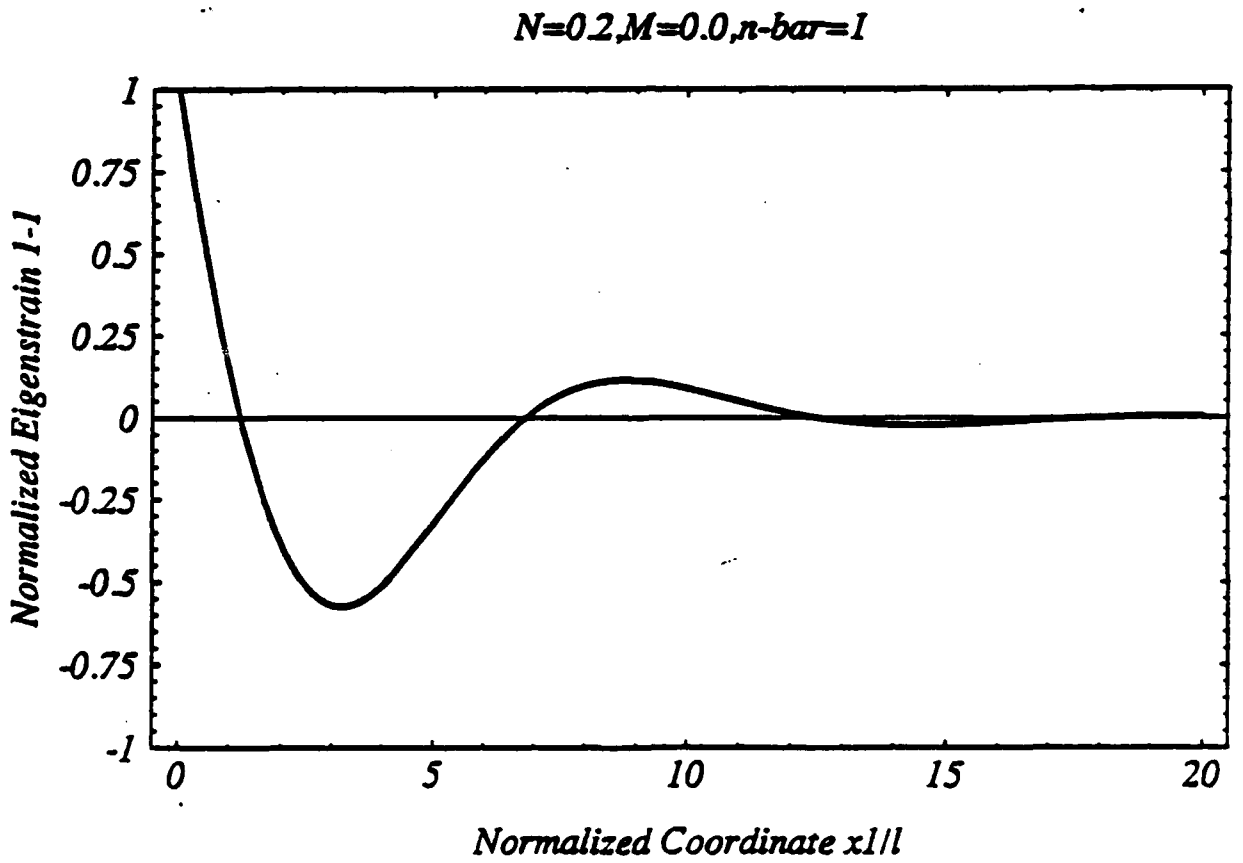

FIG 6a: Decay of EigenStrain at Instability

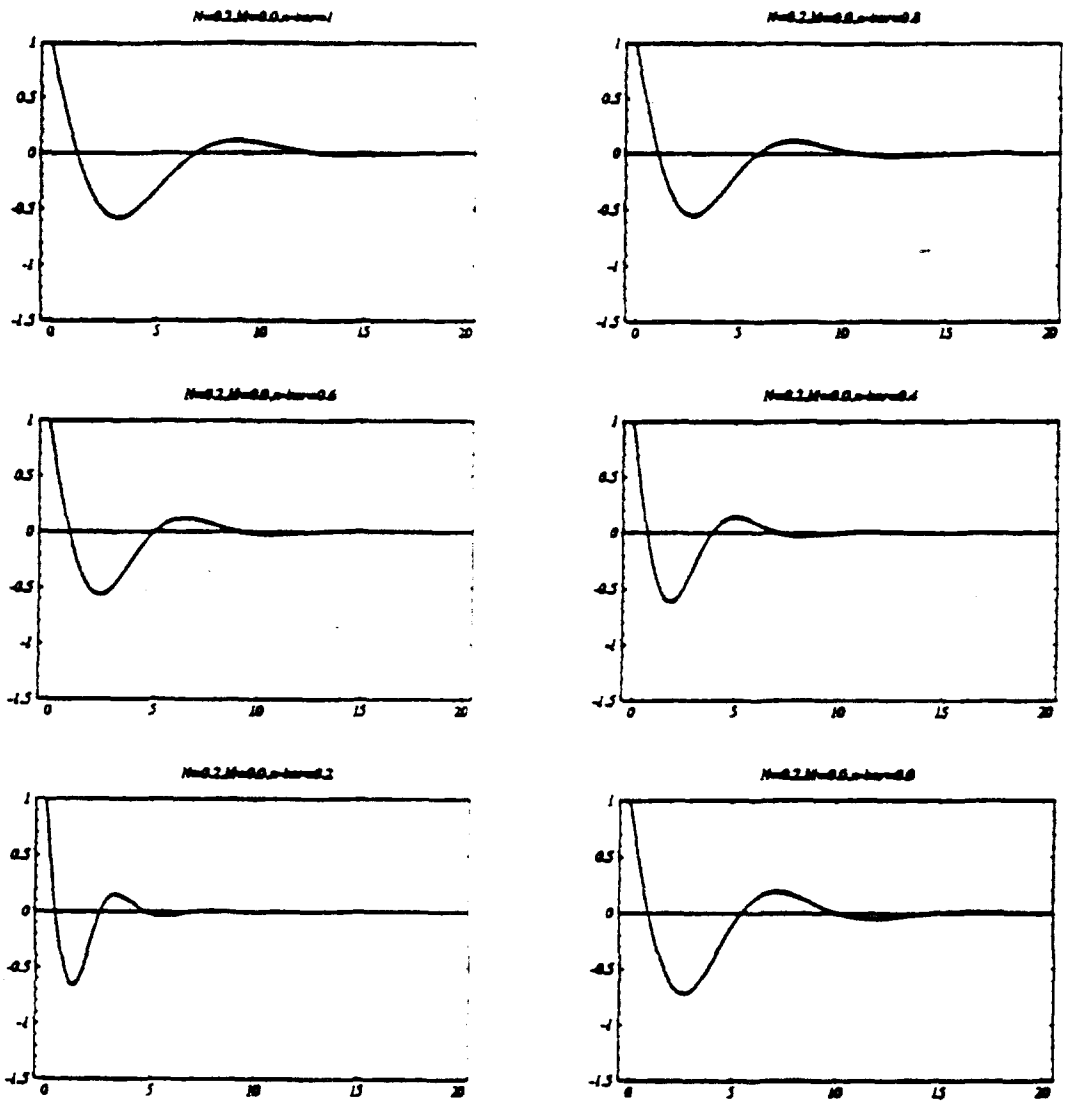

FIG 6b: Animation of Figure 6a

APPENDIX

```
Mathematica 2.0 for MS-DOS 386/7
Copyright 1988-91 Wolfram Research, Inc.
In[1]:= DSolve[(1 + n)u''''[x] - mpi^2 b u''[x] +
        mpi^4 c u[x] == 0, u[x], x] //Short

                                                    C[1]
Out[1]//Short= {{u[x] -> ------------------------------------------ + <<3>>}}
                                                        2
                                (mpi Sqrt[b - Sqrt[b  + <<2>>]] x)/(<<2>>)
                               E
In[2]:= solution = u[x]/.%[[1]];
In[3]:= solution1 = C[1] Coefficient[solution,C[1]] +
        C[3] Coefficient[solution,C[3]];
In[4]:= eqn1 = D[solution1,{x,2}] + mpi^2 solution1
In[5]:= eqn2 = (1 + n) D[solution1,{x,3}] - mpi^2 p D[solution1,x];
In[6]:= x=0;
In[7]:= t11 = Coefficient[Collect[eqn1,C[1]],C[1]];
In[8]:= t12 = Coefficient[Collect[eqn1,C[3]],C[3]];
In[9]:= t21 = Coefficient[Collect[eqn2,C[1]],C[1]];
In[10]:= t22 = Coefficient[Collect[eqn2,C[3]],C[3]];
In[11]:= t11 t22 - t12 t21 //Short
```

```
                          2   mpi  (b + Sqrt[b  + <<2>>])
Out[11]//Short= -((mpi  + --------------------------) <<1>>) + <<1>>
                                  2 (1 + n)

In[12]:= Simplify[%] //Short
Out[12]//Short= <<1>>
In[13]:= temp = Coefficient[Collect[%,mpi^5],mpi^5];
In[14]:= temp1 = temp[[1]];
In[15]:= temp2 = temp[[2]];
In[16]:= temp1^2 - temp2^2 //Short
                                 2                                    2
                (b - Sqrt[b  - 4 c - 4 c n]) <<1>> (b + <<1>> - 2 p)
Out[16]//Short= ------------------------------------------------------ + <<1>>
                                          3
                                   32 (1 + n)

In[17]:= ExpandAll[%]//Short
                       2       2
                -32 b  Sqrt[b  - 4 c - 4 c n]
Out[17]//Short= ------------------------------ + <<23>>
                                 2       3
                  32 + 96 n + 96 n  + 32 n

In[18]:= Simplify[%]//Short
                      2                          2                    2
                Sqrt[b  - 4 c - 4 c n] (-b  + c + <<13>> - n p )
Out[18]//Short= ------------------------------------------------
                                        2
                                 (1 + n)

In[19]:= final1=%;
In[20]:= final2 = final1[[3]];
In[21]:= p = (lambda^2 + 1 + xi1 - xi2)/(xi1 +xi2);
In[22]:= b = ((lambda^2 + 1) (1 - xi2) - (lambda^2 - 1) xi1)/(xi1 + xi2);
In[23]:= c = lambda^2 (xi2 - xi1)/(xi1 + xi2);
In[24]:= final2//Short
In[25]:= Simplify[%]//Short
In[26]:= final3 = %; s =m gamma^nn/(1 + m gamma^nn); lambda =Sqrt[(1+s)/(1-s)];
In[27]:= xi2 = 1/(2nn (1-s)); xi1 = gamma xi2;
In[28]:= final3//Short
In[29]:= Simplify[%]//Short
In[30]:= temp3=%; temp4 = temp3[[3]];
In[31]:= finalsolution = Simplify[temp4]//Short
                          3          2 + nn                          2
Out[31]//Short= -8 gamma  - 8 gamma       m + <<15>> - 16 gamma nn
In[32]:= Collect[%,gamma]//Short
In[33]:= finalsolution
In[34]:= Collect[%,gamma]
          2       3                  nn                    nn        2
Out[34]= n  + gamma  (-8 - 8 gamma   m - 8 n - 8 gamma   m n - n ) + 8 n nn +

          2        2           nn                   nn        2
     16 nn  + gamma  (-8 gamma   m - 4 n - 8 gamma   m n - n  - 16 nn -

                                 2                  2
>       8 n nn) + gamma (4 n + n  + 16 nn - 16 nn )
In[35]:= n = 0;
In[36]:= %%
               3                nn           2           nn                    2
Out[36]= gamma  (-8 - 8 gamma   m) + gamma  (-8 gamma   m - 16 nn) + 16 nn  +

                          2
     gamma (16 nn - 16 nn )
```